Attosecond Ionisation Dynamics in Long Range Potentials

vorgelegt von
Diplom-Physiker
Jivesh Kaushal
geb. New Delhi, Indien

von der Fakultät II - Mathematik und Naturwissenschaften der
Technischen Universität Berlin
zur Erlangung des akademischen Grades
Doktor der Naturwissenschaften
Dr. rer. nat.

genehmigte Dissertation

Promotionausschuss:
Vorsitzender: Prof. Dr. Michael Lehmann
Berichter/Gutachter: Dr. Olga Smirnova
Berichter/Gutachter: Prof. Dr. Andreas Knorr
Berichter/Gutachter: Prof. Dr. David Tannor

Tag der wissenschaften Aussprache: 18 April 2016

Berlin, 2016

Contents

List of Figures

List of Tables

Eidesstattliche Versicherung

Hiermit versichere ich an Eides statt die Dissertation mit dem Titel

Attosecond Ionisation Dynamics in Long Range Potentials

selbstständig verfasst zu haben. Alle benutzten Quellen und Hilfsmittel sind in der Dissertation aufgeführt.

Die Dissertation beinhaltet fünf veröffentlichte Artikel. Ich versichere weiter, dass die Darstellung des Eigenanteils in der Erklärung zu bereits veröffentlichten Teilen der Dissertation zutreffend ist.

Datum/ Unterschrift

Abstract

Strong Field Ionisation has been an active research field for well over five decades, since the pioneering work of L. V. Keldysh. It has offered an unprecedented insight into, and control over, electron dynamics, not only in simple atoms but also in more complex molecular systems, on a time scale down to a few tens of attosecond (1 attosecond = 10^{-18} sec). Analytical theories have been an essential cornerstone for application and research in this subject. For about five decades, one of the main theoretical problems has remained the development of a rigorous analytical description of the interaction of a strongly laser-driven electron with the long-range potential of the atomic or molecular core.

In this dissertation, attosecond dynamics initiated by atomic ionisation in strong, optical to near-infrared laser fields is studied analytically, with the focus on long-range electron-core interaction. The Analytical R-matrix (ARM) method is the central formalism developed rigorously and used for describing ionisation by strong circularly and elliptically polarised long and few-cycle laser pulses.

In particular, we analyse the principle of angular streaking, which maps electron detection angles to instants of ionisation in (nearly) circularly polarised fields and provides the foundation for the so-called attoclock set-up. Angular streaking provides a sensitive probe of attosecond-scale dynamics in strong field ionisation. Establishing an accurate map between photoelectron detection angle and ionisation time is therefore an essential requirement for the attoclock. We discuss the calibration of the attoclock, especially the validity of the standard assumptions used for interpreting current state of the art experiments. We show that these assumptions fail conclusively at the level of accuracy commensurate with modern experiments.

We also propose and describe the Attosecond Larmor Clock – a new method for defining delays in strong field ionisation. Our proposal takes advantage of the Spin-Orbit (SO) interaction. The idea develops and extends the mapping of the phase of electron wave-function to ionisation time from one-photon ionisation to the strong field regime. The evolution of the photoelectron spin as well as the spin of the hole left in the parent atom during ionisation is used to time the ionisation process. Using the example of a noble gas atom it is shown that electron-hole entanglement leads to phase delays which cannot be directly mapped into ionisation time delays. The conventional barrier penetration problem is compared with strong field tunnelling and the role of the ionisation potential in the latter is discussed to define ionisation time delays.

With the aim to complete the general formalism of the ARM method, strong field ionisation from bound atomic states of arbitrary symmetry is also rigorously derived for long-range potentials and applied to noble gas atoms. After calibrating the attoclock setup for p^-/p^+ orbitals in long-range potentials, it is shown that the sense of electron rotation in the initial orbital can be recorded in the attoclock observables: angle- and energy-resolved photoelectron spectra. It opens an exciting opportunity to detect ring currents excited in atoms and molecules using the attoclock set-up.

Finally, we focus on the emission of spin-polarised electrons during ionisation from systems with long-range electron-core interaction potentials. Ionisation by a few cycle, circularly polarised laser field is shown to lead to qualitatively different results for spin polarised electrons produced in short- and long-range potentials. Specifically, we find that interaction with long-range potentials induces asymmetry in the angular distribution of spin polarised electrons, in contrast to the short-range case. Long-range potentials also further accentuate spin-polarisation towards higher energy of direct photoelectron spectrum. The advantage of few-cycle pulses in photoelectron spin polarisation is the control offered via the Carrier Envelope Phase (CEP) phase of the laser pulse. It allows one to steer the direction of spin polarised electrons.

Zusammenfassung

Starkfeldionisation ist seit über fünf Jahrzehnten ein aktives Forschungsgebiet, seit der Pionierarbeit von L.V. Keldysh. Es hat einen noch nie dagewesenen Einblick in, und Kontrolle über die Elektronendynamik in nicht nur einfachen Atomen sondern auch in komplexeren molekularen Systemen geboten, auf einer Zeitskala von nur einigen zehn Attosekunden (1 Attosekunde = 10^{-18} s). Analytische Theorien sind ein wesentlicher Grundstein für die Anwendung und Forschung in diesem Gebiet gewesen. Seit etwa fünf Jahrzehnten ist eines der wichtigsten theoretischen Probleme die Entwicklung einer exakten analytischen Beschreibung der Wechselwirkung eines vom Laserfeld getriebenen Elektrons mit dem weitreichenden Potential des atomaren oder molekularen Kerns geblieben.

In dieser Dissertation wird die Attosekunden-Dynamik ausgelöst durch atomare Ionisation in starken, optischen bis nahinfraroten Laserfeldern analytisch untersucht, mit dem Schwerpunkt auf Elektron-Kern-Wechselwirkungen mit großer Reichweite. Die Analytische R-Matrix (ARM) Methode ist der zentrale Formalismus, der konsequent entwickelt und zur Beschreibung von Ionisation durch zirkular und elliptisch polarisierte lange und Einige-Zyklen Laserpulse angewandt wird.

Insbesondere analysieren wir das Prinzip des winkelaufgelösten Streaking, welches die Detektionswinkel der Elektronen auf die Zeitpunkte der Ionisation in (beinahe) zirkular polarisierten Feldern abbildet und die Grundlage für den sogenannten Attouhr-Aufbau darstellt. Winkelaufgelöstes Streaking stellt eine empfindliche Messmethode der Attosekunden-Dynamik in Starkfeldionisation dar. Die Feststellung einer präzisen Abbildung des Photoelektron-Detektionswinkels auf die Ionisationszeit ist daher eine wesentliche Voraussetzung für die Attouhr. Wir diskutieren die Kalibrierung der Attouhr, insbesondere die Gültigkeit der üblichen Annahmen die für die Interpretation aktueller, hochmoderner Experimente verwendet werden. Wir zeigen, dass diese Annahmen für den Grad der Genauigkeit der in den modernen Experimenten erreicht wird ungültig sind.

Weiterhin schlagen wir die Attosekunden Larmor-Uhr vor – eine neue Methode um Verzögerungen in Starkfeldionisation zu definieren. Unser Vorschlag nutzt die Spin-Bahn-Wechselwirkung aus. Die Idee entwickelt und erweitert die Methode der Abbildung der Phase der Elektronwellenfunktion auf die Ionisationszeit vom Bereich der Einphotonenonisation hin zum Starkfeld-Regime. Die zeitliche Entwicklung des Photoelektronspins sowie des Spins des Lochs, das im Mutteratom während der Ionisation zurückbleibt, wird zur zeitlichen Bestimmung des Ionisationsprozesses genutzt. Am Beispiel eines Edelgasatoms wird gezeigt, dass die Elektron-Loch-Verschränkung zu Phasenverzögerungen führt, die nicht direkt auf Ionisationszeitverzögerungen abgebildet werden können. Das herkömmliche Problem des Durchdringens einer Barriere wird mit dem Starkfeldtunneln verglichen und die Rolle des Ionisationspotentials im letzteren wird diskutiert um Ionisationszeitverzögerungen zu definieren.

Mit dem Ziel den allgemeinen Formalismus der ARM-Methode zu vervollständigen, ist die Starkfeldionisation von gebundenen Atomzuständen mit beliebiger Symmetrie ebenfalls für Potentiale großer Reichweite konsequent hergeleitet und auf Edelgasatome angewandt. Nach der Kalibrierung des Attouhr-Aufbaus für p^-/p^+ Orbitale in weitreichenden Potentialen, wird gezeigt, dass die Richtung der Elektronenrotation im Anfangsorbital in den Attouhr-Observablen erfasst ist: in den winkel- und energieaufgelösten Photoelektronenspektren. Dies eröffnet eine hervorragende Möglichkeit um angeregte Kreisströme in Atomen und Molkülen mittels des Attouhr-Aufbaus zu messen.

Schließlich konzentrieren wir uns auf die Emission von spinpolarisierten Elektronen während der Ionisation von Systemen mit einem weitreichenden Elektron-Kern-Wechselwirkungspotential. Wir zeigen, dass Ionisation durch ein zirkular polarisiertes Einige-Zyklen-Laserfeld zu qualitativ unterschiedlichen Ergebnissen für spinpolarisierte Elektronen führt, abhängig davon ob die die Elektronen in kurzreichenden oder weitreichenden Potentialen erzeugt werden. Im Besonderen finden wir, dass die Wechselwirkung mit weitreichenden Potentialen eine Asymmetrie in der Winkelverteilung der spinpolarisierten Elektronen hervorruft, im Gegensatz zum Fall der kurzreichenden Potentialen. Desweiteren heben Potentiale mit großer Reichweite die Spinpolarisation zu höheren Energien in direkten Photoelektronspektren hervor. Der Vorteil von Einige-Zyklen Pulsen für Photoelektronenspinpolarisation ist die Kontrolle, die sich aus der Träger-Einhüllenden-Phase (CEP) des Laserfeldes ergibt. Diese erlaubt es die Richtung der ultrakurzen spinpolarisierten Elektronenpakete zu steuern.

Acknowledgements

First and foremost, I would like to express my gratitude to my Supervisor, Dr. Olga Smirnova. Her constant and meticulous guidance, patience and encouragement throughout these years have been essential towards these initial accomplishments in my early scientific career. None of it would have been possible, however, if it weren't for Prof. Dr. Misha Ivanov. I am indebted to him beyond words for offering me such a privileged opportunity to work with some of the brightest and most ambitious minds in this field. I am grateful for the support provided by Prof. Dr. Thomas Elsasser, without which my thesis might not be complete today. I have benefitted greatly from the support and friendly guidance provided me at many important and crucial times during these years of my study, by Felipe Morales and Maria Richter. To thank them here is the least I could do to express the inestimable value I harbour for their friendly acquaintance. Working with Lisa Torlina, I have learnt the important lessons of perseverance and dedication which are essential for any pursuit. Her insight and determination have been inspiring equally. Knowing the brilliant, yet humble fellow-PhD students, Valeria Serbinenko and Danilo Brambila, has been a pleasant experience, and I am glad to have had interesting and illuminating discussions which we partook in.

Getting to know the Strong Field community through various conferences and poster sessions has been a great learning experience. A glimpse of state-of-the-art methods available through Quantemol-N, afforded to me by Prof. Dr. Jonathan Tennyson during my secondment at University College London, as well as comprehending the business side of such an enterprise, helped me to better understand the diversity of research topics presented in this field. The discussions that I had the opportunity to have with Prof. Dr. Hugo van der Haart, from Queen's University Belfast, in the technical aspects of numerical R-matrix methods, were my first encounter in briefly confronting the challenges and ingenuity necessary to deal with the complex and intriguing physical processes involved in strong field ionisation of deceptively "simple" atomic systems. I am grateful to have had these, and many other edifying discourses with the foremost authorities in the field, and the young and brilliant scientists likewise.

Chapter 1

Introduction

Tunnelling of particles through a potential barrier is a purely quantum-mechanical phenomenon, which has been studied extensively and thoroughly in various fields, including, but not limited to, solid state physics, cosmology, nuclear physics, atomic and molecular optical physics, and high energy physics. Even after several decades of research on this phenomenon, including several real-world applications based upon it (e.g., scanning tunnelling microscope, tunnelling junctions in semiconductors), there still are many active research domains, both from an academic and commercial point of view, invested on this subject. Among them, tunnelling ionisation of atoms and molecules under the influence of strong, ultrashort laser fields, with intensities in the range of $10^{13} - 10^{20}$ W/cm^2 and durations in pico- (10^{-12} s) to femtosecond (10^{-15} s), and in the recent decade, even the sub-femtosecond domain, is one of rapidly evolving subfields, that studies the concepts related to the dynamics and control of electrons in atoms and molecules on a timescale commensurate with the rapid evolution of the system. A reliable and rigorous theoretical model to understand the underlying physics of the process is essential to investigate, and eventually control, the ionisation of photoelectrons which constitute the Above Threshold Ionisation (ATI) spectrum, or their subsequent dynamics, either leading to recombination generating High-Order Harmonics (High Harmonic Generation, HHG), or higher order scattering effects leading to High-order Above Threshold Ionisation (HATI) [1].

Since the pioneering work of Keldysh [2], followed immediately by the detailed theory on ionisation of atoms in intense, monochromatic, non-resonant laser fields by Perelomov, Popov, Terentév, and Kuznetsov [3–6], strong field physics has progressed tremendously in experimental and theoretical domains. Experimental developments have aided the theoretical pursuits in better understanding the role of atomic or molecular core interaction with the ionising electron, studying their imprints left on the ionisation process, and in turn, allowing for new methods to study electron dynamics and interactions on an attosecond timescale.

We first consider the earlier work and theory of strong field ionisation in this chapter, and the various motivating threads for this thesis. Atomic units are used throughout ($m_e = e = \hbar = 1$), unless otherwise stated.

1.1 Keldysh Theory of Tunnelling Ionisation

Ionisation in the perturbative regime was the first step towards confronting the quantum nature of radiation and matter, leading to the revolutionary ideas that laid the foundation for Quantum Mechanics [7, 8].

Among the many new mathematical techniques developed for this new and counter-intuitive perspective on natural phenomena [9], perturbation theory has been an essential tool for studying light-matter interactions [10–12] and beyond, including quantum field theory and high-energy physics [13]. But what happens when we approach the domain of intense sources of coherent radiation, where the strength of the electric field is commensurate with the field strength found

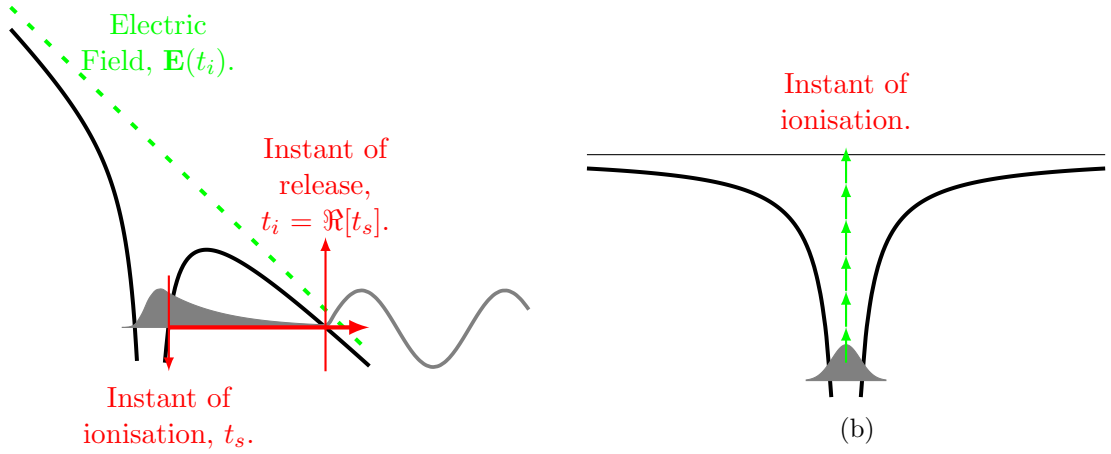

Figure 1.1: Schematic of Strong Field Ionisation. (a) The initial wavepacket rests in the valence bound state of the core potential, which is then modulated by the strong laser field (——). Tunnelling ionisation occurs in the high-intensity, low-frequency domain ($\gamma \ll 1$). The direction of the field maximum, in the present case along the positive-x axis, depresses the potential barrier sufficiently for the electron to escape into the continuum. The instant of ionisation is complex-valued, t_s, and is determined by Eq. (1.18). The electron emerges from under the barrier at time instant $t_i = \Re[t_s]$, **when the complex time transitions to the real time**. (b) Multiphoton ionisation is on the other end ($\gamma \gg 1$) of possible ionisation pathways in strong laser fields. In the weak field the ionisation proceeds through absorption of multiple photons.

within the atom? Does the traditional perturbation theory provide an accurate description of the ionisation process? And what are the dominant pathways through which the electron is liberated from the atom? These were the questions tackled by Leonid V. Keldysh in his seminal paper [2] of strong field laser-matter interactions. The expressions for ionisation rates obtained in [2] naturally led to identification of two ionisation regimes delineated by the Keldysh parameter γ:

$$\gamma = \frac{\omega}{\omega_t} = \frac{\omega\sqrt{2I_p}}{\mathcal{E}_0}, \tag{1.1}$$

where I_p is the binding energy of an electron, required to liberate the electron from the bound state and launch into the continuum, $\mathcal{E}_0$ is the field strength and ω is the angular frequency of the ionising field (for the case of solids, the expression is changed slightly, but that topic is out of the scope of this work. See [2] for further details.). The Keldysh parameter is therefore a measure of the rapidity with which the electron escaping from the atom responds to the changes in the laser field during its cycle. Expressions for probability of ionisation were derived for arbitrary γ, with physical pictures associated with important limits, $\gamma \ll 1$ and $\gamma \gg 1$, depicted schematically in Fig. 1.1a and 1.1b, respectively.

In the former case, $\gamma \ll 1$, the experimental set-up of the atom in a high intensity and non-resonant, low-frequency field was considered. The intensity is sufficiently strong, manifesting the high flux of the photons as a modulation to the classical core-potential barrier, resulting in tunnelling ionisation, where the tail-end of the electron wavefunction burrows through the modulated barrier created under the combined influence of the core and the laser field potential interacting with the electron (Fig. 1.1a). Since the motion is effectively realised in a classical forbidden region, the instant of ionisation t_s, when the electron barges through the barrier, is complex. On emerging from underneath the barrier into the continuum, **which leads to the time-scale settling along the real axis**, the electron is assumed to be free. This assumption is particularly valid for short-range potentials (SRPs) modelling core interaction with the ionising

electron. It was noted in [2] that the influence of long-range potentials (LRPs), e.g. Coulomb-type potentials, will lead to significant modification of the dependence of ionisation rate on field strength compared to SRP results, following the results on ionisation in static fields [10].

For a frequency in resonance with an atomic transition, we will need to take into account excitation pathways before tunnelling ionisation is realised, resulting in enhanced ionisation rates. Further work for theoretical study of resonance excitation in strong fields was considered in [14].

The other limit is multiphoton ionisation, with weak intensities and high frequencies, where the ionisation process can be modelled as the simultaneous absorption of multiple photons (Fig. 1.1b). Multiphoton ionisation is in itself a thoroughly developed and advanced field, both in research and applications [15–19].

A general phenomenon known as Above Threshold Ionisation (ATI) was first experimentally observed in [20] in the multiphoton regime. In these experiments it was found that the photoelectrons are capable of absorbing more than the minimum number of photons required to ionise the atom and promote the electron to the continuum. Interestingly, **above-threshold ionisation is predicted in the seminal paper of L. V. Keldysh**, but this prediction had not been noticed at the time.

It is a remarkable fact that the results for both ionisation regimes can be derived from the same theory that lays emphasis on the quasiclassical pathways from the bound to continuum state of the electron, be they traversing under the barrier, or through multiphoton ionisation channels. However, for noble gas atoms, the separation between the ground and first excited state in the neutral system requires frequencies in the VUV regime (~ 10 eV), whereas we will be considering mostly the optical and infrared domain of the spectrum (~ 1 eV), that is, the nonadiabatic and tunnelling ionisation regime ($\gamma \simeq 1$ and $\gamma \ll 1$, respectively). In this regime real excitations prior to tunnelling are negligible.

One of the crucial steps in deriving the ionisation rates made in [2] was of approximating the ionising electron with Gordon-Volkov states [21, 22], which are accurate, quantum-mechanical states of a free electron in a laser field. Historically, the appeal of such states for describing strong-field phenomena has been demonstrated by H. Reiss [23, 24]. The argument for this approximation was motivated by the dominance of the laser field in a region sufficiently far from the core, especially if the core-potential falls of faster than a Coulomb potential, e.g. in the case of a Short Range Potential (SRP). It was therefore assumed that the interaction of the electron with the core would make insignificant contributions, at least to the exponential order, if not to the prefactors.

The other, tacit approximation, was to discard the effects of the laser field on the initial bound state of the electron. In the absence of any approximations for the final state of the laser driven electron, including the effect of the laser field on the initial state is not required. However, this is no longer true if the final state is approximated. Yet, even though the fields are strong, they are weak within the precincts of the atom where the atomic field strength is significantly stronger than the laser field strengths we will consider here. These approximations constitute what is now known as the Strong Field Approximation (SFA), a very powerful theoretical tool used ubiquitously to describe a plenitude of strong field phenomena [1].

Until the work by Keldysh, ionisation in strong fields was considered theoretically within the domain of ionisation rates exceeding the frequency of the radiation field (the adiabatic approximation [25]), allowing a very small window of ionisation near the peak of the field. One of the essential conclusions in [25] was the fact that for an atom interacting sufficiently long with a radiation field, ionisation was an inevitable consequence, whether direct or via excitation to an intermediate state.

We consider ionisation of atoms in strong fields, and gaseous medium where the atom can be modelled as an isolated system, free from the perturbations by and interactions with other atoms. In the adiabatic limit, realised by the laser field frequency being much smaller than the

response time of the electron, $\omega \ll \omega_t$, $\gamma \ll 1$, the ionisation rates bear resemblance [2,3,5] to the expressions for ionisation in a static field [10,26].

The typical ionisation amplitude in Keldysh theory to find the electron, initially bound in a ground state $|g\rangle$, with drift momentum $\mathbf{p}$ registered at the detector far away from the atom, is:

$$a_{\rm SFA}(\mathbf{p}) = -i \int_{t_0}^{T} dt \left\langle \mathbf{p}^{\rm GV}(t) \middle| \hat{V}_{\rm int} \middle| g \right\rangle e^{iI_p t}, \tag{1.2}$$

where $\left|\mathbf{p}^{\rm GV}(t)\right\rangle$ is the Gordon-Volkov (GV) continuum states, describing a free electron in a laser field, $V_{\rm int}$ is the interaction potential operator that instigates the ionisation step, and I_p is the ionisation potential to remove the electron from the ground state $|g\rangle$ of the atom/molecule under consideration. The time limits are defined as follows: t_0 is a time sufficiently far away in the past before the laser field was turned on and the atom was in a field-free state, and time instant T is the moment of observation of the ionised photoelectron and is a time instant well after the laser field is swtiched off and the electron is far away from the core to settle into the drift momentum $\mathbf{p}$ at the detector.

The interaction potential term, $\hat{V}_{\rm int}$, is the electron-laser interaction potential (in length gauge, as originally used by Keldysh). Note that once the core potential is neglected, the theory becomes gauge non-invariant: the results for ionisation rates are different in the length and velocity gauges for all potentials, except zero-range potential with the initial s-state [27]. Only the length gauge results reproduce the static limit in the case $\omega \to 0$. For atoms, length gauge has been repeatedly espoused as the correct choice to make reliable predictions [28–31], and so we will adhere to it in this thesis. But we note that velocity gauge is usually the better choice when considering numerical studies of strong field ionisation [32–34], on account of the fact that the canonical momentum is simply the drift momentum, obviating the wide excursion amplitudes observed in trajectories derived from the length-gauge kinematic momentum $\mathbf{v}_{\mathbf{p}}(t)$, which can be troublesome to contain in numerical calculations.

The bound state $|g\rangle$, in which the electron is strongly ensnared by the atomic/molecular core, is assumed to be affected feebly by the laser field, and hence we can use the field-free bound state. The continuum GV electron is defined by the non-relativistic, quantum-mechanical wavefunction

$$\left\langle \mathbf{r} \middle| \mathbf{p}^{\rm GV}(t) \right\rangle = \frac{1}{(2\pi)^{3/2}} e^{i\mathbf{v}_{\mathbf{p}}(t)\cdot\mathbf{r} - iS_{\rm GV}(t)}, \tag{1.3}$$

$$S_{\rm GV}(t) = \frac{1}{2} \int_{t}^{T} d\tau \, v_{\mathbf{p}}^2(\tau). \tag{1.4}$$

$S_{\rm GV}(t)$ is the temporal phase accumulated by the continuum electron from the time instant t, when the interaction potential $\hat{V}_{\rm int}$ "kicks in" and drives the electron away from its bound atomic state to the continuum state. No effect of the core potential is recorded by the electron after time instant t, an approximation which is the most accurate for SRPs modelling core interactions with the ionising electron, the delta-potential well being a special case. The laser-field velocity is defined as $\mathbf{v}_{\mathbf{p}}(t) = \mathbf{p} + \mathbf{A}(t)$, where $\mathbf{p}$ is the drift momentum that will be registered at the momentum detector long after the laser field is switched off, and $\mathbf{A}(t)$ is the vector potential defining the laser field.

We are using the Göppert-Mayer gauge (see e.g. [35]), which is obtained from the Coulomb gauge by the gauge transformation

$$\phi'(\mathbf{r},t) = \phi(\mathbf{r},t) - \frac{\partial \chi(\mathbf{r},t)}{\partial t}, \quad \mathbf{A}'(\mathbf{r},t) = \mathbf{A}(\mathbf{r},t) + \nabla\chi(\mathbf{r},t) \tag{1.5}$$

where $\chi(r,t) = -(\mathbf{r}-\mathbf{r}_0)\cdot\mathbf{A}(\mathbf{r}_0,t)$, and $\mathbf{r}_0$ is the position of the nucleus. The Hamiltonian is

transformed to:

$$\hat{H}' = \frac{1}{2}\big(\hat{\mathbf{p}} - q\mathbf{A}'(\mathbf{r},t)\big)^2 + V_{\text{Coul}}(\hat{\mathbf{r}}) + q(\mathbf{r}-\mathbf{r}_0)\cdot\frac{\partial\mathbf{A}(\mathbf{r}_0,t)}{\partial t} \tag{1.6}$$

$$= \frac{1}{2}\big(\hat{\mathbf{p}} - q\mathbf{A}'(\mathbf{r},t)\big)^2 + V_{\text{Coul}}(\hat{\mathbf{r}}) - \mathcal{D}(\mathbf{r},t)\cdot\mathbf{E}(\mathbf{r},t) \tag{1.7}$$

for an arbitrary charge q, and the laser field $\mathbf{E}(\mathbf{r},t) = \partial\mathbf{A}(\mathbf{r}_0,t)/\partial t$. In the dipole approximation, it is reasonable to approximate the vector potential with its value at the nulceus, that is, $\mathbf{A}(t) \equiv \mathbf{A}(\mathbf{r}_0,t)$. Thus, we can consistently define the electric field $\mathbf{E}(t)$ through the vector potential $\mathbf{A}(t)$ from the expression:

$$\mathbf{E}(t) = -\frac{\partial\mathbf{A}(t)}{\partial t}. \tag{1.8}$$

The velocity of light, which in atomic units is the inverse of the fine structure constant, $c = 1/\alpha \approx 137.036$, is subsumed in the amplitude for the vector potential $\mathbf{A}(t)$.

We are interested in obtaining an analytical expression for Eq. (1.2). We will follow the derivation presented in [27], as it allows us to follow pre-exponential factors in a more straightforward way than in the original Keldysh paper. Since $\hat{V}_{\text{int}} = \hat{V}_F(t)$ in Keldysh theory, and we know for the GV continuum states that

$$i\frac{\partial|\mathbf{p}^{\text{GV}}(t)\rangle}{\partial t} = \left(\frac{\hat{\mathbf{p}}^2}{2} + \hat{V}_F(t)\right)|\mathbf{p}^{\text{GV}}(t)\rangle, \tag{1.9}$$

combining $\hat{V}_{\text{int}}(t)$ with $\langle\mathbf{p}^{\text{GV}}(t)|$, we get

$$a_{\text{SFA}}(\mathbf{p}) = -i\int_{t_0}^{T} dt\left[-i\frac{\partial\langle\mathbf{p}^{\text{GV}}(t)|}{\partial t}|g\rangle - \left\langle\mathbf{p}^{\text{GV}}(t)\middle|\frac{\hat{\mathbf{p}}^2}{2}\middle|g\right\rangle\right]e^{iI_pt}. \tag{1.10}$$

For the ground state $|g\rangle$, we know that

$$\left(\frac{\hat{\mathbf{p}}^2}{2} + \hat{V}_{\text{core}}\right)|g\rangle = -I_p|g\rangle = i\frac{\partial\big(|g\rangle e^{iI_pt}\big)}{\partial t}, \tag{1.11}$$

from which, after interchanging the time-derivative in the first term of the integrand in Eq. (1.10), we get

$$a_{\text{SFA}}(\mathbf{p}) = i\int_{t_0}^{T} dt\left(I_p\langle\mathbf{p}^{\text{GV}}(t)|g\rangle + \left\langle\mathbf{p}^{\text{GV}}(t)\middle|\frac{\hat{\mathbf{p}}^2(t)}{2}\middle|g\right\rangle\right)e^{iI_pt}. \tag{1.12}$$

For the second term, since $\hat{\mathbf{p}}|\mathbf{p}^{\text{GV}}(t)\rangle = \mathbf{v}_{\mathbf{p}}(t)|\mathbf{p}^{\text{GV}}(t)\rangle$, and also realising that the inner product $\langle\mathbf{p}^{\text{GV}}(t)|g\rangle$, when resolved on spatial coorindates $\mathbf{r}$, is simply the Fourier transform of the bound state:

$$\Phi_g(\mathbf{v}_{\mathbf{p}}(t)) = \int d\mathbf{r}\, e^{-i\mathbf{v}_{\mathbf{p}}(t)\cdot\mathbf{r}}\Psi_g(\mathbf{r}). \tag{1.13}$$

the expression for ionisation amplitude simplifies to

$$a_{\text{SFA}}(\mathbf{p}) = i\int_{t_0}^{T} dt\left(I_p + \frac{v_{\mathbf{p}}^2(t)}{2}\right)\langle\mathbf{p}^{\text{GV}}(t)|g\rangle e^{iI_pt}. \tag{1.14}$$

Substituting for the Gordon-Volkov continuum state $\langle\mathbf{r}|\mathbf{p}^{\text{GV}}(t)\rangle$, Eq. (1.3) and (1.4), in Eq. (1.14), we get the ionisation amplitude:

$$a_{\text{SFA}}(\mathbf{p}) = -i\int_{t_0}^{T} dt\left(I_p + \frac{v_{\mathbf{p}}^2(t)}{2}\right)e^{-iS_{\text{SFA}}(t,\mathbf{p})}\Phi_g(\mathbf{v}_{\mathbf{p}}(t)). \tag{1.15}$$

We have now defined the SFA action

$$S_{\mathrm{SFA}}(t,\mathbf{p}) = \frac{1}{2}\int_t^T d\tau\, v_{\mathbf{p}}^2(\tau) - I_p t. \tag{1.16}$$

The instant of ionisation t is distributed over the entire possible range of time, which is equivalent to integrating over all possible paths allowable between the bound state of the electron and the continuum state with drift momentum $\mathbf{p}$ [36].

We are finally left with one single time-integral to solve. This simplification of the combined spatial and time-integral was possible due to the Strong Field Approximation, which decoupled the continuum electron from any influence of the core potential, while at the same time the bound state $\Psi_g(\mathbf{r})$ is free from any time-dependent polarisation by the laser field. The overall approximation is virtually (it still loses the Stark-shift of the bound state) exact for Short-Range Potentials (SRPs), especially the delta-potential $\propto \delta(\mathbf{r})$, but not reliable for Long-Range Potentials (LRPs). This point will be further discussed in the next section after introducing the PPT theory in LRPs. Another issue with using the Fourier transform Eq. (1.13) for LRP is the higher-order pole encountered in the momentum domain while calculating the ionisation rates. This point will become clear when discussing ionisation rates in PPT theory in SRP core.

We can apply the saddle point approximation to solve the time-integral in Eq. (1.15) [2,37]. Such an approximation is valid when the integrand has a rapidly varying in time phase term, which in our case is $S_{\mathrm{SFA}(t)}$. The prefactor is the momentum representation of the bound state, and varies slowly with time. The rapidly oscillatory term then acts as a type of filter for the prefactor $\Phi_g(\mathbf{v_p}(t))$, masking out all contribution far away from stationary point t_s, which allows us to approximate the prefactor with its value at the stationary point $\Phi_g(\mathbf{v_p}(t_s))$ and take this term out of the time-integral.

Requiring that we expand the SFA action about the stationary point t_s in a Taylor series, where the saddle point is defined from the condition that the derivative of SFA action w.r.t. time is zero, $\partial S_{\mathrm{SFA}}(t_s)/\partial t = 0$, the time-integral can be approximated as:

$$I_t = -\int_{t_0}^{T} dt\, e^{-iS_{\mathrm{SFA}}(t_s) - i\frac{(t-t_s)^2}{2}\partial_t^2 S_{\mathrm{SFA}}(t_s)} \left(I_p + \frac{v_{\mathbf{p}}^2(t)}{2}\right)\Phi_g(\mathbf{v_p}(t)). \tag{1.17}$$

In Eq. (1.17), $\partial_t^2 S_{\mathrm{SFA}}(t_s)$ is the second derivative of S_{SFA} w.r.t time. Further details, modifications and justification of the saddle point method can be found in [37]. The only step left now is to set up the definitions of the time-instants t_0 and T that would provide us with an analytical expression of the integral in Eq. (1.17): since the second term is localized in time, we can extend the integration limits setting $t_0 \to -\infty$ and $T \to \infty$.

If the time instant t_s had been confined along the real axis, we would have simply settled the action on its stationary point. However, on writing down the defining equation for t_s, using Eq. (1.16),

$$\frac{\partial S_{\mathrm{SFA}}}{\partial t} \equiv -\frac{v_{\mathbf{p}}^2(t_s)}{2} - I_p = 0, \tag{1.18}$$

we find that the time instant t_s is necessarily raised into the complex plane, leading to two possible solutions to Eq. (1.18), one defining the steepest point of ascent and other of descent, and form a complex conjugate pair. The one that can describe a physically plausible event like ionisation is that for which the exponential in Eq. (1.19) does not blow up, that is, the point of steepest descent with a positive imaginary part for t_s. This constitutes the saddle point approximation to solve the time-integral Eq. (1.17).

The time-integral in Eq. (1.17) is now solvable and is well-known, to give us:

$$I_t = -\sqrt{\frac{\pi}{\left|\partial_t^2 S_{\mathrm{SFA}}(t_s)\right|}}\, e^{-iS_{\mathrm{SFA}}(t_s)} \left(I_p + \frac{v_{\mathbf{p}}^2(t_s)}{2}\right)\Phi_g(\mathbf{v_p}(t_s)). \tag{1.19}$$

Note that the prefactor $I_p + v_{\mathbf{p}}^2(t_s)/2$ cancels the pole in the Fourier transform of the ground state wave-function for the short-range potential, yielding finite result for I_t.

A complex time of ionisation implies the trajectory to be complex-valued. Such a motion is not possible classically, and can only be realised in a classically forbidden region, which in this case is under the time-dependent potential barrier created by the combined effect of the core and laser field. The bound state therefore tunnels through the laser-field modulated barrier into a continuum state, as shown in Fig. 1.1a which is the snapshot of the time-dependent field at one particular instant when it takes on its maximum value in one direction (towards positive-x axis in the figure). For a monochromatic linearly polarised field, where there are two maxima in each cycle around which the probability of ionisation is maximum and the electron wavepacket is shot into the continuum, the field will provide two windows of ionisation in opposite directions in each laser cycle. In a monochromatic circular field, where the field retains a constant strength but changes direction axially, the ionisation window sweeps the entire plane of polarisation of the field. In an enveloped field, i.e. for a few-cycle laser pulse, we see isolated instances of ionisation which can then be used to time the ionisation events.

Complex trajectories are an essential part of quantum treatment. They affect the amplitudes and thus influence the observables. In the present case, these trajectories arise *after* applying the saddle point method for time. If time had been real, so would the trajectories, as is the case with classical methods in strong field physics.

However, trajectories can be complex to begin with, if we consider methods like Complex WKB and Bohmian Mechanics with Complex Action (BOMCA) [38–41], the latter being developed over Bohmian Mechanics (BM). Complex WKB follows the standard WKB method, but takes into account the contribution of the amplitude term to evolution of the nonclassical (and complex) trajectories. BOMCA applies the saddle point approximation to trajectories, by expanding around near-classical paths. At this point, it departs from the conventional WKB methods, and also allows to retain only leading order terms in complex phase while still maintaing a high accuracy. For the interested reader, the details of this approach are presented in the Appendix 1.A.

Returning back to the SFA method, the final expression of ionisation amplitude for the photoelectron to end up in the continuum with final drift momentum $\mathbf{p}$ is:

$$a_{\mathrm{SFA}}(\mathbf{p}) = i\sqrt{\frac{\pi}{S''_{\mathrm{SFA}}(t_s)}}e^{-iS_{\mathrm{SFA}}(t_s)}\chi_g(\mathbf{v}_{\mathbf{p}}(t_s)),\ \chi_g(\mathbf{v}_{\mathbf{p}}(t_s)) = \left(I_p + \frac{v_{\mathbf{p}}^2(t_s)}{2}\right)\Phi_g(\mathbf{v}_{\mathbf{p}}(t_s)). \quad (1.20)$$

The ionisation amplitude so derived is reliable for expressing momentum distribution in experiments for strong field ionisation from a SRP core, which is usually assumed for negative ions. In noble gas atoms (He, Ne, Ar, Kr, etc.), a long-range potential (LRP) more accurately emulates the core interaction with the valence electron that is removed. As was already emphasised by Keldysh using the comparison with the known results for ionisation rates of hydrogen in static field, and later discussed and further developed by PPT, results of type Eq. (1.20) are significantly (by several orders of magnitude) inaccurate for LRP cores, and long-range interactions with the electron become important to ascertain the right amplitude of ionisation. The explicit expression for the prefactor in Eq. (1.20), which also depends on the geometry of the bound state will be given in the next section where we discuss the issue of higher-order poles in LRP. Accurate estimation of the prefactor requires additional correction to SRP ionisation amplitudes associated with the presence of the long-range potential of the core.

We present next the PPT theory for strong field ionisation in monochromatic fields and Coulomb-corrections introduced to SRP results [Eq. (1.20)].

1.2 PPT Theory and Long-Range Effects

We consider here the theory of strong field ionisation developed by Perelomov, Popov, and Teréntev (PPT), first presented in [3]. Following the theory of strong field ionisation for hydrogen-like atoms in the ground state, ionisation rates for arbitrary quantum numbers were derived by PPT, first for linear and circular polarisation [3] and subsequently arbitrary elliptical polarisation [4], within the quasistatic limit for the field ($\omega \ll \omega_t$) and rates derived specifically for the peak of the distribution using the saddle point method. With the PPT theory, accurate derivation of prefactors for short-range potential was presented in detail; the important influence of Coulomb-type potential in strong field ionisation under time-varying fields was considered in [5]. The Coulomb effects were already known to significantly modify the dependence of ionisation amplitudes and rates on field strength by many orders of magnitude [2, 10, 42]. While the PPT derivation is virtually rigorous for short-range potentials, including Coulomb corrections involved several ad-hoc steps in the derivation. For short-range potentials, either Keldysh or PPT theory can be derived consistently, with requisite approximations defined under SFA, using either the forward or reverse-time S-matrix formalism [43]. Our focus will be on the first three papers [3–5] derived by PPT.

The PPT theory dealt with ionisation amplitudes which assume the ionisation step to be completed as soon as the electron emerges from the under barrier, even in a LRP. The LRP is a Coulomb-type potential approximation for non-hydrogen atoms, which is a valid approximation for radial range $r \gg 1/\kappa$, where $1/\kappa$ is the characteristic dimension of the atom under consideration which makes κ a parameter with dimensions of momentum. In the PPT theory the terms describing the contribution of the ionisation rate from long-range interactions were, strictly speaking, only valid for ionisation events at the peak of the linearly polarised laser field, i.e., there were no sub-cycle dynamics reflected in such terms. These dynamics become crucial for ionisation in few-femtosecond circularly polarised pulses, e.g., in the so-called attoclock setup [44, 45]. As will be mentioned later, a nonadiabatic theory developed within the formalism of the so-called Analytical-R Matrix (ARM) method [46] allows one to overcome these limitations and describe such dynamics [47].

One crucial development of PPT theory, which also becomes essential in deriving a dynamical theory of strong field ionisation in LRP within the ARM method, was the boundary-matching scheme which was based on the quasiclassical approximation [5]. What this method entails is joining the asymptotic quantum wavefunction valid for $r \gg 1/\kappa$ to the continuum wavefunction defined in the presence of the LRP (Coulomb-type potential) *and* the time-varying laser field with the core potential treated quasiclassically as a pertubation to the continuum GV states. The results obtained, however, cut off the core LRP effects as soon as the electron emerged from the barrier, giving Coulomb corrections to rates and amplitudes applicable only near the peak of the field where the highest ionisation rates are possible. The matching scheme was only applicable in the quasistatic limit, and a more rigorous derivation will be presented in Chapter 2, where we will present a matching scheme for frequencies in the nonadiabatic regime ($\gamma \gtrsim 1$).

The 3D bound state in a general LRP in the asymptotic limit $\kappa r \gg 1$ can be written as:

$$\Psi_0(\mathbf{r}, t) = C_{\kappa\ell}\kappa^{3/2}\frac{e^{-\kappa r}}{\kappa r}(\kappa r)^{Q/\kappa}Y_{\ell m}(\theta, \phi)e^{-iE_0 t}, \tag{1.21}$$

where $C_{\kappa\ell}$ is the state-specific constant for the field-free bound state of the atom, Q is the effective LRP charge experienced by the ionising electron, $\kappa = \sqrt{2I_p}$ is the characteristic momentum of the electron in the bound state with ionisation potential $I_p = -E_0$, and $Y_{\ell m}$ is the spherical harmonic with angular momentum quantum number ℓ and magnetic quantum number m. For $Q = 0$ we get results for a SRP core, typically used for modelling ionisation from negative ions. A tug-of-war exists in defining the appropriate range for the radial range r, between the lower bound to validate the asymptotic expression Eq. (1.21) and the upper bound to validate approximating the total polarised wavefunction with the field-free bound state wavefunction

Eq. (1.21) (this approximation is only expected to be valid in the vicinity of the core): $r \gg 1/\kappa$ to begin with for the asymptotic approximation, and $r \ll r_*$, where:

$$r_* = \frac{\kappa}{\omega} \ln\left(1 + \frac{\gamma}{\gamma_*}\right) = \begin{cases} \frac{1}{\kappa}\sqrt{\frac{F_0}{F}}, \text{ for } \gamma \ll \gamma_* \\ \kappa/\omega, \text{ for } \gamma \gtrsim \gamma_*, \end{cases} \tag{1.22}$$

$\gamma_* = F_0/F \gg 1$, after which distance the difference between polarised and bound state wavefunction starts to become significant (see Appendix in [6]).

We therefore need strong fields to make tunnelling the dominant mechanism for ionisation, while at the same time not too strong to distort the wavefunction significantly in the region near the core that feeds the continuum part of the wavefunction to ionisation. Typical intensity range for these fields is $10^{13} - 10^{14}$ W/cm^2, and wavelengths $\lambda > 600$ nm used in this estimate to further suppress multiphoton ionisation pathways.

We first present the PPT derivation in Short-Range Potentials (SRPs) and then in Long-Range Potentials (LRPs), comparing the points of similarities and differences in the two methods, and discuss the assumptions that are essential to the PPT theory.

1.2.1 PPT theory in SRPs

The early results in the PPT approach [3,4] were derived for a SRP-core model, in the frequency domain for ionisation rates. In a SRP model, there is only one bound state supported by the core:

$$\Psi_0^{\text{SRP}}(\mathbf{r}, t) = C_{\kappa\ell}\kappa^{3/2}\frac{e^{-\kappa r}}{\kappa r}Y_{\ell m}(\theta, \phi)e^{-iE_0 t}, \tag{1.23}$$

with energy $E_0 = -I_p = -\kappa^2/2$, where I_p is the ionisation potential and κ the characteristic momentum of the system. An advantage of the SRP-model is the direct cancellation of the pole in momentum space in the Fourier transform of the bound-state wavefunction Eq. (1.23), which is an asset in the derivation of ionisation amplitudes/rates, as we saw in Section 1.1 in Eq. (1.20).

The total wavefunction, in the combined effect of the SRP-core and the time-varying laser field, is defined by

$$\Psi(\mathbf{r}, t) = -i\int_{-\infty}^{t} dt' \int d\mathbf{r}'\, G^{\text{GV}}(\mathbf{r}, t; \mathbf{r}', t')V_{\text{SRP}}(\mathbf{r}')\Psi(\mathbf{r}', t'), \tag{1.24}$$

where $V_{\text{SRP}}(\mathbf{r}')$ is the SRP-core potential and $G^{\text{GV}}(\mathbf{r}, t; \mathbf{r}', t')$ is the Green's function for the continuum Gordon-Volkov (free) electron in a laser field:

$$G^{\text{GV}}(\mathbf{r}, t; \mathbf{r}', t') = \frac{1}{(2\pi)^3}\int d\mathbf{k}\, \exp\left[i(\mathbf{v}_\mathbf{k}(t)\cdot\mathbf{r} - \mathbf{v}_\mathbf{k}(t')\cdot\mathbf{r}') - \frac{i}{2}\int_{t'}^{t} d\tau\, v_\mathbf{k}^2(\tau)\right]. \tag{1.25}$$

In Eq. (1.24) we have omitted an extra term, which is irrelevant for the analysis of ionisation rates.

We now approximate the total wavefunction in the integral in Eq. (1.24) by the field-free, bound-state wavefunction for a SRP core [Eq. (1.23)]. This approximation is justified by the assumption that the SRP limits the spatial integral in the expression for the wavefunction to the very narrow region where the core potential dominates the laser field, the assumption particularly appealing for a delta-function potential [3].

We therefore get:

$$\Psi(\mathbf{r}, t) = -i\int_{-\infty}^{t} dt' \int d\mathbf{r}'\, G^{\text{GV}}(\mathbf{r}, t; \mathbf{r}', t')V_{\text{SRP}}(\mathbf{r}')\Psi_0^{\text{SRP}}(\mathbf{r}')e^{-iE_0 t'}. \tag{1.26}$$

From the Schrödinger equation for the field-free Hamiltonian in a SRP potential, we know that

$$\left[-\frac{1}{2}\nabla^2 + V_{\rm SRP}(\mathbf{r})\right]\Psi_0^{\rm SRP}(\mathbf{r}) = -\frac{\kappa^2}{2}\Psi_0^{\rm SRP}(\mathbf{r}), \text{ or} \tag{1.27}$$

$$V_{\rm SRP}(\mathbf{r})\Psi_0^{\rm SRP}(\mathbf{r}) = \left(\frac{1}{2}\nabla^2 - \frac{\kappa^2}{2}\right)\Psi_0^{\rm SRP}(\mathbf{r}), \tag{1.28}$$

which when substituted in Eq. (1.26), gives us

$$\Psi(\mathbf{r},t) = -i\int_{-\infty}^{t} dt' \int d\mathbf{r}'\, G^{\rm GV}(\mathbf{r},t;\mathbf{r}',t')\left(\frac{1}{2}\nabla'^2 - \frac{\kappa^2}{2}\right)\Psi_0^{\rm SRP}(\mathbf{r}')e^{iI_p t'}. \tag{1.29}$$

The advantage of this substitution is the fact that the Laplacian operator ∇'^2 transforms into a number, $v_{\mathbf{k}}^2(t')$, once it acts to the left, i.e. on the Green's function $G^{\rm GV}$ given by Eq. (1.25). The expression for the Fourier Transform (FT) of the bound-state wavefunction is now needed, and since we have a SRP, the FT for it is straightforward:

$$\Phi_0(\mathbf{v}_{\mathbf{k}}(t')) = \frac{r_{\ell m}}{v_{\mathbf{k}}^2(t') + \kappa^2}Y_{\ell m}(\hat{\mathbf{v}}_{\mathbf{k}}(t')), \tag{1.30}$$

where $r_{\ell m} = \sqrt{2\kappa/\pi}C_{\kappa\ell}$. We note a pole in the momentum representation of the bound-state wavefunction at $v_{\mathbf{k}}(t') = \pm i\kappa$. But, from the saddle point analysis of the time-integral, which will be used in the PPT theory as well, we know from Eq. (1.18) that the instant of ionisation is defined by $v_{\mathbf{k}}(t'_s) = i\kappa$. Therefore, the pole arises exactly at the position of the saddle point. However, in the PPT approach for SRP the pole cancels out as can be seen from the discussion below. The expression for $\Psi(\mathbf{r},t)$ now is

$$\Psi(\mathbf{r},t) = \frac{i}{(2\pi)^3}\int_{-\infty}^{t} dt' \int d\mathbf{k}\, e^{-i\mathbf{v}_{\mathbf{k}}(t)\cdot\mathbf{r} - \frac{i}{2}\int_{t'}^{t} d\tau\, v_{\mathbf{k}}^2(\tau)}\frac{1}{2}\big(v_{\mathbf{k}}^2(t') + \kappa^2\big)\Phi_0(\mathbf{v}_{\mathbf{k}}(t'))e^{iI_p t'}, \tag{1.31}$$

and from Eq. (1.30), we know that the singularity exactly cancels out, *but only for a SRP core*; in a LRP, even if we had somehow circumvented the other complications arising because of the distortion of the wavefunction in the region $\kappa r' \gtrsim 1$, we would have ended up with a higher order pole than in the case of the SRP [27]. In this case the recipe for the application of the saddle point method should be modified [2, 48, 49] and may lead to additional terms in the prefactor.

As detailed in the next subsection, in the PPT theory, the Coulomb effects were included by introducing the Coulomb correction to the electron action and adopting the prefactor coming from the short-range theory. Therefore, in the PPT theory, we need to be careful with the assumptions and approximations that were crucial to make an extension to the LRP case.

Equation (1.31) can be used to derive the ionisation rates in the PPT theory, as we present in the Appendix 1.B. The final result for the total ionisation rate is a summation over partial ionisation rates describing the process of the electron absorbing n-photons:

$$w(\mathcal{E},\omega) = \sum_{n\geq n_0} w_n(\mathcal{E},\omega), \tag{1.32}$$

$$w_n(\mathcal{E},\omega) = 2\pi\int d\mathbf{p}\,\delta\left(\frac{1}{2}\left(p^2 + \kappa^2 + \frac{\kappa^2 x}{2\gamma^2}\right) - n\omega\right)|F_n(\mathbf{p})|^2, \tag{1.33}$$

$$F_n(\mathbf{p}) = \frac{1}{2\pi}\int_{-\pi}^{\pi} d\alpha\, \exp\left[-i\frac{\omega_0}{\omega}\int_0^{\alpha} d\beta\left\{\frac{v_{\mathbf{p}}^2(\beta)}{\kappa^2} + 1\right\}\right]\frac{1}{2}[v_{\mathbf{k}}^2(\alpha) + \kappa^2]\Phi_0(\mathbf{v}_{\mathbf{p}}(\alpha)),\ \alpha = \omega t'. \tag{1.34}$$

Here, $x = 1 + \varepsilon^2$, where ε is the ellipticity of the polarised field, and $\omega_0 = \kappa^2/2$. The lower limit for the summation in Eq. (1.32) represents threshold ionisation, giving the minimum number of photons required to liberate the electron in the given laser field, and is defined as:

$$n_0 = \frac{\omega_0}{\omega}\left(1 + \frac{1+\varepsilon^2}{2\gamma^2}\right). \tag{1.35}$$

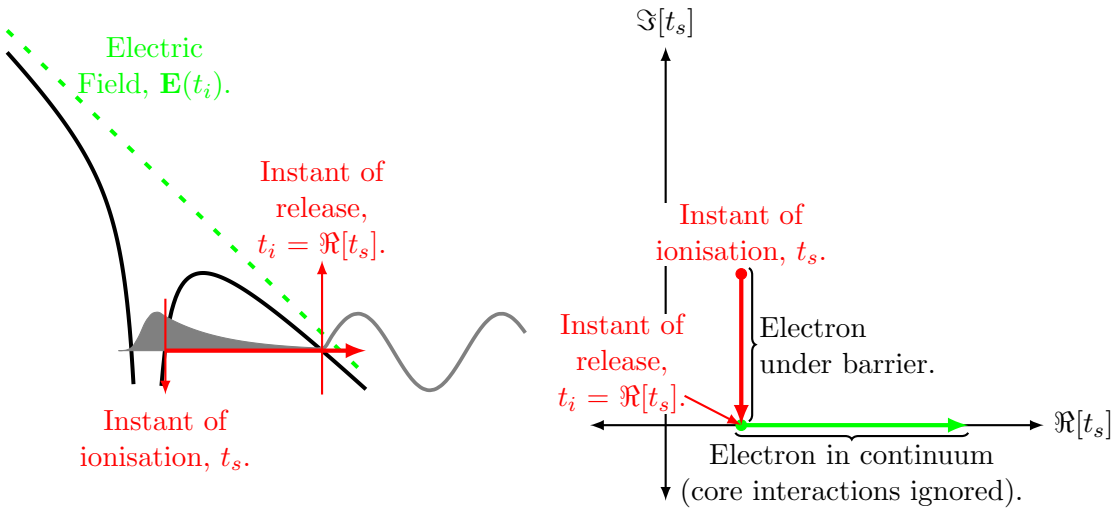

Figure 1.2: Events in optical tunnelling ionisation mapped onto the complex-time plane. The instant the electron is "kicked" by the laser field into the nonclassical under-the-barrier region is defined by a complex time t_s [evaluated through Eq. (1.18)]. As long as the electron traverses under the barrier, the time variable follows parallel to the imaginary time-axis, until it reaches the instant $t_i = \Re[t_s]$, when the electron is defined to be "born" into the continuum and can be described classically. The quantum-mechanical properties of the tunnelling process are retained in the complex trajectory of the electron due to the complex instant of ionisation, t_s.

The summation in Eq. (1.32) represents Above Threshold Ionisation (ATI) peaks, given by the partial ionisation rates in Eq. (1.33) for n-photons absorbed by the photoelectron, which can go beyond the minimum required threshold value of n_0. To derive analytical expressions for the ionisation rate, it is necessary to evaluate the integral for $F_n(\mathbf{p})$. In PPT theory [3,4], additional approximations were made in the components of the drift momentum $\mathbf{p}$ for this term, to derive these expressions. We will, however, not need these approximations for calculations of ionisation rates and amplitudes in the Analytical R-Matrix (ARM) approach defined in the next chapter.

1.2.2 PPT theory in LRPs

The application of the saddle point method within the PPT theory has led the authors to a simple and intuitive physical model of strong field ionisation, which describes tunnelling in the time domain. In this picture, tunnelling proceeds along one specific trajectory (defined for each final electron momentum) evolving in complex time. The starting point of this trajectory is associated with the instant when the electron is "kicked" into the classically forbidden under-the-barrier region by the laser field. The time the electron reaches the barrier exit and emerges from under the barrier is associated with the time instant when the time variable becomes purely real and the trajectory further progresses along the real time axis, as in classical mechanics. (Fig. 1.2). The imaginary action accumulated under the barrier along this trajectory gives the expression for the exponential part of the ionisation rate. With this lucid model we get a clear insight into the physical process, allowing a straightforward prescription to include Coulomb effects to the ionisation amplitudes, while simplifying the original, frequency-domain formal approach tremendously. This model is commonly known as the Imaginary Time Method (ITM) [50, 51], which has been developed extensively to describe strong field ionisation processes in Coulomb potentials over a wide range of the Keldysh parameter, from the original quasistatic domain [4,6] to the high-frequency, multiphoton regime [52, 53].

Motivated by this insight from ITM, the quasiclassical scheme for describing strong field ionisation in the presence of a Coulomb-type potential [5] was also developed within the adiabatic

limit of PPT theory. The method provides an intuitive picture crucial for the subsequent development of the PPT theory, but it was lacking rigorous justification in several aspects concerning the inclusion of LRP interactions in the theory. In this subsection, we present the basic ideas for those derivations which were pursued within PPT(K) theory in [5, 6], while expounding on those steps in the derivation process that were not sufficiently detailed in the original papers, and which we consider to be essential for a coherent presentation for its application.

The most important contributions of the Coulomb-type potential were expected to be realised through an enhancement of the ionisation rates/amplitudes by 1-2 orders of magnitude, judging from the results for the static case [10]. Keeping that in mind, along with the ITM approach, PPT [5] considered the perturbation to the SRP action, $S_{\rm SRP}$, due to the Coulomb perturbation. The starting point is the contracted action S:

$$S = \int_{t_s'}^{0} dt \left[\frac{\dot{\mathbf{r}}^2}{2} - V(\mathbf{r},t) - \frac{\kappa^2}{2}\right] = S_0 + \delta S, \tag{1.36}$$

$$V(\mathbf{r},t) = V_L(\mathbf{r},t) + \delta V_C(\mathbf{r}), \tag{1.37}$$

$$\delta V_C(\mathbf{r}) \approx -\frac{Q}{r}, \text{ for } \kappa r \gg 1. \tag{1.38}$$

Here S_0 is the action for the short-range potential and δS is the Coulomb correction to the SRP result. The prescription given here is valid for the optimal momentum (the final momentum corresponding to ionisation at the peak of the linearly polarised laser field within the optical cycle), for which reason the upper limit of the time-integral is zero, as t_s' at the optimal momentum in linear fields is purely imaginary. For this optimal momentum, the trajectory is also real (no imaginary component) in the continuum. For a monochromatic elliptical/circular field, at the optimal momentum, the real part of the ionisation time is set to zero as well (or can be set to zero in the circular field case, without loss of generality since the results are isotropic anyway).

The next step is to find an expression for the first-order variation of the action S, giving us:

$$\delta S = \int_{t_s'}^{0} dt \left[\dot{\mathbf{r}}\cdot\delta\dot{\mathbf{r}} - \nabla V_L\cdot\delta\mathbf{r} - \delta V_C\right] - \left[\frac{\dot{\mathbf{r}}^2}{2} - V_L - \frac{\kappa^2}{2}\right]\Bigg|_{t=t_s'}. \tag{1.39}$$

We next make a zero-order iteration on the trajectories $\mathbf{r}(t)$, by defining them solely in the laser field potential: $\ddot{\mathbf{r}}_L = -\nabla V_L(\mathbf{r})$. Along with the condition that at the exit point of the barrier, $\dot{\mathbf{r}}_L = 0$ (which is also **valid only for the peak of the linearly polarised laser field**, but not for any other instant of ionisation within the optical cycle; for circular fields it is also not true even for the optimal momentum, see Fig. 2.6, in Chapter 2), we can write this as

$$\delta S = -\int_{t_s'}^{0} dt\, \delta V_C(\mathbf{r}_L(t)) - \left[\dot{\mathbf{r}}_L\cdot\delta\dot{\mathbf{r}}_L + \left(\frac{\dot{\mathbf{r}}_L - \kappa^2}{2} - V_L(\mathbf{r}_L(t),t)\right)\delta t\right]\Bigg|_{t=t_s'}. \tag{1.40}$$

Fixing the end-point of the perturbed trajectory, we have $\mathbf{r}(t_s' + \delta t_s') = 0$ (where δt_s is the possible correction to the ionisation time t_s' due to Coulomb potential. However, these corrections were not considered explicitly and were only presented in the variational analysis), we get the boundary condition on the zeroth-order trajectory:

$$\delta\mathbf{r}(t_s') = -\dot{\mathbf{r}}(t_s')\delta t_s', \tag{1.41}$$

which gives after substitution in Eq. (1.40)

$$\left[\dot{\mathbf{r}}\cdot\delta\dot{\mathbf{r}} + \left(\frac{\dot{\mathbf{r}} - \kappa^2}{2} - V_L(\mathbf{r},t)\right)\delta t\right]\Bigg|_{t=t_s'} = [E_0 - H_L(\mathbf{r},t)]|_{t=t_s'} = 0, \tag{1.42}$$

that is, the saddle point condition on t_s' [Eq. (1.18)]. The final result for the perturbation to the SRP action therefore is:

$$\delta S = -\int_{t_s'}^{0} dt\, \delta V_C(\mathbf{r}(t)), \tag{1.43}$$

where $\mathbf{r}(t)$ is the zeroth-order trajectory defined only by the laser-field potential $V_L(\mathbf{r},t)$.

We can now write the expression for the ionisation amplitude valid for the optimal momentum of the photoelectron in a Coulomb potential:

$$a(\mathbf{p},t) = \sqrt{\frac{2\pi}{|S''_{\mathrm{SFA}}(t'_s)|}} e^{-iS_{\mathrm{SFA}}(t'_s,\mathbf{p}) - i\int_{t'_s}^{0} d\tau\, V_C(\mathbf{r}_s(\tau))} Y_{\ell m}\big(\theta_{v_{\mathbf{p}}}(t'_s), \phi_{v_{\mathbf{p}}}(t'_s)\big), \tag{1.44}$$

where the trajectory entering into the Coulomb terms is defined as

$$\mathbf{r}_s(\tau) = \int_{t_s}^{\tau} d\zeta\, \mathbf{v}_{\mathbf{p}}(\zeta). \tag{1.45}$$

The immediate problem with this expression is apparent: a singularity at the lower-limit of time $\tau = t'_s$ for the Coulomb-correction term in Eq. (1.44), where the trajectory goes to zero [Eq. (1.45)]. To obviate this singularity and obtain physically plausible results, the purpose here is to transform the Coulomb correction in Eq. (1.43) by regularising the integral. The issue arises because of limitation in the quasiclassical analysis near the quantum atom. In the PPT approach, regularisation was accomplished by breaking the diverging part of the integral away from the well-behaved region. The non-classical part was defined before an arbitrary point $r = a$, beyond which the classical phase was used to represent the wavefunction accurately. The time instant at which the trajectory reaches $r = a$ is t'_a. After this time, quasiclassical results hold.

This implies the perturbation due to the core to be redefined as

$$\delta S = -i\frac{Q}{\kappa}\ln \kappa a - \int_{t'_a}^{0} dt\, \delta V_C(\mathbf{r}(t)),\ a = r(t'_a) \tag{1.46}$$

The first term represents the long-range, asymptotic part of the ground state wave-function. Therefore the field-free bound wave-function and its quasiclassical "tail" can be matched together to avoid the singularity. This procedure allows us to establish the lower limit for the integral in the second term, which cuts out the singularity, "absorbing" it into the bound state wave-function.

Using the asymptotic expression for the bound state in the long range potential in the final expression for the prefactor of the ionisation rate derived only for the short range case is an ad-hoc step made in the PPT theory. The A*R*M theory developed in this Thesis shows how Coulomb effects can be included consistently, without ad-hoc assumptions, and is not limited to the ionisation events that occur at the peak of the field, making it possible to consider sub-cycle Coulomb effects. This becomes particularly important for few-cycle pulses and the analysis of attosecond ionisation dynamics within the attoclock setup.

Below we show how the a-dependence in Eq. (1.46) can be cancelled in the quasistatic limit ($\omega \to 0$, $\gamma \to 0$) following the results of the PPT theory. We need to consider two cases of field polarisation for this purpose, which was presented in PPT theory: linear and arbitrary elliptical polarisation.

Linear Fields

In linear fields, assuming the vector potential time-variation to be $\mathbf{A}(t) = -A_0 \sin\omega t\, \hat{\mathbf{z}}$, the momentum at which the ionisation amplitude is maximum (the optimal momentum) is defined by the extremum of the SFA action, S_{SFA}, which gives us

$$\frac{\partial S_{\mathrm{SFA}}}{\partial \mathbf{p}} = 0 \Rightarrow \mathbf{p}_0 = 0, \tag{1.47}$$

simplifying the laser field trajectory on which the action is evaluated to:

$$z_{\text{opt}}(t) = \int_{t_s'}^{t} d\tau\, v_{\mathbf{p},\text{opt}}(\tau) = p_0(t - t_s') + \frac{A_0}{\omega}(\cos\omega t - \cos\omega t_s') = \frac{A_0}{\omega}(\cos\omega t - \cos\omega t_s'). \tag{1.48}$$

The quasiclassical LRP integral is then analytically solvable [5]:

$$\int_{t_a'}^{t_i'} d\tau\, V_C(\mathbf{r}_s(\tau)) = \int_{i\tau_a'}^{0} d\tau \left(-\frac{Q}{r_s(\tau')}\right) = i\frac{Q}{A_0}\int_0^{\omega\tau_a'} \frac{d(\omega\tau')}{\cosh\omega\tau_i' - \cosh\omega\tau} = i\frac{Q}{\kappa}\ln\left[\frac{\tanh(\omega\tau_i'/2) + \tanh(\omega\tau_a'/2)}{\tanh(\omega\tau_i'/2) - \tanh(\omega\tau_a'/2)}\right], \tag{1.49}$$

where we have used the definition for τ_i' at optimal momentum, $\sinh\omega\tau_i' = \gamma$ [3] and the quasistatic approximation $\omega \ll \omega_0$ (implying $\gamma \ll 1$).

Combining the quasiclassical LRP term with the asymptotic quantum term, we get:

$$\delta S(t_s', 0) = -i\frac{Q}{\kappa}\ln\left[(\kappa a)\sinh\left(\frac{\alpha_i + \alpha_a}{2}\right) \Big/ \sinh\left(\frac{\alpha_i - \alpha_a}{2}\right)\right]. \tag{1.50}$$

Since $\kappa a \gg 1$, we are in the quasiclassical domain to make use of the complex trajectory expression Eq. (1.48):

$$a = z_{\text{opt}}(t_a') = \frac{A_0}{\omega}(\cos\omega t_a' - \cos\omega t_s') = 2\frac{A_0}{\omega}\sinh\left(\frac{\alpha_i - \alpha_a}{2}\right)\sin\left(\frac{\alpha_i + \alpha_a}{2}\right), \tag{1.51}$$

which simplifies Eq. (1.50) to:

$$\delta S(t_s', 0) = -i\frac{Q}{\kappa}\ln\left[2\frac{A_0}{\omega}\sinh^2\left(\frac{\alpha_i + \alpha_a}{2}\right)\right]. \tag{1.52}$$

We now make use of the adiabatic approximation, $\gamma \ll 1$ realised through an extremely slowly varying field $\omega \ll \omega_0 = \kappa^2/2$. Under this limit $\alpha_a = \omega\tau_a' \to \alpha_i = \omega\tau_i' \approx \gamma$ near the optimal momentum in linear fields. The final result for this boundary matching scheme is

$$\delta S(t_s', 0) = -i\frac{Q}{\kappa}\ln\left(\frac{2F_0}{F}\right), \tag{1.53}$$

which leads to

$$\exp(-\Im[\delta S]) = \left(\frac{2F_0}{F}\right)^{Q/\kappa}, \tag{1.54}$$

where $F_0 = \kappa^3$ is the characteristic atomic field strength, and F is the peak strength of the monochromatic laser field.

The final result of the ionisation amplitude, independent of the boundary term $r' = a$, is:

$$a_{\text{LRP}}(\mathbf{p}, t) = \sqrt{\frac{2\pi}{S''_{\text{SFA}}(t_s')}}\left(\frac{2F_0}{F}\right)^{Q/\kappa} e^{-iS_{\text{SFA}}(t_s', \mathbf{p}_0)} Y_{\ell,m}\big(0, \phi_{v_{\mathbf{p}_0}}(t_s')\big). \tag{1.55}$$

Elliptical Polarisation

For an elliptical field, defined by the vector potential

$$A_x(t) = -A_0\cos\omega t, \quad A_y(t) = -\varepsilon A_0\sin\omega t, \tag{1.56}$$

where ε is the field ellipticity parameter defined in the range, $-1 \leq \varepsilon \leq 1$. The positive values are for right-circularly polarised and negative values for left-circularly polarised field.

The direction of optimal momentum at the detector is defined perpendicular to the maximum electric field strength. In present case of Eq. (1.56), the electric field maximum lies along the positive x-axis, which results in the optimal momentum directed along the positive y-axis. The detection angle aligns with the instant of ionisation, which gives us $\omega t_i' = \phi_p = \pi/2$.

The magnitude of the optimal momentum is obtained by defining a parameter ζ, such that

$$\sinh \omega\tau_i' = \sqrt{\frac{\zeta^2 + \gamma^2}{1 - \zeta^2}}, \tag{1.57}$$

a relation which is valid for all ellipticities. From this, and using the fact that the real part of the ionisation time t_s', is $\omega t_i' = \pi/2$, we get

$$p_0 = \frac{\kappa}{\gamma}(\varepsilon - \zeta_0)\sqrt{\frac{1 + \gamma^2}{1 - \zeta_0^2}}. \tag{1.58}$$

The optimal momentum defined in terms of ζ is at a specific value ζ_0, defined by the implicit equation [4] (again derived from $\partial S/\partial \mathbf{p} = 0$):

$$\sqrt{\frac{\zeta_0^2 + \gamma^2}{1 + \gamma^2}} = \tanh\left[\frac{\varepsilon}{\varepsilon - \zeta_0}\sqrt{\frac{\zeta_0^2 + \gamma^2}{1 + \gamma^2}}\right]. \tag{1.59}$$

Therefore, Eq. (1.58) is an implicit equation in p_0. The motion now being defined in two dimensions, the prefactor has a new term [5]:

$$a_{\mathrm{LRP}}(\mathbf{p}, \varepsilon) = \left[\frac{2F_0}{F} C(\gamma, \varepsilon)\right]^{Q/\kappa} e^{-iS_{\mathrm{SFA}}(t_s', \mathbf{p}_0)} Y_{\ell m}(\pi/2, \phi_{v_{\mathbf{p}_0}}(t_s')), \tag{1.60}$$

where

$$C(\gamma, \varepsilon) = \frac{\alpha_i}{2\gamma} \exp\left[\int_0^{\alpha_i} d\alpha \left\{\frac{\gamma}{F(\gamma, \varepsilon)} - \frac{1}{\alpha_i - \alpha}\right\}\right], \tag{1.61}$$

$$F(\gamma, \varepsilon) = \sqrt{(\cosh \alpha_i - \cosh \alpha)^2 - \varepsilon^2 \alpha^2 \left(\frac{\sinh \alpha_i}{\alpha_i} - \frac{\sinh \alpha}{\alpha}\right)^2}. \tag{1.62}$$

In Eqs. (1.61) and (1.62), $\alpha_i = \omega\tau_i'$, where τ_i' is the imaginary part of the complex ionisation time t_s', and $\alpha = \omega\tau$ is the integration variable defined for the time domain corresponding to motion of the electron under the barrier.

The boundary matching scheme in elliptical fields was again realised by taking the matching point in the limit $\tau_a' \to \tau_i'$, which is only valid for quasistatic fields $\omega \ll \omega_0$.

The PPT results for ionisation amplitude in LRP, Eqs. (1.55) and (1.60), fix the prefactor correctly, especially taking into account the enhancement of ionisation rates by several orders of magnitude in a LRP, compared to SRP. Equations (1.55) and (1.60) are valid only in the adiabatic range when $\gamma \ll 1$ due to the slow field frequency compared to the response time of the unperturbed electron. Conventional and state-of-the-art experiments presently operate in a frequency range within an order of magnitude of the characteristic frequency of the atom [44, 45, 54–58]. The nonadiabatic motion of the barrier must therefore affect the ionisation process, even as the electron propagates into the continuum once emerging from under the barrier. Unlike the PPT theory, therefore, the ionisation process may not end right when the electron is born into the continuum, and we need to consider in further detail nonadiabatic ionisation in a LRP under a strong laser field. For the more general domain of nonadiabatic field frequencies, where $\gamma \gtrsim 1$, we will present the ARM formulation in Chapter 2, with rigorous generalisation described in Chapter 3 for a bound state with arbitrary (ℓ, m)-numbers.

1.3 Floquet Theory in Strong Fields

While in the Keldysh and PPT theory, we ignore the polarisation of the bound states by the strong laser field, modifications of the energy levels in the presence of strong fields could be significant. In this section, we consider the effect of strong laser fields on the bound state energy shifts and its relevance in the laser field parameter range we consider.

One consistent method to include the laser field effects completely on the bound state is the Floquet theory [59–62] which is applicable for time-periodic Hamiltonians. We start with the Schrödinger equation in the periodic, monochromatic field:

$$i\frac{\partial\Psi}{\partial t} = \hat{H}\Psi, \tag{1.63}$$

with the periodic condition

$$\hat{H}(t+T) = \hat{H}, \tag{1.64}$$

where $T = 2\pi/\omega$ is the time-period of the laser field with angular frequency ω.

From the Floquet theorem, the solution to Eq. (1.63) with the condition (1.64) defines the Quasienergy State (QES):

$$\Psi(\mathbf{r},t) = e^{-i\epsilon t}\Phi_\epsilon(\mathbf{r},t), \tag{1.65}$$

where $\Phi(\mathbf{r},t)$ satisfies the periodicity condition

$$\Phi_\epsilon(\mathbf{r},t+T) = \Phi_\epsilon(\mathbf{r},t). \tag{1.66}$$

The parameter ϵ is real and called the quasienergy of the system, in analogy with the concept of quasimomentum in Bloch eigenstates for a spatially periodic system.

Substituting Eq. (1.65) into Eq. (1.63), we get the eigenvalue problem:

$$\hat{\mathscr{H}}(\mathbf{r},t)\Phi_\epsilon(\mathbf{r},t) = \epsilon\Phi_\epsilon(\mathbf{r},t). \tag{1.67}$$

with $\hat{\mathscr{H}} = \hat{H} - i\partial/\partial t$ and periodicity condition in Eq. (1.66), from which we also observe that if the system is in a QES with quasienergy ϵ, then it gives rise to a ladder of quasienergy levels $\epsilon + n\omega$ (for arbitrary integer n, $\hbar = 1$). The quasienergies can be interpreted as the "total" energy of the combined laser field and atomic system under consideration, with n often referred to as the number of photons absorbed by the atomic system. The QES with different quasienergies are orthogonal and serve the same purpose as bound states in time-independent Schrödinger equation, with concomitant theorems and principles applicable (virial theorem, variational principle, etc.).

The conventional Floquet approach is conveniently applicable only to bound state dynamics. Indeed, for real-valued ϵ, the decay of the initially bound state can only be represented by a superposition of a continuum of quasienergy states. On the other hand, adiabatic turn-on of the laser field should transform a bound ground state into a single quasi-bound QES. To incorporate ionisation consistently, we need to include the possibility of complex quasienergies. Two common ways for this are:

1. complex scaling transformation [63–65], which involves promoting the spatial domain to complex domain with $\mathbf{r} \to \mathbf{r}\exp(i\alpha)$, leading to a non-Hermitian Hamiltonian and complex quaisenergies, or

2. quasi-stationary, quasi-energy states (QQES) [66–68], which allow for complex quasienergies by using complex boundary conditions for an outgoing electron in a continuum state

What pertains to our analysis and review of theoretical methods in optical tunnelling in a strong laser fields, is the validity of approximating the total wavefunction in the combined effects of the core potential and the strong laser field by the laser field-free bound state and

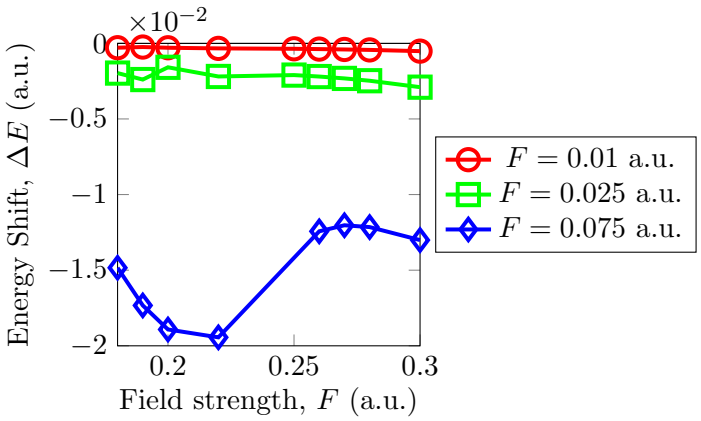

Figure 1.3: Energy shifts for Hydrogen atom ($1s$ state), calculated from complex scaled QQES approach by Chu [64, 65], for field strengths $F = 0.01$ a.u. (), $F = 0.025$ a.u. (), and $F = 0.075$ a.u. (). The unperturbed energy of the bound state H-atom is at $E_0 = -0.5$ a.u.

energy in the vicinity of the core. The real part of quasi-energies also include the AC Stark shift of the unperturbed energy levels in the presence of strong fields, thus allowing us to gauge the significance of this shift. From the complex scaling method [64], we know that the distortions of the quasienergy states for field strengths in the vicinity of $F = 0.01 - 0.10$ a.u. is, at the most, an order of magnitude smaller than the bound state energy, for laser field frequency range $0.18 < \omega < 0.30$ a.u. (Fig. 1.3).

In optical tunnelling regime, we consider frequencies at least an order of magnitude smaller than the ones used in [64, 65], $\omega < 0.1$ a.u., and field strengths at least one or two orders of magnitude smaller than the atomic field strength, $0.01 < F_0 < 0.075$ a.u. typically. With the general trend of field shifts of quasienergy states decreasing with decreasing field frequencies, we can safely assume that the energy of the field-dressed state can be approximated to the bound state, with the resulting error limited to less than $3 - 4$ orders of magnitude in energy. This conclusion is also corroborated by the QQES theory of Manakov et. al. (for circularly polarised field, especially, see [69]).

For the QQES approach to model ionisation, we consider its application in the Time-Dependent Effective Range (TDER) theory, which combines the QQES method to Zero-Range Potential (ZRP) models used for describing ionisation in negative ions. ZRP models rely on describing the core potential by a delta-type well, or a binding potential active in a finite region of space. There are some limitations to this model, which we explain in the next section, and present an outline of the TDER theory that surmounts these limitations to provide a generalised theory of strong field detachment in anions.

1.4 Time-Dependent Effecive Range Theory

The zero-range potential model has been used extensively [3,4,70] to study strong field processes in atoms, owing to its simplicity and efficacy in modelling core potential interaction of the ionising electron in strong fields, at least qualitatively for atoms and quantitatively for negatively charged ions. However, one limitation of ZRP models is that it supports exactly one bound state, and an s-state only, to describe the bound electron [10]. But it is well known that the symmetry of the initial bound state of the electron is crucial in deciphering the angular distributions of the photoelectron in experiments and understanding the various strong field processes [71–76].

The Time Dependent Effective Range (TDER) theory provides a solution to this problem in ZRPs, by combining the effective range theory [10] (with two modelling parameters) with the QQES theory mentioned in the previous section, and allowing for a bound state of arbitrary angular momentum. Within the TDER approach, the electron interaction with both the core

and the laser field potential is treated non-perturbatively, and thus can be used to model a wide range of strong field phenomena in short-range potentials supporting arbitrary angular quantum numbers. Thus, the theory goes beyond the standard Keldysh Approximation (KA).

The starting point is defining a core potential $U(r)$ to model the ZRP, but this time with two parameters, the binding energy E_0 and the asymptotic coefficient $C_{\kappa\ell}$ in the wavefunction at large distances. For this we define the cut-off point for the potential, r_c, such that,

$$U(r) = 0, \text{ for } r \gtrsim r_c. \tag{1.68}$$

To harbour a shallow bound state in the field-free case in this potential, we require $r_c \ll 1/\kappa$. In the asymptotic limit, $\kappa r \gg 1$, the radial part of the wavefunction can be approximated as

$$R_{\kappa\ell} \approx C_{\kappa\ell} \frac{e^{-\kappa r}}{r}, \tag{1.69}$$

and $C_{\kappa\ell}$ thus controls the definition of the core potential $U(r)$.

The next step is to invoke the QQES formalism of the previous section. For this purpose, we again solve the time-dependent eigenvalue problem satisfied by the time-periodic part of QQES:

$$\hat{\mathscr{H}}(\mathbf{r}, t)\Phi_\epsilon(\mathbf{r}, t) = \epsilon\Phi_\epsilon(\mathbf{r}, t), \tag{1.67}$$

but with complex values for quasienergy ϵ. As $U(r) = 0$ for $r > r_c$, in that radial domain the outgoing electron solutions are simply the free electron states (GV) in a laser field. To solve for ϵ, we need to match these continuum states with the solution for Eq. (1.67) inside the potential well.

The application of TDER for short-range potential systems as negative ions can be used to study threshold effect of channel-closing in strong fields [77]. Channel closing refers to the phenomenon of lost multiphoton ionisation channels due to increase in Stark shifts of the bound states as well as the ponderomotive energy shift of the continuum threshold, as the laser field intensity increases. The TDER theory captures this nonperturbative effect when plotting the complex quasienergies as a function of intensity, where channel closing manifests as irregularities in the energy shifts and discontinuities in detachment rates simultaneously.

Conversely, channel-opening effects can also be observed within the TDER theory by plotting the complex quasienergies as a function of laser field frequency. In channel-opening, as the field frequency increases, a new, lower-photon transition channel becomes available for detachment of the electron into the continuum.

These two effects, along with other features of quasienergy variations with field intensity and frequency, can be used to distinguish between the bound-state orbital magnetic number m participating in the process. For example, the Stark shifts for $m = 0$ states are significantly higher than for $|m| = 1$, due to unavailability of virtual electron transitions to s-state in the latter case. Threshold effects are also more easily perceived in $m = 0$ states than for $|m| \neq 0$, due to sharper dependence of detachment cross section on the angular momentum for $m = 0$ than for $|m| = 1$. The effective range theory provides an exact solution for all strong field phenomena for short-range potentials. Therefore it can be used to check the validity of various approximations. For example, [30] shows that Keldysh (length gauge SFA) result is reproduced in the effective range theory once the rescaterring effects are excluded.

1.5 Further Literature

A generalisaton of Keldysh theory was provided in the Keldysh-Faisal-Reiss (KFR) model [78–81]. The difference between Keldysh and KFR theories, historical perspective on their development, and further extension to include LRP effects over a wide range of Keldysh parameter is detailed comprehensively in [82]. The extension of Keldysh theory to intensities and electron

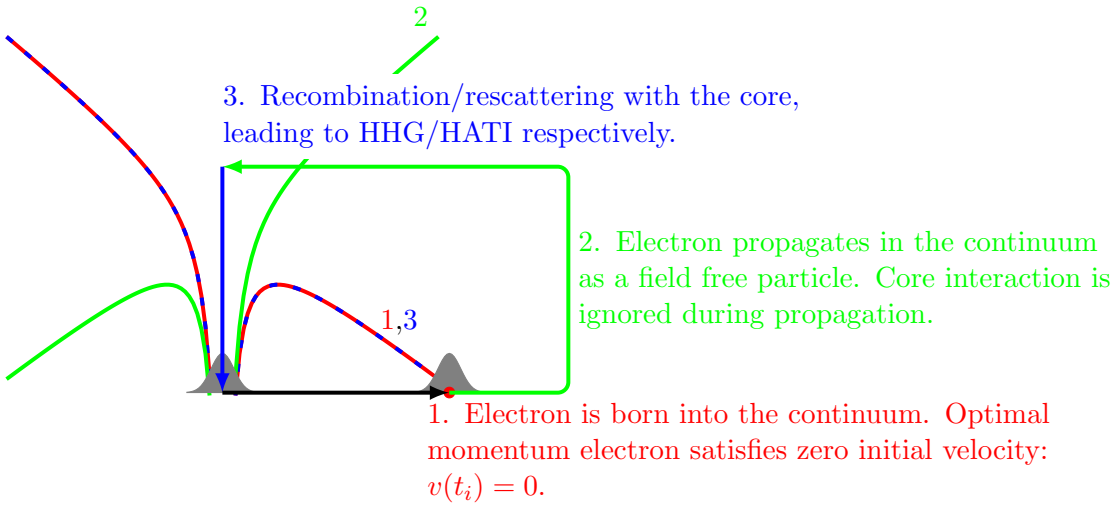

Figure 1.4: Classical three-step model for strong field ionisation. The non-classical tunnelling under the barrier step is not included and the electron is assumed to be born into the continuum as a free electron in laser field state.

energies approaching the relativistic limit was first presented by Nikishov and Ritus [83], and later by Reiss in a thorough, comprehensive Physical theory of strong field ionisation [43, 84]. The subject of multiphoton ionisation [85–94], Above Threshold Ionisation (ATI) [95–101], Multielectron Processes [102–111], High Harmonic Generation (HHG) [112–129], have since been thorougly expatiated in the literature. Below we outline some key results pertinent to the work developed in this Thesis.

1.5.1 Simple models for strong field phenomena

An intuitive and easy to implement model prevalent in strong field ionisation is the three step model [130], which was preceeded by a two-step model as a source for ATI [131], and posits a classical, simpleman's theory of strong field ionisation. See also [132, 133] for the model of an "atomic antenna" and the quasistatic theory [96, 134–136], along with the necessity of recollision as the additional third step [137–140]. As the name suggests, the model consists of three steps: (1) ionisation of the electron by the strong laser field through modulation of the core potential barrier (Fig. 1.1a), (2) the propagation of the electron in the laser field ignoring distortions by the core potential, and (3) either recombination or recollision with the parent ion resulting in the production of HHG or higher energy electrons (HATI, $E > 2U_P$), as the electron is steered back by the laser field. A schematic for the 3-step model is presented in Fig. 1.4. The ionising electron is considered to be the sole active electron in what might be a complex collection of several electrons and nuclei in a molecule. This supposition is the Single Active Electron (SAE) approximation.

While this model has provided an invaluable and remarkably simple visualisation for a wide array of strong-field phenomena, as we venture into studying more complex systems (e.g., molecules with multiple ionisation channels), or delve deeper into the region of energy spectrum where the assumptions made in the Simple Man Model (SMM) are questionable, a more comprehensive theory is desired. For example, in the SMM, for phase (1), the electron is assumed to emerge from under the barrier with a zero velocity. This adiabatic assumption at the very start of the ionisation process has been called into question recently, both from theoretical [46, 141–144] and experimental [55, 57] point of view. In step (2), the effects of core potential on electron dynamics is ignored, on account of the usually large energy imparted to the electron by the laser field. This assumption is not valid for low-energy electrons in the ATI spectrum, where the

core potential plays a prominent role in deciding the features observed in experiments [145–147]. Even for moderate energy, direct photoelectrons, core interactions have already been known to significantly affect the ionisation rates and amplitudes from the early days of Keldysh and PPT results. For the last event (3), it is implied that the electron recombines to the same state of the ion, usually the ground state, in which it left it in the beginning. However, as shown in recent studies on molecules [129,148], more than one channel can be active during the ionisation process, and hence available on the recombination/recollision stage, explaining some of the most crucial features in the HHG spectrum [129].

1.5.2 Numerical and Analytical methods: the pre-attosecond and attosecond era

Coincident with the analytical approach, numerical methods have also been developed to study strong field ionisation, beginning with the pioneering work of Kulander [149], followed by several approaches developed [150, 151] within the Single-Active Electron (SAE) approximation, where all but one electron in the system are considered to be ensconced in a placid state of tranquillity from the agitations of the strong laser field, save for the screening effect that can be imputed to the core electrons, so as to affect the effective charge felt by the ionising electron. A numerical approach based on the Floquet theorem [152] for laser-dressed states, exploiting the time periodicity of interaction between the ionising electron and the laser field, is also available [60, 63, 153–157].

With these developments, a basic theory of strong field ionisation was established, accompanied by simultaneous progress on the experimental front, beginning from the first study of multiphoton ($I_p/\hbar\omega \approx 7$) ionisation of Xenon [158], the observation of above threshold ionisation (ATI) peaks [20, 159] which unequivocally signified the breakdown of lowest-order perturbation theory (LOPT) for strong field ionisation, tunnelling ionisation in noble gas atoms [160], high-harmonic generation (HHG) [112–129, 161], the discovery of high-energy electron plateau in ATI [97, 162–165], electron-electron correlations in non-sequential (NSDI) [102, 103, 105, 166–169] and lately, sequential double ionisation (SDI) [55, 56, 170–173].

Starting from the first half of the new millennium, short-cycle, femtosecond pulses were readily available with high peak intensity and optical field frequencies, which ushered in the era of experimental studies of light-matter interaction towards the sub-femtosecond domain [118, 174, 175], including the first stereo-ATI experiment [123, 176–178], which is essentially the double-slit experiment performed in the attosecond domain, production of carrier-envelope offset phase (CEP) stabilised light beams to study CEP effects on HHG [179], and resulting in routine generation of attosecond pulses [54] opening the new era of attosecond dynamical imaging. New imaginag techniques with high temporal and spatial resolution were introduced, such as the attosecond streak camera [44], the attoclock [45], laser-induced electron diffraction [180–182], tomographic imaging of molecular orbits [183, 184]. High harmonic spectroscopy has also been developed, that focuses on studying the vibrational and multielectron dynamics in intense fields. Intriguing questions about attosecond dynamics triggered by ionisation have also been addressed, such as attosecond time-delay measurement in ionisation of noble gas atoms [44, 45, 55, 185, 186] and probing the hole dynamics in noble gas ions after strong field ionisation [54, 187]. Furthermore, after nearly five decades, it was discovered that for the nonadiabatic domain ($\gamma \simeq 1$), strong field tunnel ionisation by a circularly polarised radiation from valence p-orbitals, specifically noble gas atoms, has a proclivity towards liberating electrons "rotating" counter-clockwise relative to the field, i.e. with magnetic quantum number (m_ℓ) opposite to field polarisation [142, 143]. These and other new effects in strong field ionisation, such as observation of Low-Energy Structures (LES) [145–147, 188–195], time-resolving subcycle tunnelling dynamics [44, 45, 55, 196–199], have made the subject of early Keldysh and PPT works topical, while also demanding significant upgrades of these and other existing theoretical methods.

First, the originally developed analytical theories were still lacking the dynamical aspects

of the ionisation process, i.e., the rates derived applied for end-of-time observations but not sub-cycle timescales.

Second, the conventional adiabatic theory of ionisation [2–6], and the generalisaton in the Keldysh-Faisal-Reiss (KFR) theory [78,79,81] is suitable for deriving ionisation rates for long duration, nearly-monochromatic fields, and accurately applicable for systems manifesting electron-core interactions via short-range potentials, i.e., negative ions [29, 200–203]. In the presence of long-range interactions, the usual theories working within the limits of SFA are not accurate qualitatively at times, let alone the issue of quantitative agreement. For example, the photoelectron angular distributions exhibits no left-right or inversion symmetry predicted by SFA [204]. The SFA approach also fails to account for the effects of Coulomb-singularity observed for transverse distribution [205], and the Coulomb focussing effects [206, 207]. Since Keldysh [2] and PPT's work [5] it has been known that Coulomb-type corrections are crucial for the prefactor, and an estimate was made in [5] of this correction enhancing the ionisation probability by 2 to 3 orders of magnitude. Inclusion of Coulomb-correction to ionisation rates was carried out in a rather adhoc, albeit physically intuitive manner, which lead to the idea of boundary-matching scheme developed within the quasiclassical approximation method for non-stationary systems: an ingenious contrivance in predicting reliable theoretical expressions for ionisation rates in long-range potentials, albeit in the quasistatic limit ($\omega \to 0$).

Third, as stronger and shorter field pulses have been generated at a remarkable pace over the course of a few decades, we have ventured into the experimental domain where the Keldysh paramter γ, which is a measure of the nonadiabaticity of the ionisation process, has explored adiabatic tunnelling domain ($\gamma \ll 1$), the strongly multiphoton ionisation pathways ($\gamma \gg 1$), and, most importantly, a hybrid of the two extremes for $\gamma \simeq 1$ [141], which has been the domain of operation for recent experiments [55, 57, 187].

Fourth, ionisation models developed within the scope of SAE approximation also do not take into account the interactions of the ionising electron with ensemble retained in the ion, or interaction of these core electrons with the laser fields, and polarisation effects. Electron-electron correlation specifically become important in Non-Sequential Double Ionisation (NSDI) and have been shown to be important even in Sequential Double Ionisation (SDI) processes experimentally [55, 170] and expounded on theoretically [171–173], albeit in a classical framework.

These factors taken together create a demand for a theory, which is able to model sub-cycle nonadiabatic Coulomb and multielectron effects faithfully.

The Intense-field Many-body S-matrix Theory (IMST) [208] is a quantum mechanical theory to take into account electron-electron correlations in a perturbative scheme. The standard KFR ionisation rate can be derived within the framework of IMST, by the right partition of the total Hamiltonian and choice of the interaction potential. The first amplitude in the series defined in different IMST approaches is equivalent to the SFA result, with subsequent corrections provided by additional terms. This theory allows one to tackle double ionisation, laser-induced electron diffraction and holography. Combining the main principles of this theory with the method of quantum orbits [209], based on the Saddle Point Method (SPM), significant progress in understanding attosecond dynamics in HHG [210, 211], High-order Above Threshold Ionisation (HATI) [212–218], X-ray atom scattering [150, 219–222], Laser-assisted electron-ion recombination [223, 224] or laser-assisted electron-atom scattering [225–228] and Non-Sequential Double Ionisation (NSDI) [229–231], has been achieved.

A complimentary perspective is provided by numerical methods. The brute-force *ab initio* solution of the Time Dependent Schrödinger [232] Equation (TDSE) is presently limited to two electron-systems (e.g., Helium) in a strong IR field. State of the art alternatives include: time-dependent multi-configuration approaches in strong fields [233–236] time-dependent density functional methods (TDDFT) [237], the multichannel approach [238], the time-dependent R-matrix method [239] and hybrid approaches combining quantum chemical and strong field methods [240–247]. Except for approximate and semi-analytical approaches [240–242, 245–247],

all these become computationally very expensive in the regime of intense mid-infrared laser fields, which is extremely important for the dynamic imaging [248, 249] (for example, the electron holography experiments [250] have been done for light wavelength between 7 and 16 μm). To overcome this obstacle, partitioning of the configuration space was suggested. It lies at the core of the very successful new method for calculating strong field continuum dynamics in two-electron systems (t-SURFF) [251, 252]. This method combines solution of the TDSE in the region of $\sim 100 - 200$ Bohr around the core, with analytical propagation of the electron in the laser field outside this region using the Volkov functions. The family of new numerical methods to describe multielectron dynamics in strong fields also includes the following very recent developments: the time-dependent generalized-active-space configuration interaction (TD-GASCI) method [253], the B-spline algebraic diagrammatic construction [254] and periodic von Neumann (PvB) method [255].

Including nonadiabatic, sub-cycle Coulomb effects is a central effort undertaken in this thesis. Coulomb-type corrections to the ionisation process, within the adiabatic limit, were first proposed in [2,5]. Developing on the Imaginary Time Method (ITM) [5,6], Coulomb corrections to ionisation rates and photoelectron angular distribution can be taken into account through corrections to the quantum-orbits in the adiabatic and nonadiabatic domain [50–53]. The subsequent approaches can be grouped as follows:

1. the ad-hoc methods, which assume that the effect of Coulomb and laser field interactions can be factorised in the electronic wavefunction. This Coulomb-Volkov approximation for the states of the continuum electron was an early attempt to take into account Coulomb-phase distortions in the plane wave Volkov states [256]. This adhoc method performs reasonably well for large excursion amplitudes of the free electron propagating in a strong laser field with a comparatively weaker Coulomb potential, and it has been applied to study Coulomb effects on ATI spectrum [192, 194, 257]. Several other methods to include Coulomb-type potential effects on the ionisation amplitudes have also been proposed [258–264]. These models are well-suited when the electron is removed by a highly energetic photon, allowing the Coulomb effects to be taken into account only in the prefactor, and exhibit no distortion of the spatial part of the phase. It is, however, not applicable in the optical and infrared frequency regime [265] where the Coulomb-Laser field coupling effect on the continuum electron cannot be ignored.

2. significant upgrade of the original PPT approach and extension to very large Keldysh parameter γ has been detailed in [266].

3. the approach based on propagating an ensemble of classical trajectories born at the tunnel exit, with initial conditions defined according to the PPT theory and corrected within the Coulomb-Corrected SFA (CCSFA) approach of Popruzhenko-Bauer [51, 52] has lead to significant progress in understanding Coulomb effects in ATI [249], and low-energy structures [146].

Finally, with this thesis, we present the Analytical R-Matrix (ARM) method [46, 148, 267–271], a quantum-mechanical framework to describe strong-field ionisation processes in systems with arbitrary long-range potential profiles, with specific focus on accurately and rigorously deriving the theory of Coulomb-Laser coupling for the ionising electron, as well as study in detail the effects of correlation interactions leading to laser-induced nonadiabatic transitions in ion during the ionisation process. The effect of the long-range core interaction with the ionising electron is taken into account through a nonadiabatic quasiclassical method, with an expression for the eikonal-Volkov electron [267] which models the distortions in the wavefront by the core potential. Since the fundamental effect is on the phase of the continuum electron, we can take into account long-range effects while the electron is tunnelling *under the barrier*, and consider corrections to the ionisation times defined through the saddle point method, which

will be subject of the next chapter. At high ellipticities of field polarisation, Coulomb-effects are known to specifically modify the ionisation process at the tunnel exit [207], and we present a theory to calibrate the time of ionisation through ARM method.

With recent experiments [55, 129, 187], it has become apparent that orbitals other than the valence could partake in the ionisation dynamics. A multichannel theory of ionisation in quantum mechanical regime is therefore indispensable in comprehending the complete dynamical process. Multichannel theories focussing on hole dynamics upon ionisation have been proposed in the recent years [143, 272, 273]. In the future we hope to apply multielectron theory of ARM, developed in [148], to study correlation channels arising in noble gas atoms and ions, with special empahsis on correlation effects in Sequential Double Ionisation (SDI), which have recently gained attention in theoretical [171–173] as well as experimental [55, 170] study of SDI in noble gas atoms.

1.6 Thesis Outline

The outline for this thesis is as follows: in Chapter 2 we derive the Analytical R-Matrix (ARM) formalism in circularly polarized fields. This approach allows one to take into account effects of long range core potential on ionisation dynamics. The core potential is consistently included to the first order of magnitude in its phase distortion of the continuum wavefunction of laser-driven electron.

Specifically, this Chapter extends the Analytical R-Matrix (ARM) method to the case of strong field ionisation by circularly and elliptically polarized laser fields. An application highlighting the importance of the nonadiabatic character of the ionisation process in long-range potentials is then presented, with the discussion of the attoclock setup and its improved calibration to take into account the electron interaction with the core potential. The usual assumptions of adiabaticity for the ionisation process is shown to be inaccurate in the regime of present day experiments.

The results of this Chapter were published in the paper: J. Kaushal and O. Smirnova, Nonadiabatic Coulomb effects in strong-field ionisation in circularly polarised laser fields, Phys. Rev. A, v. 88, 013421, (2013).

Next, in Chapter 4, we use and expand the ARM results of Chapter 2, to propose a new clock which is able to time the ionisation dynamics in strong laser fields. This clock exploits the spin-orbit interaction in noble gas atoms. This new "attoclock" has the inherent advantage of being "built-in" to the atom under investigation and provides a natural way to study delay times in strong field ionisation. Theoretically, we develop a consistent map which links the rotation of the electron or hole spin with ionisation time delays, from one-photon to multi-photon / tunnel ionisation regimes. Essential to deriving these time delays are expressions for phase delays induced through the (model) long- and short-range interactions between the outgoing electron and the core. We also analyse the similarities and difference between the standard barrier problem and strong field tunnel ionisation, elucidating the role of ionisation potential I_p through a concise expression for time delays associated with long-range interactions.

The results of this Chapter were published in the paper: J. Kaushal, F. Morales, L. Torlina, M. Ivanov, and O. Smirnova, Spinorbit Larmor clock for ionisation times in one-photon and strong-field regimes, J. Phys. B, v. 48, 234002, 2015.

One of the cornerstones of the R-matrix theory is the need to match the wavefunction obtained in the so-called "inner" and "outer" regions, at the boundary of the R-sphere surrounding the ionic core. The issue of boundary-matching for bound states with arbitrary quantum numbers is discussed in Chapter 3, where we present a rigorous derivation and generalisation to the effectively adhoc approach developed by PPT [3–6]. With this generalised and rigorous boundary-matching scheme, we also show a method to include modification of the electron momentum distribution due to electron-core interactions right from the very instant the electron

plunges into the non-classical region. This matching scheme is a crucial step required to include the effects of Long-Range Potential (LRP) interactions on ionisation dynamics.

We also present in this chapter a general derivation of Coulomb-corrected complex ionisation times, which unifies the Larmor clock delay times [Chapter 4] and the numerical validation of delay times presented in [269, 270].

The results of this Chapter were published in the paper: J. Kaushal, F. Morales, and O. Smirnova, Opportunities for detecting ring currents using an attoclock setup, Phys. Rev. A, v. 92, 063405, (2015).

Effects of spin-orbit interaction on spin polarisation of electrons emitted during strong-field ionisation is presented in Chapter 5. Spin polarised sources of electrons is a thoroughly studied subject and is a research field in itself [274]. However, the possibility of spin polarisation in strong field ionisation has been predicted only recently [144, 273]. This chapter is motivated by the study of spin polarisation during strong field ionisation from short-range potentials [144,273]. We include the Coulomb effects and study in detail the response of noble gas atoms, as well as alkali ions, in strong laser fields. We also consider the effects of long range interactions on the magnitude and directional properties of the spin-polarised electrons. A comparison with the zero range potential results shows subtle distortions in the degree and direction of spin polarisation, evincing signs of symmetry breaking in the process, besides the usual asymmetries induced in photoelectron angular distributions [204].

1.A Complex WKB and BOMCA

There have been many attempts at elucidating the counter-intuitive nature of quantum mechanics through graspable ideas of trajectories. Using the standard ansatz for a wavefunction:

$$\Psi(\mathbf{r},t) = A(\mathbf{r},t)\exp\left(\frac{i}{\hbar}S(\mathbf{r},t)\right) \tag{1.70}$$

with a real amplitude $A(\mathbf{r},t)$ and real phase $S(\mathbf{r},t)$, which, after substituting into the Schrödinger equation, gives us two coupled equation in *real* amplitude A and phase S:

$$\frac{\partial S}{\partial t} + \frac{(\nabla S)^2}{2m} + V = \frac{\hbar^2}{2m}\frac{\nabla^2 A}{A}, \tag{1.71}$$

$$\frac{\partial A}{\partial t} + \frac{\nabla A\cdot\nabla S}{m} + \frac{A\nabla^2 S}{2m} = 0. \tag{1.72}$$

The standard, quasiclassical WKB approach is to write a series in powers of Planck's constant $\hbar$, which allows us to interpret the wavefunction being defined through a (semi-)classical trajectory. In the Feynman Path Integral formulation, this corresponds to a saddle point approximation over all the paths available.

While this method is reliable in estimating the character of several physical processes, including strong field ionisation, to probe the quantum mechanical nature of atomic phenomena, we need a truly quantum mechanical theory. One of the limiting features of quasiclassical methods is its failure at the nodes of a wavefunction, which manifest as caustics in the classical trajectories. We need to go beyond the classical approach to accurately define the wavefunction at these points.

Recently, two new and closely related methods have been developed to tackle these issues: Complex WKB and Bohmian Mechanics with a Complex Action (BOMCA) [38, 40, 41]. Both Complex WKB and BOMCA start out with the same ansatz for the wavefunction:

$$\Psi(\mathbf{r},t) = \exp\left(\frac{i}{\hbar}S(\mathbf{r},t)\right), \tag{1.73}$$

from which we get a single quantum Hamilton-Jacobi (HJ) equation:

$$\frac{\partial S}{\partial t} + \frac{(\nabla S)^2}{2m} + V = \frac{i\hbar}{2m}\nabla^2 S. \tag{1.74}$$

Here, $S(\mathbf{r},t)$ is complex. From this point on, both methods diverge in two different groups.

1.A.1 Complex WKB

For Complex WKB, we first make use of the conventional series expansion in $\hbar$, $S(\mathbf{r},t) = \sum_{n=0}^{\infty} S_n(\mathbf{r},t)\hbar^n$. After following the standard rule of collecting all the terms for a given $\hbar^n$ and setting them individually to zero, we get the following set of equations for $S_n(\mathbf{r},t)$:

$$\partial_t S_0 + \frac{1}{2m}(\nabla S_0)^2 + V(\mathbf{r}) = 0, \tag{1.75}$$

$$\partial_t S_n + \frac{\nabla S_0}{m}\cdot\nabla S_n = -\frac{1}{2m}\sum_{m=1}^{n-1}\nabla S_m\cdot\nabla S_{n-m} + \frac{i}{2m}\nabla^2 S_{n-1}, \qquad n = 1,2,\ldots \tag{1.76}$$

While in conventional WKB, we are limited to only first few terms in S_n, in complex WKB we have the possibility of going to high orders in the expansion series of S by following the evolution of second derivatives of the form appearing in Eq. (1.76) upto a given n. This entails knowing derivatives up to order $2n$.

Complex WKB struggles with the same limitations that the quasiclassical WKB methods suffer from: caustics. It is, however, possible to regularize these singularities to integrate through the system of equations in Eqs. (1.75)–(1.76). We still are working with equivalent of classical trajectories, and we still have to relay on the power expansion approach of quasiclassical method.

BOMCA is a formalism based on the trajectory-based methods that employ the saddle point approximation around a near-classical path. This new approach allows us to consider deviation from the classical methods and consider a more effective formulation of trajectory-based quantum mechanics.

1.A.2 BOMCA

The essential difference between Complex WKB and BOMCA is that in former, we use the conventional WKB approach of adding more terms to get better accuracy, while in latter, we attain higher order accuracy by manipulating the paths on which the approximations are applied. Both make use of complex trajectories defined through the initial wavefunction. The flexibility in choosing paths in BOMCA allows to achieve a faithful quantum mechanical description through near-classical trajectories, while still easing the computational overhead by limiting to leading order terms.

In the quasiclassical WKB methods, the influence of the quantum potential, $Q = \hbar^2/2m\nabla^2 A/A$ is usually ignored, allowing us to define classical characteristic trajectories. In Bohmian Mechanics (BM), this is the crucial term leading to "quantum trajectories" and nonlocality that is characteristic of quantum mechanics. The apparent difference in conventional BM and BOMCA is that the amplitude part is subsumed into the phase, giving us a single, complex phase.

In BM, we use the full, quantum trajectories, defined through the expression:

$$\dot{\mathbf{r}} = \frac{\hbar}{m}\Im[\nabla \log \Psi(\mathbf{r}, t)], \tag{1.77}$$

whereas the trajectories implemented in BOMCA are perturbations around the classical trajectories. This is an advantage in favour of BOMCA: the velocities derived from quantum trajectories diverge at nodes of the wavefunction. With BOMCA we can gradually study the process around these and similar points where classical methods fail (e.g., due to caustics) while still retaining a sufficiently faithful representation of the wavefunction through these near-classical trajectories.

Compared to conventional, classical WKB-type analysis in initial step, BOMCA emphasises on the inclusion of the quantum potential, which is the essential ingredient of BM. Within BOMCA, a large number of coupled ODEs are solved to estimate the wavefunction. This is achieved by defining the equations of motion:

$$\frac{d\mathbf{r}}{dt} = \mathbf{v}, \quad \text{where, } \mathbf{v} = \frac{\nabla S}{m}, \tag{1.78}$$

which, along with Eq. (1.74), defines the evolution equations:

$$\frac{d\mathbf{v}}{dt} = -\frac{1}{m}\nabla V(\mathbf{r}) + \frac{i\hbar}{2m^2}\nabla^2(\nabla S), \text{ and} \tag{1.79}$$

$$\frac{dS}{dt} = \frac{1}{2m}\mathbf{v}^2 - V(\mathbf{r}) - \frac{i\hbar}{2m}\nabla^2 S. \tag{1.80}$$

The nonlocality due to the quantum potential, $i\hbar\nabla^2 S/2m$, deters any closed-form solutions to these equations.

The approach in BOMCA is to gather information on evolution of the Laplacian and higher derivative in Eqs. (1.80) and (1.79), through higher spatial derivatives of Eq. (1.80), until a specific order n that truncates all terms beyond differential order $2n$.

Since we are now considering complex trajectories, the wavefunction and associated action are analytically continued to the complex plane. It is shown that using a small set of trajectories

sufficiently reproduces the exact wavefunction once this quantum force term is also taken into account within the formalism of BOMCA [38]. This has applications in Strong Field Physics, where saddle point analysis was used to isolate a small set of trajectories to describe the physical processes [36].

1.B Ionisation Rates in PPT theory

We present here a succinct derivation of ionisation rates in SRP core within the PPT theory. The starting point is the expression for total wavefunction from Eq. (1.31):

$$\Psi(\mathbf{r},t) = \frac{i}{(2\pi)^3}\int_{-\infty}^{t} dt' \int d\mathbf{k}\, e^{-i\mathbf{v_k}(t)\cdot\mathbf{r} - \frac{i}{2}\int_{t'}^{t} d\tau\, v_{\mathbf{k}}^2(\tau)} \frac{1}{2}\big(v_{\mathbf{k}}^2(t') + \kappa^2\big)\Phi_0(\mathbf{v_k}(t'))e^{iI_p t'}. \tag{1.31}$$

We present here results for ionisation rates in an arbitrary elliptically polarised fields, linear and circular polarisation being special cases. The results will be derived with the approximations of the PPT approach [4] in mind. A more accurate derivation for ionisation rates, taking into account LRP core and for circular polarisation (which is straightforward to extend to elliptical polarisation) will be presented in Chapter 2.

The ionisation rate is defined as the flux of the probability current $\mathbf{j}$ through a plane at infinity perpedicular to the polarisation of the laser field. For an arbitrary elliptical field, with plane of polarisation set along the xy-plane and the direction of propagation set along the z-axis, this plane at infinity is a curved surface set at radius $r \to \infty$. Since we know the formal expression for the wavefunction in spatial domain from Eq. (1.31), the probability current is

$$\begin{aligned}\mathbf{j}(\mathbf{r},t) &\equiv \frac{i}{2}(\Psi\nabla\Psi^* - \Psi^*\nabla\Psi)\\ &= \frac{1}{2(2\pi)^3}\int d\mathbf{k}_2 d\mathbf{k}_1\, [\mathbf{v}_{\mathbf{k}_1}(t) + \mathbf{v}_{\mathbf{k}_2}(t)] I_{\ell m}(\mathbf{k}_1,t)^* I_{\ell m}(\mathbf{k}_2,t)\times\\ &\qquad \exp\left[i(\mathbf{k}_2-\mathbf{k}_1)\cdot(\mathbf{r}-\boldsymbol{\xi}(t)) - \frac{i}{2}(p_2^2 - p_1^2)t\right],\end{aligned} \tag{1.81}$$

where,

$$I_{\ell m}(\mathbf{k},t) = \int_{-\infty}^{t} dt'\, \frac{1}{2}\big(v_{\mathbf{k}}^2(t') + \kappa^2\big)\Phi_0(\mathbf{v_k}(t'))\exp\left[-\frac{i}{2}\int_{t'}^{T} d\tau\, v_{\mathbf{k}}(\tau) + \frac{\kappa^2}{2}t'\right]. \tag{1.82}$$

The plane at infinity, to be chosen for elliptically polarised field defined as

$$\mathbf{F}(t) = F_0(\cos(\omega t)\,\hat{\mathbf{x}} + \varepsilon\sin(\omega t)\,\hat{\mathbf{y}}), \tag{1.83}$$

is a cylinder of radius $R \to \infty$ with its axis along the z-axis. The integral of the probability current $\mathbf{j}(\mathbf{r},t)$ through this cylinder is represented by $\mathcal{J}(R,t)$, and using the relations:

$$\begin{aligned}\int_{-\infty}^{\infty} dz \int_0^{2\pi} d\phi\, R\exp\{i(\mathbf{k}_1-\mathbf{k}_2)\cdot\mathbf{r}\}(\mathbf{v}_{\mathbf{k}_1}(t) + \mathbf{v}_{\mathbf{k}_2}(t))\cdot\hat{\mathbf{r}} = 4\pi^2 i\delta(k_{1z}-k_{2z})\times\\ \big(v_{k_1}^2(t) - v_{k_2}^2(t)\big)\frac{RJ_1(R\|\mathbf{k}_{1\rho}-\mathbf{k}_{2\rho}\|)}{\|\mathbf{k}_{1\rho}-\mathbf{k}_{2\rho}\|}\end{aligned} \tag{1.84}$$

$$\lim_{R\to\infty}\frac{RJ_1(R\|\mathbf{k}_{1\rho}-\mathbf{k}_{2\rho}\|)}{\|\mathbf{k}_{1\rho}-\mathbf{k}_{2\rho}\|} = 2\pi\delta(\mathbf{k}_{1\rho}-\mathbf{k}_{2\rho}),\ \text{(Appendix 1.C)} \tag{1.85}$$

we get

$$\lim_{R\to\infty}\mathcal{J}(R,t) = \frac{i}{2}\int d\mathbf{k}_1 d\mathbf{k}_2\,\delta(\mathbf{k}_1-\mathbf{k}_2)\big[v_{\mathbf{k}_1}^2(t) - v_{\mathbf{k}_2}^2(t)\big]I_{\ell m}^*(\mathbf{k}_1,t)I_{\ell m}(\mathbf{k}_2,t). \tag{1.86}$$

Applying the delta-function rightaway would have given zero result because $\mathbf{v}_{\mathbf{k}_1}(t) = \mathbf{v}_{\mathbf{k}_2}(t)$; it is the singularity in $I_{\ell m}$ that will remove the zero in the integrand of Eq. (1.86). For the elliptical field defined by Eq. (1.83), using Fourier series expansion of the periodic integrand in Eq. (1.82), we get:

$$I_{\ell m}(\mathbf{k},t) = -i\sum_{n=-\infty}^{\infty} F_n(\mathbf{k})\frac{\exp(i\Omega_n t)}{\Omega_n - i\delta},\ \delta\to 0^+ \tag{1.87}$$

$$\Omega_n = \frac{k^2}{2} + \frac{\kappa^2}{2}\left(1+\frac{1+\varepsilon^2}{2}\right) - n\omega, \tag{1.88}$$

the Fourier coefficients, $F_n(\mathbf{k})$ are the crucial element to the whole derivation scheme in PPT theory, and is defined as

$$F_n(\mathbf{k}) = \frac{1}{2\pi}\int_{-\pi}^{\pi} d\alpha\ \exp\left[-i\frac{\omega_0}{\omega}\int_0^{\alpha} d\beta\left\{\frac{v_{\mathbf{k}}^2(\beta)}{\kappa^2}+1\right\}\right]\frac{1}{2}[v_{\mathbf{k}}^2(\alpha)+\kappa^2]\Phi_0(\mathbf{v}_{\mathbf{k}}(\alpha)),\ \alpha=\omega t'. \tag{1.89}$$

Substituting Eq. (1.87) in Eq. (1.86), we get:

$$\lim_{R\to\infty}\mathcal{J}(R,t) = \frac{i}{2}\int d\mathbf{k}_1 d\mathbf{k}_2\,\delta(\mathbf{k}_1-\mathbf{k}_2)\sum_{n_1,n_2=-\infty}^{\infty}\frac{\left[v_{\mathbf{k}_1}^2(t)-v_{\mathbf{k}_2}^2(t)\right]}{(\Omega_{n_1}+i\delta)(\Omega_{n_2}-i\delta)}F_{n_1}^*(\mathbf{k}_1)F_{n_2}(\mathbf{k}_2). \tag{1.90}$$

After interchanging the infinite (n_1,n_2)-summation with the $(\mathbf{k}_1,\mathbf{k}_2)$-integral on account of the integrand being convergent, and solving the (k_{1z},k_{2z})-integral with the delta function $\delta(k_{1z}-k_{2z})$ $(k_{1z}=k_{2z}=k_z)$, and similarly for the (ϕ_{1k},ϕ_{2k})-integral (i.e., $\phi_{1k}=\phi_{2k}=\phi_k$), we are left with

$$w(\mathcal{E},\omega) = \sum_{n_1,n_2=-\infty}^{\infty}\frac{i}{2}\int dk_z d\phi_k\int_0^{\infty} dk_{1\rho}\,k_{1\rho}\frac{F_{n_1}^*(k_{1\rho},\phi_k,k_z)}{(\Omega_{n_1}+i\delta)}\times$$
$$\int_0^{\infty} dk_{2\rho}\,k_{2\rho}\delta(k_{1\rho}-k_{2\rho})\frac{\left[v_{\mathbf{k}_{1\rho}}^2(t)-v_{\mathbf{k}_{2\rho}}^2(t)\right]}{(\Omega_{n_2}-i\delta)}F_{n_2}(k_{2\rho},\phi_k,k_z), \tag{1.91}$$

where we have used the property of delta function:

$$\delta(\mathbf{k}_{1\rho}-\mathbf{k}_{2\rho})|_{\phi_{2k}=\phi_{1k}} = \lim_{k_{2\rho}\to k_{1\rho}}\frac{k_{1\rho}-k_{2\rho}}{\|\mathbf{k}_{1\rho}-\mathbf{k}_{2\rho}\|}\delta(k_{2\rho}-k_{1\rho})\Big|_{\phi_{2k}=\phi_{1k}} = \delta(k_{2\rho}-k_{1\rho}) \tag{1.92}$$

For convenience, we rewrite and define some terms for the denominator:

$$\Omega_{n_i} = \frac{k_\rho^2}{2}+\frac{k_z^2}{2}+\frac{\kappa^2}{2}\left(1+\frac{1+\varepsilon^2}{2\gamma^2}\right)-n_i\omega = \frac{1}{2}(k_\rho^2+K_i) \tag{1.93}$$

$$K_i = k_z^2+\kappa^2\left(1+\frac{1+\varepsilon^2}{2\gamma^2}\right)-2n_i\omega,\ i=1,2. \tag{1.94}$$

The $(k_{1\rho},k_{2\rho})$-integral can now be written as:

$$w(\mathcal{E},\omega) = 2i\sum_{n_1,n_2=-\infty}^{\infty}\int dk_z d\phi_k\int_0^{\infty} dk_{1\rho}\,k_{1\rho}\frac{F_{n_1}^*(k_{1\rho},\phi_k,k_z)}{(k_{1\rho}^2+K_1+i\delta)}\times$$
$$\int_0^{\infty} dk_{2\rho}\,\delta(k_{1\rho}-k_{2\rho})\left[v_{\mathbf{k}_{1\rho}}^2(t)-v_{\mathbf{k}_{2\rho}}^2(t)\right]\frac{F_{n_2}(k_{2\rho},\phi_k,k_z)}{(k_{2\rho}^2+K_2-i\delta)}. \tag{1.95}$$

We will first solve the $k_{2\rho}$-integral, treating the product of delta "function" with other functions as a regular function, and use the complex residue method for the $k_{2\rho}$-integral. Therefore, we start with

$$I_{k_{2\rho}} = \int_0^{\infty} dk_{2\rho}\,\delta(k_{1\rho}-k_{2\rho})(k_{1\rho}-k_{2\rho})(k_{1\rho}-k_{2\rho}-2\mathbf{A}(t)\cdot\hat{\mathbf{k}}_{1\rho})\frac{F_{n_2}(k_{2\rho},\phi_k,k_z)}{(k_{2\rho}^2+K_2-i\delta)}, \tag{1.96}$$

where we have expanded $\left[v^2_{\mathbf{k}_{1\rho}}(t) - v^2_{\mathbf{k}_{2\rho}}(t)\right]$ with the condition that $\phi_{1k} = \phi_{2k}$ that makes the directional vectors $\hat{\mathbf{k}}_{1\rho} = \hat{\mathbf{k}}_{2\rho}$. After solving the $k_{2\rho}$-integral, the zero provided by $(k_{1\rho} - k_{2\rho})$ in the numerator of Eq. (1.96) should cancel out with the pole of $(k^2_{1\rho} + K_1 + i\delta)$ to ensure a non-zero result. This requirement provides us with a way to choose the right poles for the integrand of $k_{2\rho}$, as well as fix the summation indices (n_1, n_2).

Now, if $K_2 \neq K_1$, then $n_1 \neq n_2$, which implies that the pole in $k_{1\rho}$ will not cancel with any zero from $k_{2\rho}$ [after solving Eq. (1.96)]. Therefore, we need $n_2 = n_1 = n$. Furthermore, if $K_i > 0$, then the poles for $k_{2\rho}$ lie along the imaginary axis with equal and opposite contributions to the residue. This makes the ionisation rate again zero. Hence, we need $K_i < 0$. From these two conditions, we get the lower bound on the summation index n:

$$n \geq n_0 = \frac{1}{\omega}\left[\frac{k_z^2}{2} + \frac{\kappa^2}{2}\left(1 + \frac{1+\varepsilon^2}{2\gamma^2}\right)\right], \tag{1.97}$$

since this condition holds for all k_z, it necessarily is true for $k_z = 0$, which gives us the absolute lower bound for threshold ionisation:

$$n_0 \equiv \frac{\kappa^2}{2\omega}\left(1 + \frac{1+\varepsilon^2}{2\gamma^2}\right) = \frac{\omega_0}{\omega}\left(1 + \frac{1+\varepsilon^2}{2\gamma^2}\right). \tag{1.98}$$

Expanding out the second-order poles in Eq. (1.96) to two first order ones, and carrying out the summation through the two residues $(k_{2\rho} = \pm\sqrt{-K} \pm i\delta/2\sqrt{-K})$, we get:

$$\begin{aligned} w(\mathcal{E}, \omega) &= 2\pi \sum_{n \geq n_0} \int_{-\infty}^{\infty} dk_z \int_0^{2\pi} d\phi_k \left| F_n\left(\sqrt{-K}, \phi_k, k_z\right)\right|^2 \\ &= 2\pi \sum_{n \geq n_0} \int d\mathbf{k} \left|F_n(\mathbf{k})\right|^2 \delta\left[\frac{k^2}{2} + \frac{\kappa^2}{2}\left(1 + \frac{1+\varepsilon^2}{2\gamma^2}\right) - n\omega\right], \end{aligned} \tag{1.99}$$

which is the required expression for ionisation rates in SRP in PPT theory.

1.C Ancillary Expressions

We derive here the result

$$\lim_{\rho \to \infty} \frac{\rho J_1(\rho d(\mathbf{k}_{1\rho}, \mathbf{k}_{2\rho}))}{d(\mathbf{k}_{1\rho}, \mathbf{k}_{2\rho})} = 2\pi\delta(\mathbf{k}_{1\rho} - \mathbf{k}_{2\rho}), \tag{1.100}$$

where $d(\mathbf{k}_{1\rho}, \mathbf{k}_{2\rho}) = \|\mathbf{k}_{1\rho} - \mathbf{k}_{2\rho}\|$ is the distance operator. We start from the integral

$$I_\rho = \int_0^{2\pi} d\phi \int_0^{\rho} d\rho'\, \rho' e^{i(\mathbf{k}_{1\rho} - \mathbf{k}_{2\rho})\cdot\rho'}. \tag{1.101}$$

This integral can be written as

$$\begin{aligned} I_\rho &= \int_0^{2\pi} d\phi \int_0^{\rho} d\rho'\, \rho' e^{i(k_{1\rho}\rho' \cos(\phi - \phi_{1k}) - k_{2\rho}\rho' \cos(\phi - \phi_{2k}))} \\ &= \int_0^{2\pi} d\phi \int_0^{\rho} d\rho'\, \rho' \sum_{n_1=-\infty}^{\infty} i^{n_1} J_{n_1}(k_{1\rho}\rho') e^{in_1(\phi - \phi_{1k})} \sum_{n_2=-\infty}^{\infty} (-i)^{n_2} J_{n_2}(k_{2\rho}\rho') e^{-in_2(\phi - \phi_{2k})} \\ &= 2\pi \int_0^{\rho} d\rho'\, \rho' J_0(\rho' d(\mathbf{k}_{1\rho}, \mathbf{k}_{2\rho})). \end{aligned}$$

In going from step 2 to step 3, we first perform the integral over ϕ and then use the Graf generalization of Neumann summation. The integral over ρ' is simple:

$$\int_0^{\rho} d\rho'\, \rho' J_0(\mathbf{k}_{1\rho}, \mathbf{k}_{2\rho}) = \frac{\rho J_1(\rho d(\mathbf{k}_{1\rho}, \mathbf{k}_{2\rho}))}{d(\mathbf{k}_{1\rho}, \mathbf{k}_{2\rho})}. \tag{1.102}$$

Therefore

$$I_\rho = 2\pi \frac{\rho J_1(\rho d(\mathbf{k}_{1\rho}, \mathbf{k}_{2\rho}))}{d(\mathbf{k}_{1\rho}, \mathbf{k}_{2\rho})}. \tag{1.103}$$

Now, by definition,

$$\begin{aligned}(2\pi)^2 \delta(\mathbf{k}_{1\rho} - \mathbf{k}_{2\rho}) &= \int_0^{2\pi} d\phi \int_0^{\infty} d\rho'\, \rho' e^{i(\mathbf{k}_{1\rho} - \mathbf{k}_{2\rho})\cdot\rho'} \\ &= \lim_{\rho\to\infty} \int_0^{2\pi} d\phi_{1k} \int_0^{\rho} d\rho'\, \rho' e^{i(\mathbf{k}_{1\rho} - \mathbf{k}_{2\rho})\cdot\rho'} \\ &= \lim_{\rho\to\infty} 2\pi \frac{\rho J_1(\rho d(\mathbf{k}_{1\rho}, \mathbf{k}_{2\rho}))}{d(\mathbf{k}_{1\rho}, \mathbf{k}_{2\rho})}.\end{aligned}$$

And we get

$$\lim_{\rho\to\infty} \frac{\rho J_1(\rho d(\mathbf{k}_{1\rho}, \mathbf{k}_{2\rho}))}{d(\mathbf{k}_{1\rho}, \mathbf{k}_{2\rho})} = 2\pi\delta(\mathbf{k}_{1\rho} - \mathbf{k}_{2\rho}), \tag{1.104}$$

which is the desired result.

Chapter 2

Analytical R-Matrix

The Anayltical R-Matrix (ARM) method is a new technique [46, 148, 268] developed to incorporate, in a rigorous and consistent manner, the effects of long-range potential interactions of the core with the ionising electron. In this chapter, we introduce the formalism for the method and develop the theory for strong field ionisation in a Coulomb binding potential, for circularly polarised fields.

2.1 Formalism

For an N-electron system, the evolution of the N-electron state, $\left|\psi^N\right\rangle$ under the influence of the Coulomb Potential V_C and Laser Field Potential V_L can be written as

$$i\frac{\partial}{\partial t}\left|\psi^N(t)\right\rangle = \hat{H}^N(t)\left|\psi^N(t)\right\rangle \tag{2.1}$$

where $\hat{H}^N(t)$ is the N-electron Hamiltonian in the Laser-field dressed atom/molecule.

We consider here the case of a Single Active Electron (SAE) approximation, wherein all but a single electron in the valence shell are assumed to be frozen and thereafter the corresponding dynamics of the system is defined from the interaction of this single active electron with the laser field and the Coulomb potential.

Equation (2.1) is therefore reduced to the Schrödinger equation for a single electron, under the influence of an arbitrary long-range potential $\hat{V}_C$ and the laser field potential $\hat{V}_L(t)$,

$$i\frac{\partial}{\partial t}|\psi(t)\rangle = \hat{H}(t)|\psi(t)\rangle \tag{2.2}$$

$|\psi(t)\rangle$ defines the state vector in Hilbert space of the one-electron system under the SAE approximation. Here $\hat{H}(t) = \hat{\mathbf{p}}^2/2 + \hat{V}_C + \hat{V}_L(t)$ is the effective Hamiltonian of the one-electorn system in the non-relativistic limit.

We now introduce the a mathematical construct partitioning the configuration space through a 3-dimensional sphere. We use this sphere as a demarcation of the configuration space into a Core-dominated Inner Region (Region I) and a Field-dominate Outer Region (Region II) (Fig. 2.1).

In the Core-dominated region, the influence of the core-potential, $\hat{V}_C$ is stronger than the laser field, such that the laser field effects of state-polarisation, channel-coupling etc. can be ignored. In the Field-dominated region, the electron wavefunction is primarily defined by the Volkov-electron defining a free electron in the laser field, along with the Core-potential effects included in the quasiclassical limit taking into account the phase distortion of the electron wavefunction due to the core. This is the Eikonal-Volkov approximated (EVA) electron [267].

With this partitioning scheme, we provide a rigorous and consistent approach to define the mathematical formalism with which we can reliably take into account the influence of the core

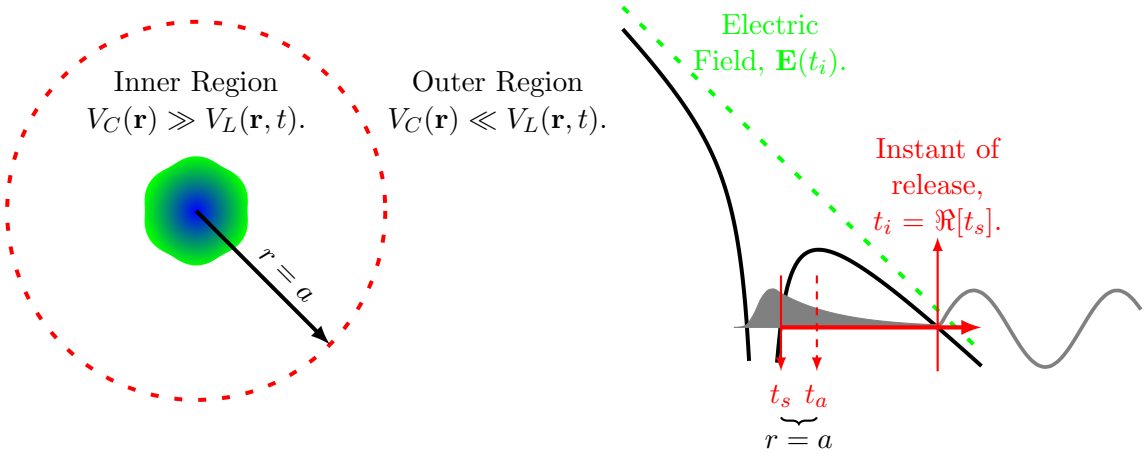

Figure 2.1: The Analytical R-Matrix (ARM) method to partition the configuration space, via the mathematical construct of a R-sphere at radius $r = a$, into a core-dominated (inner) region and field dominated (outer) region. The electron crosses the R-sphere at the time instant t_a, which is required to be close to the instant t_s when the electron launches into the barrier. The proximity of the two time instants ensures that approximating the total, polarised wavefunction by the field-free bound state for $r < a$ is sufficiently accurate, and also provides a consistent boundary-matching scheme that is essential to produce expressions for physical observables, like ionisation rates and momentum spectrum, that are independent of parameters defining the R-sphere.

potential on the ionising electron. The mathematical construct of the R-sphere also allows us to rigorously derive a boundary matching scheme that ensures the final results for physical observables like ionisation rates, amplitudes, momentum distributions etc. are independent from the value of the R-sphere. In the PPT approach, discussed in the previous Chapter, we had observed ad-hoc treatment of this issue when taking into account LRP (Coulomb-type) interactions of the ionising electron with the core. The primary aim of ARM is to provide a consistent formalism for such systems, where the coupling between the core and laser field potential cannot be approximated in a series perturbation in either of these interactions.

Mathematically, this partition into a core- and field-dominated region is achieved by adding and subtracting the Bloch operator $L^{(+)}(a)$ defined as

$$L^{(+)}(a) = \delta(r-a)\left(\frac{d}{dr} + \frac{1}{r}\right), \tag{2.3}$$

to the Hamiltonian in Eq. (2.2). This operator is necessary to ensure that the Hamiltonian of the system is Hermitian in the Core-dominated region defined in the radial domain $0 < r < a$ (see Appendix 2.A).

Similarly, to ensure that the Hamiltonian in the Field-dominated region is Hermitian, we need to add the outer-Bloch operator $L^{(-)}(a)$ (for the domain $a < r < \infty$) to the Hamiltonian, defined as

$$L^{(-)}(a) = -L^{(+)}(a) = -\delta(r-a)\left(\frac{d}{dr} + \frac{1}{r}\right), \tag{2.4}$$

The second term in parenthesis in either Eq. (2.3) or (2.4) is already Hermitian and so the Hermiticity of the Hamiltonian is left unaffected for an arbitrary constant term multiplied to it. We will use this fact to simplify our calculations for the current flux and probability density for strong field ionisation, in particular by using a constant term Q/κ, where Q is the effective charged of the atomic/molecular species under consideration, and κ is the effective momentum of the active electron corresponding to it's ground state energy level.

The exact solution for Eq. (2.2) can be written as:

$$|\Psi(t)\rangle = \hat{U}(t, t_0)|\Psi(t_0)\rangle. \tag{2.5}$$

here t_0 is the time instant marking the evolution of the system in the absense of the Laser field, usually in the distant past, and t is the present time instant parametrising the state of the electron, $|\Psi(t)\rangle$. $\hat{U}(t, t_0)$ is the unitary operator defining the evolution of the complete Atom + Laser field system, and is evaluated from the equation

$$i\frac{\partial \hat{U}(t, t_0)}{\partial t} = \hat{H}(t)\hat{U}(t, t_0) \tag{2.6}$$

The use of the Bloch operator effectively allows us to carry out Dyson-series expansion in alternating configuration spaces outlined by the operator. In this way, our ARM approach differs from other series expansions, where the interacting term is a physical potential, while here it is a geometric operator. This fact allows for a robust method to extend the short-range theory of Perelomov, Popov and Terentév (PPT) to arbitrary core-potentials.

We now make the first Dyson series expansion of Eq. (2.5), with the first step being the evolution from the Core-dominated region to the Bloch sphere at $r = a$, that is,

$$\hat{U}(t, t_0) = U_B^{(+)}(t, t_0) + i\int_{t_0}^{t} dt'\, U(t, t')L^{(+)}(a)U_B^{(+)}(t', t_0) \tag{2.7}$$

Here $\hat{U}_B^{(+)}(t, t_0)$ defines the evolution operator in the Core-dominated region, it's evolution goverened by the "inner" Hamiltonian $H_B^{(+)} = \hat{H} + L^{(+)}(a)$, which is Hermitian for $0 < r < a$, and thus leads to a unitary evolution. The first term defines the evolution of the system confined specifically to the inner region, and so this term does not contribute to the ionisation flux. The second term entails the evolution of the wavefunction in Region I through the interactions confined only in that domain, until it reaches the Bloch sphere at $r = a$ at time instant t', following which the electron evolves according to the complete system of Core and Laser field potentials acting on the electron.

Since only the second term in Eq. (2.7) contributes to the ionisation current, we consider only that term for Eq. (2.5), giving us the wave function contributing to ionisation current as

$$|\Psi(t)\rangle = i\int_{t_0}^{t} dt'\, \hat{U}(t, t')L^{(+)}(a)\hat{U}_B^{(+)}(t', t_0)|\Psi(t_0)\rangle. \tag{2.8}$$

We now consider a second expansion, on the full evolution operator $\hat{U}(t, t')$, which traverses the complete spatial domain, specifically the radial: $0 < r < \infty$. Since after reaching the Bloch sphere, we are considering only that electron flux that contributes to ionisation, the second expansion on $\hat{U}(t, t')$ in Eq. (2.8) confines the evolution solely to the Field-dominated region via the expansion

$$\hat{U}(t, t') = \hat{U}_B^{(-)}(t, t') + i\int_{t'}^{t} dt''\, \hat{U}(t, t'')\hat{L}^{(-)}(a)\hat{U}_B^{(-)}(t'', t'). \tag{2.9}$$

The second term defines the moment when the electron returns back to the Bloch sphere, *from outside*, and is of no concern to us here, although it can play an important role for describing High Harmonic Generation (HHG).

The final expression, defining the outgoing electron wavefunction contributing to strong-field ionisation, can therefore be written as

$$|\Psi(t)\rangle = i\int_{t_0}^{t} dt'\, \hat{U}_B^{(-)}(t, t')L^{(+)}(a)\hat{U}_B^{(+)}(t', t_0)|\Psi_g(t_0)\rangle. \tag{2.10}$$

We have also made here the additional approximation of equating the exact wave function at time t_0, $|\Psi(t_0)\rangle$, to the ground state wave function of the atomic/molecular species under consideration, in the absence of the laser field.

Physically, this expansion and approximation of the wave function implies that we consider the evolution of the electron wave function in the Region I, confining it geometrically to the Core-dominated space to define it's dynamics, ignoring the effects of the outer, Laser-dominated region. This is a reasonable assumption, as in the Core-dominated region the effects of the Laser field intensities that we are considering are significantly smaller compared to the overall wave function defined in the field-free case. After reaching the Bloch sphere, we consider the dynamics of the electron primarily defined in the strong Laser field in Region II, with the Coulomb interaction included perturbatively as defined by EVA [267].

We will use Eq. (2.10) in subsequent discussions to derive the ionisation rates and amplitudes for electron dynamics in strong laser fields, in the presence of long-range core-potentials.

2.2 Ionisation Amplitudes

We consider noble-gas atoms or similar species, where the energy separation between the ground states, and first and subsequeny excited states is large enough, resulting in exponential suppression of any pathway that might proceed from excitations through these levels.

This allows us to approximate the evolution operator for Core-dominated space by the Laser-free atomic/molecular evolution operator confined to only the ground state till time t' in Eq. (2.10), thus giving us

$$|\Psi(t)\rangle = i\int_{t_0}^{t} dt'\, \hat{U}_B^{(-)}(t,t')L^{(+)}(a)|\Psi_g(t')\rangle. \tag{2.11}$$

We consider tunnelling ionisation to be the dominant mechanism here, for the intensity ($10^{13} < I < 10^{14}$ W/cm^2) and frequency range ($800 < \lambda < 3200$ nm) we are considering. The ionisation process is thus governed by the exponentially decaying tale of the wave function, tunnelling out under the barrier thinning along the direction of suppression by the laser field vector.

Therefore, the long-range tail, usually Coulomb-like, is sufficient for describing the wave function profile in the region we are interested in, that is, under the barrier, from which the ionisation flux emerges. The atomic/molecular wave function with a Coulomb tail is (asymptotically):

$$\Psi_g(\mathbf{r},t) = \langle \mathbf{r}|\Psi_g(t)\rangle = \varphi_{\kappa\ell}(r)Y_{\ell m}(\theta,\phi)e^{iI_P t} = C_{\kappa\ell}\kappa^{3/2}\frac{e^{-\kappa r}}{\kappa r}(\kappa r)^{Q/\kappa}Y_{\ell,m}(\theta,\phi)e^{iI_P t} \tag{2.12}$$

where $C_{\kappa\ell}$ is the asymptotic state-specific coefficient for the radial part of the wave function, Q is the effective charge of the species under consideration, I_P is the ionisation potential, $\kappa = \sqrt{2I_P}$ is the characteristic momentum corresponding to the ground energy level, (ℓ, m) are the angular quantum numbers associated with the level. For molecules or other multi-electron atoms, the valence orbital wave function is usually described by a linear sum of atomic wave functions of the type described by Eq. (2.12).

As was mentioned in the previous section, the second term in parenthesis of the equation defining the inner Bloch operator $L^{(+)}(a)$, Eq. (2.3) is invariant under multiplication by a constant factor, and we use the term $(-Q/\kappa + 1)$ for this constant factor. This allows us, using Eq. (2.12), to write the product $L^{(+)}(a)|\Psi_g(t')\rangle$ as

$$\begin{aligned} L^{(+)}(a)\langle \mathbf{r}'|\Psi_g(t')\rangle &= \delta(r'-a)\left(\frac{d}{dr'} - \frac{Q/\kappa - 1}{r'}\right)\Psi_g(\mathbf{r}',t') \\ &= -\kappa\delta(r'-a)\Psi_g(\mathbf{r}',t') \end{aligned} \tag{2.13}$$

The ionisation amplitude is now defined by projectng the final state $|\Psi(T)\rangle$ over the momentum space:

$$a(\mathbf{p},T) = \langle \mathbf{p}|\Psi(T)\rangle = -i\kappa \int_{-\infty}^{T} dt' \int d\mathbf{r}' \left\langle \mathbf{p}\middle|\hat{U}_B^{(-)}(T,t')\middle|\mathbf{r}'\right\rangle \delta(r'-a)\Psi_g(a,\theta',\phi',t') \tag{2.14}$$

Since we consider the propagator $\hat{U}^{(-)}(t,t')$ to be active in the Laser-field domain (Region II), approximating it with the EVA propagator [268] is valid. The projection of the EVA porpagator between the momentum and co-ordinate space can be derived to be

$$\begin{aligned}\left\langle \mathbf{p}\middle|\hat{U}_B^{(-)}(T,t')\middle|\mathbf{r}'\right\rangle &\approx \left\langle \mathbf{p}\middle|\hat{U}^{\mathrm{EVA}}(T,t')\middle|\mathbf{r}'\right\rangle \\ &= \frac{1}{(2\pi)^{3/2}} \exp\Big[-i\mathbf{v}_{\mathbf{p}}(t')\cdot\mathbf{r}' - \frac{i}{2}\int_{t'}^{T} d\tau\, v_{\mathbf{p}}^2(\tau) - iG_C(\mathbf{p},T;\mathbf{r},t) - \\ &\qquad iG_{0\mathbf{p}}(\mathbf{r}_L(T;\mathbf{r},\mathbf{p},t))\Big]\end{aligned} \tag{2.15}$$

after assuming that the field-free distortions $G_{0\mathbf{p}}(\mathbf{r}_L(T;\mathbf{r},\mathbf{p},t))$ vary slowly at large distances, and where T is the time at which the laser field is switched off. The core-potenatial phase,

$$G_C(\mathbf{p},T;\mathbf{r},t) = -\int_{T}^{t} d\tau\, U(\mathbf{r}_L(\tau;\mathbf{r},\mathbf{p},t)) \tag{2.16}$$

is the phase accumulated by the electron on account of travelling in the potential of the core, along the trajectory $\mathbf{r}_L(\tau;\mathbf{r},\mathbf{p},t) = \mathbf{r} + \int_t^\tau d\zeta\, \mathbf{v}_{\mathbf{p}}(\zeta)$ defined solely by the strong laser field in Region II.

Since the time T for the turn off of the laser field occurs when the free electron wavepacket is sufficienty far from the core, the phase-front distortion $G_{0\mathbf{p}} \to 0$ as $T \to \infty$.

Unlike the case of linear fields [46], the momentum $\mathbf{p}$ is prominent in two dimensions, which means the Coulomb correction is also ϕ'-dependent due to the dot product between $\mathbf{r}'$ and $\mathbf{v}_{\mathbf{p}}(t)$, where ϕ' is the azimuthal angle and θ' is the polar angle in the spherical coordinate system.

By construction, the Coulomb correction is a small perturbation to the electron-Laser interaction in the continuum. Therefore, we can approximate the argument $\mathbf{r}_L(\tau;\mathbf{r}',\mathbf{p},t')$ of the Coulomb correction by expanding it about the classical trajectories corresponding to tunnelling. The direction for these trajectories is set by the stationary point of the phase term $\mathbf{a}\cdot\mathbf{v}_{\mathbf{p}}(t')$, which defines spatial dependence in the SFA action. A physical interpretation for this saddle point becomes apparent once we use the stationary phase method to fix the ionisation time t_s'.

The stationary point ϕ_s' is for the highly oscillating part in equation (2.14):

$$\begin{aligned}F(\phi') = \mathbf{a}\cdot\mathbf{v}_{\mathbf{p}}(t') &= \mathbf{a}\cdot\big(\mathbf{p}+\mathbf{A}(t')\big) \\ &= a\big[p_\rho\cos(\phi'-\phi_p) - A_0\cos(\phi'-\omega t')\big]\sin\theta' + ap_z\cos\theta'\end{aligned}$$

We then get:

$$\begin{aligned}\frac{\partial F}{\partial \phi'} &= -a\big[p_\rho\sin(\phi'-\phi_p) - A_0\sin(\phi'-\omega t')\big] = 0 \\ \Rightarrow \tan\phi_s' &= \frac{k_\rho\sin\phi_k - A_0\sin(\omega t')}{k_\rho\cos\phi_k - A_0\cos(\omega t')} = \tan\phi_v(t')\end{aligned} \tag{2.17}$$

and,

$$\begin{aligned}\left.\frac{\partial F}{\partial \theta'}\right|_{\phi'=\phi_s'} &= a\big[p_\rho\cos(\phi_s'-\phi_p) - A_0\cos(\phi_s'-\omega t')\big]\cos\theta' - ap_z\sin\theta' = 0 \\ \Rightarrow \tan\theta_s' &= \frac{v_\rho(t')}{p_z} = \tan\theta_v(t')\end{aligned} \tag{2.18}$$

which gives us:

$$\int_T^{t'} d\tau\, U\big(\mathbf{r}_L(\tau;\mathbf{r},\mathbf{p},t')\big) \to \int_T^{t'} d\tau\, U\big(\mathbf{r}_L(\tau;a,\theta_v(t'),\phi_v(t'),\mathbf{p},t')\big) \tag{2.19}$$

As we will see later, this dependence on time t' of the saddle points θ'_s, ϕ'_s can be used to interpret it as the tunnelling angle. Thus, by selecting Coulomb correction along ϕ'_s only, we are focussing on the classical tunnelling trajectories. Deviations from these trajectories are met with exponential suppression and hence don't contribute significantly. Vector $\mathbf{a}$ can now be written as:

$$\begin{aligned}\mathbf{a} &= a(\sin\theta'_s(t')\cos\phi'_s(t')\,\hat{\mathbf{x}} + \sin\theta'_s(t')\sin\phi'_s(t')\,\hat{\mathbf{y}} + \cos\theta'_s(t')\,\hat{\mathbf{z}}) \\ &= \frac{a}{v(t')}\mathbf{v}(t')\end{aligned} \tag{2.20}$$

The saddle point in time is given by the combined SFA action along with the boundary term $\mathbf{a}\cdot\mathbf{v}(t')$ that arises because of the R-matrix sphere:

$$\frac{\partial S^{\mathrm{SFA}}}{\partial t'} + \mathbf{a}\cdot\frac{\partial \mathbf{v}_{\mathbf{p}}(t')}{\partial t'} = -\frac{1}{2}\Big(v_{\mathbf{p}}^2\Big(t_a'^{(0)}\Big) + \kappa^2\Big) + \mathbf{a}\cdot\partial_{t'}\mathbf{v}_{\mathbf{p}}\Big(t_a'^{(0)}\Big) = 0 \tag{2.21}$$

The saddle point t'_a can be considered as a correction over the SFA saddle point t'_s that is commonly used. We consider this "correction" to only first order in the R-matrix sphere a, by expanding the terms in Eq. (2.21) about the SFA saddle point to only first order in a, which gives us:

$$\Big(t_a'^{(0)} - t_s'^{(0)}\Big) = \frac{\mathbf{a}\cdot\partial_{t'}\mathbf{v}\Big(t_s'^{(0)}\Big)}{\mathbf{v}\Big(t_s'^{(0)}\Big)\cdot\partial_{t'}\mathbf{v}\Big(t_s'^{(0)}\Big)} \tag{2.22}$$

Using Eq. (2.20), and the fact that $v\Big(t_s'^{(0)}\Big) = i\kappa$, we get:

$$t_a'^{(0)} - t_s'^{(0)} = \frac{a}{i\kappa} \tag{2.23}$$

We can now expand the long-range action G_C around the saddle point $\mathbf{r}_s'^{(0)} \equiv (a,\theta'_s(t'),\phi'_s(t'))$, upto quadratic terms:

$$\begin{aligned}G_C(\mathbf{p},T;\mathbf{a},t') = G_C\Big(\mathbf{p},T;\mathbf{r}_s'^{(0)},t_a'^{(0)}\Big) + \Big(\mathbf{a}-\mathbf{r}_s'^{(0)}\Big)\cdot\nabla G_C\Big(\mathbf{p},T;\mathbf{r}_s'^{(0)},t_a'^{(0)}\Big) + \\ (t'-t_a'^{(0)})\partial_{t'}G_C\Big(\mathbf{p},T;\mathbf{r}_s'^{(0)},t_a'^{(0)}\Big) + \frac{1}{2}\Big(t'-t_a'^{(0)}\Big)\partial_{t'}^2 G_C\Big(\mathbf{p},T;\mathbf{r}_s'^{(0)},t_a'^{(0)}\Big)\end{aligned} \tag{2.24}$$

The term involving the mixed derivative $\Big(\mathbf{a}-\mathbf{r}_s'^{(0)}\Big)\Big(t'-t_a'^{(0)}\Big)\nabla\partial_{t'}G_C\Big(\mathbf{p},T;\mathbf{r}_s'^{(0)},t_a'^{(0)}\Big)$ is omitted from Eq. (2.24) as a higher order correction, since $\nabla G_C\Big(\mathbf{p},T;\mathbf{r}_s'^{(0)},t_a'^{(0)}\Big)$ is multiplied to $\Big(t'-t_a'^{(0)}\Big) \propto \mathcal{O}(G_C)$. The term involving the second derivative w.r.t. the spatial coordinates on the surface of the sphere, $\frac{1}{2}\Big(\mathbf{a}-\mathbf{r}_s'^{(0)}\Big)^2\nabla^2 G_C\Big(\mathbf{p},T;\mathbf{r}_s'^{(0)}\Big)$, is equal to 0 for a Coulomb-type potential tail, since $\nabla U(r) = \delta(r)$, and the argument of the potential U is a trajectry starting at the surface of the sphere and propagating outside it: this trajectory never reaches the origin, and hence its contribution is zero.

Substituting this expansion back into Eq. (2.14), we get

$$\begin{aligned}a(\mathbf{p},T) = -\frac{i\kappa a^2}{(2\pi)^{3/2}}\varphi_{\kappa\ell}(a)N_{\ell m}\int_{-\infty}^{T}dt'\int d\phi'\int d\theta'\sin\theta'\, e^{-i\mathbf{v}_{\mathbf{p}}(t')\cdot\mathbf{a}}\times \\ e^{-iS^{\mathrm{SFA}}\left(\mathbf{p},T;\mathbf{r}_s'^{(0)},t'\right) - iG_C\left(\mathbf{p},T;\mathbf{r}_s'^{(0)},t_a'^{(0)}\right) - \left(\mathbf{a}-\mathbf{r}_s'^{(0)}\right)\cdot\nabla G_C\left(\mathbf{p},T;\mathbf{r}_s'^{(0)},t_a'^{(0)}\right)}\times \\ e^{-i\left(t'-t_a'^{(0)}\right)\partial_{t'}G_C\left(\mathbf{p},T;\mathbf{r}_s'^{(0)},t_a'^{(0)}\right)}Y_{\ell m}(\theta',\phi')\end{aligned} \tag{2.25}$$

We note here that the gradient of G_C is nothing but the momentum shift, $\Delta\mathbf{p}$ induced due to the interaction of the ionising electron with the long-range core potential,

$$\Delta\mathbf{v}_{\mathbf{p}}^{c}(t') = -\nabla G_C\Big(\mathbf{p}, T; \mathbf{r}_s'^{(0)}, t_a'^{(0)}\Big) \tag{2.26}$$

Thus, we introduce a momentum shift term in the phase factor through a rigorous derivation.

Usually, at this point, some approximations are evoked to solve the spatial integrals over (θ', ϕ'). However, we will perform an exact analysis for these integrals, using the integral relations of Bessel functions and associated Legendre polynomials [275].

We start with the ϕ'-integral. The relevant integral $I_{\phi'}$ is,

$$I_{\phi'} = \int_0^{2\pi} d\phi'\, e^{-iav_{\mathbf{p}}^{c}(t')[\sin\theta' \sin\theta_v^{c}(t')\cos(\phi' - \phi_v^{c}(t'))]} e^{im\phi'} \tag{2.27}$$

where $\mathbf{v}_{\mathbf{p}}^{c}(t') = \mathbf{v}_{\mathbf{p}}(t') + \Delta\mathbf{v}_{\mathbf{p}}^{c}(t')$ is the long-range (usually Coulomb-like) corrected velocity that enters into the phase factor, and hence the prefactor of our formulation of the ionisation amplitude.

We now use the Jacobi-Anger relation [275] to expand the first ϕ'-dependent exponential term using:

$$e^{iz\cos\vartheta} = \sum_{n=-\infty}^{\infty} i^n J_n(z) e^{in\vartheta} \tag{2.28}$$

and then solving Eq. (2.27) for the only non-zero term possible in it over the summation index n in Eq. (2.28), we get

$$I_{\phi'} = 2\pi(-i)^m e^{im\phi_v^{c}(t')} J_m\big(av_{\mathbf{p}}^{c}(t')\sin\theta_v^{c}(t')\sin\theta'\big) \tag{2.29}$$

this leaves us with the θ'-integral,

$$I_{\theta'} = 2\pi(-i)^m e^{im\phi_v^{c}(t')} \int_0^{\pi} d\theta'\, \sin\theta' J_m\big(av_{\mathbf{p}}^{c}(t')\sin\theta_v^{c}(t')\sin\theta'\big) P_\ell^m(\cos\theta') e^{-iak_z\cos\theta'} \tag{2.30}$$

for which we use the result from [275] regarding the integral of the product of a Bessel function and associated Legendre polynomials of the type in Eq. (2.30), to get:

$$I_{\theta'} = 4\pi(-i)^\ell(-1)^m e^{im\phi_v^{c}(t')} P_\ell^m(\cos\theta_v^{c}(t')) j_\ell\big(av_{\mathbf{p}}^{c}(t')\big) \tag{2.31}$$

where j_ℓ is the spherical Bessel function of order ℓ. With this result, we complete the spatial integrals and are only left with the time-domain integral in Eq. (2.14)

$$\begin{aligned} a(\mathbf{p}, T) = (-i)^\ell(-1)^{m+1}\frac{2i\kappa a^2}{\sqrt{2\pi}}\varphi_{\kappa\ell}(a) N_{\ell m} e^{iG_C\left(\mathbf{p},T;\mathbf{r}_s'^{(0)},t_a'^{(0)}\right)+\mathbf{r}_s'^{(0)}\cdot\Delta\mathbf{v}_{\mathbf{p}}^{c}(t')}\times \\ \int_{-\infty}^{T} dt'\, e^{im\phi_v^{c}(t')} P_\ell^m\big(\cos\theta_v^{c}(t')\big) j_\ell\big(av_{\mathbf{p}}^{c}(t')\big) e^{-iS^{\mathrm{SFA}}\left(\mathbf{p},T;\mathbf{r}_s'^{(0)},t'\right)}\times \\ e^{-i\left(t'-t_a'^{(0)}\right)\partial_{t'}G_C\left(\mathbf{p},T;\mathbf{r}_s'^{(0)},t_a'^{(0)}\right)} \end{aligned} \tag{2.32}$$

For the time-integral, we use the saddle point approximation to evaluate the integral. This is a standard method employable for the atom and laser field paramteres under consideration for optical tunnelling in strong field ionisation [3–5].

Since the core-potential correction to the SFA saddle point should not be comparable to the SFA saddle point itself, it is reasonable to assume that the speed of the electron at the modified saddle point, expressed as $t_a'^{(1)}$, is still close to $v_{\mathbf{p}}\left(t_s'^{(0)}\right) = i\kappa$. But the radius of the R-matrix

sphere is so adjusted that $\kappa a \gg 1$, thus allowing us to approximate the spherical Bessel function $j_\ell(av_{\mathbf{p}}(t'))$ for the large argument case:

$$j_\ell\left(av_{\mathbf{p}}^c(t')\right) \approx \frac{1}{2av_{\mathbf{p}}^c(t')}\left(e^{i\left(av_{\mathbf{p}}^c(t')-(\ell+1)\pi/2\right)} + e^{-i\left(av_{\mathbf{p}}^c(t')-(\ell+1)\pi/2\right)}\right) \tag{2.33}$$

The two terms correspond to contributions from the diametrically opposite points on the boundary surface a, from where we propagate the electron outwards. The point farther from the detector by a distance of $2a$ compared to the point nearer causes an additional exponential decay for propagation from the former. Such a term did not appear in [46], as there saddle-point analysis on the $\mathbf{k}$ integral was used, thus isolating one particular trajectory. Not using the saddle point in our case will naturally lead to interference effects between the contribution from the two points, but under the given condition ($\kappa a \gg 1$) those effects will be exponentially small. This way, an interference will be produced on every point throughout every circular disk for different θ on the sphere $r' = a$. The contribution of each is weighed by the momentum distribution, encoded in $e^{im\phi_v^c(t')}P_l^m(\cos\theta_v^c(t'))$. The maximum contribution comes from the region around the saddle point. However, our analysis keeps all contributions, and also takes into account non-zero perpendicular momenta ($p_z \neq 0$).

Taking the second term in Eq. (2.33), which is exponentially the dominant one, we can expand the exponential term as,

$$\begin{aligned} e^{-i\left(av_{\mathbf{p}}^c(t')-(\ell+1)\pi/2\right)} &\approx e^{-i\left(av_{\mathbf{p}}(t')-a\Delta\mathbf{v}_{\mathbf{p}}^c(t')\cdot\mathbf{v}_{\mathbf{p}}(t')/v_{\mathbf{p}}(t')-(\ell+1)\pi/2\right)} \\ &= e^{-i(av_{\mathbf{p}}(t')-(\ell+1)\pi/2)}e^{i\mathbf{r}_s'^{(0)}\cdot\Delta\mathbf{v}_{\mathbf{p}}^c(t')} \end{aligned} \tag{2.34}$$

The last exponential in Eq. (2.34) cancels with the spurious term arising from the Taylor expansion of the long-range core potential phase term.

The final terms in the phase factor contributing towards the modified saddle point is $S^{\mathrm{SFA}} + \left(t' - t_a'^{(0)}\right)\partial_{t'}G_C + \frac{1}{2}\left(t' - t_a'^{(0)}\right)^2\partial_{t'}^2 G_C - av_{\mathbf{p}}(t')$. The core-potential modified saddle point is therefore defined as

$$\partial_{t'}S^{\mathrm{SFA}} + \partial_{t'}G_C + \left(t' - t_a'^{(0)}\right)\partial_{t'}^2 G_C + a\partial_{t'}v_{\mathbf{p}}(t') = 0 \tag{2.35}$$

We consider here corrections of only first order in G_C, and hence after taking into account the boundary dependent, SFA-type saddle point, $t_a'^{(0)}$, the correction attributed to the core-potential to this saddle point is,

$$\Delta t_a'^{(0)} = -\frac{\partial_{t'}G_C\left(t_a'^{(0)}\right)}{\partial_{t'}^2 S_a^{\mathrm{SFA}}\left(t_a'^{(0)}\right)} \tag{2.36}$$

where $S_a^{\mathrm{SFA}} = S^{\mathrm{SFA}} + av_{\mathbf{p}}(t')$ is the SFA-equivalent, but also R-matrix boundary-dependent, action. The additional approximation in the second step is validated from the fact that the resulting error is second order in R-matrix sphere radius a, which is the domain of the polarisation of the wavefunction by the external field, effects that are being ignored in the current analysis. Note that there is a boundary-dependence in the long-range core-potential correction, $\Delta t_a'^{(0)}$, due to the numerator, as well as the $av_{\mathbf{p}}(t')$ term in the denominator of Eq. (2.36).

The final saddle point, $t_a'^{(1)} = t_a'^{(0)} + \Delta t_a'^{(0)}$, that enters the pre-factors in Eq. (2.32) finally gives us the *boundary-dependent* ionisation amplitude for long-range core potential systems:

$$\begin{aligned} a(\mathbf{p},T) = (-i)^\ell(-1)^{m+1}N_{\ell m}\frac{\varphi_{\kappa\ell}(a)a}{\sqrt{S''\left(t_a'^{(1)}\right)}}e^{im\phi_v^c\left(t_a'^{(1)}\right)}P_\ell^m\left(\cos\theta_v^c\left(t_a'^{(1)}\right)\right)\times \\ e^{-iS^{\mathrm{SFA}}\left(\mathbf{p},T;\mathbf{r}_s'^{(0)},t_a'^{(1)}\right)-iG_C\left(\mathbf{p},T;\mathbf{r}_s'^{(0)},t_a'^{(0)}\right)} \end{aligned} \tag{2.37}$$

We now need to eliminate the inherent dependence of this expression on the R-matrix boundary sphere at $r = a$, in order for it to have a real, physical significance.

2.2.1 Boundary Matching

Boundary dependence of saddle point correction

We consider here the crucial issue of obtaining physical results free of R-sphere boundary at $r = a$. In this chapter, the method presented is limited in two ways:

1. We are only considering the question of boundary matching for the phase of the wavefunction. Boundary matching for higher order terms, e.g. gradients of phase, will be presented in Chapter 3. There we will also present a more generalised approach to boundary matching, for arbitrary final momentum of the photoelectron.

2. We are only considering boundary matching for the optimal momentum, and for $\ell = 0$ bound states. A more rigorous and general approach to studying sub-cycle dynamics for arbitrary (ℓ, m) bound states will be presented in Chapter 3.

The saddle point correction, $\Delta t_a'^{(0)}$, using the relation for the partial time derivative of G_C [267]:

$$\partial_{t'} G_C = -\mathbf{v_p} \cdot \nabla G_C - U(\mathbf{r}), \tag{2.38}$$

and the fact that $S_a^{\mathrm{SFA}} = S^{\mathrm{SFA}} + a v_{\mathbf{p}}(t')$, can be written as

$$\Delta t_a'^{(0)} = \frac{-\mathbf{v_p}\left(t_a'^{(0)}\right) \cdot \Delta \mathbf{v_p}\left(t_a'^{(0)}, T\right) + U(a)}{\mathbf{E}\left(t_a'^{(0)}\right) \cdot \mathbf{v_p}\left(t_a'^{(0)}\right) + a \partial_{t'} \mathbf{v_p}\left(t_a'^{(0)}\right)}, \tag{2.39}$$

after using the relation $\Delta \mathbf{v_p}(t', T) = -\nabla G_C$.

Starting from the numerator, the first point to note is that $\mathbf{v_p}\left(t_a'^{(0)}\right) \approx \mathbf{v_p}\left(t_s'^{(0)}\right)$, on account of the fact that since it is in a dot product with the boundary-dependent momentum shift, any error incurred for the above approximation will be of the order of $\mathcal{O}(a^2)$, and hence can be ignored.

For the denominator, we start by Taylor-expanding $\partial_{t'}^2 S_a^{\mathrm{SFA}}\left(t_a'^{(0)}\right)$ around $t_s'^{(0)}$ upto first order in a,

$$\partial_{t'}^2 S_a^{\mathrm{SFA}}\left(t_a'^{(0)}\right) = \partial_{t'}^2 S_a^{\mathrm{SFA}}\left(t_s'^{(0)}\right) + \left(t_a'^{(0)} - t_s'^{(0)}\right) \partial_{t'}^3 S_a^{\mathrm{SFA}}\left(t_s'^{(0)}\right). \tag{2.40}$$

Now, $\partial_{t'}^2 S_a^{\mathrm{SFA}} = \mathbf{E}(t') \cdot \mathbf{v_p}(t') + a \partial_{t'}^2 v_{\mathbf{p}}(t')$, and

$$\partial_{t'}^3 S_a^{\mathrm{SFA}}(t') = \partial_{t'}^3 S^{\mathrm{SFA}}(t') + \mathbf{v_p}(t') \cdot \mathbf{E}(t') \frac{\partial_{t'} v_{\mathbf{p}}(t')}{v_{\mathbf{p}}(t')} - \frac{a}{v_{\mathbf{p}}(t')} \partial_{t'} \left(\mathbf{v_p}(t') \cdot \mathbf{E}(t')\right). \tag{2.41}$$

When evaluated at $t_s'^{(0)}$, the last term in Eq. (2.41) cancels with the one in Eq. (2.40) [upto terms of the order of $\mathcal{O}(a^2)$]. The second term in Eq. (2.40) is of the order of $\mathcal{O}(\mathbf{E}^2)$, and hence is dropped.

Therefore, to within $\mathcal{O}(a^2)$ and $\mathcal{O}(\mathbf{E}^2)$, we have,

$$\partial_{t'}^2 S_a^{\mathrm{SFA}}\left(t_a'^{(0)}\right) = \partial_{t'}^2 S^{\mathrm{SFA}}\left(t_s'^{(0)}\right), \tag{2.42}$$

and the saddle point time correction can thus be written as

$$\Delta t_a'^{(0)} = -\frac{\partial_{t'} G_C\left(t_a'^{(0)}\right)}{\partial_{t'}^2 S_a^{\mathrm{SFA}}\left(t_s'^{(0)}\right)}. \tag{2.43}$$

For the numerator, we first use Eq. (2.38),

$$\partial_{t'} G_C\left(t_a'^{(0)}\right) = -\mathbf{v_p}\left(t_a'^{(0)}\right) \cdot \nabla G_C\left(t_a'^{(0)}\right) - U(\mathbf{a}). \tag{2.44}$$

To remove the R-matrix boundary sphere dependence for this term, we first consider the matching technique along the short-range equivalent optimal momentum, as outlined in [268]. Due to the cylinderical symmetry inherent in the ionisation of an atom by a monochromatic, circularly polarised field, without loss of generality, we can consider the boundary matching method for one specific detection angle, which for our discussions we take to be $\phi_p = 0$.

In the polarisation plane, the optimal momentum $\mathbf{p}_{\text{opt}} = (p_{\text{opt}} \cos\phi_p, p_{\text{opt}} \sin\phi_p)$ is given from the implicit relation [142]:

$$p_{\text{opt}} = A_0 \sqrt{1+\gamma^2} \sqrt{\frac{1-\zeta_0}{1+\zeta_0}}, \tag{2.45}$$

for any angle ϕ_p. The parameter $0 \leq \zeta_0 \leq 1$ satisfies the equation $\sqrt{\frac{\zeta_0^2+\gamma^2}{1+\gamma^2}} = \tanh \frac{1}{1-\zeta_0} \sqrt{\frac{\zeta_0^2+\gamma^2}{1+\gamma^2}}$ [3, 142, 143]. Note that $\zeta_0 \simeq \gamma^2/3$ for $\gamma \ll 1$, and $\zeta_0 \simeq 1 - 1/\ln\gamma$ for $\gamma \gg 1$ [3]. An alternative expression for p_{opt} is

$$p_{\text{opt}} = A_0 \frac{\sinh \omega \tau_i'^{(0)}}{\omega \tau_i'^{(0)}}, \tag{2.46}$$

where $\tau_i'^{(0)} = \Im\left[t_s'^{(0)}\right]$, is the imaginary part of the saddle-point solution for time, also known as the "tunnelling time." The advantage of the second expression is that it provides a compact connection between the optimal momentum and the tunnelling time, however, one has to keep in mind that in a circular field $\tau_i'^{(0)}$ depends on the final radial momentum p [3, 142, 143]:

$$\omega \tau_i'^{(0)} = \cosh^{-1}\eta, \quad \eta(\mathbf{p}) = \frac{A_0}{2p_\rho}\left[\left(\frac{p}{A_0}\right)^2 + \gamma^2 + 1\right], \tag{2.47}$$

and thus, in Eq. (2.46), $\tau_i'^{(0)}$ depends on p_{opt} itself.

Since the time $t_a'^{(0)}$ is complex, the momentum $\Delta\mathbf{p}\left(t_a'^{(0)}, T\right)$ will also be complex:

$$\Delta p_y\left(t_a'^{(0)}, T\right) = \Delta p_y^{\text{re}}(a) + i\Delta p_y^{\text{im}}(a), \tag{2.48}$$

$$\Delta p_x\left(t_a'^{(0)}, T\right) = \Delta p_x^{\text{re}}(a) + i\Delta p_x^{\text{im}}(a). \tag{2.49}$$

After some algebra (see Appendix 2.B.1) we obtain:

$$\Delta p_y^{\text{im}}(a) \simeq \mathcal{O}\left(\frac{1}{\kappa a}\right) \to 0, \tag{2.50}$$

$$\Delta p_x^{\text{re}}(a) = \Delta p_x^{\text{re}}, \quad \Delta p_y^{\text{re}}(a) = \Delta p_y^{\text{re}}, \tag{2.51}$$

$$\Delta p_x^{\text{im}}(a) \simeq \mathcal{O}\left(\frac{1}{\kappa a}\right) \to 0, \tag{2.52}$$

where the boundary-independent momentum is

$$\Delta\mathbf{p}^{\text{re}} = -\int_{\Re\left[t_s'^{(0)}\right]}^{T} d\tau\, \nabla U\left(\mathbf{r}_e'^{(0)} + \int_{\Re\left[t_s'^{(0)}\right]}^{\tau} d\zeta\, \mathbf{v}_{\mathbf{p}_{\text{opt}}}(\zeta)\right), \tag{2.53}$$

and the coordinate $\mathbf{r}_e'^{(0)}$, known as the coordinate of exit from the tunnelling barrier, is defined as

$$\mathbf{r}_e'^{(0)} = \int_{t_s'^{(0)}}^{\Re\left[t_s'^{(0)}\right]} d\zeta\, \mathbf{v}_{\mathbf{p}_{\text{opt}}}(\zeta). \tag{2.54}$$

Substituting Eqs. (2.50), (2.51), (2.52), and (2.53) for $\Delta\mathbf{p}\left(t_a'^{(0)}, T\right)$ from the previous section into Eq. (2.39) and taking into account that in our geometry

$$E_y\left(t_s'^{(0)}\right) = E_y^{\mathrm{re}}, \quad E_y^{\mathrm{re}} = E_0 \cosh \omega\tau_i'^{(0)}, \tag{2.55}$$

$$E_x\left(t_s'^{(0)}\right) = iE_x^{\mathrm{im}}, \quad E_x^{\mathrm{im}} = -E_0 \sinh \omega\tau_i'^{(0)}, \tag{2.56}$$

$$v_y\left(t_s'^{(0)}\right) = iv_y^{\mathrm{im}}, \quad v_y^{\mathrm{im}} = -A_0 \sinh \omega\tau_i'^{(0)}, \tag{2.57}$$

$$\begin{aligned} v_x\left(t_s'^{(0)}\right) = v_x^{\mathrm{re}}, \quad v_x^{\mathrm{re}} &= p_{\mathrm{opt}} - A_0 \cosh \omega\tau_i'^{(0)} \\ &= \frac{a_0}{\tau_i'^{(0)}}\left(\sinh \omega\tau_i'^{(0)} - \omega\tau \cosh \omega\tau_i'^{(0)}\right), \end{aligned} \tag{2.58}$$

where $a_0 = E_0/\omega^2$ is the electron oscillation amplitude, yielding

$$\mathbf{E}\left(t_s'^{(0)}\right) \cdot \mathbf{v}_{\mathbf{p}_{\mathrm{opt}}}\left(t_s'^{(0)}\right) = ip_{\mathrm{opt}}E_0 \sinh \omega\tau_i'^{(0)} = iv_y^{\mathrm{im}}p_{\mathrm{opt}}\omega, \tag{2.59}$$

we obtain

$$\Re\left[\Delta t_a'^{(0)}\right] = \frac{-v_x^{\mathrm{re}}\Delta p_x^{\mathrm{im}}/v_y^{\mathrm{im}} - \Delta p_y^{\mathrm{re}}}{p_{\mathrm{opt}}\omega}, \tag{2.60}$$

$$\Im\left[\Delta t_a'^{(0)}\right] = \frac{v_x^{\mathrm{re}}\Delta p_x^{\mathrm{re}}/v_y^{\mathrm{im}} - U(a)/v_y^{\mathrm{im}} - \Delta p_y^{\mathrm{im}}}{p_{\mathrm{opt}}\omega}. \tag{2.61}$$

Since $U(a)/v_y^{\mathrm{im}} \simeq \Delta p_y^{\mathrm{im}} \simeq \mathcal{O}\left(\frac{1}{\kappa a}\right) \to 0$ (see Appendix 2.B.1), $\Delta p_x^{\mathrm{im}} \simeq \mathcal{O}\left(\frac{1}{\kappa a}\right) \to 0$, we obtain a boundary-independent correction to the real ionisation time $\Re\left[\Delta t_s'^{(0)}\right] = \Re\left[\Delta t_a'^{(0)}\right]$ and imaginary ionisation time $\Im\left[\Delta t_s'^{(0)}\right] = \Im\left[\Delta t_a'^{(0)}\right]$:

$$\Re\left[\Delta t_s'^{(0)}\right] = -\frac{\Delta p_y^{\mathrm{re}}}{p_{\mathrm{opt}}\omega} = -\frac{\Delta p_y^{\mathrm{re}}}{E_0}\frac{\omega\tau_i'^{(0)}}{\sinh \omega\tau_i'^{(0)}}, \tag{2.62}$$

$$\Im\left[\Delta t_s'^{(0)}\right] = \frac{\Delta p_x^{\mathrm{re}}v_x^{\mathrm{re}}}{v_y^{\mathrm{im}}p_{\mathrm{opt}}\omega} = -\frac{\Delta p_x^{\mathrm{re}}}{E_0}\frac{\sinh \omega\tau_i'^{(0)} - \omega\tau \cosh \omega\tau_i'^{(0)}}{\sinh^2 \omega\tau_i'^{(0)}}, \tag{2.63}$$

where the subscript "s" denotes that the results for corrections to the SFA saddle point $t_a'^{(0)}$ are now independent of the boundary $r' = a$. Thus we can write the saddle point as

$$t_s'^{(1)} = t_s'^{(0)} + \Delta t_s'^{(0)}. \tag{2.64}$$

Matching for the tunnelling angle is now trivial, since all variables entering for $\phi_v^c\left(t_a'^{(1)}\right)$ are now proved to be boundary independent:

$$\tan \phi_v^c\left(t_a'^{(0)} + \Delta t_a'^{(0)}\right) = \frac{v_y\left(t_s'^{(0)}\right) - \Delta p_y - \Delta t_s'^{(0)}E_y}{v_x\left(t_s'^{(0)}\right) - \Delta p_x - \Delta t_s'^{(0)}E_x}. \tag{2.65}$$

Boundary Matching for the Prefactor

The required boundary matching of the present solution for the ionisation amplitude, valid in the range $a < r < \infty$, to the region $0 < r < a$ has to be achieved by removing the dependence on the R-matrix boundary in several steps.

First, we consider the terms $\varphi_{\kappa\ell}(a)a\,e^{iG_C\left(\mathbf{p},T;\mathbf{r}_s'^{(0)},t_a'^{(0)}\right)}$, with $\mathbf{r}_s'^{(0)} = a\hat{\mathbf{v}}_{\mathbf{p}}\left(t_a'^{(0)}\right)$. Recalling the expression for the asymptotic radial part of the bounded wavefunction, Eq. (2.12), we can rewrite it as,

$$\varphi_{\kappa\ell}(a) = C_{\kappa\ell}\kappa^{3/2}\frac{e^{-\kappa a}}{\kappa a}(\kappa a)^{Q/\kappa} = C_{\kappa\ell}\kappa^{3/2}\frac{e^{-\kappa a}}{\kappa a}e^{\,i\int_{t_a'^{(0)}}^{t_\kappa'^{(0)}}d\tau\,U\left(\int_{t_s'^{(0)}}^{\tau}d\zeta\,i\kappa\right)}. \tag{2.66}$$

and as needed, we define the complex time $t_\kappa'^{(0)} = t_s'^{(0)} - i/\kappa^2$. We have assumed here a Coulomb-type potential, which is a valid approximation at distances $\kappa a \gg 1$. Also, we assume in the second step that the speed of the electron under the barrier for the complex time between $t_\kappa'^{(0)}$ and $t_a'^{(0)}$ is nearly constant at the value of $i\kappa$.

For the core-potential phase term, $G_C\left(\mathbf{p},T;\mathbf{r}_s'^{(0)},t_a'^{(0)}\right)$, because of the small time interval between the complex time instants $t_s'^{(0)}$ and $t_a'^{(0)} = t_s'^{(0)} - ia/\kappa$, we can approximate the saddle-point co-ordinate as

$$\mathbf{r}_s'^{(0)} = a\frac{\mathbf{v}_{\mathbf{p}}\left(t_a'^{(0)}\right)}{v_{\mathbf{p}}\left(t_a'^{(0)}\right)} \approx \int_{t_s'^{(0)}}^{t_a'^{(0)}} d\zeta\,\mathbf{v}_{\mathbf{p}}(\zeta), \tag{2.67}$$

giving us,

$$\begin{aligned} G_C\left(\mathbf{p},T;\mathbf{r}_s'^{(0)},t_a'^{(0)}\right) &= -\int_T^{t_a'^{(0)}} d\tau\,U\left(\mathbf{r}_s'^{(0)} + \int_{t_a'^{(0)}}^{\tau} d\zeta,\mathbf{v}_{\mathbf{p}}(\zeta)\right) \\ &\approx -\int_T^{t_a'^{(0)}} d\tau\,U\left(\int_{t_s'^{(0)}}^{\tau} d\zeta,\mathbf{v}_{\mathbf{p}}(\zeta)\right). \end{aligned} \tag{2.68}$$

Comparing the result of this approximation, Eq. (2.68), with Eq. (2.66), we finally get the boundary-independent core-potential phase factor:

$$(\kappa a)^{Q/\kappa}e^{-iG_C\left(\mathbf{p},T;\mathbf{r}_s'^{(0)},t_a'^{(0)}\right)} = e^{\,i\int_T^{t_\kappa'^{(0)}}d\tau\,U\left(\int_{t_s'^{(0)}}^{\tau}d\zeta\,\mathbf{v}_{\mathbf{p}}(\zeta)\right)}. \tag{2.69}$$

The $1/\kappa a$ factor in Eq. (2.66) removes the extra a term present in Eq. (2.37) along with $\varphi_{\kappa\ell}(a)$.

For the SFA action being evaluated at $t_a'^{(1)}$ (there is no $\mathbf{r}_s'^{(0)}$-dependence in S^{SFA}, but it is mentioned in its parenthesis for the sake of symmetry with the long-range core potential phase factor G_C), we note that the substitution of $t_a'^{(1)}$ by the long-range core potential corrected SFA saddle point, $t_s'^{(1)}$, incurs errors of the order of $\mathcal{O}(a^2)$, which we have already ignored on account of the polarisation effects of the wavefunction by the strong laser field becoming relevant in that range. Therefore, we have

$$S\left(\mathbf{p},T;\mathbf{r}_s'^{(0)},t_a'^{(1)}\right) = S\left(\mathbf{p},T;\mathbf{r}_s'^{(0)},t_s'^{(1)}\right) + \mathcal{O}\left(\left(t_a'^{(1)} - t_s'^{(1)}\right)^2\right). \tag{2.70}$$

Similarly, we remove the boundary-dependence in the velocity angles $\theta_v^c\left(t_a'^{(1)}\right), \phi_v^c\left(t_a'^{(1)}\right)$, with the core-potential corrected saddle point $t_s'^{(1)}$:

$$\left(\theta_v^c\left(t_a'^{(1)}\right),\phi_v^c\left(t_a'^{(1)}\right)\right) = \left(\theta_v^c\left(t_s'^{(1)}\right),\phi_v^c\left(t_s'^{(1)}\right)\right) + \left(\mathcal{O}(a^2),\mathcal{O}(a^2)\right). \tag{2.71}$$

We finally have the boundary-independent ionisation amplitude for the case of a long-range core potential:

$$\begin{aligned} a(\mathbf{p},T) = (-i)^\ell(-1)^{m+1}C_{\kappa\ell}N_{\ell m}\sqrt{\frac{\kappa}{\left|S''\left(t_s'^{(1)}\right)\right|}}e^{im\phi_v^c\left(t_s'^{(1)}\right)}P_\ell^m\left(\cos\theta_v^c\left(t_s'^{(1)}\right)\right)\times \\ e^{-iS^{\mathrm{SFA}}\left(\mathbf{p},T;\mathbf{r}_s'^{(0)},t_s'^{(1)}\right)-iG_C\left(\mathbf{p},T;\mathbf{r}_s'^{(0)},t_\kappa'^{(0)}\right)}. \end{aligned} \tag{2.72}$$

We see another advantage of the ARM method here: we now do not have a complicated radial r' integral and the corresponding higher order pole in the momentum-space representation of the wave function. The upshot of the analysis in short-range potentials [142] was that the pole in the momentum-space representation of the wave function was canceled with the zero in the momentum integral at the same point $v\left(t_s'^{(0)}\right) = i\kappa$. However, for wave functions corresponding to long range potentials, we would have had a $(Q/\kappa + 1)$-order pole in the momentum space, leaving a (Q/κ)-order pole in the final momentum integral. Using the ARM method, the Bloch operator isolates the wave function at the boundary $r' = a$ through a δ function, making that integral straightforward, thus bypassing the pole encountered if the integral was performed over the whole radial domain. At the same time we also get a more robust result, taking into account the Coulomb correction for the ionisation rate both during and after ionisation.

2.3 Physical picture of ionisation in long range potentials

In circularly polarized fields, the electron liberated at different times will be "directed" by the laser field into different angles. This idea is called "angular streaking" and the corresponding "time-to-angle" mapping is unique for nearly single-cycle pulses with a stable carrier-envelope phase, underlying the idea of the attoclock [44,45,55,57]. The angular streaking principle makes single and double ionisation in circularly polarized strong laser fields a sensitive probe of the attosecond dynamics [44,45,55,57,170,187].

However, reconstruction of this dynamics requires the calibration of the attoclock, i.e., establishing the mapping between the direction of the laser polarisation vector at the time of ionisation and the direction of the electron momentum at the detector. When one strives to achieve the accuracy of, say, 10 as, using an 800-nm carrier as a clock, one needs to know this mapping with an accuracy of about 1°.

Simple analytical calibration can be made if one neglects the electron interaction with the long-range core potential during and after ionisation. For short-range potentials the mapping is illustrated in Fig. 2.2. For the laser field defined as

$$\mathbf{E}(t) = E_0(-\sin(\omega t)\,\hat{\mathbf{x}} + \cos(\omega t)\,\hat{\mathbf{y}}), \tag{2.73}$$

the connection between the real part of the ionisation time and the observation angle is [3,143]:

$$\omega t_i'^{(0)} = \omega \Re\left[t_s'^{(0)}\right] = \phi_p + 2\pi(r-1),\ r \in \mathbb{N}. \tag{2.74}$$

The detector placed along the positive direction of the x axis will detect the electron liberated at $t_i'^{(0)} = 0$, i.e., when the laser field $\mathbf{E}(t) = E_0\hat{\mathbf{y}}$ is pointing towards the positive direction of the y axis. The electron exits the barrier in the negative direction of the y axis, corresponding to the angle $-\pi/2$. The velocity at the exit, $v_y\left(t_i'^{(0)}\right) = 0$, $v_x\left(t_i'^{(0)}\right) = p_{\rm opt} - A_0$, and $v_x\left(t_i'^{(0)}\right)$, tends to 0 in the tunnelling limit ($\gamma \ll 1$): $v_x\left(t_i'^{(0)}\right) = \sqrt{2I_p}\gamma/6$. Thus, the angle between the direction of the field at the moment of ionisation and the electron momentum at the detector is $\pi/2$.

How is this mapping affected when the interaction with the long-range core potential is taken into account?

2.3.1 Coulomb correction to the ionisation time, initial electron velocity

Even in the tunnelling limit, our analysis shows that due to the effects of the long-range potential, the electron has nonzero velocity $(-\Delta p_y^{\rm re})$ in the negative direction of the y axis when the field is pointing in the positive y direction, i.e., at $t = 0$ in our notations. This is by no means surprising and the corresponding velocity has a very simple explanation: it is required to overcome the

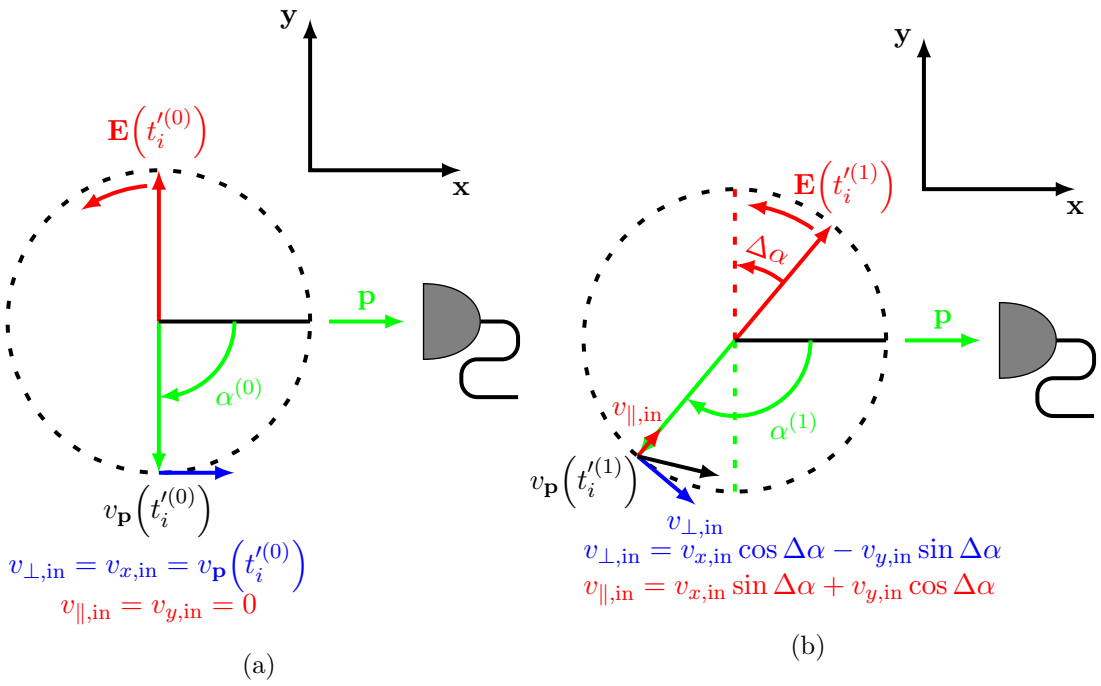

Figure 2.2: Kinematics of electron tunnelling through the rotating barrier. The right circularly polarized laser field E creates a tunnelling barrier rotating counter-clockwise. (a) Short-range potential: The electron observed at the detector placed along the x axis, exits the barrier along the negative direction of the y axis at angle $\alpha^{(0)} = -\pi/2$. (b) Long-range potential: The electron observed at the detector placed along the x axis, exits the barrier at the angle $\alpha^{(1)} = -\pi/2 - \Delta\alpha$, $\Delta\alpha = \left|\omega\Delta t_i'^{(0)}\right|$, and $\Delta t_i'^{(0)} < 0$.

attraction of the Coulomb potential, which the electron will experience all the way towards the detector. Had the electron been born with zero velocity the in long-range potential, it would never have reached the detector placed in the positive direction of the x axis. One expects the same result within the adiabatic tunnelling picture. The question is: Is the magnitude of Δp_y^{re} consistent with the adiabatic ionisation model, which would suggest that the electron was liberated slightly before $t = 0$ but with zero velocity?

To answer this question, we need to analyze the changes in the ionisation time due to the effects of the long-range potential. The corrections to ionisation times associated with electron interaction with the long-range potential are given by Eqs. (2.63) and (2.62). The shift of the saddle point in time $\Re\left[\Delta t_s'^{(0)}\right]$ corresponds to the shift in the direction of the force of the electric field $-\mathbf{E}(t)$ from $-\pi/2$ to $-\pi/2 + \omega\Re\left[\Delta t_s'^{(0)}\right]$.

Let us first discuss the initial conditions for the electron continuum dynamics in the tunnelling limit $\gamma \ll 1$. In this limit, the electron moves in static electric field $[\mathbf{E}(t) = E_0\,\hat{\mathbf{y}}]$ and the momentum shift is accumulated along the electron trajectory,

$$y^{\mathrm{tun}}(t) = -\left[\frac{I_p}{E_0} + \frac{1}{2}E_0\left(t - t_i'^{(0)}\right)^2\right]\hat{\mathbf{y}}, \tag{2.75}$$

where $y^{\mathrm{tun}}\left(t_i'^{(0)}\right) = -I_p/E_0$ is the coordinate of the exit point in the tunnelling limit. Taking into account that $U = -Q/(-y)$, $\nabla U = -Q\hat{\mathbf{y}}/y^2$ and substituting this trajectory into the expression for $\Delta\mathbf{p}$, Eq. (2.53), we obtain

$$\Re[\Delta p_y] = -Q\int_{t_i'^{(0)}}^{T}\frac{d\tau}{(y^{\mathrm{tun}})^2} = -\frac{0.78\sqrt{2}}{I_p^{3/2}}QE_0. \tag{2.76}$$

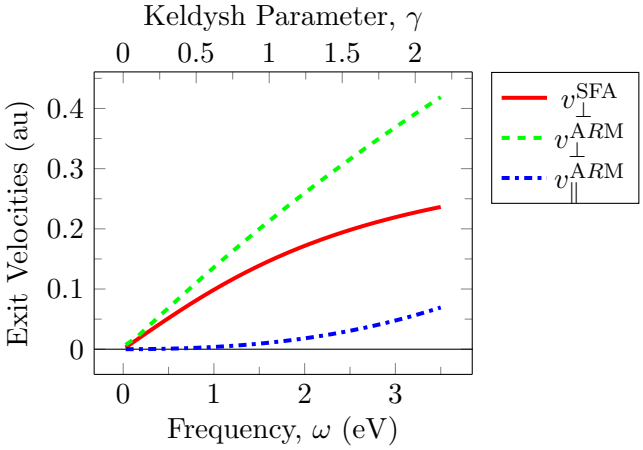

Figure 2.3: Initial velocity corresponding to the center of the velocity distribution: $v_\perp$ [dashed (green) line] [Eq. (2.82)] and $v_\parallel$ [dot-dashed (blue) line] [Eq. (2.83)] vs. frequency for $\mathcal{E}_0 = 3\times10^{10}$ V/m (= 0.06 au and $I_0 = 2.6\times10^{14}$ W/cm^2) and $I_p = 14$ eV. $v_\perp^{\mathrm{SFA}}$ [solid (red) line] shows the result arising in the nonadiabatic short-range theory (the PPT theory; see [3,142,143]) and in the length-gauge SFA.

It is easy to see that Eq. (2.62) in the tunnelling limit yields $\Re\left[\Delta t_s'^{(0)}\right] = -\Delta p_y^{\mathrm{re}}/E_0$, thus we obtain from Eq. (2.76):

$$\Delta t_i'^{(0)} = -\frac{0.78Q\sqrt{2}}{I_p^{3/2}} \approx -I_p^{3/2}. \tag{2.77}$$

From Eq. (2.77), we find that the correction to the ionisation time $\Re\left[\Delta t_s'^{(0)}\right]$ is negative, the electron is born before $\mathbf{E}(t)$ points down, and the Coulomb corrected angle $-\pi/2+\omega\Re\left[\Delta t_s'^{(0)}\right]$ has a negative value. At this (earlier) ionisation time the electron velocity is lower than at $t_i'^{(0)}$, and in the tunnelling limit:

$$\begin{aligned} v_x &= p_{\mathrm{opt}} - A_0\cos\left(\omega t_i'^{(0)} + \omega\Re[\Delta t_s'^{(0)}]\right) - \Delta p_x \\ &\approx p_{\mathrm{opt}} - A_0 + \mathcal{O}(G_C^2) \approx \gamma\sqrt{2I_p}/6 + \mathcal{O}(G_C^2), \end{aligned} \tag{2.78}$$

$$v_y = -\Delta p_y - A_0\sin\left(\omega t_i'^{(0)} + \omega\Re[\Delta t_s'^{(0)}]\right) = -\Delta p_y - A_0\omega\Re[\Delta t_s'^{(0)}] \approx 0 + \mathcal{O}(G_C^2). \tag{2.79}$$

Thus, in the tunnelling limit $\gamma\to0$, the electron velocity indeed tends to 0 at the exit from the barrier. The effect of the Coulomb potential is reduced to the modification of the angle between the direction of the laser field at the moment of exit $\mathbf{E}\left(t_i'^{(0)}\right)$ and the direction of the final electron momentum $\mathbf{p}$, registered at the detector. For short-range potentials this angle is $\pi/2$, and for long-range potentials this angle is larger; in the tunnelling limit it is $\pi/2+\omega I_p^{-3/2}$, (see Fig. 2.2).

However, most of the experiments are currently performed in the regime of nonadiabatic ionisation, when the Keldysh parameter γ is not that small. In this regime the exit velocities (with $t_i'^{(0)} = 0$),

$$v_x = p_{\mathrm{opt}} - A_0\cos\left(\omega\Re[\Delta t_s'^{(0)}]\right) - \Delta p_x, \tag{2.80}$$

$$v_y = -\Delta p_y - A_0\sin\left(\omega\Re[\Delta t_s'^{(0)}]\right), \tag{2.81}$$

become significant already for small γ. The longitudinal electron velocity $v_\parallel$ along the direction of the field and the transverse electron velocity $v_\perp$ orthogonal to the field are also non-zero

(Fig. 2.3). The longitudinal and transverse velocities are obtained from Eqs. (2.80) and (2.81) ($\Delta\alpha = \left|\omega\Delta t_i'^{(0)}\right|$):

$$v_\perp = v_x\cos(\Delta\alpha) - v_y\sin(\Delta\alpha), \tag{2.82}$$
$$v_\parallel = v_x\sin(\Delta\alpha) + v_y\cos(\Delta\alpha). \tag{2.83}$$

Ignoring the non-zero initial velocity of the electron will generally lead to errors in the two-step reconstruction of time delays in the angular streaking method. In the next section we illustrate the degree of uncertainty that can arise in reconstructing the time from the attoclock measurement using examples of Ar and He atoms.

2.3.2 Calibration of the attoclock

The attoclock observable is the angular offset. This angular offset either can appear due to electron interaction with the core potential $\Delta\alpha$, as described above, or can be associated with other delays, e.g., delays accumulated due to nontrivial tunnelling, polarisation, or excitation dynamics, $\Delta\alpha^U$ (the superscript U stands for "unknown," since the respective $\Delta\alpha^U$ is associated with the dynamics that we may not know). Since the attoclock can only measure the total offset $\Delta\alpha^T = \Delta\alpha^U + \Delta\alpha$, to get access to the unknown (e.g., tunnelling) times one has to calculate the offset $\Delta\alpha$ and subtract it from the measurable offset $\Delta\alpha^T$. The uncertainty in the calculation of $\Delta\alpha$ will lead to the corresponding uncertainty in reconstructing, say, the tunnelling time.

In this section we consider the angular offset $\Delta\alpha$ and analyze the associated uncertainties in the time reconstruction for three models.

i. *The two-step adiabatic model.* This model assumes that the peak of the photoelectron distribution corresponds to the electron trajectory with specific initial conditions, namely, the initial coordinate defined according to the quasistatic tunnelling picture for short-range potentials, or in the limit of a sufficiently thick barrier ($4E_0 \ll I_p^2$): $x_e^{\rm qs}\left(t_i'^{(0)}\right) = 0$, $y_e^{\rm qs}\left(t_i'^{(0)}\right) = -I_p/E_0$. The initial electron velocity is 0 (both transversal and longitudinal): $v_x^{\rm qs}\left(t_i'^{(0)}\right) = 0$, $v_y^{\rm qs}\left(t_i'^{(0)}\right) = 0$.

ii. *The two-step nonadiabatic model.* The peak of the photoelectron distribution corresponds to the electron trajectory. The initial coordinate is defined according to the PPT theory $y_e'^{(0)} = \int_{t_s'^{(0)}}^{\Re\left[t_s'^{(0)}\right]} d\zeta\,[p_{\rm opt} + A_y(\zeta)]$ [see also Eq. (2.54)]. The initial electron velocity is nonzero in the direction orthogonal to the field polarisation at the time of exit: $v_x\left(t_i'^{(0)}\right) = p_{\rm opt} - A_0$, $v_y\left(t_i'^{(0)}\right) = 0$ [see Eq. (2.46) for the definition of $p_{\rm opt}$]. This nonzero velocity reflects the presence of a "cross-wind": the effect of the second component of the circularly polarized field. Note that, both orthogonal components of the circular field are always non-zero in sub-barrier region, when electron trajectory evolves in complex time.

iii. *ARM model.* The ARM model is a consistent quantum approach which does not require the knowledge of the "initial conditions" to calculate the offset angle. However, since the ARM method naturally incorporates the concept of trajectories, the initial conditions can be obtained within the ARM model, as discussed in the previous sub-section. Both $v_x\left(t_i'^{(0)}\right)$ and $v_y\left(t_i'^{(0)}\right)$ are nonzero due to the nonadiabatic Coulomb effects [see Eqs. (2.80) and (2.81)].

To ensure that all three models use the same level of approximation for the electron continuum dynamics, in two-step models we propagate the trajectories from the point of exit to

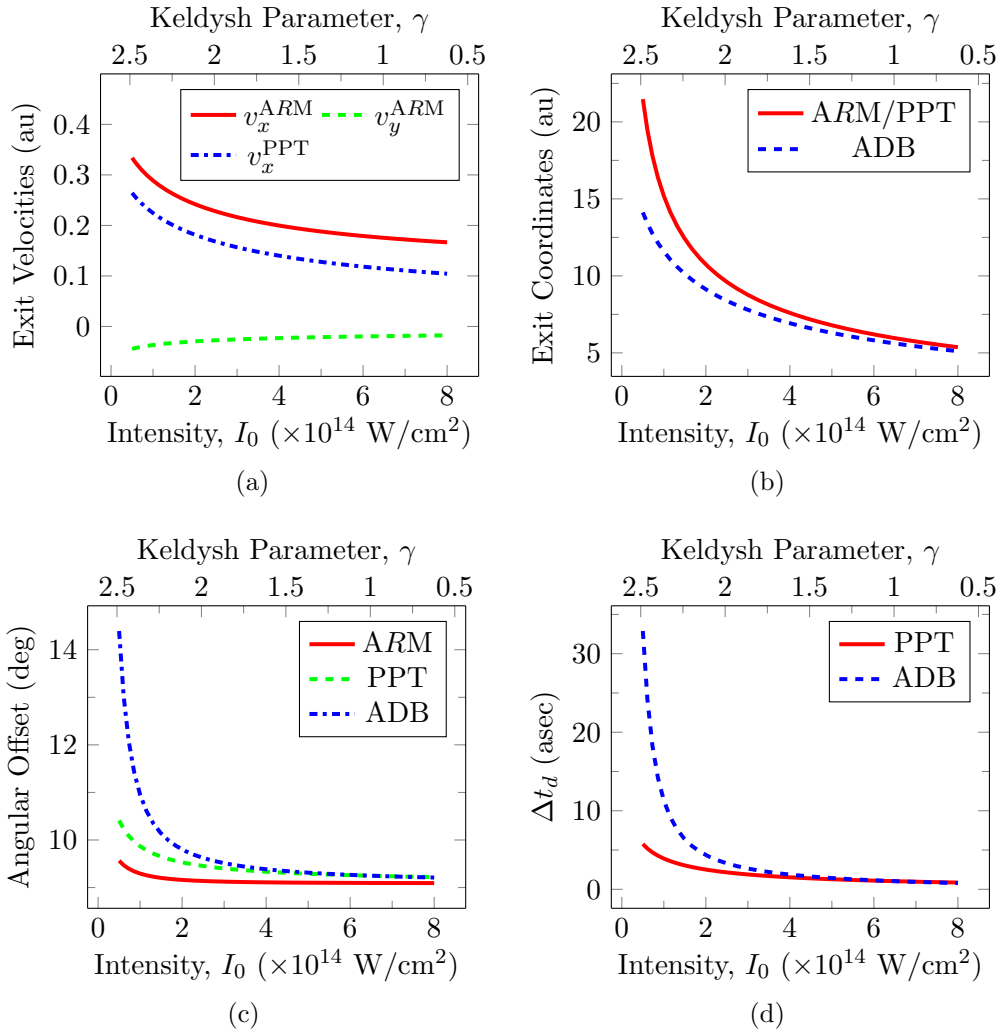

Figure 2.4: Calibration of the attoclock for an Ar atom with $I_p = 15.7$ eV. (a) Initial velocities v_x [solid (red) curve] and v_y [dashed (green) curve] resulting from the A*R*M theory and v_x [dot-dashed (blue) curve] from the nonadiabatic short-range theories [3, 142, 143] for the geometry specified in Fig. 2.2. (b) Initial coordinate (exit point) in the A*R*M and the PPT [3, 142, 143] theories [solid (red) curve], and I_p/E_0 in the adiabatic theory [dashed (blue) curve]. (c) Angular offset $\Delta\alpha$ corresponding to the A*R*M [solid (red) curve], nonadiabatic short-range [dashed (green) curve] and adiabatic [dot-dashed (blue) curve] theories. (d) Uncertainty in the calibration of time in the attoclock corresponding to (i) the nonadiabatic two-step model [solid (red) curve] and (ii) adiabatic two-step model [dashed (blue) curve].

the detector using the EVA instead of solving Newton's equations exactly. Formally, this means that the classical equation for Coulomb plus laser field (used in the two-step model),

$$\frac{d\mathbf{r}}{dt} = \mathbf{v}(t), \quad \frac{d\mathbf{v}}{dt} = -\mathbf{E}(t) - \frac{Q}{r^3(t)}\mathbf{r}(t), \tag{2.84}$$

$\mathbf{r}(t) = (x(t), y(t))$, is solved iteratively. The zeroth-order trajectory (neglecting the Coulomb term) is used in the argument of the Coulomb potential. For the two-step adiabatic model, we obtain

$$v_x^{\mathrm{ADB}} = A_0 + \Delta p_x^{\mathrm{ADB}}, \quad v_y^{\mathrm{ADB}} = \Delta p_y^{\mathrm{ADB}}, \quad \Delta\alpha^{\mathrm{ADB}} = \tan^{-1}\left(\frac{v_y^{\mathrm{ADB}}}{v_x^{\mathrm{ADB}}}\right), \tag{2.85}$$

where $\Delta p_x^{\mathrm{ADB}}$ and $\Delta p_y^{\mathrm{ADB}}$ are defined as ($\phi = \omega t$, $\phi_T = \omega T$, $T \to \infty$)

$$\Delta p_x^{\mathrm{ADB}} = -\frac{Q\omega}{A_0^2}\int_0^{\phi_T} d\phi \frac{x^{\mathrm{ADB}}(\phi)}{\left[\left(x^{\mathrm{ADB}}(\phi)\right)^2 + \left(y^{\mathrm{ADB}}(\phi)\right)^2\right]^{\frac{3}{2}}}, \tag{2.86}$$

$$\Delta p_y^{\mathrm{ADB}} = -\frac{Q\omega}{A_0^2}\int_0^{\phi_T} d\phi \frac{y^{\mathrm{ADB}}(\phi)}{\left[\left(x^{\mathrm{ADB}}(\phi)\right)^2 + \left(y^{\mathrm{ADB}}(\phi)\right)^2\right]^{\frac{3}{2}}}, \tag{2.87}$$

$$x^{\mathrm{ADB}}(\phi) = -\sin\phi + \phi, \tag{2.88}$$

$$y^{\mathrm{ADB}}(\phi) = \cos\phi - 1 - \gamma^2/2. \tag{2.89}$$

For the two-step nonadiabatic model, we obtain

$$v_x^{\mathrm{PPT}} = p_{\mathrm{opt}} + \Delta p_x^{\mathrm{PPT}}, \quad v_y^{\mathrm{PPT}} = \Delta p_y^{\mathrm{PPT}}, \quad \Delta\alpha^{\mathrm{PPT}} = \tan^{-1}\left(\frac{v_y^{\mathrm{PPT}}}{v_x^{\mathrm{PPT}}}\right), \tag{2.90}$$

where $\Delta p_x^{\mathrm{PPT}}$ and $\Delta p_y^{\mathrm{PPT}}$ are defined as

$$\Delta p_x^{\mathrm{PPT}} = -\frac{Q\omega}{A_0^2}\int_0^{\phi_T} d\phi \frac{x^{\mathrm{PPT}}(\phi)}{\left[\left(x^{\mathrm{PPT}}(\phi)\right)^2 + \left(y^{\mathrm{PPT}}(\phi)\right)^2\right]^{\frac{3}{2}}}, \tag{2.91}$$

$$\Delta p_y^{\mathrm{PPT}} = -\frac{Q\omega}{A_0^2}\int_0^{\phi_T} d\phi \frac{y^{\mathrm{PPT}}(\phi)}{\left[\left(x^{\mathrm{PPT}}(\phi)\right)^2 + \left(y^{\mathrm{PPT}}(\phi)\right)^2\right]^{\frac{3}{2}}}, \tag{2.92}$$

$$x^{\mathrm{PPT}}(\phi) = -\sin\phi + \frac{p_{\mathrm{opt}}}{A_0}\phi, \tag{2.93}$$

$$y^{\mathrm{PPT}}(\phi) = \cos\phi - \eta(p_{\mathrm{opt}}). \tag{2.94}$$

and $\eta(p_{\mathrm{opt}})$ is given by Eq. (2.47). Note that $x^{\mathrm{ADB}}(\phi)$, $y^{\mathrm{ADB}}(\phi)$ and $x^{\mathrm{PPT}}(\phi)$, $y^{\mathrm{PPT}}(\phi)$ are the respective trajectories in units of E_0/ω^2. While this approximation can slightly affect the absolute values of the offset angles $\Delta\alpha$, the error is essentially identical for all three models. Thus, the time uncertainty, determined by the relative offset given by the two-step models with respect to the ARM method, is virtually unaffected.

Figure 2.4c shows the angular offsets for Ar atoms for all three models. The discrepancy between the models increases with the decrease in the laser intensity, reaching $\delta\alpha \approx 4.5^o$ relative offset between the adiabatic model and the ARM model (for $E_0 = 0.0267$ a.u., corresponding to 0.5×10^{14} W/cm^2). The discrepancy is due to the different initial conditions in these models. We stress that the ARM theory does not require knowledge of the initial conditions to obtain $\Delta\alpha$, because it does not need to split the entire quantum process into two steps. However, the initial conditions can be obtained from the ARM theory, if needed.

Figure 2.4a compares the initial velocities resulting from the ARM and the nonadiabatic short-range theories [3, 142, 143] for the geometry specified in Fig. 2.2. For the adiabatic model both v_x and v_y are 0 [not shown in Fig. 2.4a]. The difference in the initial coordinates in the nonadiabatic theory for short-range potentials and the adiabatic model is shown in Fig. 2.4b. The initial coordinate in the ARM model is essentially the same as in the nonadiabatic short-range theory, since the respective Coulomb correction is an order higher than the first-order Coulomb effects considered in the current implementation of the ARM method. The difference in the offset angle $\delta\alpha$ maps into uncertainty in the delay time: $\delta t_d = \delta\alpha/\omega$ [Fig. 2.4d]. The uncertainty in the reconstruction of the time delay becomes less significant at higher intensities and ranges from 30 as for low fields to 3 as near the barrier suppression intensity [Fig. 2.4d]. The uncertainty δt_d strongly decreases if nonadiabatic initial conditions are used in the two-step model, ranging from 5 as for low intensities to 2 as for high intensities.

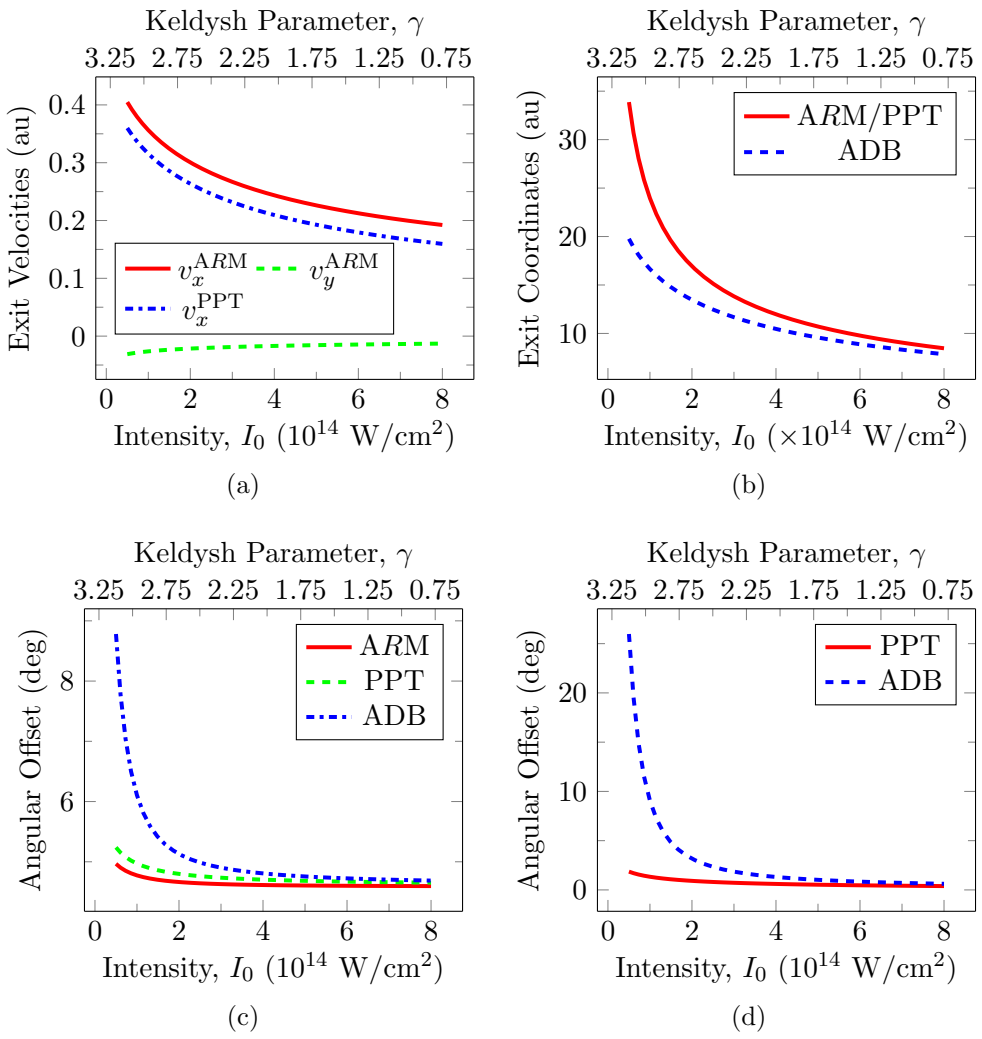

Figure 2.5: Calibration of the attoclock for a He atom with $I_p = 24.6$ eV. (a) Initial velocities v_x [solid (red) curve] and v_y [dashed (green) curve] resulting from the A*R*M theory and v_x [dot-dashed (blue) curve] from the nonadiabatic short-range theories [3, 142, 143] for the geometry specified in Fig. 2.2. (b) Initial coordinate (exit point) in the A*R*M and the PPT [3, 142, 143] theories [solid (red) curve], and I_p/E_0 in the adiabatic theory [dashed (blue) curve]. (c) Angular offset $\Delta\alpha$ corresponding to the A*R*M [solid (red) curve], nonadiabatic short-range [dashed (green) curve] and adiabatic [dot-dashed (blue) curve] theories. (d) Uncertainty in time reconstruction associated with the nonadiabatic [solid (red) curve] two-step model and the adiabatic two-step model [dashed (blue) curve].

Qualitatively we find the same picture for He atoms (Fig. 2.5), however, quantitatively the discrepancy between the different models is smaller and the time uncertainty is almost negligible for the highest intensities. For He atoms, using nonadiabatic initial conditions in the two-step model reduces the uncertainty to 1.5 as and even less for higher intensities.

2.3.3 Coulomb correction to the electron "tunnelling angle"

The complex tunnelling angle characterizes the direction of the electron velocity at the complex ionisation time $t_s'^{(1)}$: $\tan\phi_v\left(t_s'^{(1)}\right) = \frac{v_y\left(t_s'^{(1)}\right)}{v_x\left(t_s'^{(1)}\right)}$. The ionisation rate is proportional to the imaginary part of the tunnelling angle $w \propto e^{2m\Im[\phi_v(t_s'^{(1)})]}$, where m is the magnetic quantum number. In the case of a spherically symmetric initial state (s state) $m = 0$ and the ionisation

rate does not depend on the tunnelling angle, because the electron density in the initial state is the same in all directions. For p states, however, the direction of electron tunnelling, defined by the tunnelling angle, becomes important. In particular, it leads to the sensitivity of ionisation to the sense of rotation of the electron in the initial state. For short-range potentials this effect was predicted and analyzed in [142, 143]. In this section we discuss the nonadiabatic Coulomb corrections to the tunnelling angle and show how the results in [142, 143] are affected by the electron interaction with the long-range core potential.

The tunnelling angle in the case of short-range potentials is

$$\tan\phi_v\left(t_s'^{(0)}\right) = \frac{p_y - A_0\sin\left(\omega t_s'^{(0)}\right)}{p_x - A_0\cos\left(\omega t_s'^{(0)}\right)}. \tag{2.95}$$

The Coulomb potential leads to two equally important effects: (i) the modification of the complex ionisation time ($t_s'^{(0)}+\Delta t_s'^{(0)}$ in the long-range potential vs. just $t_s'^{(0)}$ in the short-range potential), and (ii) the momentum shift due to the deceleration of the electron by the long-range potential of the core (see derivation in Sec. 2.2.1):

$$\tan\phi_v^c(t_s') = \frac{v_y\left(t_s'^{(0)}\right) - \Delta p_y - \Delta t_s'^{(0)}E_y}{v_x\left(t_s'^{(0)}\right) - \Delta p_x - \Delta t_s'^{(0)}E_x}. \tag{2.96}$$

In this section we focus on the imaginary part of the complex tunnelling angle $\phi_v^c(t_s') = \tan^{-1}(x+iy)$, since it contributes to the ionisation probability. The imaginary part of $\phi_v^c(t_s')$ can be cast in the form

$$\Im[\phi_v^c(t_s')] = -\frac{1}{4}\ln\left(\left(1-x^2-y^2\right)^2+4x^2\right) + \frac{1}{2}\ln\left((1+y)^2+x^2\right). \tag{2.97}$$

Note that the real part $x \simeq \mathcal{O}(G_C)$ is of the first order with respect to long-range potential and therefore the x^2 terms have to be omitted. The ratio between ionisation rates for p^- and p^+ orbitals is

$$\frac{w_{p^-}}{w_{p^+}} = \left|\frac{e^{-i2\phi_v^c(t_s'^{(1)})}}{e^{i2\phi_v^c(t_s'^{(1)})}}\right| = e^{4\Im[\phi_v^c(t_s'^{(1)})]} = \left(\frac{1+y}{1-y}\right)^2, \tag{2.98}$$

$$y = \frac{v_y^{\rm im} - \Im[\Delta t_s'^{(0)}]E_y^{\rm re}}{v_x^{\rm re} - \Delta p_x^{\rm re} + \Im[\Delta t_s'^{(0)}]E_x^{\rm im}}. \tag{2.99}$$

Finally,

$$y = \frac{v_y^{\rm im} + \Delta p_x^{\rm re}v_x^{\rm re}/[p_{\rm opt}\tanh\omega\tau]}{v_x^{\rm re} - \Delta p_x^{\rm re} + \Delta p_x^{\rm re}v_x^{\rm re}/p_{\rm opt}}. \tag{2.100}$$

Figure 2.6 shows how the nonadiabatic Coulomb effects change the ratio between the ionisation rates for the p^+ and p^- orbitals. Modifications come solely from the alteration of the tunnelling angle. The nonadiabatic Coulomb corrections (W_{C1} and W_{C2}) do not contribute to the ratio of the ionisation rates, as also noted in [142]. The decrease in the p^-/p^+ ratio at high frequencies in long-range potentials is consistent with the opposite propensity rules in one-photon ionisation, where p^+ is preferred over p^- for right circularly polarized fields.

2.4 Subcycle Ionisation Amplitude: General Formalism

We now consider the case of subcycle ionisation amplitudes in time domain, to replace $T \to t$. The formalism presented here can only be apploed for $\ell = 0$ bound states of the atom. This limitation will be overcome in Chapter 3.

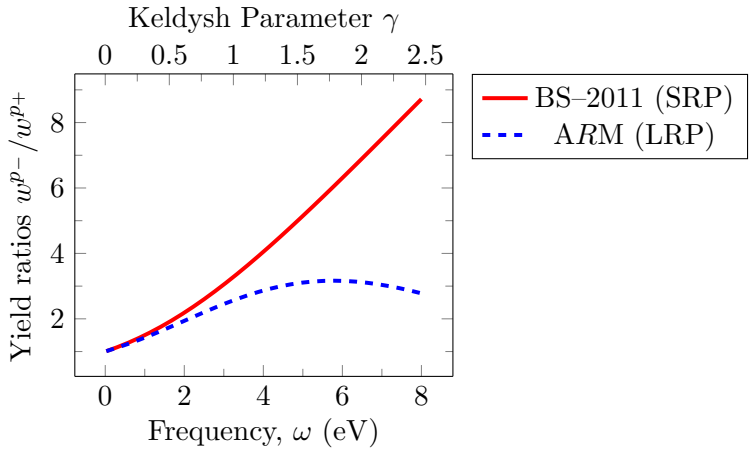

Figure 2.6: Ratio of ionisation rates from p^- and p^+ orbitals for a Ne atom ($I_p = 21.5645$ eV) and $\mathcal{E}_0 = 7.7 \times 10^{10}$ V/m ($= 0.15$ a.u. and $I_0 = 1.6 \times 10^{15}$ W/cm^2), with w_{p^-}/w_{p^+} for a right circularly polarized field: short-range potential [solid (red) curve] [142], and long-range potential [dashed (blue) curve].

The subcycle ionisation amplitude is defined as

$$a_{\mathbf{p}}(t) = -i \int_{\mathbf{a}} d\mathbf{r}\, \langle \mathbf{p} + \mathbf{A}(t) | \mathbf{r} \rangle \psi(\mathbf{r}, t). \tag{2.101}$$

Back-propagating the solution $\psi(\mathbf{r}, T)$, we can write $\psi(\mathbf{r}, t)$ as

$$\psi(\mathbf{r}, t) = \int_{\mathbf{a}} d\mathbf{r}'\, G(\mathbf{r}, t; \mathbf{r}', T)\psi(\mathbf{r}', T) - i \int_T^t dt' \int_{\mathbf{a}} d\mathbf{r}'\, G(\mathbf{r}, t; \mathbf{r}', t')\delta(r' - a)B(a, \theta', \phi', t'). \tag{2.102}$$

The second term represents that part of the wave function that remains bounded within the confines of the Coulomb potential near the atom after ionisation. But the wave function contained in that region after ionisation is negligible compared to the current flux in continuum, thus making the contribution from the former almost 0. So we can write equation (2.101) as

$$\begin{aligned} a_{\mathbf{p}}(t) &= -i \int_{\mathbf{a}} d\mathbf{r}\, \langle \mathbf{p} + \mathbf{A}(t) | \mathbf{r} \rangle \int_{\mathbf{a}} d\mathbf{r}'\, G^{\mathrm{EVA}}(\mathbf{r}, t; \mathbf{r}', T)\psi(\mathbf{r}', T) \\ &= i \int_{\mathbf{a}} d\mathbf{r} \int_{\mathbf{a}} d\mathbf{r}' \int d\mathbf{k}\, \frac{e^{-i(\mathbf{p}+\mathbf{A}(t))\cdot\mathbf{r}}}{(2\pi)^{3/2}} \frac{e^{i(\mathbf{k}+\mathbf{A}(t))\cdot\mathbf{r} - i\mathbf{k}\cdot\mathbf{r}'}}{(2\pi)^3} e^{-i\int_T^t d\tau\, U(\mathbf{r}_L(\tau;\mathbf{r},\mathbf{k},t))} e^{-\frac{i}{2}\int_T^t d\tau\, v^2(\tau)} \psi(\mathbf{r}', T) \\ &= \frac{1}{(2\pi)^3} \int_{\mathbf{a}} d\mathbf{r} \int d\mathbf{k}\, e^{i(\mathbf{k}-\mathbf{p})\cdot\mathbf{r} - \frac{i}{2}\int_T^t d\tau\, v_{\mathbf{k}}^2(\tau)} e^{-i\int_T^t d\tau\, U(\mathbf{r}_L(\tau;\mathbf{r},\mathbf{k},t))} a_{\mathbf{k}}(T). \end{aligned}$$

Before we can perform the integration on $\mathbf{r}$, we need to address the $(\mathbf{r}, \mathbf{k})$ dependence of the Coulomb correction in the above equation. Similarly to Sec. 2.2, we expand the Coulomb phase term $G_C(\mathbf{r}, t; \mathbf{k}, T) = \int_T^t d\tau\, U\big(\mathbf{r} + \int_t^\tau d\zeta\, \mathbf{v}_{\mathbf{k}}(\zeta)\big)$, about the appropriate saddle point $\mathbf{r}_s$ up to quadratic terms in deviation $(\mathbf{a} - \mathbf{r}_s)$. We need the saddle point for the phase term:

$$S^{\mathrm{SFA}}(\mathbf{r}, \mathbf{k}, t) = (\mathbf{k} - \mathbf{p}) \cdot \mathbf{r} - \frac{1}{2} \int_{t_s'}^t d\tau\, v_{\mathbf{k}}^2(\tau). \tag{2.103}$$

Therefore,

$$\nabla_{\mathbf{k}} S^{\mathrm{SFA}} = 0 \Rightarrow \mathbf{k}_s^{(0)} = \frac{\mathbf{r} - \mathbf{r}_0}{t - t_s'^{(0)}} \tag{2.104}$$

and

$$\nabla_{\mathbf{r}} S^{\mathrm{SFA}}\Big(\mathbf{r}, \mathbf{k}_s^{(0)}(\mathbf{r})\Big) = 0 \Rightarrow \mathbf{r}_s^{(0)} = \int_{t_s'^{(0)}}^t d\tau\, [\mathbf{p} + \mathbf{A}(\tau)]. \tag{2.105}$$

So the classical trajectory can be written as

$$\mathbf{r}_s^{(0)} = \int_{t_s'}^{t} d\tau\, \mathbf{v}_{\mathbf{p}}(\tau). \tag{2.106}$$

After expanding the Coulomb phase term $G_C(\mathbf{r}, t; \mathbf{k}, T)$ about the saddle points $\left(\mathbf{r}_s^{(0)}, \mathbf{k}_s^{(0)}\right)$ as in Sec. 2.2, we can write the subcycle transition amplitude as

$$a_{\mathbf{p}}(t) = \frac{1}{(2\pi)^3} \int d\mathbf{k} \int d\mathbf{r}\, e^{i(\mathbf{k}-\mathbf{p})\cdot\mathbf{r} - \frac{i}{2}\int_T^t d\tau\, v_{\mathbf{k}}^2(\tau) - iG_C(\mathbf{r}_s,t;\mathbf{p},T) - i(\mathbf{r}-\mathbf{r}_s)\cdot\nabla G_C(\mathbf{r}_s,t;\mathbf{p},T)} a_{\mathbf{k}}(T). \tag{2.107}$$

Note the argument $\mathbf{p}$ in G_C: the phase term is evaluated for the asymptotic momentum $\mathbf{p}$ and hence the corresponding momentum shift from this Taylor expansion $\Delta\mathbf{p} = -\nabla G_C$ is also evaluated for the asymptotic momentum $\mathbf{p}$ and not for the intermediate momentum $\mathbf{k}$ on which we have to perform the integration.

Following our analysis, we first propagate the electron till the detector after ionisation, and to find the momentum shifts at any point of time during this motion, we propagate it back through the EVA Green's function and thus have information on sub-cycle momentum shifts also.

We can now write

$$\int_T^t d\tau\, U\left(\mathbf{r} + \int_t^\tau d\zeta\, \mathbf{v}_{\mathbf{k}}(\zeta)\right)\Big|_{\mathbf{r}=\mathbf{r}_s,\mathbf{k}_s=\mathbf{p}} = \int_T^t d\tau\, U\left(\int_{t_s'}^\tau d\zeta\, \mathbf{v}_{\mathbf{p}}(\zeta)\right). \tag{2.108}$$

And we can combine this with

$$\int_T^{t_\kappa'^{(0)}} d\tau\, U\left(\int_{t_s'^{(0)}}^\tau d\zeta\, \mathbf{v}(\zeta)\right), \tag{2.109}$$

in $a_{\mathbf{p}}(T)$ Eq. (2.72), to get

$$\int_T^t d\tau\, U\left(\int_{t_s'^{(0)}}^\tau d\zeta\, \mathbf{v}(\zeta)\right) + \int_{t_\kappa'^{(0)}}^T d\tau\, U\left(\int_{t_s'^{(0)}}^\tau d\zeta\, \mathbf{v}(\zeta)\right) = \int_{t_\kappa'^{(0)}}^t d\tau\, U\left(\int_{t_s'^{(0)}}^\tau d\zeta\, \mathbf{v}(\zeta)\right), \tag{2.110}$$

which solves the Coulomb correction for $a_{\mathbf{p}}(t)$. The integral on $\mathbf{r}$ in Eq. (2.107) yields $(2\pi)^3\delta(\mathbf{k} - \mathbf{p} - \Delta\mathbf{p}(t,T))$, and the integral on $\mathbf{k}$ then gives $\mathbf{k} = \mathbf{p} + \Delta\mathbf{p}(t,T)$. The Coulomb shift $\Delta\mathbf{p}(t,T)$ is now *added* instead of being subtracted, which is due to the back-propagation of the electron from the detector with observable $(\mathbf{k}, T)$ to $(\mathbf{r}, t)$. We finally get

$$a_{\mathbf{p}}(t) = (-1)^{m+1} C_{\kappa\ell} N_{\ell m} \sqrt{\frac{\gamma}{\omega p_\rho \sqrt{\eta^2-1}}} e^{-i\int_{t_\kappa'^{(0)}}^t d\tau\, U\left(\int_{t_s'}^\tau d\zeta\, \mathbf{v}_{\mathbf{p}}(\zeta)\right)} e^{-\frac{i}{2}\int_{t_s'^{(0)}}^t d\tau\, v_{\mathbf{p}+\Delta\mathbf{p}}^2(\tau) + i\kappa^2 t_s'^{(0)}/2} \times$$
$$e^{i\mathbf{r}_s\cdot\Delta\mathbf{p}} P_\ell^m\left(\frac{p_z^c}{v_{\mathbf{p}^c}\left(t_s'^{(1)}\right)}\right) e^{im\phi_v^c\left(t_s'^{(1)}\right)}, \tag{2.111}$$

where we have ignored corrections of the order of $\mathcal{O}(G_C^2)$ and greater, which would arise from the Coulomb phase and the Coulomb-shifted velocity phase ϕ_v^c after taking $\mathbf{k} = \mathbf{p} + \Delta\mathbf{p}(t,T)$. Expanding $\int_{t_s'^{(0)}}^t d\tau\, v_{\mathbf{p}+\Delta\mathbf{p}}^2(\tau)$ up to first order in $\Delta\mathbf{p}$, it will cancel the spurious term $\mathbf{r}_s \cdot \Delta\mathbf{p}$. Also, $\mathbf{p}^c$ is defined as $\mathbf{p}^c = \mathbf{p} - \Delta\mathbf{p}\left(t_a'^{(0)}, t\right) \simeq \mathbf{p} - \Delta\mathbf{p}\left(t_i'^{(0)}, t\right)$, (from discussions in Sec. 2.B.1) and hence is boundary independent. The final expression for the sub-cycle transition amplitude

is:

$$a_{\mathbf{p}}(t) = (-1)^{m+1} C_{\kappa\ell} N_{\ell m} \sqrt{\frac{\gamma}{\omega p_\rho \sqrt{\eta^2 - 1}}} e^{-i \int_{t_\kappa'^{(0)}}^{t} d\tau\, U\left(\int_{t_s'}^{\tau} d\zeta\, \mathbf{v}_{\mathbf{p}}(\zeta)\right)} e^{-\frac{i}{2} \int_{t_s'^{(0)}}^{t} d\tau\, v_{\mathbf{p}}^2(\tau) + i\kappa^2 t_s'^{(0)}/2} \times$$
$$P_\ell^m \left(\frac{p_z^c}{v_{\mathbf{p}^c}\left(t_s'^{(1)}\right)} \right) e^{im\phi_v^c\left(t_s'^{(1)}\right)}. \quad (2.112)$$

2.A Bloch Operator and Hermiticity in finite spaces

Here we show how the Bloch operator can be used to ensure an arbitrary Hamiltonian, $\hat{H}$, defined by

$$\hat{H} = \frac{\hat{\mathbf{p}}^2}{2} + \hat{V}, \tag{2.113}$$

remains Hermitian in a finite region demarcated by the R-matrix sphere.

We take the radius of this R-sphere at $r = a$, for which the "inner" Bloch operator is

$$\hat{L}^{(+)}(a) = \delta(r-a)\left(\frac{d}{dr} + \frac{b_0}{r}\right), \tag{2.114}$$

where b_0 is some arbitrary constant that we can fix as fits the problem at hand. Introducing this Bloch operator to the Schrödinger equation, we get:

$$\imath\frac{\partial|\Psi\rangle}{\partial t} = \hat{H}|\Psi\rangle \tag{2.115}$$

$$= \left[\hat{H} + \hat{L}^{(+)}(a)\right]|\Psi\rangle - \hat{L}^{(+)}(a)|\Psi\rangle = \hat{H}^{(+)}|\Psi\rangle - \hat{L}^{(+)}(a)|\Psi\rangle, \tag{2.116}$$

and we have defined the reduced Hamitlonian: $\hat{H}^{(+)} = \hat{H} + \hat{L}^{(+)}(a)$. We now have to show that within the spatial domain $0 < r < a$, this reduced Hamiltonian $\hat{H}^{(+)}$ is indeed Hermitian, ensuring Unitary evolution of the wavefunction $|\Psi\rangle$ within that region of space.

To that end, we evaluate the difference of the inner product

$$I = \left(\left\langle\Psi\middle|\hat{H}^{(+)}\right)|\Phi\rangle - \langle\Psi|\left(\hat{H}^{(+)}\middle|\Phi\right\rangle\right), \tag{2.117}$$

for arbitrary state vectors $(|\Psi\rangle, |\Phi\rangle)$ in the Hilbert space $\mathcal{H}$.

Resolving on the configuration basis $|\mathbf{r}\rangle$, we have to solve the following integral:

$$I = \int_0^a d\mathbf{r}\left[\hat{H}^{(+)*}\Psi^*(\mathbf{r})\Phi(\mathbf{r}) - \Psi^*(\mathbf{r})\hat{H}^{(+)}\Phi(\mathbf{r})\right]. \tag{2.118}$$

The potential operator, $\hat{V}$ in Eq. (2.113), is assumed to strictly depend on the spatial coordinate $\mathbf{r}$, and therefore is Hermitian by default. We need to test the Hermiticity of $\hat{H}^{(+)}$ in its derivative operators, i.e., for $\hat{\mathbf{p}}^2/2$ and the derivative in $\hat{L}^{(+)}(a)$, which will make finite, non-zero contributions at the integral limit $r = a$. Furthermore, since the Bloch operator involves a radial derivative (d/dr), the reduced Hamiltonian is Hermitian in angular-(θ, ϕ) coordinates, since $\hat{\mathbf{p}}^2/2$ is Hermitian. We are therefore left to establish Hermiticity only for the radial coordinate r.

Expanding out the terms involving radial derivatives we get:

$$I = \int_0^a dr\, r^2\left[\left\{\left(\frac{\hat{p}_r^2}{2}\Psi^*(\mathbf{r})\right)\Phi(\mathbf{r}) - \Psi^*(\mathbf{r})\left(\frac{\hat{p}_r^2}{2}\Phi(\mathbf{r})\right)\right\} + \left\{\delta(r-a)\left(\frac{\partial}{\partial r}\Psi^*(\mathbf{r})\right)\Phi(\mathbf{r}) - \Psi^*(\mathbf{r})\delta(r-a)\left(\frac{\partial}{\partial r}\Phi(\mathbf{r})\right)\right\}\right] = I_1 + I_2. \tag{2.119}$$

Since $\hat{p}_r^2 = -\frac{1}{r^2}\frac{\partial}{\partial r}\left(r^2\frac{\partial}{\partial r}\right)$, after expanding the terms in the first braces in Eq. (2.119), and then using the integration rule for products twice, we will get

$$I_1 = \int_0^a dr\, r^2\left\{\left(\frac{\hat{p}_r^2}{2}\Psi^*(\mathbf{r})\right)\Phi(\mathbf{r}) - \Psi^*(\mathbf{r})\left(\frac{\hat{p}_r^2}{2}\Phi(\mathbf{r})\right)\right\} = - a^2\frac{\partial\Psi^*}{\partial r}\bigg|_{r=a}\Phi(a) + a^2\Psi^*(a)\frac{\partial\Phi}{\partial r}\bigg|_{r=a}. \tag{2.120}$$

But from the terms in the second braces of Eq. (2.119), we see clearly that

$$I_2 = \int_0^a dr\, r^2 \Big\{ \delta(r-a)\Big(\frac{\partial}{\partial r}\Psi^*(\mathbf{r})\Big)\Phi(\mathbf{r}) - \Psi^*(\mathbf{r})\delta(r-a)\Big(\frac{\partial}{\partial r}\Phi(\mathbf{r})\Big)\Big\} = a^2 \frac{\partial \Psi^*}{\partial r}\Big|_{r=a} \Phi(a) - a^2 \Psi^*(a) \frac{\partial \Phi}{\partial r}\Big|_{r=a} = -I_1, \quad (2.121)$$

which proves that the reduced Hamiltonian $\hat{H}^{(+)}$ is Hermitian within the R-sphere $0 < r < a$. Similarly, the reduced Hamiltonian $\hat{H}^{(-)} = \hat{H} + \hat{L}^{(-)}(a)$ is Hermitian outside the R-sphere $a < r < \infty$.

2.B Supplementary information for boundary matching

2.B.1 Complex momentum shifts at the boundary

The goal of this section is to calculate the momentum shift at the matching point a,

$$\Delta\mathbf{p}(a) = -\int_{t_a'^{(0)}}^{T} d\tau\, \nabla U \Big(\mathbf{r}_s'^{(0)} + \int_{t_a'^{(0)}}^{\tau} d\zeta\, \mathbf{v}_\mathbf{p}(\zeta) \Big), \quad (2.122)$$

and show that it does not depend on the position of the boundary under the matching conditions. We first split the integral into two parts:

$$\Delta\mathbf{p}(a) = -\int_{t_a'^{(0)}}^{\Re[t_s'^{(0)}]} d\tau\, \nabla U \Big(\mathbf{r}_s'^{(0)} + \int_{t_a'^{(0)}}^{\tau} d\zeta\, \mathbf{v}_\mathbf{p}(\zeta) \Big) - \int_{\Re[t_s'^{(0)}]}^{T} d\tau\, \nabla U \Big(\mathbf{r}_s'^{(0)} + \int_{t_a'^{(0)}}^{\tau} d\zeta\, \mathbf{v}_\mathbf{p}(\zeta) \Big). \quad (2.123)$$

Physically, these two parts can be interpreted as accumulated before,

$$\Delta\mathbf{p}^{\mathrm{ub}}(a) = -\int_{t_a'^{(0)}}^{\Re[t_s'^{(0)}]} d\tau\, \nabla U \Big(\mathbf{r}_s'^{(0)} + \int_{t_a'^{(0)}}^{\tau} d\zeta\, \mathbf{v}_\mathbf{p}(\zeta) \Big), \quad (2.124)$$

and after,

$$\Delta\mathbf{p}^{\mathrm{ic}}(a) = -\int_{\Re[t_s'^{(0)}]}^{T} d\tau\, \nabla U \Big(\mathbf{r}_s'^{(0)} + \int_{t_a'^{(0)}}^{\tau} d\zeta\, \mathbf{v}_\mathbf{p}(\zeta) \Big), \quad (2.125)$$

where the superscripts "ub" and "ic" stand for "under-the-barrier" and "in-continuum", respectively. The tunnel exit defined as the coordinate at the time $\Re\big[t_s'^{(0)}\big]$,

$$\mathbf{r}_e'^{(0)} = \int_{t_s'^{(0)}}^{\Re[t_s'^{(0)}]} d\zeta\, \mathbf{v}_\mathbf{p}(\zeta), \quad (2.126)$$

is a straightforward extension of Eq. (2.54). The second part, $\Delta\mathbf{p}^{\mathrm{ic}}(a)$, does not depend on the boundary. In the following we show that the first part $\Delta\mathbf{p}^{\mathrm{ub}}(a)$ is negligible under the matching condition $\kappa a \gg 1$.

We first note that $\Delta p_y^{\mathrm{ub}}(a)$ is purely imaginary, while $\Delta p_x^{\mathrm{ub}}(a)$ is purely real. In the same geometry that we use in the text, $t_a'^{(0)} = i\tau_a'^{(0)}$, and the complex under-the-barrier trajectory is $\mathbf{R} = \mathbf{r} + i\boldsymbol{\rho}$:

$$\mathbf{r} = -a_0 \Big[\cosh\phi_i'^{(0)} - \cosh\phi \Big] \hat{\mathbf{y}} = -a_0 \bar{r} \hat{\mathbf{y}}, \quad (2.127)$$

$$\boldsymbol{\rho} = a_0 \left[\frac{\phi}{\phi_i'^{(0)}} \sinh\phi_i'^{(0)} - \sinh\phi \right] \hat{\mathbf{x}} = a_0 \bar{\rho} \hat{\mathbf{x}}, \quad (2.128)$$

where $\phi_i'^{(0)} = \omega\tau_i'^{(0)}$, $\phi = \omega\xi$, $a_0 = A_0/\omega$, and ξ is imaginary integration time variable. The Coulomb potential takes the form (details of the analytical continuation of the Coulomb potential to the complex plane will be addressed in our subsequent publication [47]):

$$U(\mathbf{R}) = -\frac{Q}{\sqrt{r^2-\rho^2}}. \tag{2.129}$$

The purely imaginary $\Delta p_y^{\rm ub}(a)$ is

$$\Delta p_y^{\rm ub}(a) = i\frac{Q\omega}{A_0^2}\int_{\phi_a'^{(0)}}^{0}\frac{\bar{r}\,d\phi}{(\bar{r}^2-\bar{\rho}^2)^{3/2}}. \tag{2.130}$$

The purely real $\Delta p_x^{\rm ub}(a)$ is

$$\Delta p_x^{\rm ub}(a) = -\frac{Q\omega}{A_0^2}\int_{\phi_a'^{(0)}}^{0}\frac{\bar{\rho}\,d\phi}{(\bar{r}^2-\bar{\rho}^2)^{3/2}}, \tag{2.131}$$

and in both cases, $\phi_a = \omega\tau_a'^{(0)}$. Also, since for the optimal trajectory $r \gg \rho$,

$$\Delta p_x^{\rm ub}(a) \simeq -\frac{Q\omega}{A_0^2}\int_{\phi_a'^{(0)}}^{0}\frac{\bar{\rho}\,d\phi}{\bar{r}^3}. \tag{2.132}$$

As $\rho = 0$ at the tunnel entrance $\left(\phi = \phi_s'^{(0)} = \omega t_s'^{(0)}\right)$ and $\rho = 0$ at the tunnel exit ($\phi = 0$), the integral is accumulated in the vicinity of $\tau_a'^{(0)}$. We make linear expansion of the integrand around this point,

$$\Delta p_x^{\rm ub}(a) \simeq v_x^{\rm re}\left(t_s'^{(0)}\right)\int_0^{\tau_a'^{(0)}} d\xi\frac{\tau_a'^{(0)}-\xi}{\left\{\kappa\left(\tau_a'^{(0)}-\xi\right)+a\right\}^3} = -C\frac{v_x^{\rm re}\left(t_s'^{(0)}\right)}{\kappa}\frac{Q}{\kappa a}, \tag{2.133}$$

where C is a numerical factor:

$$C = \int_0^{\infty}\frac{z dz}{(z+1)^3}. \tag{2.134}$$

So far we have considered $\Delta\mathbf{p}(a)$ defined through its outer-region value. We can also estimate $\Delta\mathbf{p}(a)$ using its inner-region value. The inner region value of $\Delta\mathbf{p}(a)$ can be calculated using a static approximation (or short-time propagation), since the time interval from $t_s'^{(0)}$ to $t_a'^{(0)}$ is very small. It is convenient to estimate $\Delta p_y^u(a)$ by evaluating its inner region value. In a static field, the momentum in the inner region $p_y^{\rm in}(a)$ is defined through the energy conservation:

$$-I_p = \frac{(p_y^{\rm in}(a))^2}{2} - \frac{Q}{a} - E_0 a. \tag{2.135}$$

Thus, $p_y^{\rm in}(a) = -i\sqrt{2(I_p - E_0 a - Q/a)} \simeq -i\sqrt{2(I_p - E_0 a)}(1 + Q/(2a(I_p - E_0 a)))$, yielding $p_y^{\rm in}(a) = -i\kappa(a) - iQ/\kappa(a)a$. The first term is the SFA velocity at the boundary $\kappa(a) = \sqrt{2(I_p - E_0 a)} \simeq \kappa$; the second term is the respective correction associated with Coulomb effects. Thus, $\Delta p_y^{\rm in}(a) \simeq \mathcal{O}(1/\kappa a)$. The vanishingly small value of the correction at the boundary is not surprising, since the boundary is placed in the region where the Coulomb modification to the barrier is already very small.

2.C N-Photon Ionisation Rate

To compare our results with the PPT theory [3, 4] and the recent results on nonadiabatic ionisation rates in SRP [142], we derive in this section the n-photon ionisation rate.

Following steps similar to the ones outlined in Appendix 1.B of previous Chapter, but this time derived rigorously within the ARM framework for an arbitrary (long-range) core potential, we find the n-photon partial ionisation rates to bear the expression:

$$\begin{aligned} w_n(\mathcal{E},\omega) &= 2\pi \int d\mathbf{k}\, |F_n(\mathbf{k},\omega)|^2 \delta\left[\frac{1}{2}\left(k^2+\kappa^2\left(1+\frac{1}{\gamma^2}\right)\right)-n\omega\right] \\ &= |C_{\kappa\ell}|^2 \omega\kappa \frac{2\ell+1}{8\pi^2}\frac{(\ell-|m|)!}{(\ell+|m|)!}\left(1-(-1)^\ell e^{-2\kappa a}\right)^2 \int_{-\infty}^{\infty} dk_z \int_0^{2\pi} d\phi_k \int_0^{\infty} dk_\rho \times \\ &\quad e^{-2m\Im\left[\phi_v^c\left(t_s'^{(1)}\right)\right]} \left| P_\ell^m\left(\frac{k_z^c}{v_{\mathbf{k}}\left(t_s'^{(1)}\right)}\right)\right|^2 \frac{e^{-\frac{2A_0 k_\rho \eta}{\omega}\left(\tanh^{-1}\sqrt{1-\frac{1}{\eta^2}}-\sqrt{1-\frac{1}{\eta^2}}\right)}}{A_0\eta\sqrt{1-\frac{1}{\eta^2}}} \times \\ &\quad e^{2W_{C1}+2W_{C2}} \delta\left[\frac{1}{2}\left(k^2+\kappa^2\left(1+\frac{1}{\gamma^2}\right)\right)-n\omega\right]. \end{aligned} \tag{2.136}$$

Using the Delta function, the integral over k_ρ is easily done by substituting $k_\rho = \sqrt{k_n^2 - k_z^2}$, where $k_n^2 = 2n\omega - \kappa^2\left(1+\frac{1}{\gamma^2}\right)$. We modify the definition of $\zeta = \left(\frac{2n_0}{n}-1\right)$, used in [5] to include the contribution from the trajectory perpendicular to the plane of polarisation to give

$$\zeta_{\text{eff}} = \frac{2n_0^{\text{eff}}}{n} - 1, \tag{2.137}$$

where $2n_0^{\text{eff}}\omega = \kappa_{\text{eff}}^2\left(1+\frac{1}{\gamma_{\text{eff}}^2}\right)$, $\kappa_{\text{eff}}^2 = \kappa^2 + k_z^2$, and $\gamma_{\text{eff}} = \kappa_{\text{eff}}/A_0$. The corresponding values for different functions of $\mathbf{k}$ appearing above are as follows:

$$\eta(\mathbf{k}_n) = \sqrt{\frac{1+\gamma_{\text{eff}}^2}{1-\zeta_{\text{eff}}^2}}, \tag{2.138}$$

$$\sqrt{1-\frac{1}{\eta^2(\mathbf{k}_n)}} = \sqrt{\frac{\zeta_{\text{eff}}^2+\gamma_{\text{eff}}^2}{1+\gamma_{\text{eff}}^2}}, \tag{2.139}$$

$$k_{\rho n} = \sqrt{n\omega(1-\zeta_{\text{eff}})}, \tag{2.140}$$

$$A_0 = \sqrt{\frac{n\omega(1+\zeta_{\text{eff}})}{1+\gamma_{\text{eff}}^2}}, \tag{2.141}$$

$$\frac{A_0 k_{\rho n}\eta(\mathbf{k}_n)}{\omega} = n = \frac{2n_0^{\text{eff}}}{1+\zeta_{\text{eff}}} = \frac{2n_0}{1+\zeta}. \tag{2.142}$$

For $k_z \ll k$, we can make the approximation

$$\begin{aligned} \tanh^{-1}\sqrt{1-\frac{1}{\eta^2}} - \sqrt{1-\frac{1}{\eta^2}} &= \frac{1}{2}\ln\frac{1+\sqrt{1-\frac{1}{\eta^2}}}{1-\sqrt{1-\frac{1}{\eta^2}}} - \sqrt{1-\frac{1}{\eta^2}} \\ &\approx \tanh^{-1}\sqrt{\frac{\zeta^2+\gamma^2}{1+\gamma^2}} - \sqrt{\frac{\zeta^2+\gamma^2}{1+\gamma^2}} + \sqrt{\frac{\zeta^2+\gamma^2}{1+\gamma^2}}\frac{k_z^2}{2k_n^2}. \end{aligned} \tag{2.143}$$

And since we are comparing our result with [142], we make the following approximation on the Coulomb-corrected angle ϕ_v^c: as the corrections Δk_x and Δk_y are generally small, we can expand

to first order in these deviations to write ϕ_v^c as a sum of the SFA velocity phase ϕ_v, and a small correction δ defined as

$$\tan\delta = \frac{\epsilon\tan\phi_v}{1+(1+\epsilon)\tan\phi_v}, \tag{2.144}$$

where $\epsilon = \frac{\Delta k_x}{v_x} - \frac{\Delta k_y}{v_y}$. This way we can split the exponential $e^{-2m\Im\left[\phi_v^c\left(t_s'^{(1)}\right)\right]}$,

$$e^{-2m\Im\left[\phi_v^c\left(t_s'^{(1)}\right)\right]} = e^{-2m\Im\left[\phi_v\left(t_s'^{(1)}\right)\right]} e^{-2m\Im\left[\delta\left(t_s'^{(1)}\right)\right]}. \tag{2.145}$$

A further expansion of $\phi_v\left(t_s'^{(1)}\right)$ can be achieved around $\Delta t_s'^{(0)}$ to get

$$\begin{aligned} e^{-2m\Im\left[\phi_v\left(t_s'^{(1)}\right)\right]} &= e^{-2m\Im\left[\phi_v\left(t_s'^{(0)}\right)\right]} \exp\left[-2m\Im\left\{\frac{\omega\Delta t_s'^{(0)}}{\gamma^2}\left(\frac{\zeta-\gamma^2}{1+\zeta}\right)\right\}\right] \\ &= \left(\frac{k_\rho - A_0 e^{-\cosh^{-1}\eta}}{k_\rho - A_0 e^{\cosh^{-1}\eta}}\right)^m \exp\left[-2m\Im\left\{\frac{\omega\Delta t_s'^{(0)}}{\gamma^2}\left(\frac{\zeta_{\text{eff}}-\gamma_{\text{eff}}^2}{1+\zeta_{\text{eff}}}\right)\right\}\right]. \end{aligned} \tag{2.146}$$

As the probability of escape of the electron in the direction perpendicular to the field is exponentially suppressed, we can make the approximation $k_z \ll k_n$, which gives us

$$\begin{aligned} \left(\frac{k_\rho - A_0 e^{-\cosh^{-1}\eta}}{k_\rho - A_0 e^{\cosh^{-1}\eta}}\right)^m &\approx \left[\frac{-\zeta-(1-\zeta)\frac{k_z^2}{k_n^2} + \sqrt{\frac{\zeta^2+\gamma^2}{1+\gamma^2}}\left(1+\frac{\varepsilon(k_z)}{2}\right)}{-\zeta-(1-\zeta)\frac{k_z^2}{k_n^2} - \sqrt{\frac{\zeta^2+\gamma^2}{1+\gamma^2}}\left(1+\frac{\varepsilon(k_z)}{2}\right)}\right]^m \\ &= (-1)^{|m|}\left(1+\frac{1}{\gamma^2}\right)^{|m|}\frac{1}{(1-\zeta^2)^{|m|}}\left(\sqrt{\frac{\zeta^2+\gamma^2}{1+\gamma^2}} - \zeta\,\mathrm{sgn}(m)\right)^{2|m|}, \end{aligned} \tag{2.147}$$

to first order in k_z and $\varepsilon(k_z) = \frac{k_z^2}{k_n^2}\left(\frac{1-\zeta^2}{\gamma^2+\zeta^2}\right)$.

The second term in Eq. (2.146), when expanded in powers of k_z, has a fourth-order dependence on k_z:

$$\frac{\zeta_{\text{eff}}-\gamma_{\text{eff}}^2}{1+\zeta_{\text{eff}}} = \frac{\zeta-\gamma^2}{1+\zeta}\left(1-\frac{k_z^4}{A_0^2(1+\gamma^2)^2}\right). \tag{2.148}$$

Finally, we are left with

$$\begin{aligned} w_n(\mathcal{E},\omega) = |C_{\kappa\ell}|^2\frac{\kappa}{n}\frac{2\ell+1}{4\pi}\frac{(\ell-|m|)!}{(\ell+|m|)!}\left(1-(-1)^\ell e^{-2\kappa a}\right)^2\left(\sqrt{\frac{\zeta^2+\gamma^2}{1+\gamma^2}} - \zeta\,\mathrm{sgn}(m)\right)^{2|m|} \\ \left(1+\frac{1}{\gamma^2}\right)^{|m|}\frac{1}{(1-\zeta^2)^{|m|}} e^{-\frac{4n_0}{1+\zeta}\left(\tanh^{-1}\sqrt{\frac{\zeta^2+\gamma^2}{1+\gamma^2}} - \sqrt{\frac{\zeta^2+\gamma^2}{1+\gamma^2}}\right)}\sqrt{\frac{1+\gamma^2}{\zeta^2+\gamma^2}}\, e^{-2m\Im\left[\delta\left(t_s'^{(1)}\right)\right]} \\ e^{-2m\frac{\zeta-\gamma^2}{1+\zeta}\Im\left[\frac{\omega\Delta t_s'^{(0)}}{\gamma^2}\right]} e^{2W_{C1}+2W_{C2}}\int_{-k_n}^{k_n} dk_z\, e^{-\frac{2n_0}{1+\zeta}\sqrt{\frac{\zeta^2+\gamma^2}{1+\gamma^2}}\frac{k_z^2}{k_n^2}}\left|P_\ell^m\left(\frac{k_z}{\pm i\kappa}\right)\right|^2 \end{aligned} \tag{2.149}$$

up to second order in k_z. The Coulomb correction is taken out of the integral, on account of its extremely weak dependence on the k_z component of the momentum. The above result is valid for all values of ℓ and m. An m-dependent correction due to the Coulomb potential is also seen to manifest through its effect on the SFA saddle point $t_s'^{(0)}$.

To compare with [142], we consider the case of $\ell = 1, m = \pm 1$, for which we have $P_\ell^m\left(\frac{k_z}{\pm i\kappa}\right) = -\sqrt{1+\frac{k_z^2}{\kappa^2}}$. To first approximation, we ignore the $\frac{k_z^2}{\kappa^2}$ term in the prefactor, and note that since $n \gg 1$, we can approximate the integral as:

$$\int_{-k_n}^{k_n} dk_z\, e^{-n\sqrt{\frac{\zeta^2+\gamma^2}{1+\gamma^2}}\frac{k_z^2}{k_n^2}} \approx \int_{-\infty}^{\infty} dk_z\, e^{-n\sqrt{\frac{\zeta^2+\gamma^2}{1+\gamma^2}}\frac{k_z^2}{k_n^2}} = k_n\sqrt{\frac{\pi}{n}}\left(\frac{1+\gamma^2}{\zeta^2+\gamma^2}\right)^{1/4}, \tag{2.150}$$

which gives

$$w_n(\mathcal{E},\omega) = \frac{3|C_{\kappa l}|^2 I_p}{8\sqrt{2\pi}n_0^{3/2}} \frac{e^{2(W_{C1}+W_{C2})}}{\sqrt{1-\zeta}} e^{-\frac{4n_0}{1+\zeta}\left(\tanh^{-1}\sqrt{\frac{\zeta^2+\gamma^2}{1+\gamma^2}}-\sqrt{\frac{\zeta^2+\gamma^2}{1+\gamma^2}}\right)} e^{-2m\Im\left[\delta\left(t_s'^{(1)}\right)\right]} \\ e^{-2m\frac{\zeta-\gamma^2}{1+\zeta}\Im\left[\frac{\omega\Delta t_s'^{(0)}}{\gamma^2}\right]} \left(1+\frac{1}{\gamma^2}\right)^{3/2} \left(\frac{1+\gamma^2}{\zeta^2+\gamma^2}\right)^{3/4} \left(\sqrt{\frac{\zeta^2+\gamma^2}{1+\gamma^2}} - \zeta\,\mathrm{sgn}(m)\right)^2 . \tag{2.151}$$

The main difference from Eq. (19) in [142] is the incorporation of Coulomb correction, starting from the tunnelling region and into the continuum until the electron is registered at the detector, and an orbital-dependent Coulomb correction, a result that was not expected. To derive results that apply throughout the photoelectron momentum spectrum, we need to consistently define the boundary matching scheme for momentum shifts $\mathbf{\Delta p}$ induced by the core (Coulomb) potential for arbitrary final momentum $\mathbf{p}$ of the ionising electron. This issue will be considered in detail in Chapter 3.

Chapter 3

Detecting Ring Currents Using the Attoclock Set-up

In this chapter, we consider ionisation from noble gas atoms in the presence of strong laser fields. Essential to that investigation is the extension of the ARM theory for strong field ionisation from bound states with arbitrary angular momentum (ℓ, m)-numbers, which requires a careful consideration of the boundary matching scheme in Long-Range Potentials (LRPs) for not just the phase, as was first attempted in [4,5], but also for the (complex) momentum-shifts induced by LRP core-interaction of the ionising electron, right from the instant it is launched into the non-classical, under-the-barrier domain. This chapter thus further extends the method of boundary matching presented in Chapter 2, to include the effects of distortion in the wavefunction wave front due to Coulomb potential, for the entire photoelectron spectrum.

3.1 Introduction

Interaction of matter with strong, ultrashort laser fields offers new insights into phenomena that occur on the attosecond time-scale [1], providing new opportunities for probing electron dynamics [55, 185], structure of molecules [180, 181, 276], and deciphering the dynamics of laser-induced optical tunnelling [44, 45, 56, 187].

The enticing opportunity to detect tunnelling times during strong field ionisation relies on attosecond angular streaking principle [44, 45, 56, 57], which provides the link between electron detection angle and its time of ionisation in strong infra-red circularly polarised fields. The application of ultra-short few-cycle pulses allows one to realize this principle experimentally in the so-called attoclock setup [44, 45, 56, 57]. Attoclock-based attosecond chronoscopy of strong field ionisation can only be realized once the protocol for converting the attocklock observable – the most probable electron detection angle – into ionisation time is clearly established [270]. For a benchmark system, hydrogen atom, ionisation time can be reconstructed using the combination of numerical and analytical approaches, leading to zero tunnelling delays [270]. However, such delays may become non-zero when several electrons are actively involved in the ionisation process [270], so that correlation-driven excitations during tunnel ionisation [148] are non-negligible.

New interesting questions that can be addressed by the attoclock include its sensitivity to internal electron dynamics prior to ionisation. Perhaps the simplest example is the possibility of angular separation of photoelectrons originating from strong field ionisation of two different orbitals carrying stationary currents. This is the case for, e.g., p^+ and p^- orbitals in the ground states of noble gas atoms (Ar, Kr, Xe, etc.). Indeed, one would expect that when a co-rotating or a counter-rotating electron tunnel out, the rotating laser field will spun them away differently, as they have different initial velocities orthogonal to tunnelling direction [142]. Interaction with the core potential should reveal this disparity in the initial conditions as it will affect the deflection angle, leading to angular separation of the photoelectron signals coming from the two orbitals.

Here we demonstrate that this is indeed the case.

Since the seminal work of Keldysh [2], the extended treatment by PPT [3–6] and subsequent theoretical efforts [51] to include the combined effects of the long-range core-potential and the strong laser field on the ionisation process, several theoretical methods have been proposed to describe the nonadiabatic and nonlinear character of strong field ionisation. Examples include the non-perturbative expansion techniques of Keldysh-Faisal-Reiss [2,78,79] and the Coulomb-Corrected Strong Field Approximation (CCSFA) method [51,52,249]. The latter, in particular, relies on the imaginary time method (ITM) [4] to develop a trajectory-based description of the ionisation process including the Coulomb corrections to quantum trajectories. The CCSFA method, however, requires assumptions regarding initial conditions for these trajectories.

Here we develop further our Analytical R-Matrix (ARM) method [46,47,148,268], a quantum-mechanical, gauge invariant approach which does not require any $a-priori$ assumptions regarding initial conditions for electron trajectories. The approach takes into account Coulomb interaction of the outgoing electron with the core within the time-dependent version of the Wentzel-Kramers-Brillouin (WKB) method. The concept of trajectories emerges naturally from the development of the theory and manifests in physically observable effects in the photoelectron spectrum [47].

We present a theoretical description of attosecond angular streaking in long range potentials for orbitals carrying stationary current, extending our previous results [270] beyond s-orbitals. To explore theoretically the ionisation from p^- and p^+ orbitals in the attoclock setup, we extend our earlier long-pulse results [268] to the domain of short pulses. General theoretical analysis is complemented with additional results that include explicit expressions for momentum shifts due to the electron interaction with the Coulomb potential, for arbitrary final electron momentum, and detailed derivation of ionisation delays in strong field ionisation.

Crucially, for finite frequency of the ionising circular field, the tunnelling direction is not parallel to the laser field direction at the moment of ionisation. The associated 'tunnelling angle' is determined by the direction of electron velocity at the complex-valued moment of time associated with the beginning of the tunnelling process. This angle is also complex-valued. Mathematically, unusual properties of strong field ionisation from p^- and p^+ states arise precisely from the contribution of the complex-valued 'tunnelling angle' to ionisation rates, as shown in [142] for short-range potentials. Notably, this contribution is absent for angle-independent s-states.

While the tunnelling angle for p^- and p^+ orbitals can be trivially found for short-range potentials [142], the short-range model is unable to catch the key physics underlying the attoclock setup, manifest via the long-range electron-core interaction. Within ARM, the key step in finding this angle is to establish the link between the final electron momentum $\mathbf{p}$ at the detector and the initial electron velocity that leads to this momentum $\mathbf{p}$, where the initial electron velocity is taken at the complex time associated with the beginning of the tunnelling process. This link must include electron interaction with both the laser field and the Coulomb potential. We present a scheme that establishes such a link throughout the whole tunnelling process, thus providing consistent treatment of long-range potential effects on photoelectron distributions from orbitals with arbitrary (ℓ, m) quantum numbers.

The knowledge of tunnelling angle for long range potential requires the knowledge of distribution of initial momenta at the complex instant of time associated with the beginning of the tunnelling process. Each point in this distribution is uniquely linked to the electron final momentum. In our previous work [268] we have established such link for the so-called *optimal momentum*, which corresponds to the peak of the photoelectron distribution in long laser pulses. This was sufficient for describing long-pulse ionisation dynamics discussed in [268]. However, for nearly single-cycle pulses and for states with non-zero angular momentum this is no longer sufficient, even for the peak of the photoelectron spectrum, because such peak no longer corresponds to the "optimal" momentum established for the nearly-monochromatic fields. Thus, to

obtain the attoclock spectra for p^- and p^+ orbitals we need to refine our theory and establish the Coulomb corrections to the tunnelling angle for every final momentum present in the attoclock spectrum.

The paper is organized as follows. Section 3.2 describes key ideas that we have used to extend our A*R*M method to the case of short pulse ionisation from the states with arbitrary (ℓ, m) in long-range potentials. Section 3.3 describes our results. Appendices 3.A and 3.B describe the key steps of our derivation. Particularly important are the derivations of the initial electron velocity and of the Coulomb correction to ionisation time. Section 3.4 concludes the work.

3.2 Key ideas of derivation

Along the steps in deriving the long-pulse result in [268], we encounter the following spatial integral [Eq. (18) in [268], see also Eqs. (2.14) and (2.25)]:

$$a_{\rm ARM}(\mathbf{p}, I_P) = \frac{i\kappa a^2}{(2\pi)^{3/2}} \int_{-\infty}^{T} dt' \int d\Omega'\, e^{-i\mathbf{v}_\mathbf{p}(t')\cdot\mathbf{a} - iS^{\rm SFA}(\mathbf{p},T;t') - iG_C(\mathbf{p},T;\mathbf{a},t')} \varphi_{\kappa\ell}(a) \times N_{\ell m} P_\ell^m(\cos\theta) e^{im\phi}. \quad (3.1)$$

Here $\kappa = \sqrt{2I_p}$, $\varphi_{\kappa\ell}(a)$ is the radial wave-function at the R-matrix sphere of radius $r = a$ that separates the inner and outer R-matrix regions (see [268]), $N_{\ell m}$ is the spherical harmonic normalization coefficient, $S^{\rm SFA}$ is the well-known action in the Strong Field Approximation (SFA) [2–6] for a free electron in a laser field and G_C is the complex Coulomb phase correction, as introduced in [47, 268], $\mathbf{v}_\mathbf{p}(t)$ is electron velocity in the laser field. This result also holds for arbitrary field polarisation and time profiles of the laser field envelope. In Eq. (3.1) the integral is performed over solid angle of the sphere with radius a, where the outgoing wavefunction outside the R-matrix sphere (in the so-called 'outer region') should match the wavefunction inside the R-matrix sphere (in the so-called 'inner region'). The boundary matching process has to ensure that the result is independent of the sphere radius a. In [268] this problem was solved for s-states, while for p-states it was only solved for an optimal momentum $\mathbf{p}_{\rm opt}$, which corresponds to the maximum of the photoelectron distribution in long pulses.

To find the matching scheme valid for any momentum $\mathbf{p}$, we write down the radial part of the asymptotic ground-state wavefunction

$$\varphi_{\kappa\ell}(r) = C_{\kappa\ell}\kappa^{3/2} e^{-\kappa r} (\kappa r)^{Q/\kappa - 1} = C_{\kappa\ell}\kappa^{3/2} e^{-iS_C(r)}, \quad (3.2)$$

where, $S_C(r) = -i(\kappa r - Q/\kappa \ln \kappa r) = S_C^{\rm sr} + S_C^{\rm lr}$, represents the complex, quantum-mechanical action derived through the Schrödinger Equation in the asymptotic region $\kappa r \gg 1$, $C_{\kappa\ell}$ is the standard coefficient, determining the asymptotic behaviour of the radial wave-function. $S_C^{\rm sr}(r) = -i\kappa r$ is the short-range part of S_C, responsible for generating the complex momentum $\nabla S_C^{\rm sr} = -i\kappa\,\hat{\mathbf{r}}$ in the classically forbidden region. Finally, $S_C^{\rm lr}$ provides the long-range potential correction to it, $\nabla S_C^{\rm lr}(r) = iQ/(\kappa r)\,\hat{\mathbf{r}}$, where $\hat{\mathbf{r}}$ is a unit vector of electron displacement. The main idea of wavefunction matching performed at the boundary a of the R-matrix sphere (boundary matching) is to relate this long-range part of the action to the quasiclassical (WKB) action at every point on the R-matrix sphere, and at any time.

Along the lines of the derivation performed in [268], we expand $G_C(\mathbf{p}, T; \mathbf{a}, t)$ and its long-range counterpart in $S_C(a)$ [$S_C^{\rm lr}(a)$ defined above], in a Taylor series around the SFA saddle points of integral Eq. (3.1): $t'_s = t_a$, θ'_s, ϕ'_s [see Eqs. (20)-(22) of [268]]. As discussed in [268], the saddle-point angles $\phi'_s(t')$, $\theta'_s(t')$ describe the direction of electron velocity at the time t', and t_a describes the time at which the electron trajectory crosses the R-matrix sphere boundary. Thus, there is a preferred direction along which the electron crosses the R-matrix sphere. This direction is given by the angles $\phi'_s(t')$, $\theta'_s(t')$, or simply by the vector:

$$\mathbf{r}_s^{(0)}(t) = a\hat{\mathbf{v}}_\mathbf{p}(t), \quad (3.3)$$

where $\hat{\mathbf{v}}_{\mathbf{p}}(t)$ is a unit vector along the direction of electron velocity. This vector can be written in the equivalent form

$$\mathbf{r}_s^{(0)} = \int_{t_s}^{t_a} dt\, \mathbf{v}_{\mathbf{p}}(t), \tag{3.4}$$

where t_s is the SFA saddle point, which is a solution of equation $\partial S_{\mathrm{SFA}}/\partial t' = 0$. The only non-negligible terms in a Taylor series around the spatial saddle points (as discussed in [268]), up to order $\mathcal{O}(a^2)$ and $\mathcal{O}(Q^2)$, are the following:

$$S_C^{\mathrm{lr}}(a) + G_C(\mathbf{p}, T; \mathbf{a}, t) \simeq \left[S_C^{\mathrm{lr}}\left(\mathbf{r}_s^{(0)}\right) + G_C\left(\mathbf{p}, T; \mathbf{r}_s^{(0)}, t_a\right)\right] + \left(\mathbf{a} - \mathbf{r}_s^{(0)}\right) \cdot \nabla \left[S_C^{\mathrm{lr}}(\mathbf{r}) + G_C(\mathbf{p}, T; \mathbf{r}, t_a)\right]\Big|_{\mathbf{r}=\mathbf{r}_s^{(0)}}. \tag{3.5}$$

Boundary matching for the first group of terms has been performed in [268] and it simply yields:

$$W_C(t_s, \mathbf{p}) \equiv \left[S_C^{\mathrm{lr}}\left(\mathbf{r}_s^{(0)}\right) + G_C\left(\mathbf{p}, T; \mathbf{r}_s^{(0)}, t_a\right)\right] = \int_{t_s - i\kappa^{-2}}^{T} d\tau\, U\left(\int_{t_s}^{\tau} d\xi\, \mathbf{v}_{\mathbf{p}}(\xi)\right). \tag{3.6}$$

The value of the lower limit of the integral $t_\kappa = t_s - i/\kappa^2$ plays a key role in our ability to match the asymptotic "tail" of bound wave-function $S_C^{\mathrm{lr}}(a)$ at the R-matrix sphere with the continuum "tail" $G_C(\mathbf{p}, T; \mathbf{a}, t)$ and absorb them into one common expression, continuous across the matching boundary. This term represents the phase $W_C(t_s, \mathbf{p})$ of electron wave function accumulated as it travels from the atom to the detector.

Boundary matching for the momentum term requires a new approach, and is described in the Appendix 3.A.1. This approach generalizes the matching procedure for arbitrary order of terms in the Taylor series expansion Eq. (3.5), and gives us closed-form expression for the Coulomb correction to the electron velocity $\mathbf{v}_{\mathbf{p}}(t_s)$ in a short-range potential:

$$-\Delta\mathbf{v}^C \equiv \left[\nabla S_C^{\mathrm{lr}}(\mathbf{r}_s^{(0)}) + \nabla G_C(\mathbf{p}, T; \mathbf{r}_s^{(0)}, t_a)\right] = \int_{t_s - iQ\kappa^{-3}}^{T} d\tau\, \nabla U\left(\int_{t_s}^{\tau} d\xi\, \mathbf{v}_{\mathbf{p}}(\xi)\right) + \mathbf{v}_{\mathbf{p}}(t_s), \tag{3.7}$$

Note different value for the lower limit of the integral, $t_Q \equiv t_s - iQ/\kappa^3$. Equation (3.7) represents the Coulomb correction to electron velocity $\mathbf{v}_{\mathbf{p}}(t_s)$, which takes into account the contributions of both the Coulomb and the laser fields at the complex time associated with the beginning of the tunnelling process. We need to subtract $\Delta\mathbf{v}^C$ from the SFA velocity $\mathbf{v}_{\mathbf{p}}(t_s)$ to find the correction to initial velocity due to the long-range interactions, for a fixed momentum $\mathbf{p}$ measured at the detector.

It might seem peculiar at first, as we first extend the domain of momentum generated by long-range potential deep under the barrier, and *then* subtract the short-range component in Eq. (3.7). The final velocity term contributing to the photoelectron angular distribution is $\mathbf{v}_{\mathbf{p}^c}(t_s^c) = \mathbf{v}_{\mathbf{p}}(t_s^c) - \Delta\mathbf{v}^C$; this is to be contrasted with the case of the standard PPT [3–6] and KFR [2, 78, 79] theory, where the short-range SFA velocity $\mathbf{v}_{\mathbf{p}}(t_s)$ is the only source for the angular distributions and the prefactors in the ionisation amplitudes/rates.

The fact that the matching time for momentum, $t_Q = t_s - iQ/\kappa^3$, depends directly on the charge Q in the zeroth order (unlike other complex times t_a, t_κ and t_s, which can only depend on Q through higher-order Coulomb corrections, and not in the zeroth order), is a manifestation of the short-range contribution through a long-range potential expression in Eq. (3.7). In Appendix 3.A.2, we further discuss this point, and show how $\Delta\mathbf{v}^C$ vanishes in the limit $Q \to 0$, which expresses the idea that physically, short- and long-range contributions are not separable effects, but need to be considered together to define the appropriate velocity generated in a Coulomb-laser coupled system.

The matching instant is different for the phase and its gradient (to wit, t_κ and t_Q, respectively), which is not surprising, as different matching instants arise from different quantum

boundary conditions: quasicalssical action, G_C, is matched to the action in the asymptotic limit, $S_C^{\rm lr}$, for the quantum mechanical wave function, whereas the gradient of the quasicalssical action, ∇G_C, is matched to the gradient of the action stemming from the long-range part of the quantum mechanical wave function, $\nabla S_C^{\rm lr}$. A detailed derivation of boundary matching for the two cases is discussed in the Appendix 3.A and 3.B.

After achieving the boundary matching for the momentum of the photoelectrons, we can resume the derivation scheme outlined in [268], to end up with the final ionisation amplitude:

$$a_{\rm ARM}(\mathbf{p}, I_P) = (-1)^m C_{\kappa\ell} N_{\ell m} \sqrt{\frac{\kappa}{\left|S_{tt}^{\rm SFA}(t_s^c)\right|}} e^{-iS^{\rm SFA}(t_s^c,\mathbf{p}) - iW_C(t_s^c,\mathbf{p})} P_\ell^m\left(\frac{p_z^c}{v_{\mathbf{p}^c}(t_s^c)}\right) e^{im\phi_v^c(t_s^c)}, \quad (3.8)$$

which is applicable to any arbitrary final momentum $\mathbf{p}$, short pulses of arbitrary polarisation, and initial states of arbitrary symmetry [arbitrary (ℓ, m) values], for a long-range interaction with the ionic core. The final Coulomb-corrected velocity entering into the prefactors is $\mathbf{v}_{\mathbf{p}^c}(t_s^c) = \mathbf{v}_{\mathbf{p}}(t_s^c) - \Delta\mathbf{v}^C$.

The Coulomb-corrected complex tunnelling angle is: $\phi_v^c(t_s^c) \equiv \arctan[v_{\mathbf{p}^c}^y(t_s^c)/v_{\mathbf{p}^c}^x(t_s^c)]$. The c in the superscript of t_s^c denotes the Coulomb-corrected saddle point $t_s^c \equiv t_s + \Delta t_s^c$ [270], which we derive in the Appendix 3.B and present another equivalent form for it:

$$\Delta t_s^c = -\left.\frac{dW_C(t_s,\mathbf{p})}{dI_p}\right|_{\kappa=\rm const} \equiv -\frac{\mathbf{v}_{\mathbf{p}}(t_s)\cdot\Delta\mathbf{v}^C}{\mathbf{v}_{\mathbf{p}}(t_s)\cdot\mathbf{E}(t_s)}. \quad (3.9)$$

The first equality in Eq. (3.9) has been used in [270], and independently derived through the proposd spin-orbit Larmor clock in [271]. The expression for $\Delta\mathbf{v}^C$, given by Eq. (3.7), is rigorously derived in Appendix 3.A.1, the essential point being that we can now describe the modifications of electron velocity due to long-range interactions *under the barrier* as the electron tunnels through.

3.3 Results

Fig. 3.1a and 3.1b show the photoelectron spectra for strong-field ionisation of p^-/p^+ orbitals of a Kr atom, i.e. for the Coulomb potential and the binding energy of Kr in Eq. (3.8). We used right circularly polarised field, rotating in the positive direction (counter-clockwise). The pulse was defined by its vector-potential $\mathbf{A}(t)$ as

$$\mathbf{A}(t) = -\frac{\mathcal{E}_0}{\omega}\cos^2\left(\frac{\omega t}{2N_e}\right)[\cos(\omega t)\,\hat{\mathbf{x}} + \sin(\omega t)\,\hat{\mathbf{y}}], \quad (3.10)$$

with the envelope containing two full laser cycles base-to-base ($N_e = 2$) and the field envelope is modeled by a cos^2-profile. The laser wavelength was set to $\lambda = 800$ nm, and the peak field strength was set to $\mathcal{E}_0 = 0.05$ a.u. In these spectra, we can already identify several distinguishing features between ionisation from the p^- and p^+ orbitals.

Most important is the angular off-set between the peaks of photoelectron distributions corresponding to ionisation from the p^- and p^+ orbitals. Figure 3.1 shows that for the p^- orbital, the spectrum is considerably offset, in the counter-clockwise direction, from the peak of the electron spectrum associated with the p^+ orbital. The difference between the offset angles is $\Delta\phi_{\rm off} \approx 3.9$ degrees, which is an observable shift. Note that ionisation from short range potentials does not lead to angular off-set between these two spectra, where we would obtain the peak angle at $\phi_{\rm off} = 0$ degrees for both p^- and p^+ orbitals.

This results can be understood as follows. Co-rotating and counter-rotating electrons are spun away by the attoclock differently, since they have different initial velocities orthogonal to tunnelling direction. Interaction with the core potential reveals this disparity in the initial conditions: the slower counter-rotating electron stronger sinteract with the Coulomb field and

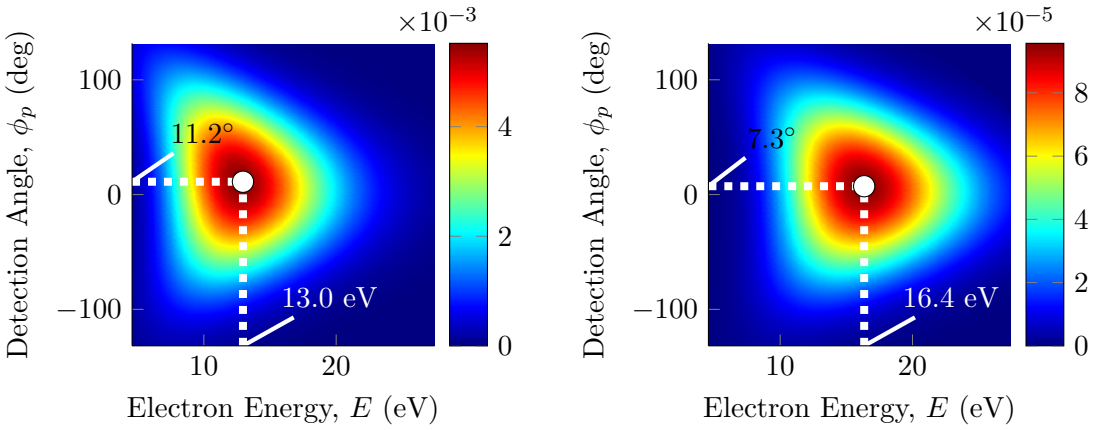

(a) p^- (b) p^+

Figure 3.1: Angle-resolved spectrum for p^- and p^+ electrons removed from a Kr atom by a 2-cycle, right circularly-polarised field, for the peak intensity $I_0 = 1.75 \times 10^{14}$ W/cm^2 ($\mathcal{E}_0 = 0.05$ a.u.), $\lambda = 800$ nm

is therefore deflected stronger. The co-rotating electron exits the barrier with higher lateral velocity, moves away faster, and is less affected by the Coulomb field. This leads to angular separation of the photoelectron signals from the two orbitals.

This picture is further confirmed by the shift of the peak energy for the two orbitals, which is also substantial, $\Delta E = 3.4$ eV, with p^+ electrons peaked at higher energy than p^-. For the present case of right-circularly polarised laser fields, the p^+ (or co-rotating, in general) electrons are always detected with higher energy than the p^- (counter-rotating electrons) as discussed above. A similar energy off-set has been found in the case of long pulses and short-range potentials [142].

We can now explore the angular profile of photoelectron distributions in more detail, and study the distinguishing features of ionisation from different orbitals. These features are determined by the long-range electron-core interaction. The distribution for p^- is more stretched out along the azimuthal angle ϕ_p, but is more compact along the radial momentum p_ρ, as compared to the corresponding distribution in p^+. The spectrum spreads out in angle in case of p^- orbital, because of the prominence of the low momentum electrons in that case, which leads to stronger Coulomb attraction and larger deflection angles.

The width of the distribution in energy E for the p^+ electron is greater than for the p^- electron. This effect is related to the dominance of high energy electrons and specific energy dependence of the Coulomb effects. For high energies, the Coulomb effects weakly decrease with increasing energy, thus preserving the original Gaussian-like distribution for the p^+ spectra, characteristic of ionisation from short-range potentials. In contrast, photoelectrons emitted from p^- orbitals "pile up" at lower energies due to Coulomb attraction.

A comparison of the ratio of angle-integrated ionisation rates for p^- and p^+ electrons, $r_X = w_X^{p^-}/w_X^{p^+}$, is shown in Fig. 3.2, for SFA (red solid) and ARM (blue dashed).

The green dashdotted curve is the photoelectron spectrum for the (dominant) p^--orbital, in arbitrary units, and the black thin, solid line represents the unity level in the ratio. We observe considerable suppression of the signal from the p^+ orbital (nearly 2 to 6 times in the range from 25 to 15 eV, and more for lower energies), versus the signal from the p^- orbital. Thus, when both orbitals are equally populated as is the case of the neutral Kr, the signal from the p^- orbital will dominate the total spectrum.

The dominance of the p^- electron has the same origin as the one described in [142] for short-range potentials and long pulses. However, here the effect is further amplified due to the Coulomb effects. Low to medium energy photoelectrons are enhanced more strongly for p^- than

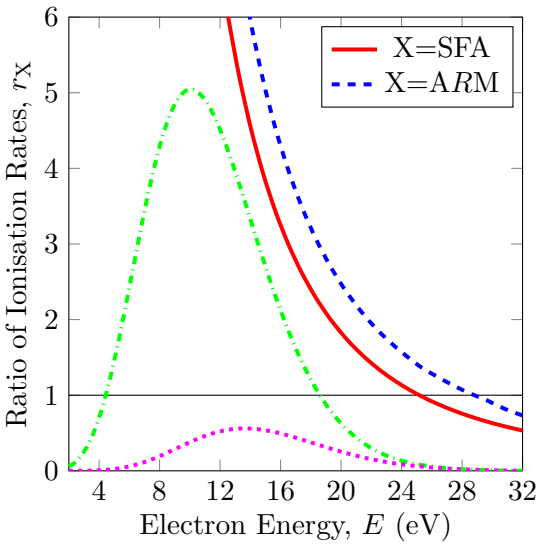

Figure 3.2: Ratio of ionisation rates for p^- to p^+ orbitals, in SFA (red solid) and ARM blue dashed). The green dash-dotted curve is the photoelectron spectrum for the (dominant) p^--orbital, the magenta dotted curve shows the spectrum for the p^+-orbital (in arbitrary units). The black thin solid line represents the unity level in the ratio. The calculations are for a Krypton atom at the peak intensity $I_0 = 1.75 \times 10^{14}$ W/cm^2 ($\mathcal{E}_0 = 0.05$ a.u.), $\lambda = 800$ nm, 2-cycle, right-circularly polarised laser field.

for p^+: for 16 eV electron energy, around 30 % more in the Coulomb potential compared to the short-range potential. The region of dominance for p^- orbital is slightly extended to higher energies, indicating the enhancement of nonadiabatic dynamics in the long-range potential. In [142], it was expected that Coulomb corrections would nearly cancel out and thus have no impact on the ratio $w_{p^-}(E)/w_{p^+}(E)$, which we find to be true for higher energy photoelectrons, but not for low to medium energy.

The dominance of counter-rotating electrons over co-rotating ones implies that the former will give the prominent contributions to the ionisation yields and angular distributions measured experimentally. In Fig. 3.3a and 3.3b we show intensity scan of the offset angle and peak energy for Argon atom. The offset angles and peak energies for an s-orbital calculated with the same ionisation potential of Argon would have appeared approximately in the middle between the graphs presented in Fig. 3.3a and 3.3b.

3.4 Conclusions

We have extended our ARM method to include the effects of the long-range potential interactions on the outgoing electron with the core, for ionisation from atomic orbitals of arbitrary symmetry, going beyond s-orbital case considered in [270]. We have studied the effects of the initial orbital momentum on the observed final angle-and energy-resolved photo-electron distribution.

We have shown the sensitivity of the attoclock observables to the internal dynamics in the initial state. The difference between the attoclock off-set angles for p^+ and p^- orbitals is about $3-4$ degrees for Ar and Kr in typical experimental conditions. Experimentally, the attoclock set-up has been applied to study ionisation from p-states in Ar atom [57]. The resulting off-set angles have been used to extract the spatial coordinate corresponding to the position of the exit from the tunnelling barrier. Our results suggest that corrections at the level of about 2 degrees might be required for this mapping, since the off-set angle for an s-orbital is about 2 degrees smaller than for the dominant p^--orbital.

We expect that the attoclock set-up could be used for detecting ring currents, excited in

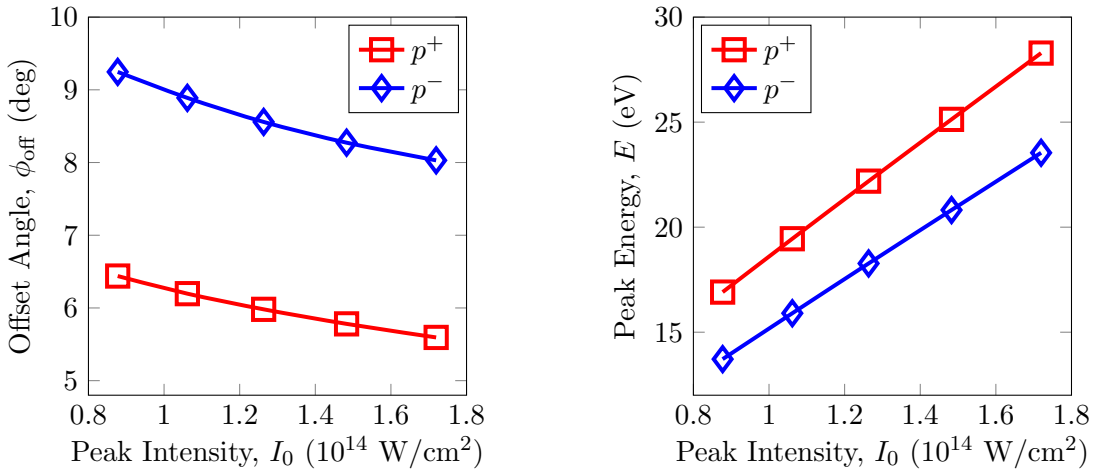

Figure 3.3: (a) Offset Angle and (b) Peak energy variation for p^- and p^+ electrons with peak intensity, for an Argon atom, $I_P = 15.76$ eV. Field Parameters: $\lambda = 800$ nm, 2-cycle, $\cos^2$-envelope, right-circularly polarised.

atoms or molecules. Ring currents of opposite direction are expected to increase or decrease the attoclock off-set angle relative to the value detected in a system, in which such currents have not been excited in the initial state.

The direction of the stationary current in the initial state is also mapped onto the strength of the signal, with the signal from a current counter-rotating with respect to the laser field dominating over the co-rotating one.

To increase the sensitivity of detecting the current direction, one can also measure angular and energy dependent photoelectron dichroism. It amounts to detecting the attoclock spectra in left and right circularly polarised fields and taking the ratio of the difference to the sum of such spectra. The resulting CD attoclock spectra will have opposite off-set angles for opposite directions of ring currents.

Finally, we note that energy separation of p^+ and p^- signals in long pulses leads to spin-polarisation [143], thus angular separation should lead to additional opportunities to create short spin-polarised electron bunches.

3.A Boundary matching for the gradient of EVA phase

3.A.1 Initial velocity and tunnelling angle

We first derive Eq. (3.7). Since $\nabla G_C\left(\mathbf{r}_s^{(0)}, t_a\right)$ is to be matched to $\nabla S_C^{\mathrm{lr}}\left(\mathbf{r}_s^{(0)}, t_a\right)$, we have:

$$\nabla S_C^{\mathrm{lr}}\left(\mathbf{r}_s^{(0)}, t_a\right) + \nabla G_C\left(\mathbf{r}_s^{(0)}, t_a\right) = i\frac{Q}{\kappa a}\hat{\mathbf{v}}_{\mathbf{p}}(t_s) + \int_{t_a}^{T} d\tau\, \nabla U\left(\int_{t_s}^{\tau} d\xi\, \mathbf{v}(\xi)\right). \tag{3.11}$$

We have used that $\nabla S_C^{\mathrm{sr}} = -i\kappa\,\hat{\mathbf{r}}$, and $\mathbf{r}_s^{(0)}$ is given by Eq. (3.3). The change of the unit vector of velocity $\hat{\mathbf{v}}_{\mathbf{p}}(t_a)$ in ∇S_C^{lr} to $\hat{\mathbf{v}}_{\mathbf{p}}(t_s)$ is validated by the fact that the first order term proportional to $(t_a - t_s)$ has exactly zero contribution to the matching point, regardless of the duration and envelope profile of the field. The second order corrections are $\propto \mathbf{E}^2$, effects which we exclude as they require consideration of the polarisation of the bound state [277]. We require

$$\nabla S_C^{\mathrm{lr}}\left(\mathbf{r}_s^{(0)}, t_a\right) = \int_{t_m}^{t_a} d\tau\, \nabla U\left(\int_{t_s}^{\tau} d\xi\, \mathbf{v}_{\mathbf{p}}(\xi)\right) + \mathbf{f}, \tag{3.12}$$

where t_m is an unknown complex matching time instant that we have to establish. Once we derive the expression for t_m, we can combine $\nabla S_C\left(\mathbf{r}_s^{(0)}, t_a\right) + \nabla G_C\left(\mathbf{p}, T; \mathbf{r}_s^{(0)}, t_a\right)$ into a single term:

$$\nabla S_C\left(\mathbf{r}_s^{(0)}, t_a\right) + \nabla G_C\left(\mathbf{p}, T; \mathbf{r}_s^{(0)}, t_a\right) = \int_{t_m}^{T} d\tau\, \nabla U\left(\int_{t_s}^{\tau} d\zeta\, \mathbf{v}_{\mathbf{p}}(\zeta)\right) + \mathbf{f}. \tag{3.13}$$

Here we have made allowance for an additional, constant vector $\mathbf{f}$ that will aid us in our matching scheme. The idea of the matching scheme is to redistribute the contributions from the terms appearing in the RHS of Eq. (3.11) in a boundary-independent form, to which purpose the constant vector $\mathbf{f}$ is introduced. The choice of $\mathbf{f}$ depends on the choice of the matching instant t_m, which as will be shown, we are free to decide upon; however, a specific choice of t_m leads to a clear physical interpretation, and hence is favoured.

First, we note that we can rewrite the integral on the RHS of Eq. 3.12 using the short-time approximation for the argument of $U(\mathbf{r}) = -Q/\|r\|$, which is justified since time instants t_s and t_a are very close to each other by construction: $|t_s - t_a| = a/\kappa \ll |t_s|$. For any τ between t_s and t_a this approximation yields:

$$\left\|\int_{t_s}^{\tau} d\zeta\, \mathbf{v}_{\mathbf{p}}(\zeta)\right\| \approx \|\mathbf{v}_{\mathbf{p}}(t_s)\|(\tau - t_s) = i\kappa(\tau - t_s) = \int_{t_s}^{\tau} d\zeta\, i\kappa, \tag{3.14}$$

using $\|\mathbf{v}_{\mathbf{p}}(t_s)\| \equiv v_{\mathbf{p}} = i\kappa$. From Eq. (3.14) we obtain:

$$\int_{t_m}^{t_a} d\tau\, \nabla U\left(\int_{t_s}^{\tau} d\xi\, \mathbf{v}_{\mathbf{p}}(\xi)\right) = Q\frac{\mathbf{v}_{\mathbf{p}}(t_s)}{v_{\mathbf{p}}^3(t_s)}\int_{t_m}^{t_a} dt'\, \frac{1}{(t' - t_s)^2}, \tag{3.15}$$

We therefore obtain the condition for the matching point t_m, using Eqs. (3.11) and (3.15) to rewrite Eqs. (3.12) as:

$$i\frac{Q}{\kappa a}\frac{\mathbf{v}(t_s)}{v(t_s)} = -Q\frac{\mathbf{v}(t_s)}{v^3(t_s)}\left[\frac{1}{t_a - t_s} - \frac{1}{t_m - t_s}\right] + \mathbf{f}. \tag{3.16}$$

Using the definition of $t_a = t_s - ia/\kappa$, the first term on the RHS cancels with the expression on the LHS, giving us the following definition for the time instant t_m:

$$\mathbf{f} = \frac{Q}{\kappa^2}\frac{1}{t_m - t_s}\hat{\mathbf{v}}_{\mathbf{p}}(t_s) \Rightarrow t_m = t_s + \frac{Q}{\kappa^2 \mathbf{f}\cdot\hat{\mathbf{v}}_{\mathbf{p}}(t_s)}. \tag{3.17}$$

The first and most obvious choice of a suitable vector $\mathbf{f}$ we can consider is what we see time and again in strong-field ionisation: $\mathbf{f} = \mathbf{v_p}(t_s)$ (the SFA velocity), which gives us

$$t_m = t_Q \equiv t_s - i\frac{Q}{\kappa^3}. \tag{3.18}$$

With this definition of matching point, the boundary-independent momentum contribution from long-range part is also clearly stated:

$$-\Delta\mathbf{v}^C \equiv \nabla S_C^{\mathrm{lr}} + \nabla G_C = \int_{t_Q}^{T} d\tau\, \nabla U\left(\int_{t_s}^{\tau} d\xi\, \mathbf{v_p}(\xi)\right) + \mathbf{v_p}(t_s), \tag{3.19}$$

$$\Delta\mathbf{v}^C = \mathbf{v}_\mathbf{p}^C(t_s) - \mathbf{v_p}(t_s), \tag{3.20}$$

$$\mathbf{v}_\mathbf{p}^C(t_s) = -\int_{t_Q}^{T} d\tau\, \nabla U\left(\int_{t_s}^{\tau} d\xi\, \mathbf{v_p}(\xi)\right). \tag{3.21}$$

$\mathbf{v}_\mathbf{p}^C(t_s)$ describes the electron velocity that includes coupled contributions of "laser-free" bound velocity and "laser-driven" continuum velocity.

The part associated with the contribution from the long-range potential obtains by subtracting the SFA velocity $\mathbf{v_p}(t_s)$ from $\mathbf{v}_\mathbf{p}^C(t_s)$. We have also defined, along with our matching scheme, a clear definition of momentum shifts induced by long-range interaction, and, the crucial point of all, taking into account the contributions from under the barrier motion to the momentum shifts induced by the Coulomb potential.

Substituting this value of t_m into Eq. (3.13) we obtain Eq. (3.7). Tunnelling angle is obtained from Eq. (3.7) as described in the main text.

3.A.2 Obtaining the SFA velocity from $\mathbf{v}_\mathbf{p}^C(t_s)$ in the limit $Q \to 0$

We underscore the peculiarity of the matching time t_Q: it is the only complex time discussed here that explicitly depends on the charge Q in zeroth order; t_a, t_κ and t_s are all independent of the effective long-range charge. The expression Eq. (3.7) not only contains the long-, but also the short-range contribution, which is the source of the complex velocity $\mathbf{v_p}(t_s) = i\kappa\,\hat{\mathbf{v}}_\mathbf{p}(t)$. Therefore, in the limit of a short-range potential ($Q \to 0$), the long-range contribution in Eq. (3.7) should converge to zero.

To demonstrate that this is indeed the case, we divide the integral in Eq. (3.7) into two parts: the integral from t_Q till the matching point t_a, up to which time we use the asymptotic, quantum action S_C for the wavefunction, and beyond which the quasiclassical action is used leading to the eikonal-Volkov [267] phase contribution. With $Q \to 0$ this latter part converges to zero as it is directly proportional to Q. From the former, we get:

$$\lim_{Q\to 0} \mathbf{v}_\mathbf{p}^C = -\lim_{Q\to 0}\int_{t_Q}^{t_a} d\tau\, \nabla U(\mathbf{r}_L) \approx \lim_{Q\to 0} Q\frac{\mathbf{v_p}(t_s)}{v_\mathbf{p}^3(t_s)}\left[\frac{1}{t_a - t_s} - \frac{1}{t_Q - t_s}\right] \tag{3.22}$$

after approximating the trajectory by its first (linear) order term in time, on account of the proximity of t_Q and t_a in the complex-time plane.

In Eq. (3.22), the first term goes to zero, since there is no dependence on charge Q in t_a or t_s. If we were considering higher order corrections to t_a, t_s, even then the first term in Eq. (3.22) would converge to zero, since the zeroth order term (independent of Q) will prevail in that case over the higher order correction (dependent on Q), leading to finite contribution from the first term even when $Q \to 0$.

The same is not true for the second term in the rectangular brackets of Eq. (3.22), because of $t_Q = t_s - iQ\kappa^{-3}$, and using this definition of t_Q, we get:

$$\lim_{Q\to 0} \mathbf{v}_\mathbf{p}^C = -\lim_{Q\to 0} Q\frac{\mathbf{v_p}(t_s)}{v_\mathbf{p}^3(t_s)}\frac{i\kappa^3}{Q} = \mathbf{v_p}(t_s) \tag{3.23}$$

which is the SFA velocity, and is precisely what we have intended to prove in the limit of $Q \to 0$. This term then cancels with $\mathbf{v}_\mathbf{p}(t_s)$ in Eq. (3.7) to give $\Delta\mathbf{v}^C = 0$ in the short-range limit.

3.B Derivation of Coulomb correction to ionisation time

We start with Eq. (35) of [268] for the Coulomb correction to the saddle-point time t_a, corresponding to the moment of time when trajectory crosses the boundary of the R-matrix region:

$$\Delta t_a^c = -\frac{\partial_t G_C\left(\mathbf{r}_s^{(0)}, t_a\right)}{\partial_t^2 S^{\mathrm{SFA}}\left(\mathbf{r}_s^{(0)}, t_a\right)} = \frac{-\mathbf{v}_\mathbf{p}(t_s)\cdot\Delta\mathbf{v}^C(t_a,T)+U(a)}{\mathbf{E}(t_s)\cdot\mathbf{v}_\mathbf{p}(t_s)} \tag{3.24}$$

We can rewrite this equation as

$$\Delta t_a^c = \frac{\mathbf{v}_\mathbf{p}(t_s)\cdot\int_{t_a}^{T} d\tau\,\nabla U\left(\int_{t_s}^{\tau} d\xi\,\mathbf{v}_\mathbf{p}(\xi)\right)+U(a)}{\mathbf{E}(t_s)\cdot\mathbf{v}_\mathbf{p}(t_s)}. \tag{3.25}$$

The following is true for any t_m between t_s and t_a:

$$\mathbf{v}_\mathbf{p}(t_m)\cdot\int_{t_m}^{t_a} dt\nabla U\left(\int_{t_m}^{t} d\tau\mathbf{v}_\mathbf{p}(\tau)\right) \simeq \frac{Q}{\mathbf{v}_\mathbf{p}(t_s)}\left[\frac{1}{t_a-t_s}-\frac{1}{t_m-t_s}\right] = \frac{Q}{i\kappa(t_m-t_s)}-\frac{Q}{a}, \tag{3.26}$$

on account of the short-time approximation as outlined above, see Eq. (3.14). Taking into account that Eq. (3.26) yields:

$$U(a) = -\frac{Q}{a} = \mathbf{v}_\mathbf{p}(t_m)\cdot\int_{t_m}^{t_a} dt\nabla U\left(\int_{t_m}^{t} d\tau\mathbf{v}_\mathbf{p}(\tau)\right) - \frac{Q}{i\kappa(t_m-t_s)}, \tag{3.27}$$

we can rewrite Eq. (3.25) as:

$$\Delta t_a^c = \frac{\mathbf{v}_\mathbf{p}(t_s)\cdot\int_{t_m}^{T} dt\nabla U\left(\int_{t_s}^{t} d\tau\mathbf{v}_\mathbf{p}(\tau)\right)+U\left(\int_{t_s}^{t_m} d\tau\mathbf{v}_\mathbf{p}(\tau)\right)}{\mathbf{E}(t_s)\cdot\mathbf{v}_\mathbf{p}(t_s)}, \tag{3.28}$$

Here t_m denotes any arbitrary complex moment of time that has to be established. Note that now the Coulomb correction Δt_a to saddle point time t_a given by Eq. (3.28) does not depend on the position of the boundary, but depends on time t_m.

We now have a similar freedom in choosing t_m for the phase, as we had for the momentum. At present, we consider the equivalent expressions obtained from two different choices of t_m.

Taking $t_m = t_\kappa$, the time instant for phase matching (as derived in Appendix 3.B.1), we get:

$$\Delta t_s^c = \frac{\mathbf{v}_\mathbf{p}(t_s)\cdot\int_{t_\kappa}^{T} dt\,\nabla U(\int_{t_s}^{t} d\tau\mathbf{v}_\mathbf{p}(\tau))+U(\int_{t_s}^{t_\kappa} d\tau\mathbf{v}_\mathbf{p}(\tau))}{\mathbf{E}(t_s)\cdot\mathbf{v}_\mathbf{p}(t_s)} \tag{3.29}$$

Note that Eq. (3.29) can be written in a compact form:

$$\Delta t_s^c = -\left.\frac{dG_C(\mathbf{p},T,\mathbf{r}_s,t_\kappa)}{dI_p}\right|_{\kappa=\mathrm{const}}, \tag{3.30}$$

which is derived in Chapter 4 using different arguments, taking advantage of the Spin-Orbit interactions in partially filled noble gas atom shells.

This form has been applied in [270], where we have used notation

$$W_C(t_s,\mathbf{p}) \equiv G_C\left(\mathbf{p},T,\mathbf{r}_s^{(0)},t_\kappa\right) = \int_{t_s-i/\kappa^2}^{T} d\tau U\left(\int_{t_s}^{\tau} d\zeta\,\mathbf{v}_\mathbf{p}(\zeta)\right). \tag{3.31}$$

The time instant t_κ is when the electron is at a distance of $1/\kappa$ from the entrance point of the tunnelling barrier.

With another choice of $t_m = t_Q$, we however get:

$$\Delta t_s^c = \frac{\mathbf{v}_\mathbf{p}(t_s) \cdot \int_{t_Q}^{T} dt\, \nabla U\left(\int_{t_s}^{t} d\tau\, \mathbf{v}_\mathbf{p}(\tau)\right) + U\left(\int_{t_s}^{t_Q} d\tau\, \mathbf{v}_\mathbf{p}(\tau)\right)}{\mathbf{E}(t_s) \cdot \mathbf{v}_\mathbf{p}(t_s)} \tag{3.32}$$

Using the fact that $U\left(\int_{t_s}^{t_Q} dt\, \mathbf{v}_\mathbf{p}(t)\right) \approx i\kappa \hat{\mathbf{v}}_\mathbf{p}$, we can rewrite Eq. (3.32) in an equivalent form:

$$\Delta t_s^c = -\frac{\mathbf{v}_\mathbf{p}(t_s) \cdot \Delta \mathbf{v}^C}{\mathbf{v}_\mathbf{p}(t_s) \cdot \mathbf{E}(t_s)}. \tag{3.33}$$

We have used here the definition of $\Delta \mathbf{v}^C$ derived in Appendix 3.A.1. A similar result was derived for the optimal momentum in [268], however that result was limited to the SFA optimal momentum and only for $\ell = 0$ bound states. To go beyond and generalise to arbitrary states, we see that finding a boundary matching scheme for the gradient was an essential requirement. The momentum shift term $\mathbf{\Delta p}$ defined in Chapter 2 was real, whereas here we get complex momentum shifts from LRP interactions for two reasons: first, the trajectories can be complex; secondly, and more importantly, we have included effects of momentum shifts from *under the barrier*, which will always ensure complex momentum shifts, even for the optimal momentum (the optimal momentum does have imaginary component, but only under the barrier).

Now with the matching scheme presented here (which is a general procedure for matching to arbitrary orders of atomic charge Q), we have a rigorous derivation valid for arbitrary final momentum $\mathbf{p}$ at the detector. We stress that for the hydrogen atom, where $Q = 1$ and $\kappa = 1$, both expressions are equivalent, since $t_Q = t_\kappa$.

3.B.1 Boundary matching for the Coulomb phase

Here we reproduce the boundary matching for the Coulomb phase term $G_C\left(\mathbf{p}, T; \mathbf{r}_s^{(0)}, t_a\right)$, as done in [268], and present a generalization for the matching scheme for the phase as well.

The idea of matching for the phase is very similar to the idea of matching for its gradient discussed above. To emphasise this similarity we will use the same steps in our derivation, and show the flexibility in choosing the matching time instant t_m for the phase, as we did for momentum.

Recalling that

$$G_C\left(\mathbf{p}, T; \mathbf{r}_s^{(0)}, t_a\right) = \int_{t_a}^{T} d\tau\, U\left(\mathbf{r}_L\left(\tau, \mathbf{r}_s^{(0)}, \mathbf{p}, t_a\right)\right), \tag{3.34}$$

where

$$\mathbf{r}_L\left(\tau, \mathbf{r}_s^{(0)}, \mathbf{p}, t_a\right) = \mathbf{r}_s^{(0)} + \int_{t_a}^{\tau} d\xi\, \mathbf{v}_\mathbf{p}(\xi) = \int_{t_s}^{\tau} d\xi\, \mathbf{v}_\mathbf{p}(\xi), \tag{3.35}$$

and $\mathbf{r}_s^{(0)} = \int_{t_s}^{t_a} d\tau\, \mathbf{v}_\mathbf{p}(\tau)$, we require that

$$S_C^{\mathrm{lr}}\left(\mathbf{r}_s^{(0)}\right) = \int_{t_m}^{t_a} d\tau\, U\left(\int_{t_s}^{\tau} d\xi\, \mathbf{v}_\mathbf{p}(\xi)\right) + \Phi, \tag{3.36}$$

where t_m is an unknown complex matching time instant, that we have to establish by fixing Φ along with it. Once it is found, we can combine $S_C^{\mathrm{lr}}\left(\mathbf{r}_s^{(0)}, t_a\right) + G_C\left(\mathbf{p}, T; \mathbf{r}_s^{(0)}, t_a\right)$ into a single term:

$$S_C^{\mathrm{lr}}\left(\mathbf{r}_s^{(0)}\right) + G_C\left(\mathbf{p}, T; \mathbf{r}_s^{(0)}, t_a\right) = \int_{t_m}^{T} d\tau\, U\left(\int_{t_s}^{\tau} d\xi\, \mathbf{v}_\mathbf{p}(\xi)\right) + \Phi. \tag{3.37}$$

Expanding the RHS of Eq. (3.36) using the proximity of t_a and t_m to t_s, we get

$$i\frac{Q}{\kappa}\ln(\kappa a) = i\frac{Q}{\kappa}\ln\left(\frac{a}{\kappa\tau_m}\right) + \Phi, \tag{3.38}$$

from which we can derive the general relation between matching time t_m and arbitrary constant Φ:

$$\Phi = i\frac{Q}{\kappa}\ln\left(\kappa^2\tau_m\right) \tag{3.39}$$

Here we have made use of the fact that $t_a = t_s - ia/\kappa$ and defined the imaginary time difference between t_s and t_m as $i\tau_m = t_s - t_m$.

If we take $t_m = t_\kappa$ ($\tau_m = 1/\kappa^2$), as was derived in [268], we get $\Phi = 0$, and

$$S_C^{\rm lr}\left(\mathbf{r}_s^{(0)}\right) + G_C\left(\mathbf{p}, T; \mathbf{r}_s^{(0)}, t_a\right) = \int_{t_\kappa}^{T} d\tau\, U\left(\int_{t_s}^{\tau} d\xi\, \mathbf{v}_\mathbf{p}(t_s)\right). \tag{3.40}$$

However, with $t_m = t_Q$ ($\tau_m = Q/\kappa^3$), Eq. (3.36) will lead to

$$S_C^{\rm lr}\left(\mathbf{r}_s^{(0)}\right) + G_C\left(\mathbf{p}, T; \mathbf{r}_s^{(0)}, t_a\right) = \int_{t_Q}^{T} d\tau\, U\left(\int_{t_s}^{\tau} d\xi\, \mathbf{v}_\mathbf{p}(t_s)\right) + i\frac{Q}{\kappa}\ln\left(\frac{Q}{\kappa}\right). \tag{3.41}$$

Equation (3.40) and (3.41) are equivalent. In both cases, the long-range contribution of the asymptotic, Coulomb action $S_C^{\rm lr}$, matches with the long-range part of the quasiclassical eikonal-Volkov phase G_C, to give the final result independent of the mathematical construct of the R-matrix sphere radius. In the latter case, the second term will end up in the prefactor in the form $(Q/\kappa)^{Q/\kappa}$ (note that the co-ordinate r_Q at time instant t_Q is Q/κ^2), which is just the long-range prefactor term $(\kappa r)^{Q/\kappa}$ at coordinate $r_Q = Q/\kappa^2$. In the short-range limit, $Q \to 0$, this prefactor converges to unity.

Similar scheme for matching the Coulomb phase, used in the PPT method [3–6], is derived for the quasistatic domain $\omega \to 0$ – and subsequent approaches [51, 277], the former using the imaginary time method (ITM) to derive ionisation rates, the latter based on the partial Fourier transform scheme – but the idea of introducing an arbitrary new constant was not considered in the way we have introduced here, especially the application to boundary matching for the momentum. See also recent review by Popruzhenko [82] for a comprehensive discussion of the multitude of theoretical approaches in Strong Field Ionisation, including study of Coulomb corrections to the short-range SFA and KFR theories.

Chapter 4

Attosecond Larmor Clock

4.1 Introduction

In the previous two chapters, we have developed the Analytical R-Matrix (ARM), which has shown us that instants of ionisation in a Long-range type potential (e.g. Coulomb) are significantly different than for Short-range type potentials. The latter SRP models have been used extensively to describe strong field ionisation, in systems where they are not valid. For a fixed final momentum, the electron has to ionise *earlier* in a LRP compared to SRP core. This implies a certain *delay* in the ionisation process in Coulomb-type systems. Estimating these tunnelling delays is a crucial goal in Physics in general.

To define the ionisation time for one-photon and multiphoton ionisation regimes within the same protocol, we extend the idea of the Larmor clock, originally introduced in [278] to define the time it takes an electron to tunnel through a barrier (see e.g. [279–281]). The Larmor clock as proposed by Baz [278] measures rotation of the electron spin in an external homogeneous magnetic field *acting exclusively inside the barrier*. The angle of rotation is the hand of the clock. Here, we introduce the analogue of this clock, which is based on the spin-orbit interaction and is naturally built into many atoms. Physically, the spin-orbit interaction can be understood by considering an electron with angular momentum ℓ orbiting around the nucleus. In the reference frame associated with the electron, the nucleus rotates around it and creates a current. The current creates the magnetic field. Precession of the electron spin in this field records time.

This Larmor clock should be applicable for arbitrary systems where spin-orbit interactions can be used as a reliable method to measure time delays, and importantly is applicable for a wide range of laser field parameters, from the multiphoton, weak field regime (characterised by the Keldysh Parameter $\gamma \gg 1$) to the adiabatic tunnelling domain ($\gamma \ll 1$), with a crucial bridge in between the two domains where $\gamma \simeq 1$.

Through this Attosecond Larmor Clock (ALC), we provide a rigorous derivation for time delays, which naturally extend the idea of Wigner-Smith (WS) time in one photon ionisation, to arbitrary photon ionisation. We also show how the rigorous derivation for time delays due to Coulomb interactions presented in the previous Chapter is in agreement with the WS time delay derived here after considering precession of the electron spin in the magnetic field induced by Spin-Orbit interactions.

4.2 Spin-orbit Larmor clock for one-photon ionisation: calibration of the clock

Quantum mechanics uses operators to predict an outcome of a measurement. However, some figures of merit, e.g. the phase of quantum electromagnetic field or the times of quantum transitions are not associated with operators. Their measurement has to rely on the operational

approach, i.e. a measurement protocol yielding a particular observable at the detector. Measuring ionisation times with attosecond accuracy has been the focus of several recent experiments [44, 185, 186, 196, 198, 282], using different measurement protocols in different ionisation regimes.

For one-photon ionisation the definition of ionisation time $\tau_{\rm WS}$, referred to as Eisenbud-Wigner-Smith time, is established [283, 284] and verified in the analysis [186, 285–288] of recent experiments [185, 186]. This definition links $\tau_{\rm WS}$ to the phase of the photoelectron wave-function ϕ through its derivative with respect to electron energy: $\tau_{\rm WS} = -d\phi/dE$. Establishing such a link between the classical concept of time and the parameters of a quantum wave-function in the regime of strong field ionisation is the goal of this chapter.

To illustrate how the clock works, consider a Gedanken one-photon ionisation experiment, where an s-electron is removed from an atom (e.g. Cs) by a right circularly polarised light field, see Fig. 4.0a. There is no spin-orbit interaction in the initial state–the ground state of a Cs atom. Spin-orbit interaction turns on upon photon absorption, since the electron angular momentum changes from $\ell = 0$ (s-state) to $\ell = 1$ with its projection on the laser propagation direction $m_\ell = 1$. Thus, photon absorption turns on the Larmor clock: the electron spin starts to precess. Spin-orbit interaction is short-range, localised near the core. Once the freed electron leaves this area, spin precession stops and the clock turns off.

However, the original Larmor clock [278] used *homogeneous* magnetic field and hence the clock hand rotated with constant speed. In our case, the spin-orbit interaction is inhomogeneous, requiring calibration of the clock: the mapping between the angle of rotation and the ionisation time. To calibrate the clock we consider rotation of electron spin during one-photon ionisation, where the ionisation time τ_{WS} is well established.

Let us prepare the electron in the initial spin-polarised state, $|s_{\rm in}\rangle = (1/\sqrt{2})[|-1/2\rangle + e^{i\varphi}|1/2\rangle]$, with the phase φ characterising the initial orientation of the spin in the polarisation plane, and calculate the angle of rotation of the electron spin in this plane during ionisation. The final state, for the final orbital momentum $m_\ell = 1$, is $|s_{\rm fin}\rangle = (1/\sqrt{2})[a_\downarrow|-1/2\rangle + a_\uparrow e^{i\varphi}|1/2\rangle]$, where the $a_\uparrow$ and $a_\downarrow$ are the ionisation amplitudes for the spin-up and spin-down ionisation pathways. The spin has rotated by the angle $\Delta\phi_{SO} = \arg[a_\uparrow a_\downarrow^*]$, equal to the phase delay between the spin-up and spin-down ionisation pathways.

The amplitudes $a_\uparrow$, $a_\downarrow$, have been originally derived by U. Fano [289]: $a_\uparrow = R_3$, $a_\downarrow = \frac{1}{3}(R_3 + 2R_1)$, where $R_{1,3}$ are the radial transition matrix elements into the degenerate continuum states with total angular momentum $j = 1/2$ and $j = 3/2$.

To find the phase difference we need to find $\arg[a_\uparrow a_\downarrow^*]$:

$$a_\uparrow a_\downarrow^* = \left[R_3\left(\frac{1}{3}(R_3^* + 2R_1^*)\right)\right] = \frac{1}{3}\left(|R_3|^2 + 2|R_1||R_3|(\cos(\phi_3^R - \phi_1^R) + i\sin(\phi_3^R - \phi_1^R))\right), \quad (4.1)$$

$$\Delta\phi_{SO} = \arg\left[R_3\left(\frac{1}{3}(R_3^* + 2R_1^*)\right)\right] = \arctan\frac{2|R_1||R_3|\sin(\phi_3^R - \phi_1^R)}{|R_3|^2 + 2|R_1||R_3|\cos(\phi_3^R - \phi_1^R)}, \quad (4.2)$$

Equation (4.2) yields:

$$\tan\Delta\phi_{SO} = \frac{\sin(-\Delta\phi_{13})}{0.5|R_3|/|R_1| + \cos(\phi_{13})}, \quad (4.3)$$

where the phase difference $\Delta\phi_{13}$ is defined as $\Delta\phi_{13} = \phi_1^R - \phi_3^R$, the relative phase between $R_{1,3}(E)$. Their dependence on electron energy E is very similar, up to a small off-set ΔE_{SO} due to the spin-orbit interaction in the ionisation channel: $R_3(E) = R_1(E - \Delta E_{SO})$ [289]. The phases are shifted accordingly: $\phi_3^R(E) = \phi_1^R(E - \Delta E_{SO})$ [1] Using Taylor expansion, we

[1] The photoionisation matrix elements we discuss here are complex, and we deal with their phases. The phase lag in a real-valued radial wave-function, corresponding to a given ionisation channel $j = 3/2$ or $j = 1/2$ discussed in [289], translates into the phase of the complex-valued photoionisation matrix element, leading to the phase difference $\Delta\phi_{13}$ of the corresponding photoionisation matrix elements discussed here.

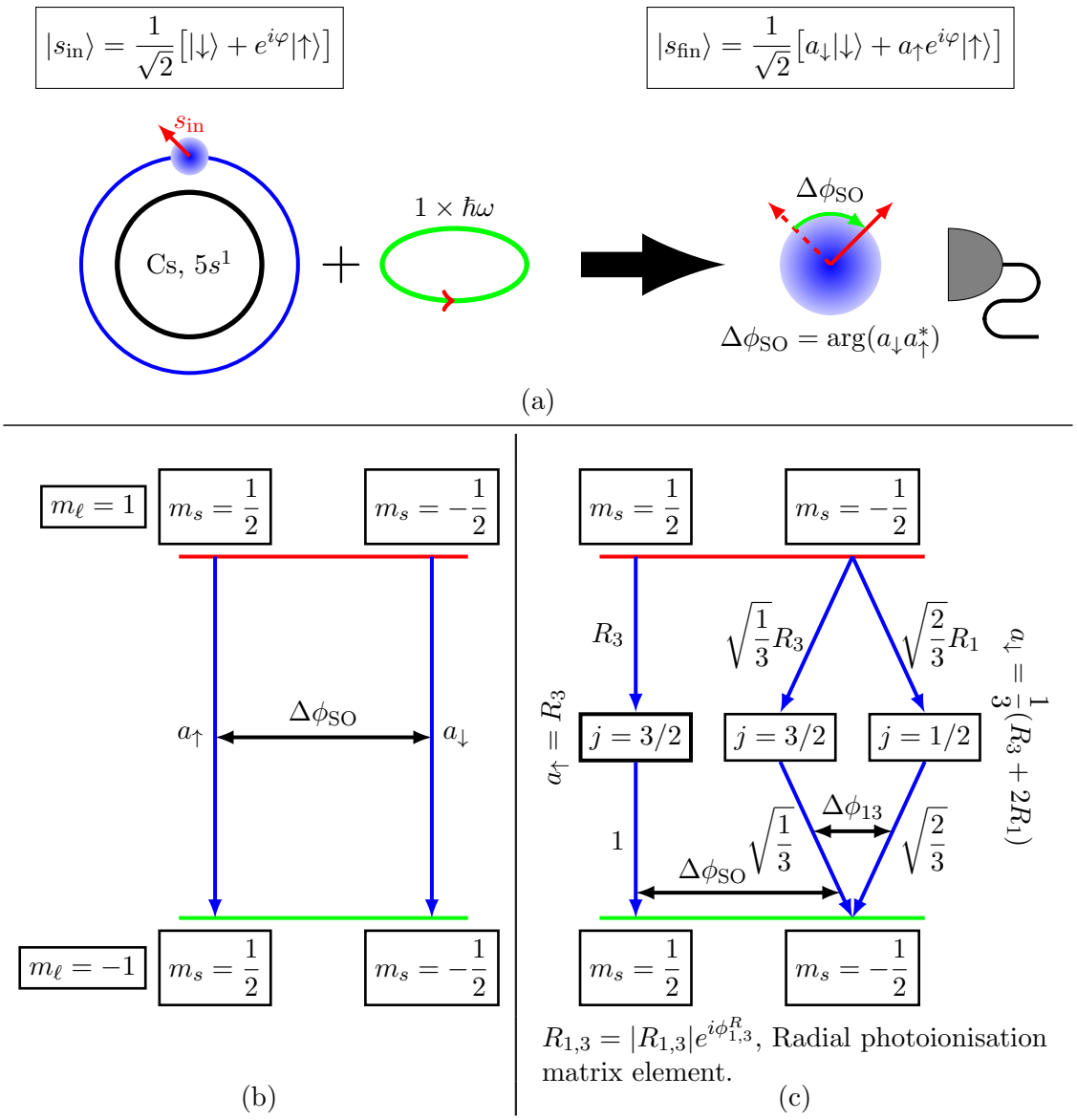

Figure 4.1: Gedanken experiment for calibrating the spin-orbit Larmor clock in one-photon ionisation. (a) Cartoon of the experiment, for a Cs atom: a circularly polarised field removes an electron from the valence $5s$ shell, prepared in a coherent superposition of the spin-up and spin-down states. In the final state, the electron spin has rotated by angle $\Delta\phi_{SO}$. (b) The spin-orbit clock operating on the electron viewed as an interferometer, a simplified view. The two arms correspond to the spin-up and spin-down pathways, with phase difference $\Delta\phi_{SO}$; Formally, the interferometer describes the following interfering pathways: $\left\langle m'_\ell, m'_s, f\middle|\hat{R}\hat{\Xi}\middle|m_\ell, m_s, g\right\rangle \propto \sum_{m_s}\left\langle m'_\ell, m'_s, f\middle|\hat{R}\middle|m_\ell = 1, m_s, g\right\rangle$, where $\hat{R}$ is the radial part of the dipole operator, $\hat{\Xi}$ is the angular part of the dipole operator, g, f are the radial parts of the initial and final state wavefunctions. We have used that $\hat{\Xi}|m_\ell = 0, m_s\rangle \propto \sum_{m_s}|m_\ell = 1, m_s\rangle$. (c) Detailed view of the spin-orbit interferometer. The spin-down path is itself a double arm, since the spin-down electron ($m_s = -1/2$) and the final orbital momentum $m_\ell = 1$ can proceed via both $j = 1/2$ and $j = 3/2$ continua. The single (spin-up) arm and the double (spin-down) arm interfere in the final continuum state with $m_\ell = 1$. Formally, it corresponds to the following interfering pathways: $\sum_{m_s,j,m_j}\left\langle m'_\ell, m'_s, f\middle|\hat{R}\middle|j, m_j\right\rangle\langle j, m_j|m_\ell = 1, m_s, g\rangle$.

find $\Delta\phi_{13} = \phi_1^R(E) - \phi_1^R(E - \Delta E_{SO}) \simeq -\tau_{WS}\Delta E_{SO}$, where $\tau_{WS} = -d\phi_1^R/dE$ is the Wigner-Smith ionisation time [283, 284, 286]. Thus, we have connected the angle of spin rotation during ionisation $\Delta\phi_{SO}$ to the Wigner-Smith ionisation time, calibrating our clock,

$$\tan\Delta\phi_{SO} = \frac{\sin(\tau_{WS}\Delta E_{SO})}{0.5|R_3|/|R_1| + \cos(\tau_{WS}\Delta E_{SO})}. \tag{4.4}$$

The inhomogeneous character of the spin-orbit interaction makes the relationship between $\Delta\phi_{SO}$ and τ_{WS} nonlinear, introducing the extra term $0.5|R_3|/|R_1|$ in the denominator, but does not invalidate the clock.

How does the spin-orbit interaction measure the ionisation time? The spin-orbit clock works like an interferometer, see Figs. 4.0b and 4.0c. The angle of rotation is given by the relative phase between the spin-up (parallel to the orbital momentum) and spin-down pathways. The spin-up pathway proceeds only via the $j = 3/2$ continuum. The spin-down pathway is a double arm: it can proceed via both the $j = 3/2$ and $j = 1/2$ states. The spin-orbit interaction introduces the phase delay $\Delta\phi_{13}$ in the double arm. This small perturbation records the ionisation time, with Eq. (4.4) connecting $\Delta\phi_{SO}$ and τ_{WS}.

4.3 Strong-field ionisation

We now turn to strong-field ionisation in intense IR fields–the regime of recent experiments [44, 198] aimed at measuring ionisation times and focus on the definition of the ionisation time in this regime.

To address this problem, consider ionisation of a Kr atom (Fig. 4.1a). The ground state of Kr^+ is spin-orbit split by the energy $\Delta E_{\rm SO} = 0.665$ eV into the $P_{3/2}$ and $P_{1/2}$ states with total angular momentum $J = 3/2, 1/2$. Both will be coherently populated by ionisation [54] in a few-cycle intense IR laser pulse, with coherence approaching 90% for nearly single-cycle pulses [54]. The loss of coherence arises when photo-electron spectra, correlated to two different core states, do not overlap or overlap only partially.

Figure 4.3 shows nearly complete overlap of these spectra for the ultrashort circularly polarised pulse used in our ab-initio calculations, see Appendix 4.A for the numerical details, confirming nearly 100% coherence of the hole motion in this case. Note that the lack of 100% coherence affects the amount of the coherently moving charge in the ion, but not the timing of its dynamics. Thus, even for coherences below 100%, one is still able to use the rotation of the spin of the hole, triggered by the spin-orbit dynamics of the electron charge in the ion, as a clock.

At the same time, the spin-orbit interaction in the ionisation channels becomes completely negligible in strong fields. The importance of this effect can be gauged using the Analytical R-matrix Approach (ARM) [46, 47, 148, 268, 270], which has been verified against ab-initio simulations in [269, 270]. Application of ARM to calculating ionisation phases is described in Appendix 4.B. In the tunnelling limit, ARM yields the following expression for the relative phase between two degenerate continuum states associated with electron total momentum $j = l + 1/2$ and $j' = l - 1/2$: $\xi_{SO} \sim 0.21\alpha^2F^2/I_p^{5/2} \sim 2.3\times10^{-7}$rad, which is completely negligible. Here α is the fine structure constant. For the estimates we used typical values of ionisation potential $I_p \simeq 0.5$ a.u. and the strength of the laser field $F = 0.06$ a.u. (see Appendix 4.B for the details of the derivation).

The formal description of the spin-orbit interferometer in Fig. 4.1b is similar to the one-photon case in Fig. 4.0c. There is no spin-orbit interaction in the ground state of Kr: the filled valence $4p^6$-shell has equal number of p^- and p^+ electrons 'rotating' in opposite directions. Ionisation by a nearly single-cycle, right-circularly polarised IR pulse breaks the balance between the co-rotating and counter-rotating electrons: intense right-circularly polarised IR pulse preferentially removes the p^- electron [142, 144, 290]. This starts the clock. The angle of rotation of

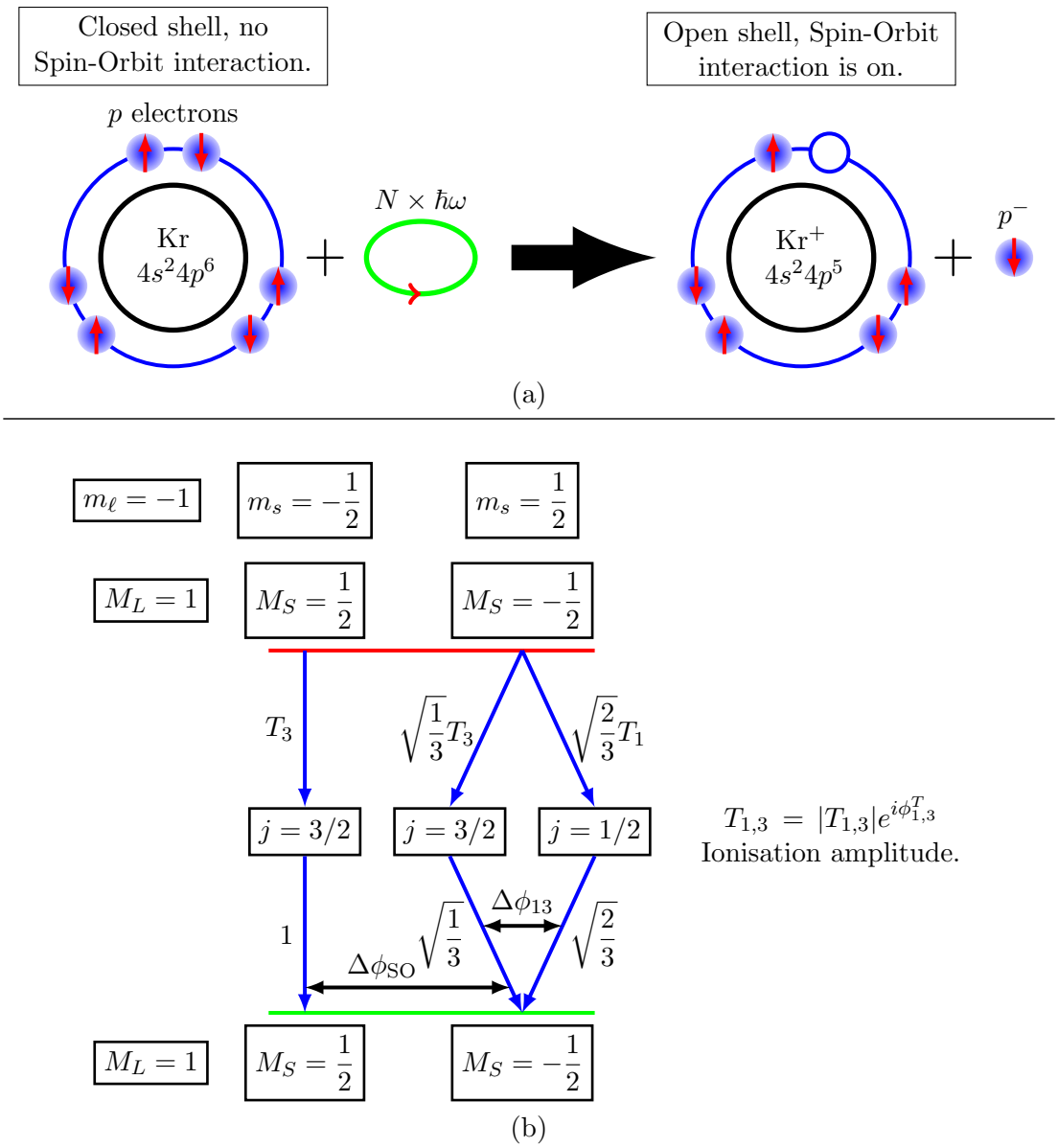

Figure 4.2: Gedanken experiment for measuring ionisation time in strong-field ionisation. (a) Cartoon of an experiment, for a Kr atom: Intense circularly polarised field removes a p^- electron from the valence $4p^6$ shell via absorption of many photons, creating a rotating hole in the ionic core. (b) The spin-orbit clock operating on the ionic core as an interferometer, for an electron removed with $m_\ell = -1$ and the ionic core left with $M_L = 1$. As in Fig. 4.0c, the spin-down path is a double arm, since for $M_L = 1$ the spin-down pathway ($M_S = -1/2$) can proceed via both $J = 1/2$ and $J = 3/2$ core states. The ionisation amplitudes, up to the angular coefficients relating the orbital momentum L, spin S, and the total angular momentum J, are T_3 (for $J = 3/2$) and T_1 (for $J = 1/2$). The relevant angular (Clebsch-Gordan) coefficients for each pathway are also indicated separately.

the core spin at a time-delay τ after the IR pulse is (see Appendix 4.C):

$$\tan\Delta\phi_{SO} = \frac{\sin(\Delta E_{SO}\tau - \Delta\phi_{13})}{0.5|T_3^-|/|T_1^-| + \cos(\Delta E_{SO}\tau - \Delta\phi_{13})}. \tag{4.5}$$

The dependence of the ionisation dynamics on the IR pulse intensity, duration, shape, etc, is fully encoded in the matrix elements T_3^- and T_1^- (Fig. 4.1b) describing strong-field ionisation

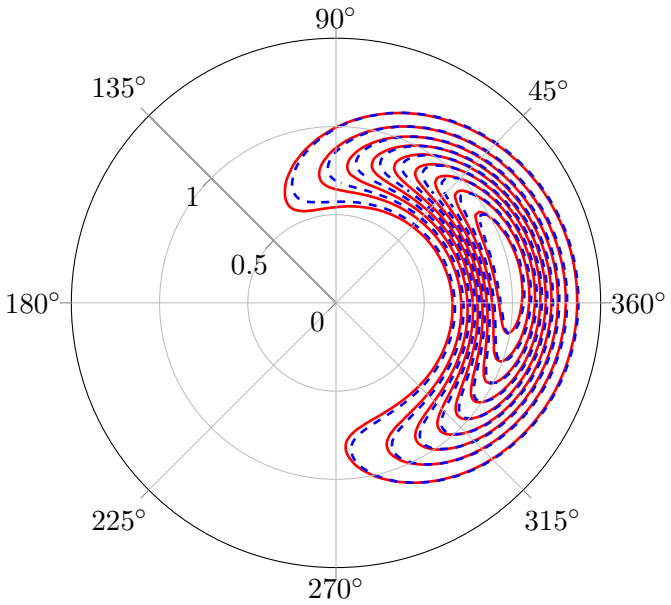

Figure 4.3: Strong-field ionisation of Krypton by a a single-cycle, circularly polarised IR pulse. Angle and momentum-resolved photo-electron spectra calculated numerically for the two ionisation potentials corresponding to the two ground states of Kr^+, $P_{3/2}$ ($I_p = 14.0$ eV) and $P_{1/2}$ ($I_p = 14.67$ eV). Red solid contours correspond to $P_{3/2}$, blue dashed contours correspond to $P_{1/2}$. The inner-most contour corresponds to 0.9 level, other contours shown in steps of 0.1. The pulse had a vector-potential $\mathbf{A}_L(t) = -(\mathcal{E}_0/\omega)\cos^4(\omega t/4)(\cos\omega t\,\hat{\mathbf{x}} + \sin\omega t\,\hat{\mathbf{y}})$ with $\mathcal{E}_0 = 0.05$ au and $\omega = 0.057$ au. The radial coordinate gives the electron momentum in atomic units.

amplitudes for the removal of $m_\ell = -1$ electron, leaving the hole in $P_{3/2}$ and $P_{1/2}$ ionic states correspondingly, for a given final electron momentum $\mathbf{p}$ at the detector. The phases of $T_{3,1}$ are ϕ_3^T and ϕ_1^T, $\Delta\phi_{13} = \phi_1^T - \phi_3^T$. For the p^+ electron ($m_\ell = 1$) the expression is similar, except that $T_{1,3}$ are different. The tiny phase shift between spin-down and spin-up ionisation amplitudes correlated to the $P_{3/2}$ state of Kr^+ due to spin-orbit interaction in ionisation channels has the same estimate as above, $\xi_{SO} \sim 0.21\alpha^2F^2/I_p^{5/2} \sim 2.3\times10^{-7}$rad, and is also negligible.

The clock angles in Eqs. (4.3), (4.5) are virtually identical, except for the term $\Delta E_{SO}\tau$ describing the hole dynamics [273] upon ionisation. The analogy in angle-time mapping in Eqs. (4.3) and (4.5) allows us to establish the definition of strong-field ionisation time. Indeed, Eq. (4.3) calibrates the clock and establishes the mapping between the angle of spin rotation and the ionisation time. Eq. (4.5) contains the same mapping. Thus, the time of hole formation is encoded in $\Delta\phi_{13} = \phi_1^T - \phi_3^T$, accumulated in the second (double) arm of the interferometer. We shall now analyse these phases to extract the strong-filed ionisation time.

The phases ϕ_1^T, ϕ_3^T encode the electron interaction with the potentials $U_{1,3}$ of the core states $P_{1/2}$ and $P_{3/2}$. These potentials have two contributions, $U_{1,3} = U^c + U^d_{1,3}$. Here U^c is common for both states and is dominated by the long-range Coulomb potential, while $U^d_{1,3}$ are different for the two core states, reflecting different spatial distributions of their electron densities, see Appendix 4.D. Thus, $\phi^T_{1,3} = \phi^c_{1,3} + \phi^d_{1,3}$.

For the same final kinetic momentum $\mathbf{p}$ of the continuum electron, in the strong-field ionisation regime, the difference between ϕ_1^c and ϕ_3^c comes from slightly different ionisation potentials into the $P_{1/2}$ and $P_{3/2}$ states: $\phi_1^c = \phi^c(I_p)$ and $\phi_3^c = \phi^c(I_p - \Delta E_{SO})$, see Appendix 4.B. Hence $\Delta\phi^c_{13} = \phi_1^c - \phi_3^c \simeq \Delta E_{SO} d\phi^c/dI_p$ and one should convert $\Delta\phi^c_{13}$ into time, dividing by the energy of spin-orbit splitting [note the 'minus' sign in Eq. (4.5)]:

$$\tau_{SI} = -\frac{\Delta\phi^c_{13}}{\Delta E_{SO}} = -\frac{d\phi^c_1}{dI_p}. \tag{4.6}$$

Equation (4.6) defines ionisation time in the strong-field regime.

The second part of the relative phase, $\Delta\phi^d_{13} = \phi^d_1 - \phi^d_3$, results from the different core potentials for the $P_{3/2}$ and $P_{1/2}$ core states, e.g. due to the different angular structure of the electron density. It does not depend on ΔE_{SO}, i.e. the period of the clock, and hence can not be converted into the time-delay in the formation of the hole.

We note that the derivation presented here is not applicable in the weak-field regime. Firstly, the neglected spin-orbit interaction in ionisation channel may become important in weak fields. However, it is a rather standard approximation to ignore spin-orbit interaction in the ionisation channel compared to the spin-orbit interaction for the core electrons (see e.g. [272]), since the core electrons are plenty and stay near the core, where the spin-orbit interaction is strong, while the sole continuum electron leaves the core region. Secondly, the explicit dependence of phases $\phi_{1,3}$ on ionisation potential, used in deriving Eq. (4.6), arises naturally only in the strong-field regime, see Appendix 4.B. Therefore, the expression Eq. (4.6) may not hold in the weak field regime.

4.4 Reading spin-orbit Larmor clock in strong-field regime

In the Gedanken experiment described in Section 4.3, Eq. (4.5) is sufficient to introduce the strong-field ionisation time τ_{SI} by comparing it to Eq. (4.4) which has calibrated the clock. In contrast to the one-photon case, where the clock stops as soon as the liberated electron leaves the range of the spin-orbit interaction potential, the discussion in Section 4.3 does not involve stopping the clock. Indeed, the clock operates on the states of the ion $P_{3/2}$ and $P_{1/2}$. The hole spin periodically rotates after ionisation is completed. Thus, the clock continues to count time after it has recorded the rotation angle related to the ionisation time. To stop the clock and read the information out we can apply the second pulse. It allows us to get direct access to the phase $\Delta\phi_{13}$, which records time in the spin-orbit interferometer shown in Fig. 4.1b.

Here is how it works. Consider the pump-probe experimental scheme shown in Fig. 4.3a. The pump, which starts the clock, is a nearly single cycle right circularly polarised IR pulse. The probe, which stops the clock, is a left circularly polarised attosecond XUV pulse. It comes with an attosecond-controlled delay τ and promotes the core into an excited S-state, where the spin-orbit splitting is absent, e.g. $4s4p^6$ or any other suitable state. Broad bandwidth of the attosecond probe pulse couples both $P_{3/2}$ and $P_{1/2}$ to the same final S-state, as in [54]. As opposed to the Gedanken experiment above, in laboratory experiments the initial spin-up and spin-down components of the ground state are incoherent, and the single arm of the interferometer yields background for the interference in the double arm in Fig. 4.3b. Left-polarised probe ensures that the final S-state can be reached only if the electron missing in the Kr core after ionisation is the p^- electron.

The population w of the final state is (see Appendix 4.E):

$$w = |A_1|^2 + |A_3|^2 + 2|A_1||A_3|\cos(\Delta E_{SO}\tau - \Delta\phi_{13}(\mathbf{p})) + |\tilde{A}_3|^2. \tag{4.7}$$

Here, $A_1 = T_1^-(\mathbf{p})d_{1/2}F_\omega(\Omega_1)\sqrt{2/27\pi}$ and $A_3 = T_3^-(\mathbf{p})d_{3/2}F_\omega(\Omega_3)\sqrt{1/27\pi}$ are the transition amplitudes for the two interfering pathways corresponding to the removal of the spin-down p^- electron. In addition to the multi-photon ionisation matrix elements $T^-_{1,3}(\mathbf{p})$ they include the real-valued radial transition matrix elements $d_{1/2}$ and $d_{3/2}$ between the $P_{1/2}, P_{3/2}$ and the final S-state of Kr^+, and the spectral amplitudes of the attosecond pulse, $F_\omega(...)$, at the excitation energies $\Omega_{3,1}$ from the $P_{3/2,1/2}$ states to the final S-state. The background $|\tilde{A}_3|^2$, $\tilde{A}_3 = \tilde{T}_3^-(\mathbf{p})d_{3/2}F_\omega(\Omega_3)\sqrt{1/27\pi}$, corresponds to the removal of the *spin-up* p^- electron (See Appendix 4.E for details of derivation). Modulation of w vs. pump-probe delay τ yields the phase $\Delta\phi_{13}(\mathbf{p})$ between A_1 and A_3. It can be measured, e.g. using attosecond transient absorption [54]. The sensitivity of the phase $\Delta\phi_{13}(\mathbf{p})$ to the final momentum $\mathbf{p}$, and the errors that it can introduce into the transient absorption measurement of ionisation time, are discussed below.

The phase $\Delta\phi_{13}$ includes two contributions: (i) the relative phase due to the same core potential in both ionisation pathways, $\Delta\phi^c_{13}$, which can be translated into time-delay and (ii) the phase $\Delta\phi^d_{13}$, related to the different electron-core potentials in the two ionisation channels. This phase reflects correlation between the electron and the core and can not be translated into time. If an experiment does not distinguish between these two contributions to $\Delta\phi_{13}$, the phase $\Delta\phi^d_{13}$ related to the electron-hole correlation will look like a time shift.

Figure 4.5a shows how the total phase (red squares), which can be measured by transient absorption, and its two separate parts $\Delta\phi^c_{13}$ (blue circles) and $\Delta\phi^c_{13}$ (green triangles), depend on the laser wavelength, i.e. the minimum number of photons $N = I_p/\omega$ required to reach the ionisation threshold, for fixed laser intensity. Figure 4.5b shows τ_{SI} (blue circles) and apparent time delays $\tau_{eh} = -\Delta\phi^d_{13}/\Delta E_{SO}$ (green triangles). The apparent delay τ_{eh} is not negligible for $P_{3/2}$ and $P_{1/2}$ states of Kr.

To obtain results in Figs. 4.5a and 4.5b, we have calculated the phases accumulated due to the Coulomb potential and the short range components of the core potential for the two ionisation channels, corresponding to the ionic states $P_{3/2}$ and $P_{1/2}$.

Note that the short-range potentials in these two channels are different, see Appendix 4.D. To obtain time-delays, we have divided the relative phases by the difference in the ionisation potentials, ΔE_{SO}. The phases were calculated using the ARM method [46, 47, 148, 268, 270], for the characteristic momentum of the photo-electron distribution $p_0 = A_0 \sinh(\omega\tau_T)/(\omega\tau_T)$, where A_0 is the amplitude of the field vector potential and $\tau_T \equiv \mathrm{Im}[t_s(p_0)]$ is the so-called 'Keldysh tunnelling time', the imaginary part of the saddle point $t_s(p_0)$, see Appendix 4.C. For this momentum, which is very close to the peak of the distribution for the short laser pulse, the ionisation phases have simple analytical expressions in the tunnelling limit:

$$\Delta\phi^c_{13} \simeq -\Delta E_{SO}/I_p^{3/2}, \tag{4.8}$$

$$\Delta\phi^d_{13} \simeq -0.4F^2/I_p^{5/2}. \tag{4.9}$$

Note that $\Delta\phi^c_{13}$ is proportional to ΔE_{SO} and therefore leads to proper time-delay, while the phase $\Delta\phi^d_{13}$ accumulated due to the different short-range potentials does not scale with ΔE_{SO} and cannot be translated into proper time. Thus, every time is phase, but not every phase is time.

Since transient absorption experiments do not detect the final energy (or the momentum) of the electron, we have also checked that the phases and the resulting times are only very weakly sensitive to the final electron momenta within the region surrounding the peak of the photo-electron signal. This analysis is presented in Fig. 4.6, where the ionisation time-delays are overlayed with the electron spectrum generated by the single-cycle pump pulse with the vector-potential $\mathbf{A}_L(t) = -A_0 \cos^4(\omega t/4)(\cos(\omega t)\,\hat{\mathbf{x}} + \sin(\omega t)\,\hat{\mathbf{y}})$, with $A_0 = \mathcal{E}_0/\omega$, $\mathcal{E}_0 = 0.05$ a.u. and $\omega = 0.0465$ a.u. The difference in ionisation times within the full width at the half-maximum of the distribution is ± 5 asec. This number provides an estimate for possible errors in transient absorption measurements of ionisation delays caused by averaging over the photo-electron distribution. Note that such measurements will also inevitably include the apparent delays $\tau_{\mathrm{eh}} = -\Delta\phi^d_{13}/\Delta E_{SO}$ associated with the phase $\Delta\phi^d_{13}$. For the specific example shown in Fig. 4.5b $\tau_{\mathrm{eh}} \sim 10$ asec. Importantly, in the tunnelling limit τ_{SI} is intensity-independent while the apparent delay τ_{eh} is proportional to the laser intensity, see Eq. (4.9). This factor might be used to separate these two contributions.

Results presented in Fig. 4.5b show that, as we increase the laser wavelength λ and hence the number of photons $N = I_p/\omega$ required for ionisation, the ionisation time in Fig. 4.5b decreases. This dependence has simple explanation. As λ decreases, the laser frequency ω increases, ionisation becomes less adiabatic and the electron splashes out of the potential well closer to the core, see Figs. 4.5c and 4.5d. From there, it runs to the detector, accumulating the phase and consequently the time-delay τ_{SI}. The closer the electron is launched, the larger is the accumulated phase. Note that no delay is accumulated under the barrier, see Section 4.6 for details.

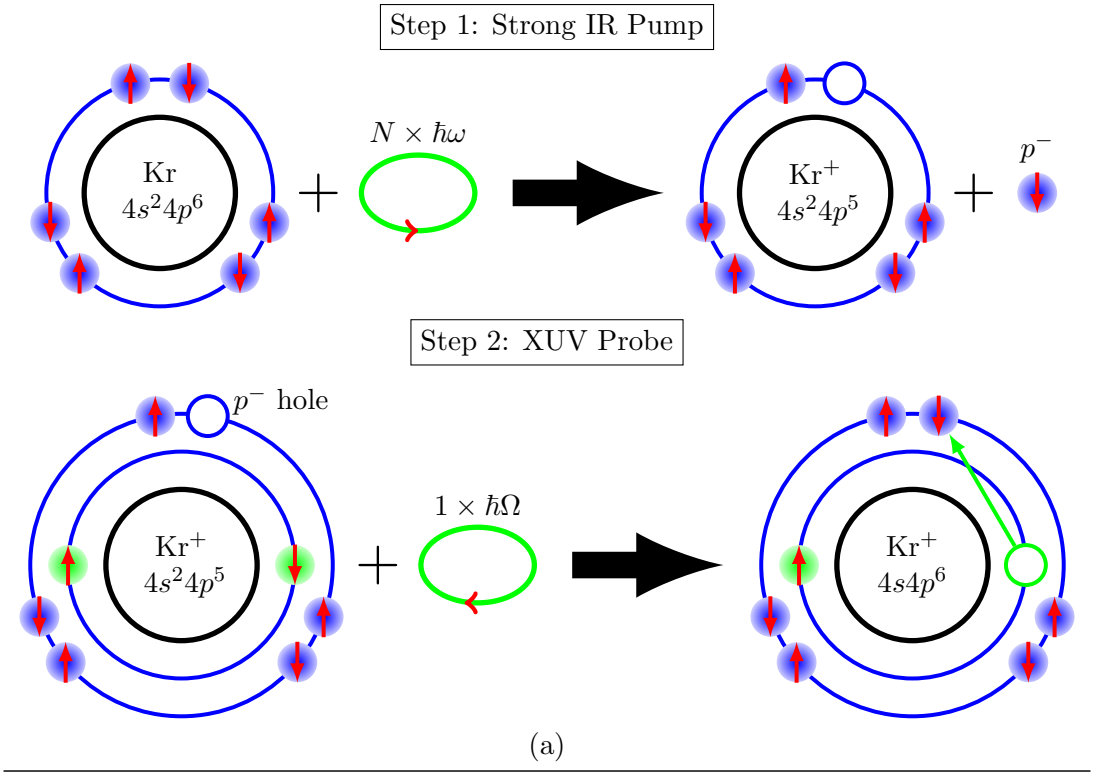

(a)

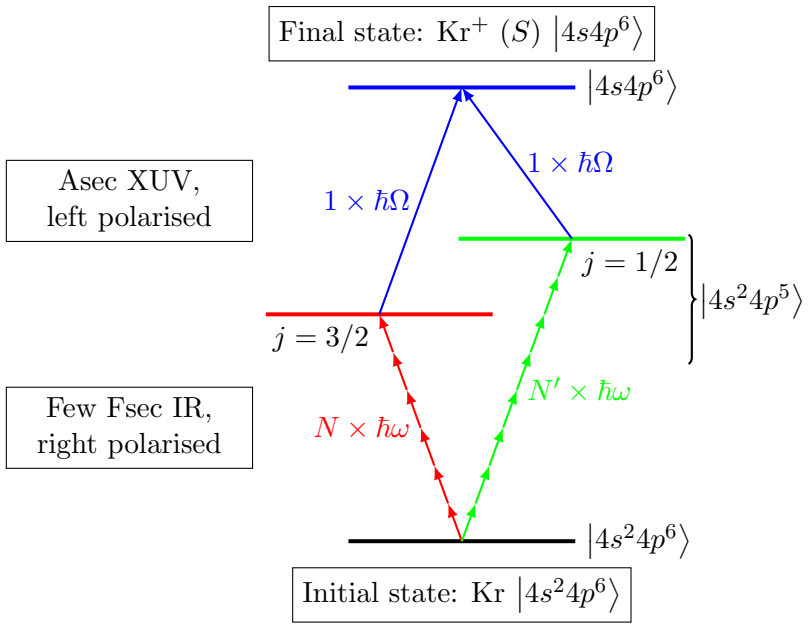

(b)

Figure 4.4: Schematic of a laboratory pump-probe experiment implementing the spin-orbit Larmor clock for strong-field ionisation, for Kr atom. (a) Cartoon of the experiment. Multiphoton ionisation with a strong, right-circularly polarised infrared pump pulse creates a P-hole in the ion and starts the clock. Attosecond extreme ultraviolet probe fills the P-hole by promoting an electron from the inner S-shell. This transition stops the spin-orbit clock, since spin-orbit interaction for S-states is absent. (b) Analysis of the experiment as a two-path interferometer. Two pathways via the $J = 1/2$ and $J = 3/2$ P-states of the ion interfere in the final S-state of the Kr^+.

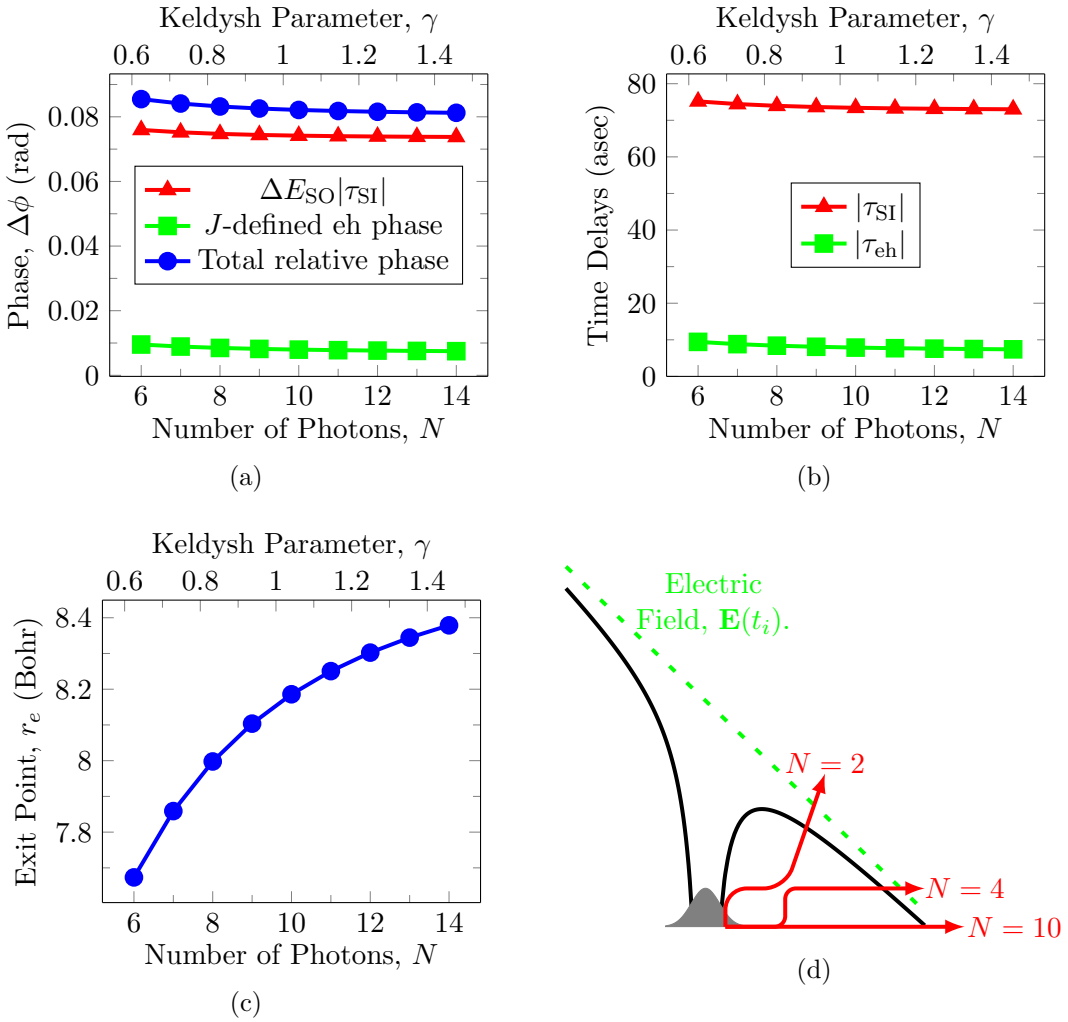

Figure 4.5: Analysis of time delays in strong-field ionisation. (a) Calculated phase $\Delta\phi_{13}$ for the pump-probe experiment, as a function of the minimum number of photons required for ionisation, $N = I_p/\omega$, I_p is ionisation potential, ω is laser frequency. The calculations were done for a Kr atom and the circular field intensity $2.5 \times 10^{14}\mathrm{W/cm}^2$. Red triangles (▲) show phase associated with the actual time-delay. Green squares (■) show the phase that does not correspond to time-delays but is a leftover from the electron-hole correlation. Total phase (●) is shown as blue circles. (b) Real (▲) and 'apparent' (■) ionisation delays as a function of the number of photons required for ionisation, N. (c,d) Physical picture underlying the results: N-dependence of the electron exit position from the potential well (see Appendix 4.B) (c) and the cartoon of the ionisation process (d).

4.5 Attoclock measurements of strong-field ionisation delay

The spin-orbit Larmor clock has offered us a general procedure for defining ionisation times in both one-photon and strong field ionisation regimes. Using the same general procedure we have arrived at two different expressions in the weak-field one-photon ionisation regime and in the strong-field regime. In the weak field regime we found the Wigner-Smith ionisation time. In the strong-field regime we found an expression which agrees with the result of a completely different derivation described in [270]. Importantly, while we have derived ionisation times using spin-orbit interaction, our results do not depend on it. Therefore, the detection of the strong-field ionisation time does not have to rely on the spin-orbit interaction.

Consider, for example, the so-called attoclock setup [44, 57], which measures angle-resolved

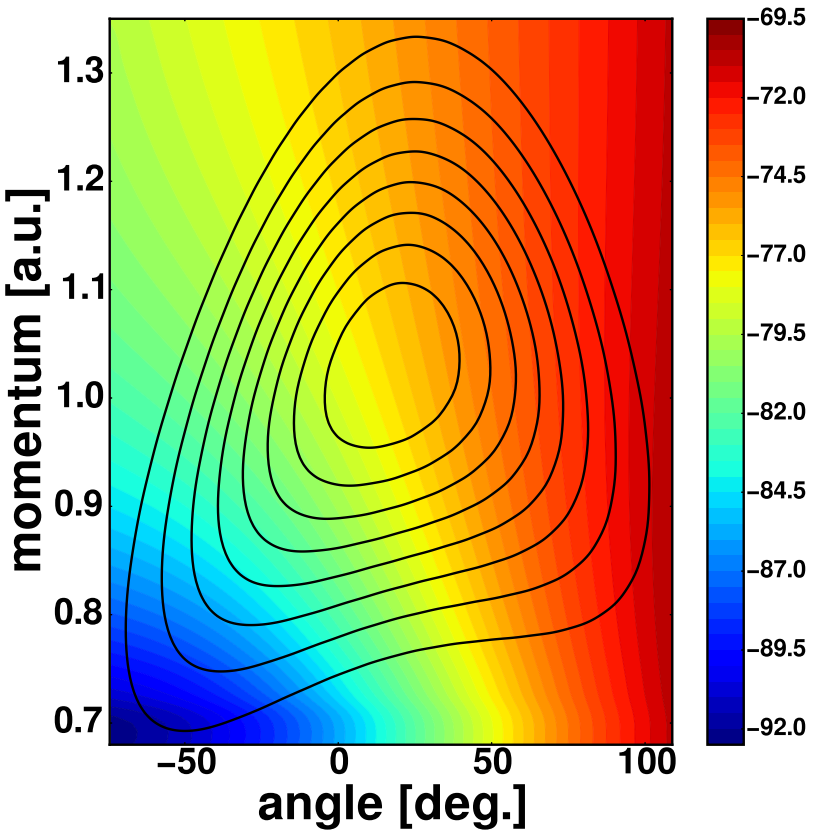

Figure 4.6: Dependence of ionisation delays τ_{SI} on the electron momentum at the detector, for Hydrogen atom. The inner-most contour in the electron spectrum corresponds to 0.9 level, other contours are shown in steps of 0.1. The color bar shows τ_{SI} in attoseconds. The pulse had a vector-potential $\mathbf{A}_L(t) = -(\mathcal{E}_0/\omega)\cos^4(\omega t/4)(\cos(\omega t)\,\hat{\mathbf{x}} + \sin(\omega t)\,\hat{\mathbf{y}})$ with $\mathcal{E}_0 = 0.05$ a.u. and $\omega = 0.0465$ a.u. Results are obtained using the ARM theory.

electron spectra produced in nearly circular, few-femtosecond IR pulses. Such pulses send electrons released at different instants of time in different directions, providing the link between the direction of electron velocity at the detector and the time of its release. Nearly single-cycle pulse creates preferred direction of electron escape, from which the ionisation delay can be reconstructed [44,57,270]. The angle $\phi_{\max}$ at which the majority of electrons are detected, relative to the detection angle expected in the absence of the core potential, is called the off-set angle. We now show that $\phi_{\max}$ can measure the ionisation delay τ_{SI} derived above, provided that effects leading to transient population trapping of released electrons and "negative" ionisation times [270] are negligible. In particular, such regime can be achieved in the long wave-length limit (but is not limited to it).

To this end, we consider the benchmark system–the hydrogen atom, where fully ab-initio simulation of ionisation dynamics in the strong circularly polarised IR field is possible. We solve the time-dependent Scrödinger equation numerically exactly and use results of the numerical experiment to find $\phi_{\max}$. Details of the calculation are described in Appendix 4.A. Red circles in Fig. 4.7 show the ionisation delay $\Delta t = (\phi_{\max} - \delta\theta)/\omega$ extracted from the ab-initio photoelectron spectra, where ω is the laser frequency and the small correction $\delta\theta$ to the off-set angle ϕ_{max} is introduced by the rapidly changing pulse envelope of the nearly single-cycle laser pulse we have used [270]. The blue curve with squares, which shows τ_{SI} Eq. (4.6), lies on top of the ab-initio results. To calculate τ_{SI} analytically, we have used the ARM theory [270].

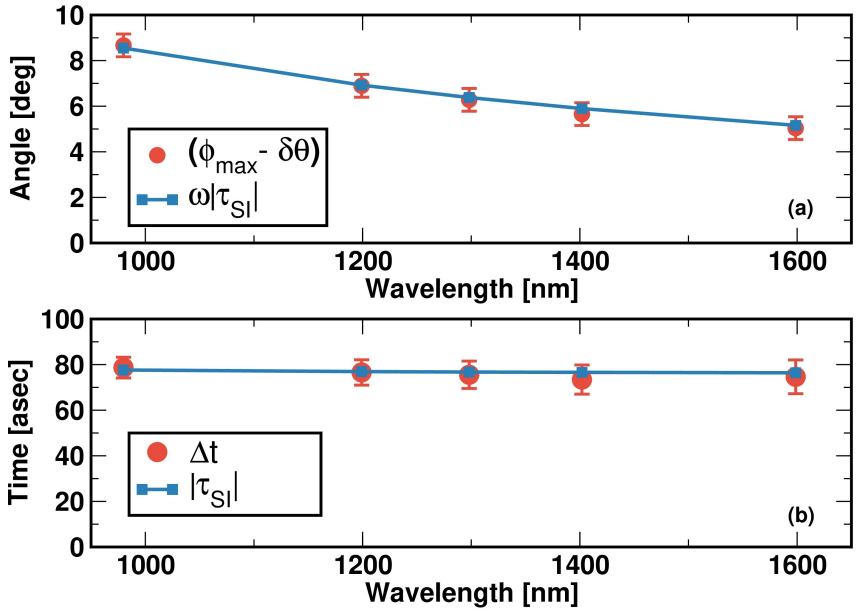

Figure 4.7: Attoclock measurements of strong-field ionisation delay. (a) Red circles show numerically calculated envelope-free offset angle $\phi_{max} - \delta\theta$. The small correction $\delta\theta$ to the off-set angle ϕ_{max} is introduced by the rapidly changing pulse envelope of the nearly single-cycle laser pulse [270] and is subtracted from ϕ_{max} to present envelope-free results for the offset angle. The blue squares connected by the blue line show $\omega|\tau_{SI}|$, the offset angle corresponding to time-delay $|\tau_{SI}|$, ω is the laser frequency. (b) Red circles show the ionisation delay $\Delta t = (\phi_{max} - \delta\theta)/\omega$ extracted from the ab-initio photoelectron spectra. The blue squares connected by the blue line show τ_{SI}. All calculations were done for a hydrogen atom and the circular field intensity $1.75 \times 10^{14}\mathrm{W/cm}^2$.

We stress that the definition of τ_{SI} is not restricted to the long-wavelengths limit shown in Fig. 4.7. It is only the ability of the attoclock set-up to measure exclusively this time delay, without additional contributions associated with transient population trapping in Rydberg states leading to negative ionisation times [270], that has restricted our consideration to the wavelength regime shown in Fig. 4.7. Nevertheless, it is important to demonstrate at least one example, where the time delay τ_{SI} derived from the idea of the spin-orbit Larmor clock can be experimentally or numerically detected.

4.6 Strong-field ionisation delay and tunnelling delay

Strong-field ionisation is often viewed as tunnelling through the barrier created by the binding potential and the laser electric field. While our analysis has never relied on the tunnelling picture, our definition is consistent with the Larmor time $-\partial\phi/\partial V$ for tunnelling through a static barrier of height V [279, 280], equal to I_p in our case (see Figs. 4.8a and 4.8b). However, Figs. 4.8a and 4.8b emphasise the difference in the two processes, which is in the boundary or initial conditions for the tunnelling dynamics. In Fig. 4.8a, the electron current is incident on the barrier and it can lead to the appearance of tunnelling delays, i.e. phase and time delays accumulated during the motion under the barrier. In Fig. 4.8b the tunnelling starts from the real-valued wave-function of the bound state. It is a plausible assumption that in this case and

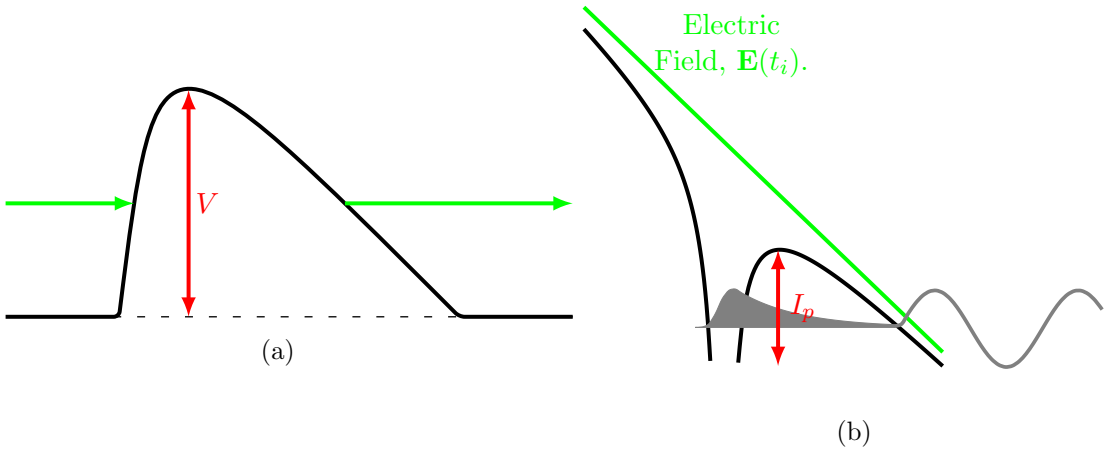

Figure 4.8: Cartoon illustrating the analogy and the difference between (a) the standard barrier penetration problem, and (b) optical tunnelling through the barrier created by the laser field and the core potential in strong-field ionisation.

for the low-frequency laser field, the polarized bound state carries negligible current incident on the barrier, and that tunnelling would occur from the tail of the initial wave-function already present under the barrier. Since the initial wave-function is real-valued in the barrier region, the phase in Eq. (4.3) may get no contribution from the tunnelling region, leading to no delay associated with the under-barrier part of the electron motion. Indeed, the analytical calculation of the phase in Eq. (4.3) yields no contribution from the under-barrier region, at least in the regime of Fig. 4.7. As it follows from excellent agreement between analytical and numerical results in Fig. 4.7(a,b), the analytical calculation of the phase is accurate, and optical tunnelling is not associated with time delay. The delay τ_{SI} is only due to electron interaction with long-range core (Coulomb) potential and is explicitly accumulated after the exit from the barrier.

4.7 Conclusions

We have illustrated the concept and the meaning of time delays in strong field ionisation. In one electron systems, these delays are related to electron interaction with the nucleus. In the tunnelling limit, comparison of numerical and analytical results unambiguously demonstrates the absence of tunnelling delays. Non-equilibrium charge dynamics excited in a many electron atom or a molecule by the laser field and the electron-electron correlations [148, 291] could lead to additional phase $\delta\phi$ [129] and additional delays $\delta\tau_{SI} = -d\delta\phi/dI_p$ contributing to τ_{SI}. Our work shows why and how ionisation delays provide a window into such dynamics in complex systems.

Production of a coherent superposition of many ionic states and hence of coherent hole dynamics is the key aspect of interaction with ultra-short light pulses. Any pump-probe experiment resolving these dynamics aims to find phases between the coherently populated states. As a result of electron-core correlations, not all phases are mapped into time: the formation of the hole wavepacket is characterised not only by the overall time-delays, but also by additional phases accumulated during the ionisation process due to the different core potentials for the different final states of the ion.

What do these phases mean? Given that the electron wavepackets correlated to different core states overlap at the detector, the hole presents a coherent wavepacket characterised by the relative phases of its different spectral components. Analysis of spectral phase is common in characterisation of ultrashort pulses in optics. Linear spectral phase records the arrival time, while non-linear phase is associated with pulse dispersion. Such dispersion is the closest analogue of the phase shifts related to electron-core correlations.

4.A Ab-initio calculations

The numerical procedure and the code are described in detail in [151,270]. The method has been monitored for convergence by changing the maximum angular momentum up to $L_{\max} = 300$, the radial grid size was increased up to $r_{\max} = 2500$ a.u., and by varying the step size of the radial grid δr down to 0.05 a.u. In the presented calculations, the step size of the radial grid was $\delta r = 0.15$ a.u., the time-step was $\delta t = 0.04$ a.u., the box size was 1500 a.u., and $L_{\max} = 150$.

For Hydrogen atom, the spectrum was obtained by projection on the exact field-free continuum states of the H-atom after the end of the laser pulse. The photoelectron spectra include the volume element $\propto p^2$, both in numerical and analytical calculations. The volume element shifts the position of the peak of the distribution and thus affects the off-set angle, however, in the exact same way for numerical and analytical spectra. In these both numerical and analytical calculations we define the laser field $\mathbf{F}_L(t) = -\partial \mathbf{A}_L(t)/\partial t$ via the vector-potential $\mathbf{A}_L(t)$:

$$\mathbf{A}_L(t) = -A_0 f(t)(\cos(\omega t)\,\hat{\mathbf{x}} + \sin(\omega t)\,\hat{\mathbf{y}}), \tag{4.10}$$

where $f(t)$ is the pulse envelope and ω is the carrier frequency,

$$f(t) = \cos^4(\omega t/4). \tag{4.11}$$

For Kr atom, the calculations have been performed using the effective one-electron model potential

$$U_{\mathrm{Kr}}(r) = \frac{1 + (36-1)\exp(-\eta\, r)}{r} + U_0, \tag{4.12}$$

based on the DFT potential used by D. Bauer and co-workers [51]. We follow the recipe described in [151], using the additional tuning potential U_0 which is added only at the first radial grid point $r_1 = 0.5$ (the radial grid step was $\Delta r = 0.05$ a.u.) and is equal to zero everywhere else. The parameter $\eta = 2.64343586965$ a.u. has been adjusted to yield the correct ionisation potential of Kr for the lowest $J = 3/2$ ionic state, with additional fine-tuning achieved by setting $U_0 = 0.0249$a.u., giving $I_p = -0.5145022731$ a.u. For the $J = 1/2$ core state the tuning potential was adjusted to $U_0 = 22.7629$ a.u., yielding $I_p = -0.5389895221$ a.u.

The photoelectron spectrum was calculated by propagating the wavefunction for sufficiently long time after the end of the laser pulse (typically 2 cycles, the convergence has been monitored up to 10 cycles), then applying a spatial mask to filter out the central part of the wavepacket within 100 Bohr from the origin, and performing the Fourier transform of the remaining part of the wavepacket. We have independently validated this procedure using the Hydrogen atom, where it has been calibrated against the projection of the wavefunction on the exact scattering continuum states for Hydrogen. The mask radius was chosen based on this calibration in Hydrogen.

4.B Calculation of the phase accumulated due to interactions in ionisation channels

4.B.1 Definition of the strong-field ionisation phase accumulated due to interactions in ionisation channels

To evaluate the relative phase between the two ionisation channels in Kr, we use the R-matrix based method (ARM) [46,148] generalised for the case of circularly polarised fields [47,268,270].

The ARM method allows one to obtain an analytical expression for the total phase accumulated in each ionisation channel:

$$\phi_J(\mathbf{p}, t_s(\mathbf{p}, I_p)) = \int_{t_s - i\kappa^{-2}}^{T} dt\, U_J\left(\int_{t_s}^{t} d\zeta\, \mathbf{v}(\zeta)\right), \tag{4.13}$$

where $U_J(\mathbf{r})$ is the potential defining the interaction, $\kappa = \sqrt{2I_p}$, I_p is the ionisation potential, $\mathbf{v}(t) = \mathbf{p} + \mathbf{A}(t)$, $\mathbf{A}(t)$ is vector-potential of the laser field, $T \to \infty$ is the observation time and $\mathbf{p}$ is the electron final momentum at the observation time.

The time $t_s(\mathbf{p}, I_p)$ (see [268,270]) is the complex-valued solution of the saddle point equations for the ionisation in circularly polarised field:

$$\frac{\partial S_{\mathrm{V}}(T, \mathbf{p}, t_s)}{\partial t_s} = I_p, \tag{4.14}$$

where $S_V(T, \mathbf{p})$ is the Volkov phase accumulated by the electron in the laser field only:

$$S_V(T, \mathbf{p}, t_s) = \frac{1}{2}\int_{t_s}^{T} dt\, [\mathbf{p} + \mathbf{A}(t)]^2. \tag{4.15}$$

The coordinate of exit presented in Fig. 4.5(c) of the main text is:

$$\mathbf{r}_0 = \int_{t_s}^{\mathrm{Re}[t_s]} d\zeta\, \mathbf{v}(\zeta). \tag{4.16}$$

Since $t_s(\mathbf{p}, I_p)$ depends on I_p, the phase $\phi_J(\mathbf{p}, t_s(\mathbf{p}, I_p))$ also depends on I_p. The phase difference in the two channels is accumulated due to the different I_p's: the difference in ionisation potentials leads to slightly different t_s and thus slightly different trajectories in the two channels. These trajectories are the arguments of U_J in Eq. (4.13). The common part of the phase is accumulated due to the Coulomb potential. The channel-specific part is accumulated due to the channel-specific core potential discussed in Appendix 4.D. The phase accumulated due to spin-orbit interaction in the ionisation channel is negligible and is estimated below.

4.B.2 The phase accumulated due to spin-orbit interaction in ionisation channel

We estimate the relative phase between the two ionisation channels corresponding to spin-up and spin-down ionisation pathways, with orbital momentum ℓ and two values of electron total momentum: $j = \ell + 1/2$, and $j' = \ell - 1/2$. We use the spin-orbit interaction potential:

$$V_{SO}(r) = -\frac{j(j+1) - \ell(\ell+1) - s(s+1)}{4c^2 r^3}, \tag{4.17}$$

where $c = 1/\alpha \approx 137$, in atomic units, $s = 1/2$ is electron spin (α being the fine-structure constant). The phase difference ξ_{SO} is expressed via the difference between the potentials corresponding to j and j':

$$\Delta V_{SO}(r) = -\frac{\ell + 1/2}{2c^2 r^3}, \tag{4.18}$$

We now calculate the phase difference using Eq. (4.13) connecting the phase to the potential. Substituting the electron trajectory in the tunnelling limit $r = r_0 + Ft^2/2$, where $r_0 = I_p/F$, F is the field strength, we obtain the following integral:

$$\xi_{SO} = -\frac{(\ell + 1/2)}{2c^2 r_0^3}\int_0^{\infty} \frac{dt}{(1 + \frac{Ft^2}{2r_0^2})^3}, \tag{4.19}$$

where l, the electron angular momentum along the trajectory, remains constant in the pure tunnelling limit. Evaluating the integral:

$$\int_0^{\infty} \frac{dt}{(1 + \frac{Ft^2}{2r_0^2})^3} = \frac{\sqrt{2r_0 F}}{F}\int_0^{\infty} \frac{dx}{(1+x^2)^3} = 0.59\frac{\sqrt{2I_p}}{F}, \tag{4.20}$$

we obtain:

$$\xi_{SO} = -\frac{(\ell+1/2)}{2c^2 r_0^3} 0.59 \frac{\sqrt{2I_p}}{F} = -0.42 \frac{(\ell+1/2)}{c^2} \frac{F^2}{I_p^{5/2}}. \tag{4.21}$$

Note that in general the angular momentum of the electron l is changing with time and should be included in the integrand. However, the integral is accumulated in the vicinity of the core and therefore for estimates in the tunnelling limit we can use the value of angular momentum l_0 when the electron exits the tunnelling barrier. In the tunnelling limit $\ell_0 \to 0$, since when the electron exits the tunnelling barrier its velocity is parallel to electron displacement. Thus, for typical field strength $F = 0.06$ a.u. and $I_p = 0.5$ a.u. the phase difference $\xi_{SO} \sim 0.21F^2/(c^2 I_p^{5/2}) \sim 2.3 \times 10^{-7}$ rad. and is completely negligible.

4.C Rotation of the core spin in strong field ionisation: Gedanken experiment in Kr atom

Consider Kr atom in its ground state. There is no spin-orbit interaction in the ground state of the neutral Kr: the P-shell is filled by 6 p-electrons, with equal number of p^- and p^+ electrons 'rotating' in opposite directions. Ionisation by strong, circularly polarised IR laser field breaks the balance between p^- and p^+ electrons [142] and starts the spin-orbit Larmor clock. Intense right-circularly polarised IR pulse prefers to remove the p^- electron [142,290], i.e. $m_\ell = -1$. Let us set the initial spin state to be $|s_{\rm in}\rangle = \alpha|-1/2\rangle + e^{i\phi}\beta|1/2\rangle$, where α, β are real numbers and the phase ϕ characterises the initial orientation of the spin. Once the p^- electron is removed, the quantum state of the core acquires uncompensated angular momentum $M_L = 1$ and uncompensated spin. The spin state of the core is $|s_{\rm in}\rangle = \alpha|1/2\rangle + e^{i\phi}\beta|-1/2\rangle$, since the spins and the angular momenta of the core and the electron are antiparallel at the moment of separation. As this state is not an eigenstate of the Hamiltonian, the core spin starts to precess.

We shall now calculate the angle of rotation of the core spin. The final spin state for the fixed orientation of the final orbital momentum $M_L = 1$ is $|s_{\rm fin}\rangle = a_\downarrow\alpha|-1/2\rangle + a_\uparrow e^{i\phi}\beta|1/2\rangle$, where the $a_\uparrow$ and $a_\downarrow$ are the strong field ionisation amplitudes for the spin-up and spin-down ionisation pathways. We first specify our notations and introduce the ionisation amplitude $T^-(I_p)$ corresponding to the removal of p^- electron, where I_p is the ionisation potential, in the absence of the spin-orbit splitting of the core state. The amplitudes T_3 and T_1, which include the spin-orbit splitting, are defined as follows: $T_3^- = T^-(I_p)$ and $T_1^- = T^-(I_p + \Delta E_{SO})$, and they correspond to the removal of the p^- electron [142,273].

Full ionisation amplitudes into the ionic eigenstates $P_{3/2}$ and $P_{1/2}$ include the projections $\langle LM_L, SM_S|JM_J\rangle$ given by the Clebsch-Gordan coefficients, $C^{JM_J}_{LM_L,\frac{1}{2}M_S}$, with $M_L = 1$. To find the final core spin state for $M_L = 1$ at a time t, we will need the projections $\langle LM_L, SM_S|JM_J\rangle = C^{JM_J}_{LM_L,\frac{1}{2}M_S}$, since the Clebsch-Gordon coefficients are real. Taking these projections into account, we find that the amplitude of ionisation into the state $J = 3/2$, $M_J = 3/2$ is T_3^-. The amplitude of ionisation into the state $J = 3/2$, $M_J = 1/2$ is $\frac{1}{\sqrt{3}}T_3^-$, the amplitude of ionisation into the state $J = 1/2$, $M_J = 1/2$ is $\sqrt{\frac{2}{3}}T_3^-$. Now, we project these states back onto the $|LM_L, SM_S\rangle$ basis to find $a_\uparrow$ and $a_\downarrow$. This yields the amplitude to find the core angular momentum $M_L = 1$ and $M_S = 1/2$ at time t, $a_\uparrow = T_3^- e^{-iE_{3/2}t}$, while the amplitude to find the core angular momentum $M_L = 1$ and $M_S = -1/2$ at the time t is $a_\downarrow = \frac{1}{3}\left(2T_1^- e^{-iE_{1/2}t} + T_3^- e^{-iE_{3/2}t}\right)$. Here $E_{3/2}$ is the energy of the ground state, $E_{1/2} = E_{3/2} + \Delta E_{SO}$.

To establish the rotation angle we need to find $\arg[a_\uparrow a_\downarrow^*]$:

$$a_\uparrow a_\downarrow^* = \frac{1}{3}\left[|T_3^-|^2 + 2|T_1^-||T_3^-|\left\{\cos(\phi_3^T - \phi_1^T + \Delta E_{SO}t) + i\sin(\phi_3^T - \phi_1^T + \Delta E_{SO}t)\right\}\right], \tag{4.22}$$

$$\arg\left[T_3\left(\frac{1}{3}(T_3^{-*}+2T_1^{-*})\right)\right] = \arctan\frac{2|T_1^-||T_3^-|\sin(\phi_3^T-\phi_1^T+\Delta E_{SO}t)}{|T_3^-|^2+2|T_1^-||T_3^-|(\cos(\phi_3^T-\phi_1^T+\Delta E_{SO}t)}. \tag{4.23}$$

Equation (4.23) yields:

$$\tan\Delta\phi_{SO} = \frac{\sin(\Delta E_{SO}t-\Delta\phi_{13})}{0.5|T_3^-|/|T_1^-|+\cos(\Delta E_{SO}t-\Delta\phi_{13})}, \tag{4.24}$$

where the phase difference $\Delta\phi_{13}$ is defined as $\Delta\phi_{13}=\phi_1^T-\phi_3^T$.

4.D Core potentials in two different ionisation channels

To illustrate the effect of electron-hole correlations on definition and measurement of time, we consider the contribution of the channel specific core potential $V_{LJM_J}(\mathbf{r})$, that arises from the Coulomb interaction between the electron and the core. This potential has the following form:

$$\begin{aligned}V_{LJM_J}(\mathbf{r}) &= \int d\mathbf{r}'\frac{\rho_{trion}(\mathbf{r}')}{\|\mathbf{r}-\mathbf{r}'\|} = \int d\mathbf{r}'\frac{1}{\|\mathbf{r}-\mathbf{r}'\|}\langle\epsilon JM_J|\mathbf{r}'\rangle\langle\mathbf{r}'|\epsilon JM_J\rangle = \\ &\sum_{M_L,M_L',M_S,M_S'} C^{JM_J}_{LM_L',\frac{1}{2}M_S'}C^{JM_J}_{LM_L,\frac{1}{2}M_S}\left\langle\frac{1}{2}M_S'\middle|\frac{1}{2}M_S\right\rangle\int d\Omega\, Y^*_{LM_L'}(\theta',\phi')Y_{LM_L}(\theta',\phi')\times \\ &\sum_{L_1=0}^{\infty}P_{L_1}(\cos\beta)\left[\int_0^r dr'r'^2\frac{r'^{L_1}}{r^{L_1+1}}\left|R(\epsilon JM_J;r')\right|^2+\int_r^{\infty}dr'r'^2\frac{r^{L_1}}{r'^{L_1+1}}\left|R(\epsilon JM_J;r')\right|^2\right],\end{aligned} \tag{4.25}$$

where, $L=J\pm1/2$, is the orbital angular momentum fixed for a given spin-orbital, β is the solid angle between the vectors $\mathbf{r}$ and $\mathbf{r}'$, and can be written as $\cos\beta=\hat{\mathbf{r}}\cdot\hat{\mathbf{r}}'$, ϵ represents the effective principle quantum number corresponding to the energy of the spin-orbital under consideration, and $R(\epsilon JM_J;r)$ is the radial part of the wavefunction associated to the said spin-orbital.

Including all terms together, we have:

$$\begin{aligned}V_{LJM_J}(\mathbf{r}) = \sum_{\substack{M_L,M_L'\\M_S}} C^{JM_J}_{LM_L,\frac{1}{2}M_S}C^{JM_J}_{LM_L',\frac{1}{2}M_S}\sum_{L_1=0}^{\infty}\frac{4\pi}{2L_1+1}\sum_{M_{L_1}=-L_1}^{L_1}Y^*_{L_1M_{L_1}}(\theta,\phi)\langle R_{L_1}\rangle\times \\ \int d\Omega\, Y^*_{LM_L'}(\theta',\phi')Y_{LM_L}(\theta',\phi')Y_{L_1M_{L_1}}(\theta',\phi').\end{aligned} \tag{4.26}$$

Here ϕ is the angle in polarisation plane, θ is the angle calculated from the laser propagation direction, and $\langle R_{L_1}\rangle$ is the expectation value of the radial component, as calculated using the Roothaan-Hartree-Fock (RHF) orbitals, defined as:

$$R_L(r) = \sum_{p,q}c_{i_p}c_{i_q}\left[\frac{1}{r^{L+1}}\gamma((\kappa_{i_p}+\kappa_{i_q})r)+r^L\Gamma((\kappa_{i_p}+\kappa_{i_q})r)\right], \tag{4.27}$$

where, c_{i_p}, c_{i_q} are the coefficients for the Slater-Type Orbitals (STO) and i_p, i_q the corresponding indices defining the nodes in the wavefunction under consideration, used for the RHF calculations [292], and γ is the lower, whereas Γ is the upper incomplete-gamma function. Taking into account Wigner $3j$-coefficients from the integral:

$$\begin{aligned}\int d\Omega\, Y^*_{LM_L'}(\theta',\phi')Y_{LM_L}(\theta',\phi')Y_{L_1M_{L_1}}(\cos\theta') = (-1)^{M_L'}(2L+1)\sqrt{\frac{2L_1+1}{4\pi}}\times \\ \begin{pmatrix}L & L_1 & L\\ M_L & M_{L_1} & -M_L'\end{pmatrix}\begin{pmatrix}L & L_1 & L\\ 0 & 0 & 0\end{pmatrix},\end{aligned} \tag{4.28}$$

we obtain the selection rules. For L_1, the selection rules are: (a) $2L+L_1$ is even (so only L_1 even are allowed in the summation over L_1) and (b) the triangle inequality $|L-L_1| \leq L \leq L+L_1$ which gives $0 \leq L_1 \leq 2L$. For all other cases the integral is zero, and $M'_L = M_L + M_{L_1}$.

Taking $L_1 = 2L'$, the expression for V_{LJM_J} is:

$$V_{LJM_J}(\mathbf{r}) = (2L+1) \sum_{M_L,M_S} \sum_{L'=0}^{L} \sum_{M_{2L'}=-2L'}^{2L'} (-1)^{M_L+M_{2L'}} C^{JM_J}_{LM_L+M_{2L'},\frac{1}{2}M_S} C^{JM_J}_{LM_L,\frac{1}{2}M_S} \times \sqrt{\frac{4\pi}{4L'+1}} \begin{pmatrix} L & 2L' & L \\ M_L & M_{2L'} & -M'_L \end{pmatrix} \begin{pmatrix} L & 2L' & L \\ 0 & 0 & 0 \end{pmatrix} Y^*_{2L'M_{2L'}}(\theta,\phi) \langle R_{2L'} \rangle. \quad (4.29)$$

From the Clebsch-Gordan coefficients, we have two conditions on M_L and M_S for a given M_J:

$$M_L + M_{2L'} + M_S = M_J, \quad (4.30)$$

$$M_L + M_S = M_J, \quad (4.31)$$

which can only be possible if $M_{2L'} = 0$. The final expression is:

$$V_{LJM_J}(\mathbf{r}) = (2L+1) \sum_{M_L,M_S} \sum_{L'=0}^{L} (-1)^{M_L} \left| C^{JM_J}_{LM_L,\frac{1}{2}M_S} \right|^2 \sqrt{\frac{4\pi}{4L'+1}} \begin{pmatrix} L & 2L' & L \\ M_L & 0 & -M_L \end{pmatrix} \times \begin{pmatrix} L & 2L' & L \\ 0 & 0 & 0 \end{pmatrix} Y^*_{2L'0}(\theta,\phi) \langle R_{2L'} \rangle \quad (4.32)$$

Using the definition of $Y_{2L'0}$, we can simplify further to give:

$$V_{LJM_J}(\mathbf{r}) = (2L+1) \sum_{M_L,M_S} \sum_{L'=0}^{L} (-1)^{M_L} \left| C^{JM_J}_{LM_L,\frac{1}{2}M_S} \right|^2 \begin{pmatrix} L & 2L' & L \\ M_L & 0 & -M_L \end{pmatrix} \times \begin{pmatrix} L & 2L' & L \\ 0 & 0 & 0 \end{pmatrix} P_{2L'}(\cos\theta) \langle R_{2L'} \rangle. \quad (4.33)$$

Note that $L' = 0$ corresponds to Coulomb potential, common in both channels. Consider the case when ionisation liberates the p^+ electron ($L = 1$) populating the core states $J = 3/2, 1/2$ and $M_J = -1/2$ (the result for p^- is the same). For the calculation of the difference between two core potentials we use the same trajectory with averaged I_p. The corrections associated with the difference in the trajectories are of higher order and are not included here.

The difference in core potentials for this trajectory is:

$$V_{1,3/2,1/2}(\mathbf{r}) - V_{1,1/2,1/2}(\mathbf{r}) = 3 \sum_{L'=0}^{1} \begin{pmatrix} 1 & 2L' & 1 \\ 0 & 0 & 0 \end{pmatrix} P_{2L'}(\cos\theta) \langle R_{2L'} \rangle \times \left[\sum_{M_L,M_S} (-1)^{M_L} \left| C^{3/2\,1/2}_{1M_L,\frac{1}{2}M_S} \right|^2 \begin{pmatrix} 1 & 2L' & 1 \\ M_L & 0 & -M_L \end{pmatrix} - \sum_{M_L,M_S} (-1)^{M_L} \left| C^{1/2\,1/2}_{1M_L,\frac{1}{2}M_S} \right|^2 \begin{pmatrix} 1 & 2L' & 1 \\ M_L & 0 & -M_L \end{pmatrix} \right]. \quad (4.34)$$

As expected for the common Coulomb potential, the difference for $L' = 0$ is zero:

$$\sum_{M_L,M_S} (-1)^{M_L} \begin{pmatrix} 1 & 0 & 1 \\ M_L & 0 & -M_L \end{pmatrix} \left[\left| C^{3/2\,1/2}_{1M_L,\frac{1}{2}M_S} \right|^2 - \left| C^{1/2\,1/2}_{1M_L,\frac{1}{2}M_S} \right|^2 \right] = \begin{pmatrix} 1 & 0 & 1 \\ 0 & 0 & 0 \end{pmatrix} \left[\frac{1}{3} \right] + (-1) \begin{pmatrix} 1 & 0 & 1 \\ 1 & 0 & -1 \end{pmatrix} \left[-\frac{1}{3} \right] = -\sqrt{\frac{1}{3}}\frac{1}{3} + \sqrt{\frac{1}{3}}\frac{1}{3} = 0. \quad (4.35)$$

The only term left is the one corresponding to $L'=1$, which gives

$$V_{1,3/2,1/2}(\mathbf{r})-V_{1,1/2,1/2}(\mathbf{r})=3\begin{pmatrix}1&2&1\\0&0&0\end{pmatrix}P_2(\cos\theta)\langle R_2\rangle\times$$
$$\sum_{M_L,M_S}(-1)^{M_L}\begin{pmatrix}1&2&1\\M_L&0&-M_L\end{pmatrix}\left[\left|C^{3/2\,1/2}_{1M_L,\frac{1}{2}M_S}\right|^2-\left|C^{1/2\,1/2}_{1M_L,\frac{1}{2}M_S}\right|^2\right]=$$
$$3\sqrt{\frac{2}{15}}P_2(\cos\theta)\langle R_2\rangle\left[\sqrt{\frac{2}{15}}\frac{1}{3}+(-1)\sqrt{\frac{1}{30}}\left(-\frac{1}{3}\right)\right]=\frac{1}{5}P_2(\cos\theta)\langle R_2\rangle=-\frac{\langle R_2\rangle}{10},\quad(4.36)$$

since for $\theta=\pi/2$, $P_2=-1/2$. The expression for $\langle R_2\rangle$ is:

$$R_2=\int_0^r dr'r'^2\frac{r'^2}{r^3}|R(\epsilon L;r')|^2+\int_r^\infty dr'r'^2\frac{r^2}{r'^3}|R(\epsilon L;r')|^2=\frac{1}{r^3}\langle r'^4\rangle_0^r+r^2\left\langle\frac{1}{r'}\right\rangle_r^\infty,\quad(4.37)$$

which can be found from the incomplete gamma functions. The difference between the two core potentials is: $V_{1\,3/2\,1/2}(\mathbf{r})-V_{1\,1/2\,1/2}(\mathbf{r})\simeq-4.444/(10r^3)$, since $\langle R_2\rangle=4.444$ a.u. for Kr [293] and the contribution of the second term in Eq. (4.37) vanishes for $r\to\infty$. To calculate the respective relative phase $\Delta\phi^d_{13}$, we use Eq. (4.13) and substitute the difference in short range core potentials given above.

4.E Pump-probe signal: the details of derivation

The goal of this section is to derive population in the final S-state of the Kr ion at the end of the pump-probe experiment, see Eq. (4.4) of the main text.

For a laboratory experiment, we need two requirements. First, we want to turn on and turn off the clock on demand, i.e. we need to stop the rotation of the core spin on demand. Second, we would like to measure the phase $\Delta\phi_{13}$ directly. The second condition is satisfied automatically, since the initial superposition of spin up and spin down states is incoherent and therefore the single arm of the interferometer (in Fig. 4.1b) will not interfere with the double arm in a real experiment. Thus, the laboratory experiment will only record the interference in the double arm, and the single arm will give background. To start the clock, we apply a nearly single-cycle right circularly polarised IR pulse to create a p-hole. To stop the clock, we apply a left circularly polarised laser field to induce a transition from the s-shell of the Kr atom, filling the hole in the p-shell and leaving the hole in s-orbital. There is no angular momentum in the s-hole, and there is no SO splitting. Thus, the left-circular probe stops the clock that was started by the right circular pump.

For a fixed final state of the continuum electron, characterised by momentum $\mathbf{p}$ at the detector, the population $S=\left|\sigma_{1/2,M_L=0}\right|^2+\left|\sigma_{-1/2,M_L=0}\right|^2$ in the final s-sate can be obtained using the following equation:

$$\sigma_{M_S,M_L=0}=\int dt\left\langle\Psi_{\rm fin}(t)\middle|\hat{d}\middle|\Psi_{\rm ion}(t)\right\rangle E_{\rm asec}(t).\quad(4.38)$$

where $\Psi_{\rm ion}=\sum_{J,M_J}a_{JM_J}\psi_{JM_J}e^{-iE_Jt}$ is the coherent superposition of the two core states, created after ionisation, for a given final momentum of the electron at the detector. Here a_{JM_J} is the complex amplitude of ionisation into core state $|J,M_J\rangle$. The wavefunction $\Psi_{\rm fin}(t)=\psi_{\rm fin}(\mathbf{r})e^{-iE_St}$ represents the final S-state of the core.

It is convenient to express ψ_{JM_J} and $\psi_{\rm fin}(\mathbf{r})$ as a product of angular and radial wave-functions: $\psi_{JM_J}=|\psi_J(r)\rangle|JM_J\rangle$, $\psi_{\rm fin}(\mathbf{r})=\psi_S(r)|LM_L,SM_S\rangle$. Taking into account that $L=0$, $M_L=0$, $S=1/2$ in the final state, we obtain: $\psi_{\rm fin}(\mathbf{r})=\psi_S(r)|0\,0,1/2\,M_S\rangle$.

The dipole operator can be factorised into the radial and angular parts, $\widehat{d} = \widehat{r}\widehat{\Xi}_\xi$, where $\xi = 1$ corresponds to the right polarised pulse, $\xi = -1$ corresponds to the left polarised pulse: $\widehat{\Xi}_\xi = d_x + i\xi d_y$. Evaluating the integral over t, we rewrite the equation in equivalent form:

$$\sigma_{M_S,M_L=0} = \sum_{J,M_J,M_L,M'_S} F_\omega(E_S - E_J) a_{JM_J} d_J \times \left\langle 0\,0, 1/2\,M_S \middle| \widehat{\Theta}_\xi \middle| 1\,M_L, 1/2\,M'_S \right\rangle \langle 1\,M_L, 1/2\,M'_S | JM_J \rangle. \quad (4.39)$$

Here, $F_\omega(E_S - E_J)$ is the Fourier image of the probe pulse $F_{\text{asec}}(t)$ taken at the transition frequency. The real-valued radial matrix element $d_J = \langle \psi_S(r)|\widehat{r}|\psi_J(r)\rangle$ describes the transition from the core state $|JM_J\rangle$ to the final S-sate. For the left circularly polarised field, the angular part of the dipole operator $\langle 0\,0, 1/2\,M_S|\widehat{\Theta}_\xi|1\,M_L, 1/2\,M_S\rangle = \delta_{M_S,M'_S} I_\xi(M_L)$ is $I_{-1}(M_L) = \sqrt{N}\sqrt{M_L^2 + M_L}$, $N = 1/3\pi$. Thus, we obtain

$$\sigma_{M_S,M_L=0} = \sum_{J,M_J,M_L} I_\xi d_J F_\omega(E_S - E_J) \langle 1\,M_L, 1/2\,M_S | JM_J \rangle a_{JM_J}. \quad (4.40)$$

The Clebsch-Gordan coefficients $C^{JM_J}_{LM_L,SM_S} = \langle LM_L, 1/2, M_S | JM_J \rangle$ are equal to: $C^{3/2,3/2}_{L=1,1,S=1/2,1/2} = 1$, $C^{3/2,1/2}_{L=1,1,S=1/2,-1/2} = 1/\sqrt{3}$, $C^{1/2,1/2}_{L=1,1,S=1/2,-1/2} = \sqrt{2/3}$. They specify the amount of each M_L component in the core state $|JM_J\rangle$. These components are probed by the delayed circularly polarised attosecond probe pulse.

Left polarised pulse picks up $M_L = 1$ component, right polarised pulse picks-up $M_L = -1$ component, linearly polarised pulse picks up $M_L = 0$. Thus, if right circularly polarised pulse is used as a pump, left circularly polarised probe will probe ionisation of p^- electron, whereas right circularly polarised probe will probe ionisation of p^+ electron. Linearly polarised probe will probe both p^+ and p^- pathways at the same time. For the left-circularly polarised probe we obtain:

$$\left|\sigma_{1/2,0}\right|^2 = \frac{N}{9} d^2_{3/2} \left|T_3^-\right|^2 |F_\omega(\Omega_3)|^2, \quad (4.41)$$

and

$$\left|\sigma_{-1/2,0}\right|^2 = \frac{N}{9} d^2_{3/2} \left|T_3^-\right|^2 |F_\omega(\Omega_3)|^2 + \frac{4N}{9} d^2_{1/2} \left|T_1^-\right|^2 |F_\omega(\Omega_1)|^2 + \frac{4N}{9} d_{1/2} d_{3/2} \left|T_1^-\right| |F_\omega(\Omega_1)| \left|T_3^-\right| |F_\omega(\Omega_3)| \cos(\Delta E_{SO}\tau - \Delta\phi_{13}), \quad (4.42)$$

where T_D is the time of arrival of the attosecond pulse, $\Omega_3 = E_S - E_{3/2}$, $\Omega_1 = E_S - E_{1/2}$, E_S is the energy of the final S-state. Transform limited attosecond pulse is assumed for this calculation. The population in S-state is $S = \left|\sigma_{1/2,M_L=0}\right|^2 + \left|\sigma_{-1/2,M_L=0}\right|^2$, and can be measured by transient absorption of the XUV probe.

Chapter 5

Spin Polarisation in Coulomb-Laser coupling

5.1 Introduction

Since the remarkable proposal of electron spin as an instrinsic property, by Uhlenbeck and Goudsmit [294] with the first analysis of spin-orbit splitting of the stationary states [294, 295], to the first attempts for direct experimental observation [296] and subsequent prediction and confirmation of Mott scattering [297, 298], the first theoretical proposition for production of polarised electrons from spin-polarised atoms [299], and the invigorated activity provided by studies in high energy physics in late 50's [300], along with extensive study of low-energy electron-atom collisions [301], spin-polarisation of electrons ejected from collisions and ionisation has developed into a rich and thoroughly studied subject [274]. Exciting applications have already been developed. They include, for example, application of spin-polarised electrons for SLAC [302], applications in nuclear physics [303], where high degree of spin polarisation is a highly desirable property for the electron source ($\approx 80\%$), the production of spin polarised electrons in semiconductor heterostructures [304], in surface science and 2D magnetism [305], in high-energy physics to study the structure of nucleons and to probe electroweak interactions. Spin polarised electrons are used to study nuclear resonance transitions [306]. Last but not least, control and sustenance of spin polarisation in quantum dots in strong magnetic fields [307], and in quantum gases [308] is an important research direction.

Electron spin-polarisation due to Spin-Orbit (SO) Interaction during one-photon ionisation was first proposed by Fano [289]. This seminal work has led to experimental and theoretical activity, including in-depth studies in for the multiphoton ionisation regime, both theoretical [309–313] and experimental [314–317].

Interesting question regarding spin-polarisation arises in the strong-field ionisation regime. On the one hand, the intrinsic spin of an electron is a purely quantum mechanical concept. On the other hand, strong field ionisation is very often, and very successfully, described semiclassically. The interplay of these two perspectives, the intrinsically quantum and the semiclassical, can provide a unique perspective into the quantum-classical correspondence on the subatomic scale.

Very recently, in [143], Spin-Orbit effects in strong field tunnelling ionisation were shown to produce spin-polarised photoelectrons. The results presented in [143] were obtained for a monochormatic, nonresonant, intense circularly polarised fields and short-range potentials. These results naturally raise questions on the role of SO effects in ultrashort pulses. Indeed, application of such pulses raises the opportunity for creating ultrashort bursts of spin-polarised electrons. Moreover, such fields offer additional control parameters. For example, one can expect the effect of varying the Carrier-Envelope offset Phase (CEP) on the efficiency of spin-polarisation. Potential opportunities may also arise due to the different response to various, controlled, pulse

shapes.

Finally, the interaction of the liberated electrons with a long-range core potential must be addressed, since, in contrast to the short-range binding potential, in the long-range potentials the ionisation process is not yet completed as soon as the electron emerges from the barrier [47].

In this Chapter, we consider spin polarisation resulting from ionisation by short-pulse, circularly polarised fields, taking into account the effects of long-range core interaction on the liberated electron. For the present case, it is shown that spin polarisation in a long-range core potential, and in a few-cycle, circularly-polarised fields is somewhat more efficient compared to the case of monochromatic fields. Due to the asymmetry instigated by the long-range interaction in the final photoelectron spectrum registered at the detector, the bursts of spin polarised electrons are also emitted in a preferred direction.

We develop the theory within the framework of the Analytical R-Matrix (ARM) [46, 47, 268], and consider the effect of the long-range potential on the velocity components through the additional methods developed in [271]. The photoelectron spectra demonstrate the high sensitivity of the ionisation process to the CEP of the laser field [318]. Deciphering the CEP in extremely short pulses is another avenue of research in the bustling field of ultrafast science [176, 319–326]. When photo-electron spectra are used for this purpose, it is the high-energy electrons that provide a reliable means to measure CEP of the laser field, due to the diminished influence of the long-range core potential. With ARM, we have a rigorous approach to including long-range interactions of the ionising electron.

Section 5.3 gives the theory involved, section 5.4 discusses the results for spin polarisation and section 5.5 finally concludes the results of this Chapter. We begin, however, with the physical picture underlying spin polarisation during strong-field ionisation, following the original discussion in [143].

5.2 Physical mechanism of spin polarisation in strong-field ionisation

Since the spin-orbit interaction is a relativistic effect, one might expect that spin polarisation should be negligible in non-relativistic conditions. However, Fano [289] has shown that, at least for one-photon ionisation, it is not always the case. But the effect predicted by Fano requires that the matrix elements of one-photon ionisation go through a zero, known as the Cooper minimum. When photo-ionisation is suppressed, weak effects of spin-orbit interaction in the continuum can manifest themselves. In one-photo ionisation, near the Cooper minimum, 100 percent spin polarisation can be achieved, but only for selected energy.

However, strong-field ionisation opens a completely new avenue for achieving high degree of spin polarisation, which does not rely on the Cooper minima or spin-orbit interaction in the continuum state. Instead, it takes advantage of spin-orbit interaction in the ionic core. It results from the interplay of the correlation between the electron and the core and the sensitivity of ionisation in circularly polarised fields to the initial electronic orbital, specifically to the projection of its angular momentum on the laser propagation direction (colloquially speaking, the sense of electron rotation relative to the sense of rotation of the ionising field).

Let us assume that the right circularly polarised field propagates in positive z-direction. Consider a noble gas atom such as Krypton, where the outer shell has six p electrons. The total angular momentum of the initial state is equal to zero and hence the spin-orbit interaction is absent. Correlation between the liberated electron and the ionic core dictates that at the instant of ionisation the projection of the total angular momentum of the electron m_j and the core M_J on z-axis satisfy the following relationship: $|m_j| = |M_J|$.

Since the electron is removed, the spin-orbit interaction arises in the ion, leading to the two final ionic states with the total angular momentum $J = 1/2$ and $J = 3/2$. Their energies are split by the spin-orbit interaction by about 0.67 eV.

Consider first ionisation that leaves the ion in the excited state $P^2_{1/2}$. For this state $|M_J| = 1/2$. In the strong-field regime, the circularly polarised field will preferentially remove a counter-rotating electron $m_l = -1$ (for right circularly polarised field) [142]. Therefore, for the electron correlated to this state of the ion $|m_j| = 1/2$ and since it is leaving with $m_l = -1$, the only possibility for the electron spin is to satisfy $m_s = 1/2$. Thus, if we would assume 100% selectivity of ionisation to the sense of rotation of the ionising orbital, we would obtain 100 % spin polarisation provided that the ion is left in the state $P^2_{1/2}$.

Following similar logic one can see that in the case of $P^2_{3/2}$ final state the more likely direction of the electron spin is given by $m_s = -1/2$. However, under the same conditions, spin-polarisation would be less than 100 %, since the total momentum of this final state $J = 3/2$ allows both projections $|m_j| = 3/2$ and $|m_j| = 1/2$ of the electron.

Thus, it is qualitatively clear that spin-polarisation should be observed if the electron spin is measured in correlation with the final ionic state. But since the directions of the electron spin in these two ionisation channels are opposite, it is not clear what the total spin polarisation would be. This is where strength of the spin-orbit interaction becomes crucial, as it determines differences in the ionisation potentials for the two ionisation channels. Strong-field ionisation is very sensitive to the ionisation potential. Hence, ionisation into the lower ionic state $P^2_{3/2}$ is generally preferred, especially for stronger spin-orbit interaction, opening the door to total spin polarisation. We now proceed to the quantitative description of the effect.

5.3 Theory

The ionisation amplitude in the Single Active Electron (SAE) approximation, taking into account long-range potential effects of the core on the liberated electron in a circular field can be written as (see Chapters 2 and 4) and [271]:

$$a_{\mathrm{SAE}}(\mathbf{p}, I_P, T) = (-1)^m C_{\kappa\ell} N_{\ell m} \sqrt{\frac{\kappa}{\left|S^{\mathrm{SFA}}_{tt}(t^c_s)\right|}} e^{-iS^{\mathrm{SFA}}(t^c_s,\mathbf{p}) - iG_C(t^c_s,\mathbf{p},\mathbf{r}_L)} \times P^m_\ell\left(\frac{p^c_z}{v_{\mathbf{p}^c}(t^c_s)}\right) e^{im\phi^c_v(t^c_s)}, \quad (5.1)$$

where, $C_{\kappa\ell}$ is the effective principal quantum number coefficient, $N_{\ell m}$ is the Spherical Harmonic normalisation coefficient, S^{SFA} is the Strong Field Approximation (SFA) action for a free electron in a laser field and G_C is the complex Coulomb phase correction, as introduced in [46,47,267,268]. The terms here are evaluated at the Coulomb corrected saddle point time concordant with [270], and the long-range effects are taken into account in the photoelectron velocity through the method developed in [271].

Due to Spin-Orbit (SO) interaction, the ground state of a singly-charged noble gas ion, say Kr^+, is split into the lower lying $Kr^+\ {}^2P_{3/2}$ and the excited $Kr^+\ {}^2P_{1/2}$. Thus, the ionisation is possible from either channel. The wavefunction of the remaining ion system is then summed over the different final states, weighed by the ionisation amplitude for that channel [143],

$$|\Psi^{m_s}(\mathbf{p}, T)\rangle = \sum_{J,M_J} a^{JM_Jm_s}(\mathbf{p}, T)|^2P_{JM_J}\rangle. \quad (5.2)$$

$|\Psi^{m_s}(\mathbf{p}, T)\rangle$ is the final state of the ion at time T, when the electron is far from the core and ionisation can be assumed to be complete, $|^2P_{JM_J}\rangle$ is the relativistic state of the ion, $a^{JM_Jm_s}(\mathbf{p}, T)$ is the corresponding probability amplitude to end in this state, with the ionising electron having final asymptotic momentum $\mathbf{p}$ and spin m_s. The above result was derived in [143] for short-range potentials and can be extended to long-range potentials easily.

Each of the amplitudes for reaching the relativistic ionic states, $a^{JM_Jm_s}$ can be written in terms of the probability amplitudes for the correspondng spin-orbitals, through the Clebsch-Gordan coefficients [143],

$$a^{JM_Jm_s}(\mathbf{p},T) = C^{J,-M_J}_{1-M_J-m_s,\frac{1}{2}m_s} a^{p_{-M_J-m_s}}_{\mathrm{ARM}}\left(\mathbf{p}, I_P^J, T\right) e^{-iI_P^J T}. \tag{5.3}$$

5.4 Results

5.4.1 Spin polarisation in Long-range potential

The results for the attostreak maps for non-relativistic p-orbitals, discussed in [271], can be used to decipher the attostreak maps for the spin-up and spin-down electrons, summed over all the contributions from different channels. For this we only need the equivalent of expressions derived in [143], for long range potentials with Coulomb correction to saddle point time:

$$\left|a^{(u)}_{\mathrm{ARM}}(\mathbf{p})\right|^2 = \frac{2}{3}\left|a^{p_-}_{ARM}\left(\mathbf{p}, I_P^{1/2}, t_s^c\right)\right|^2 + \frac{1}{3}\left|a^{p_-}_{\mathrm{ARM}}\left(\mathbf{p}, I_P^{3/2}, t_s^c\right)\right|^2 + \left|a^{p_+}_{\mathrm{ARM}}\left(\mathbf{p}, I_P^{3/2}, t_s^c\right)\right|^2 \tag{5.4}$$

$$\left|a^{(d)}_{\mathrm{ARM}}(\mathbf{p})\right|^2 = \frac{2}{3}\left|a^{p_+}_{ARM}\left(\mathbf{p}, I_P^{1/2}, t_s^c\right)\right|^2 + \frac{1}{3}\left|a^{p_+}_{\mathrm{ARM}}\left(\mathbf{p}, I_P^{3/2}, t_s^c\right)\right|^2 + \left|a^{p_-}_{\mathrm{ARM}}\left(\mathbf{p}, I_P^{3/2}, t_s^c\right)\right|^2 \tag{5.5}$$

where superscripts u and d denote spin-up and spin-down electrons, respectively, and p^- corresponds to electrons with azimuthal projection of angular momentum quantum number $m_\ell = -1$, and p_+ to $m_\ell = 1$.

The corresponding attostreak maps are shown in Fig. 5.1a and 5.1b. The calculations have been performed for an ultrashort pulse defined through its vector-potential $\mathbf{A}(t)$ as follows:

$$\mathbf{A}(t) = -\frac{\mathcal{E}_0}{\omega}\cos^2\left(\frac{\omega t}{2N_e}\right)[\cos(\omega t)\,\hat{\mathbf{x}} + \sin(\omega t)\,\hat{\mathbf{y}}], \tag{5.6}$$

with the envelope containing two full laser cycles base-to-base ($N_e = 2$) and the field envelope is modelled by a cos^2-profile.

Both maps look very similar, as the dominant contribution is from the p_- orbital with $j = 3/2$. The only noticeable difference is that the signal from spin-down electrons is somewhat stronger than the signal from the spin-up electrons. This result is the combination of two factors. First, the Clebsch-Gordan coefficients corresponding to the dominant p^- ($j = 3/2$) orbital yield a greater contribution of spin-down rather than spin-up electrons. Second, in the nonadiabatic domain, ionisation of electrons with angular momentum opposite to laser field polarisation is preferred over the co-rotating electrons [142].

The offset angle for both cases is around 10 degrees from the expected SFA peak, which lies along the zero degree line. This is the consequence of the long-range electron-core interaction.

Integrating over the detection angle ϕ_p, we can obtain the Spin-polarisation (SP) of the generated photoelectron burst as a function of its energy using the standard expression:

$$\mathrm{SP} = \frac{w^{(d)}_{\mathrm{ARM}}(E_p) - w^{(u)}_{\mathrm{ARM}}(E_p)}{w^{(d)}_{\mathrm{ARM}}(E_p) + w^{(u)}_{\mathrm{ARM}}(E_p)}, \tag{5.7}$$

where, $E_p = p^2/2$ is the drift energy of the photoelectron, and w_{ARM} is the ionisation rate evaluated through the ARM method, then we can directly compare the energy- and channel-resolved spin polarisation in long- and short-range potentials (Fig. 5.2a). The zero-point of spin polarisation is moved further in the long-range potential, preferring greater polarisation even for higher energies. This effect is a manifestation of the long-range interaction with the liberated -electron, even after the electron leaves the tunnelling barrier. The counter-rotating electron sees a longer ionisation window compared to the co-rotating electron during its motion

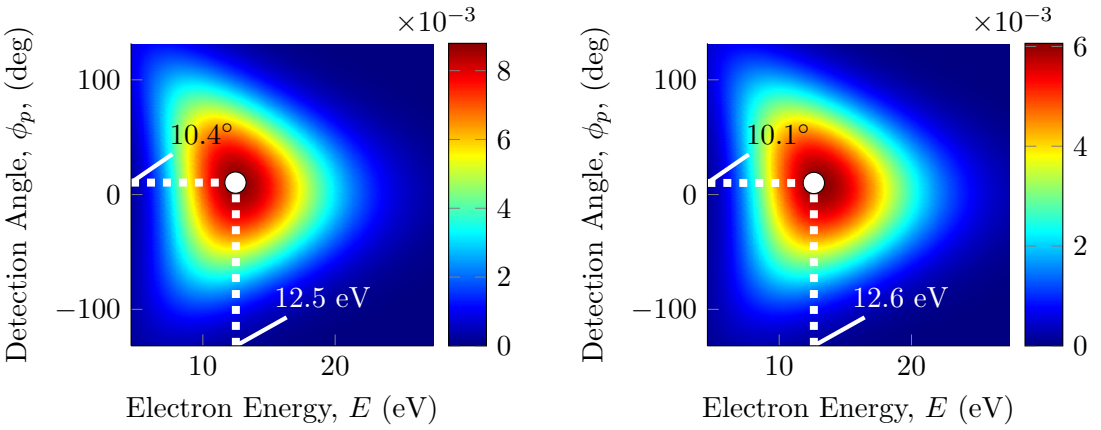

Figure 5.1: Attostreak maps for (a) spin-down and (b) spin-up electrons for Krypton atom by a 2-cycle, right-circularly polarised field with $I = 1.75\times10^{14}$ W/cm^2, $\lambda = 800$ nm. Note somewhat different scales on the two panels.

in the continuum, which is another manifestation of the nonadiabatic character of the ionisation process.

On the other hand, integrating over the energy range considered, we get a better view of the effects of long-range potentials on Spin polarisation (Figs. 5.2b, 5.2c, and 5.2d), through its dependence on the detection angle.

For the case of ionisation in a short-range potential, the spin polarisaiton is symmetric about the maximum value for each channel, whereas long-range interactions induce an asymmetry in the polarisation as a function of detection angle. Depending on the polarisation of the ionising field, one direction is preferred over the other. For the present case of a right circularly polarised field, the polarisation increases in the counter-clockwise direction, i.e. along the first quadrant of the detection angle ($\phi_p > 0$). Naturally, for a clockwise field, the effect would be reversed, giving us greater polarisation in the fourth quadrant ($\phi_p < 0$).

Additionally, we get an increase in the production of spin-down electrons over spin-up for every channel, when comparing ionisation in long- to short-range potentials. The greatest increase is seen for $^2P_{1/2}$ channel (green diamond curves, Fig. 5.2c).

5.4.2 Control via CEP Phase

Using a few-cycle laser pulse, we can harness an extra degree of control over the ionisation process through the carrier-envelope (CEP) phase offset, ϕ_{CEP}. Varying the CEP allows us to control the direction of maximum spin polarisation. Fig. 5.3 shows the energy-integrated plots for spin-polarisation from different channels versus the electron detection angle ϕ_p, for different values of the CEP offset. We use here a left-circularly polarised laser field, hence the dominance of spin-down electrons over the spin-up electrons for $j = 1/2$ (Fig. 5.3b).

While the variation of spin polarisation with energy remains virtually the same for any CEP offset, the CEP offset shifts the spin-polarisation profile over the detection angles.

Another effect we see clearly is the asymmetry induced in Spin Polarisation by the long-range interaction of the ionising electron with the ionic core. In the case of a short-range potential, the spin polarisation variation about the peak of the photoelectron distribution would have been symmetric. However, this symmetry is relinquished in the long-range potential, favouring the direction of polarisation of the electric field vector. Since, for Fig. 5.3, the field is right-circularly polarised, i.e., it rotates from the fourth quadrant towards the first, we see a similar preference of the first quadrant over the fourth in the spin polarisation.

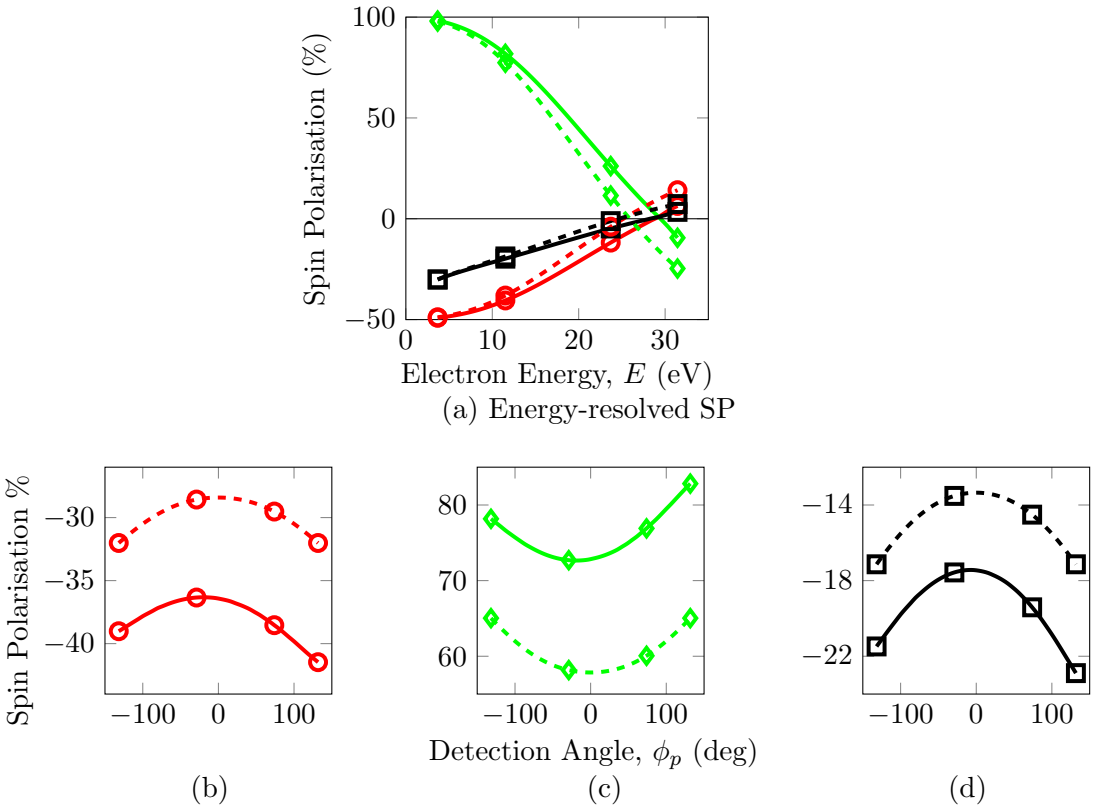

Figure 5.2: Comparison between short-range (dashed lines) and long-range (solid lines) (a) angle-, and (b,c,d) energy-integrated, channel-resolved Spin polarisation for Krypton atom. Laser Field Parametres: peak intensity $I_0 = 8.77 \times 10^{13}$ W/cm^2 ($\mathcal{E}_0 = 0.05$ a.u.), $\lambda = 800$ nm, 2-cycle, right-circularly polarised field.

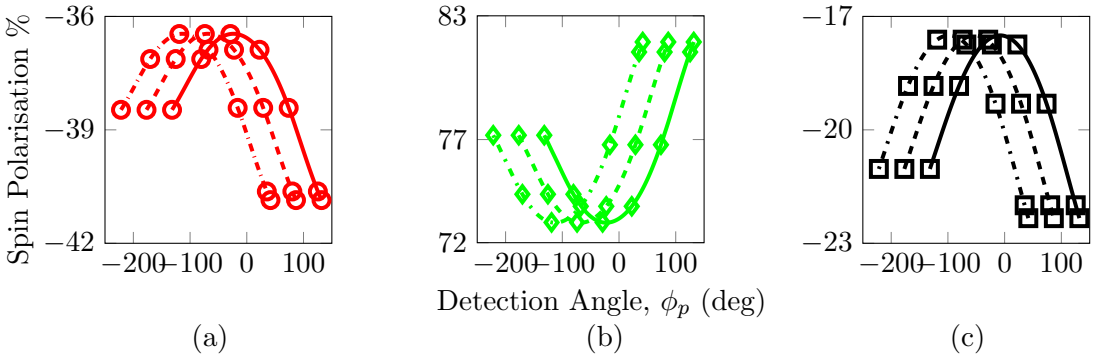

Figure 5.3: Channel-resolved variation of Energy-integrated Spin-polarisation versus the detection angle ϕ_p, for Krypton atom and different CEP offsets: $\phi_{\text{CEP}} = 0$ for solid lines, $\phi_{\text{CEP}} = \pi/4$ for dashed lines and $\phi_{\text{CEP}} = \pi/2$ for dash-dotted lines. (a) $j = 3/2$, (b) $j = 1/2$ and (c) total spin-polarisation. Field peak intensity is 1.75×10^{14} W/cm^2 ($\mathcal{E}_0 = 0.05$ a.u.), wavelength $\lambda = 800$ nm, 2-cycle, right-circularly polarised field.

5.4.3 Channel-resolved spectra

We now consider channel-resolved momentum distributions. For monochromatic fields, the distribution is isotropic with respect to the electron detection angle, unlike the case for the few-cycle pulses. Here we integrate the spectrum generated by the few-cycle pulse over all detection angles.

A comparison of the channel-resolved electron spectra for the case of short- and long-range

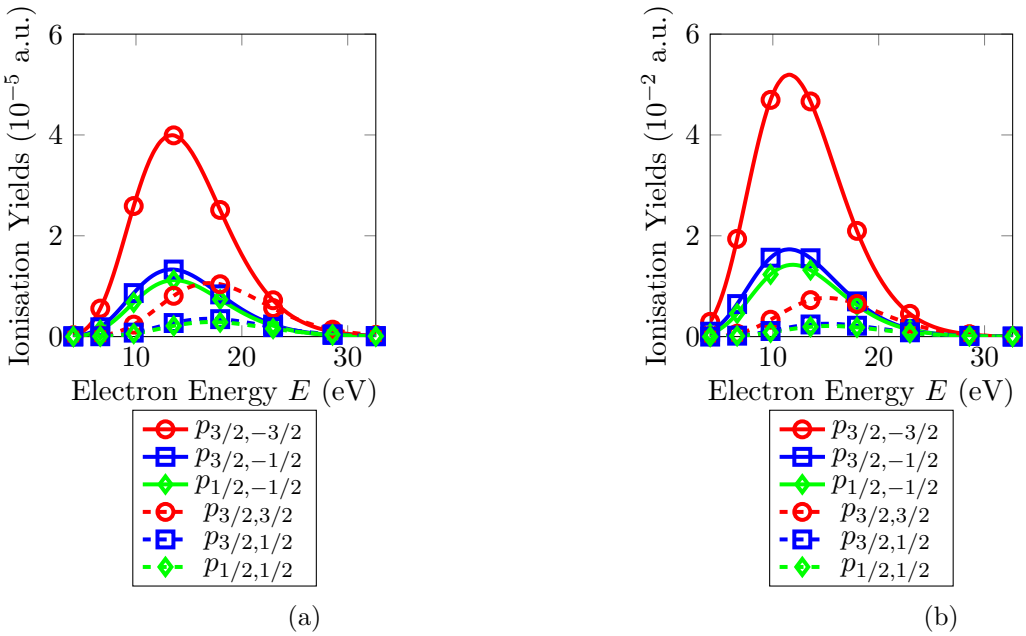

Figure 5.4: Channel-resolved ionisation signals in (a) short- and (b) long-range potentials for Krypton atom with ionising peak field intensity of $I_0 = 8.77 \times 10^{13}$ W/cm^2 ($\mathcal{E}_0 = 0.05$ a.u.), $\lambda = 800$ nm, 2-cycle, right-circularly polarised field.

(j, m_j)	$a^{p_{m_j - m_s}, j}(\mathbf{p})$
$(\frac{3}{2}, \frac{3}{2})$	$a^{p_+, \frac{3}{2}}$
$(\frac{3}{2}, -\frac{1}{2})$	$\sqrt{\frac{1}{3}} a^{p_-, \frac{3}{2}}$
$(\frac{1}{2}, -\frac{1}{2})$	$-\sqrt{\frac{2}{3}} a^{p_-, \frac{1}{2}}$

Table 5.1: Ionisation channels and amplitudes contributing to emission of spin-up ($m_s = 1/2$) electron.

(j, m_j)	$a^{p_{m_j - m_s}, j}(\mathbf{p})$
$(\frac{3}{2}, -\frac{3}{2})$	$a^{p_-, \frac{3}{2}}$
$(\frac{3}{2}, \frac{1}{2})$	$\sqrt{\frac{1}{3}} a^{p_+, \frac{3}{2}}$
$(\frac{1}{2}, \frac{1}{2})$	$\sqrt{\frac{2}{3}} a^{p_+, \frac{1}{2}}$

Table 5.2: Ionisation channels and amplitudes contributing to emission of spin-down ($m_s = -1/2$) electron.

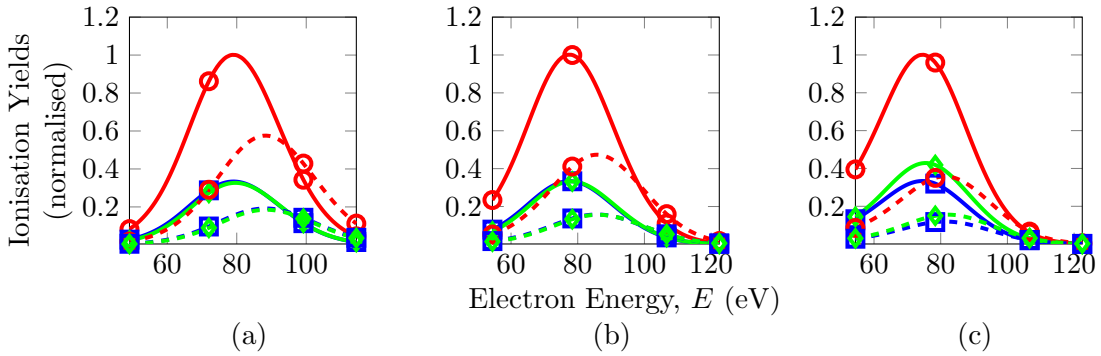

Figure 5.5: Normalised, channel-resolved ionisation yields in (a) short-range potential, (b) long-range potential with $Q = 1$, and (c) long-range potential with $Q = 2$, for peak intensity $I_0 = 1.72 \times 10^{14}$ W/cm^2 ($\mathcal{E}_0 = 0.07$ a.u.), $\lambda = 1600$ nm, for the ionisation potentials of a Krypton atom. Red solid with circles for ionisation from $p_{3/2,-3/2}$ orbital, red dashed with circles for $p_{3/2,3/2}$, blue solid with squares for $p_{3/2,-1/2}$, blue dashed with squares for $p_{3/2,1/2}$, green solid with diamonds for $p_{1/2,-1/2}$, and green dashed with diamonds for $p_{1/2,1/2}$.

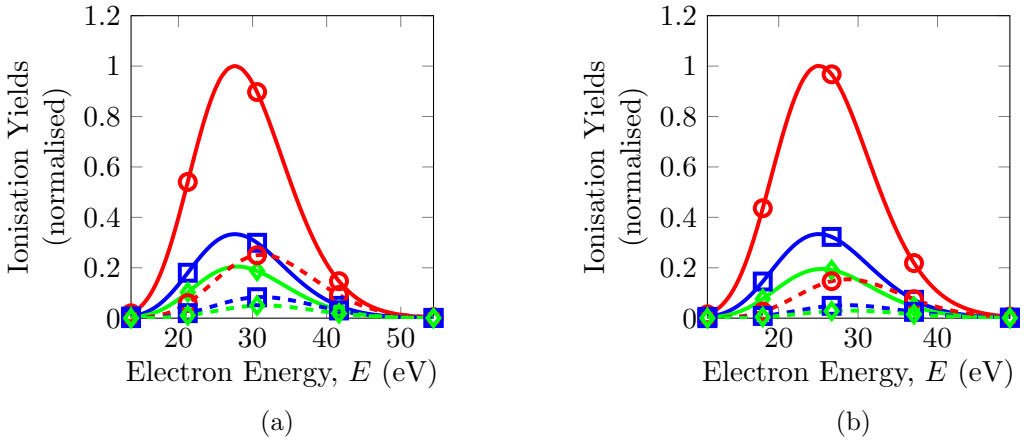

Figure 5.6: Normalised, channel-resolved ionisation yields in (a) short-range potential, (b) long-range potential with $Q = 2$, at peak intensity $I_0 = 1.72 \times 10^{14}$ W/cm^2 ($\mathcal{E}_0 = 0.07$ a.u.), $\lambda = 800$ nm for Rubidium (Rb^+) ion. Red solid with circles for ionisation from $p_{3/2,-3/2}$ orbital, red dashed with circles for $p_{3/2,3/2}$, blue solid with squares for $p_{3/2,-1/2}$, blue dashed with squares for $p_{3/2,1/2}$, green solid with diamonds for $p_{1/2,-1/2}$, and green dashed with diamonds for $p_{1/2,1/2}$.

potentials is shown in Figs. 5.4a and 5.4b. Assuming near-zero contribution from $m_\ell = 0$ projection of p-orbital, each spin-orbital has one specific spin of the electron contributing, as shown in Tabs. 1 and 2 of [273] and reproduced here for reference. Thus, signals resolved on both j and m_j provide complete information for the analysis of spin polarisation.

Figs. 5.4a and 5.4b show that, for the long-range Coulomb potential, the relative strength of ionisation signals correlated to $j = 3/2$ is greater than for $j = 1/2$, when compared with the short-range potential. In other words, while there is an overall greater preference for ionisation into $j = 3/2$ rather than $j = 1/2$, this preference is further accentuated in long-range potentials.

Within $j = 3/2$, emission of the spin-down electron is the dominant one. This can be seen by comparing the ionisation yields for $p_{3/2,3/2}$ with $p_{3/2,-3/2}$ for short- and longe-range potentials, for example: $p_{3/2,3/2}$ has only contribution from spin-up electron, while $p_{3/2,-3/2}$ only from spin-down. From Fig. 5.4a (short-range potential), the ratio of ionisation yields $w^{p_{3/2,-3/2}}/w^{p_{3/2,3/2}} \approx 4$, whereas for long-range potential from Fig. 5.4b $w^{p_{3/2,-3/2}}/w^{p_{3/2,3/2}} \approx 5$. Likewise, for a left-circularly polarised field, the spin-up electron would have the advantage.

As we approach the adiabatic limit with the Keldysh parameter $\gamma \to 0$, the channel resolved spectra exhibit a variation in the dominance of some channels over others. To illustrate this point, Figs. 5.5a and 5.5b show the energy-weighted spectra calculated for the Krypton atom, comparing short-range and long-range potentials. From Fig. 5.5a, we note that the signal from the $p_{3/2,m_j}$ orbital is almost the same as from the $p_{1/2,m_j}$ orbital, for the same m_j. Continuing further in intensity would lead to dominance of $j = 1/2$ orbitals over $j = 3/2$, whereas a decrease in intensity would allow $j = 3/2$ to again prevail.

Thus, for the short-range potential, we see that as the wavelength is increased, the ionisation yields for electrons with similar spin are almost independent of the channel they arise from. This can be seen from the distribution for the two pairs of 1) the spin-down electrons $p_{3/2,-1/2}$ (blue solid with squares) and $p_{1/2,-1/2}$ (green solid with diamonds), and 2) the spin-up electrons $p_{3/2,1/2}$ (blue dashed with squares) and $p_{1/2,1/2}$ (green dashed with diamonds).

Including the long-range interaction, as done for Fig. 5.5b, still seems to maintain this overlap in the signals for different channels corresponding to similar spin orientation. But if we take $Q = 2$, as is done for Fig. 5.5c, we see that this is no longer the case. Interestingly, ionisation from $j = 1/2$, corresponding to higher ionisation potential, starts to dominate over ionisation from $j = 3/2$, which corresponds to lower ionisation potential, for the same m_s (either 1/2 or -1/2). Note, however, that the angular momentum of the liberated electron is different in these cases, counter-rotating in the former case and co-rotating in the latter.

Thus, for a hypothetical, positively charged ion, that maintains its ground and excited, doubly-charged states corresponding to the energy levels of Kr^+ ion, the field strength at which the ionisation yields from $j = 3/2$ and $j = 1/2$ overlap is lowered, compared to the field strength for the same phenomenon in short-range potentials.

The strength of spin-up electron ionisation rates wanes as the effective charge of the core increases, which is expected according to our previous discussions.

We next consider ionisation from closed shell of positive charged ions, i.e., alkali ions. Due to the high ionisation potential required to reach the ground state of Rb^{2+} ($^2P_{3/2}$) ion, $I_p = 1$ a.u., ionisation remains in the nonadiabatic domain of $\gamma \simeq 1$ for longer wavelengths towards the infrared regime. As non-adiabatic ionisation dynamics in the long-range potential favours emission of counter-rotating electrons, channels with contributions from $m_\ell = -1$ are the stronger ones. Figures 5.6a and 5.6b show a comparison similar to Figs. 5.4a and 5.4b, for positively charged ions ($Q = 2$), for short- and long-range potentials, respectively, for laser intensity of $I = 8.77 \times 10^{13}$ W/cm^2 and wavelength $\lambda = 800$ nm for Rubidium ion. As the nonadiabatic character of the ionisation process increases, with a commensurate increase in the value of the Keldysh paramter γ, production of spin-up electrons is greatly suppressed in comparison to the spin-down electrons.

While the three channels which have contribution from $m_\ell = -1$ projection roughly maintain the same relative strength relative to the strongest channel ($p_{3/2,-3/2}$ in present case), the channels with contribution from $m_\ell = 1$ are additionally suppressed in the case of the long-range interaction (Fig. 5.6b) compared to the short-range case (Fig. 5.6a).

5.5 Conclusion

We have discussed the effects of long-range interaction on spin-polarisation in few-cycle, circularly polarised fields, and compared the spectra from different spin-orbit channels involved. We find that strong field ionisation from long-range potential leads to higher degree of spin polarisation compared to the case of the short-range potential.

Additionally, long-range interaction induces asymmetry in angle-resolved spin-polarisation, which we found for all ionisation channels.

Controlling the CEP of the ionising pulse allows one to control the direction in which spin polarised electrons are emitted, whether channel resolved or considered as a total.

Strong field ionisation of alkali ions with noble gas configuration is shown to exhibit nonadiabatic effects even in the infrared wavelength regime, with a strong preference of ionisation from channels with a specific angular momentum m_ℓ contribution, depending on the polarisation of the laser field. Thus, these ions appear to be better sources of spin-polarised electrons generated via strong-field ionisation.

Chapter 6

Conclusion and Future Work

In this thesis, the primary purpose has been to establish a rigorous formulation and description of strong field ionisation from atoms modelled with a Long-Range Potential (LRP), using the Analytical R-Matrxi (ARM) method [46, 148, 268, 270, 271] and Eikonal-Volkov Approximation (EVA) electrons [267]. The conventional approach to treating ionisation in LRP core rely on the Imaginary Time Method (ITM) [4, 50] derived from the PPT theory [4, 5]. There were several ad hoc assumptions underlying that prescriptive method, and were applicable for the adiabatic limit ($\omega \to 0$).

With the ARM formalism, expatiated in detail in Chapter 2, we present a new, more widely applicable theory of strong field ionisation in LRP, specifically in the nonadiabatic range of the Keldysh paramter ($\gamma \gtrsim 1$), where the core potential dynamics cannot be ignored and the ionisation process is not immediately completely right when the electron emerges from under the barrier, as is posited by conventional theories [2, 3, 78, 79, 130]. Signs of these nonadiabatic dynamics are imprinted on the initial electron velocity and offset of photoelectron spectrum peak [270]. Conventional attoclock setup [44, 45] relies on the time-momentum angle mapping to ascertain the dynamical aspects of the ionisation process. Calibration of this mapping is essential for an accurate model of the phenomenon, which we presented in Chapter 2 and 3.

The spin of the photoelectron can also be used to define measurement times in the ionisation process. In Chapter 4, we present a link between the phase accumulated during the ionisation process, from one-photon to multi-photon regime, and the corresponding Wigner-Smith time τ_{WS}, through a generalisation of the Larmor clock idea [278]. The magnetic field is provided by Spin-Orbit (SO) interaction activated after the removal of the photoelectron from the closely filled shell of a noble gas atoms. As a result, this Attosecond Larmor Clock is an inbuilt timing mechanism to decipher the time delays associated with tunnelling ionisation processes through evolution of spin of the photoelectron. We find two sources of ionisation phase delays with this clock: the expected LRP interaction-induce delays, as discusse in Chapter 2, common to both final states of the ion, and a short-range potential (SRP) contribution to the phase that does not translate into ionisation time delays. A suitable pump-probe scheme can be set-up to record the ionisation signal in a transient absorption spectroscopy. With this Attosecond Larmor Clock setup, we have found zero phase delays accumulated under the barrier. The SRP component of phase-delays arising from electron-core interactions is most closely an analogue of pulse dispersion in optics.

One of the expressions derived in Chapter 4 was a succinct equation to define the ionisation time delays induced by Coulomb-type potentials for a fixed final electron momentum. An analogy between the standard barrier penetration and optical tunnelling ionisation was presented, to define the role of the ionisation potential I_p in the latter case similar to the potential barrier height V in the former case. In Chapter 3, we provide a rigorous derivation of this term for arbitary final electron momentum and initial bound state configuration. This exact method for boundary matching completes the essential framework of ARM method, and allows us to

provide an accurate model to study strong field, tunnelling ionisation in for arbitrary atomic states. Momentum shifts incurred by the photoelectron while traversing under the barrier was a consequent result from this derivation scheme. It allows us to clearly define a generalised boundary matching scheme for the A*R*M formalism. We presented angle and energy resolved photoelectron spectra in LRP core under a circularly polarised field, highlighting the essential features of ionisation to the two SO-split, singly charged ionic states in noble gas atoms. It was shown that the ionisation rates in LRP enhance the nonadiabatic affinity to counter-rotating electrons discussed for SRP in [142, 143]. Based on the offset angles and peak energies, it was shown how it might be possible, in the future, to differentiate ionisation from different orbitals. This indicates preference of ring currents in one particular direction over the other, after removal of the electron. By scanning the offset angle and/or peak energies of the photoelectron spectra for the two electron spins, it would be possible to ascertain which spin orientation is favoured, as was discussed in Chapter 3.

Building on the results of the previous chapter, in Chapter 5 we take on the question of spin polarisation of photoelectrons in strong field ionisation. The first results for the tunnelling domain were discussed recently in [144], but for SRP core in a monochromatic laser field. We generalise the results for a Coulomb-type potential and enveloped fields, detailing the differences between the degree of Spin polarisation in SRP vs LRP core. An essential result of this chapter is the asymmetry induced by LRP interactions for Spin Polarisation as a function of final momentum detection angle ϕ_k. An advantage of enveloped field is the extra degree of control offered via the Carrier Envelope Phase (CEP) offset of the laser pulse. Through this CEP offset, we can steer the direction of spin polarised electrons.

We have limited this dissertation to model the LRP-Laser coupling of the continuum electron under the eikonal approximation, resulting in the eikonal-Volkov approximated (EVA) states [267], on which the A*R*M formalism is based. For low-energy electrons, as well as forward and backscattering electrons in a LRP, the eikonal approximation fails, and the momentum generated by the LRP potential becomes the main driving momentum for the ionising electron, leading to features bearing characteristic mark of the core potential, for example the Low Energy Structures (LES) as discussed in Section 1.5. With an aim to outline a rigorous derivation to include LRP interactions to arbitrary orders in continuum states, which may be called the Exact Core-Laser (EXCL) electron states. These states can be derived within the quasiclassical approach followed for EVA [267], but without any approximation on the magnitude of the momentum imparted by the core potential to the ionising electron in comparison to that by the laser field. Hence, these states provide a much more accurate description of the continuum states of the electron, especially in the low-energy spectrum of ATI. The formal derivation for EXCL electrons will the course for future work, including the new difficulties arising in the analytical continuation of these states to describe tunnelling in complex time domain, as is usually encountered in saddle-point analysis [2, 3]. Since these states take into account the LRP core exactly (within the quasiclassical approximation), the trajectories emerging naturally in the derivation posses caustic singularities [327]. These states will be the foundation for future research work to be pursued in providing a comprehensive, anayltical theory of strong field tunnelling ionisation in long-range potentials, completing an important step in the 50-year long enterprise pioneered by the Keldysh and PPTK papers.

Bibliography

[1] F. Krausz and M. Ivanov. Attosecond Physics. *Rev. Mod. Phys.*, 81:163, 2009.

[2] L. V. Keldysh. Ionization in the Field of a Strong Electromagnetic Wave. *Sov. Phys. JETP*, 20:1307, 1965.

[3] A. M. Perelomov, V. S. Popov, and M. V. Terentév. Ionization of Atoms in an Alternating Electric Field. *Sov. Phys. JETP*, 23:924, 1966.

[4] A. M. Perelomov, V. S. Popov, and M. V. Terentév. Ionization of Atoms in an Alternating Electric Field: II. *Sov. Phys. JETP*, 24:207, 1967.

[5] A. M. Perelomov and V. S. Popov. Ionization of Atoms in an Alternating Electric Field: III. *Sov. Phys. JETP*, 25:336, 1967.

[6] V. S. Popov, V. P. Kuznetsov, and A. M. Perelomov. Quasiclassical Approximation for Nonstationary Problems. *Sov. Phys. JETP*, 26:222, 1968.

[7] W. Heisenberg. Über quantentheoretische Umdeutung kinematischer und mechanischer Beziehungen [Quantum-Theoretical Re-interpretation of Kinematic and Mechanical Relations]. *Z. Phys.*, 33:879, 1925.

[8] B. L. van der Waerden. *Sources of Quantum Mechanics*. North-Holland Publishing Company, 1967.

[9] P. A. M. Dirac. *The Principles of Quantum Mechanics*. Clarendon Press, 4th edition, 1982.

[10] L. D. Landau and E. M. Lifshitz. *Quantum Mechanics: Non-relativistic Theory*, volume 3. Pergamon Press, 2nd edition, 1963.

[11] B. H. Bransden and C. J. Joachain. *Physics of Atoms and Molecules*. Pearson Education, 2nd edition, 2006.

[12] D. J. Griffiths. *Introduction to Quantum Mechanics*. Pearson Education, 2nd edition, 2008.

[13] L. H. Ryder. *Quantum Field Theory*. Cambridge University Press, 2nd edition, 1996.

[14] D. F. Zaretskiĭ and V. P. Kraĭnov. Resonance excitation of atomic levels in a strong electromagnetic field. *Zh. Eksp. Teor. Fiz.*, 66:537, 1974.

[15] N. B. Delone. Multiphoton ionization of atoms. *Usp. Fiz. Nauk*, 115:361, 1975.

[16] G. Mainfray. Multiphoton Ionization of Atoms. *J. Phys. Colloques*, 46:C1–113 – C1–125, 1985.

[17] R. Shakeshaft. Theory of multiphoton ionization of atoms by intense laser fields. *J. Opt. Soc. Am. B*, 4:705, 1987.

[18] G. Mainfray and C. Manus. Multiphoton ionization of atoms. *Rep. Prog. Phys.*, 54:1333, 1991.

[19] N. B. Delone and V. Krainov. *Multiphoton Processes in Atoms.* Number 13 in Springer Series on Atomic, Optical, and Plasma Physics. Springer, 2nd edition, 2000.

[20] P. Agostini et al. Free-Free Transitions Following Six-Photon Ionization of Xenon Atoms. *Phys. Rev. Lett.*, 42:1127, 1979.

[21] W. Gordon. Der Comptoneffekt nach der Schrdingerschen Theorie. *Z. Phys.*, 40:117, 1926.

[22] D. M. Volkov. Über eine Klasse von Lösungen der Diracschen Gleichung. *Z. Phys.*, 94:250, 1935.

[23] H. Reiss. Absorption of Light by Light. *J. Math. Phys.*, 3:59, 1962.

[24] H. Riess. A Convergent Perturbation Expansion in FirstQuantized Electrodynamics. *J. Math. Phys.*, 3:387, 1962.

[25] F. V. Bunkin and A. M. Prokhorov. The Excitation and Ionization of Atoms in a Strong Radiation Field. *Sov. Phys. JETP*, 19:739, 1964.

[26] J. R. Oppenheimer. Three Notes on the Quantum Theory of Aperiodic Effects. *Phys. Rev.*, 31:66, 1928.

[27] Gribakin and Kuchiev. Multiphoton detachment of electrons from negative ions. *Phys. Rev. A*, 55:3760, 1997.

[28] S. Beiser, M. Klaiber, and I. Yu. Kiyan. Photodetachment in a strong circularly polarized laser field. *Phys. Rev. A*, 70:011402(R), 2004.

[29] D. Bauer, D. B. Milošević, and W. Becker. Strong-field approximation for intense-laser-atom processses: The choice of gauge. *Phys. Rev. A*, 72:023415, 2005.

[30] M. N. Frolov et al. Model-Independent Quantum Approach for Intense Laser Detachment of a Weakly Bound Electron. *Phys. Rev. Lett.*, 91:053003, 2003.

[31] X. Xie et al. Time and momentum distributions of rescattering electrons. *J. Mod. Opt.*, 54:999, 2007.

[32] R. Shakeshaft. Multiphoton ionization of an atom; the choice of gauge. *Z. Phys. D*, 8:47, 1988.

[33] M. Dörr, R. Potvliege, and R. Shakeshaft. Atomic hydrogen irradiated by a strong laser field: Sturmian basis calculations of rates for high-order multiphoton ionization, Raman scattering, and harmonic generation. *J. Opt. Soc. Am. B*, 7:433, 1990.

[34] E. Cormier and P. Lambropoulos. Optimal gauge and gauge invariance in non-perturbative time-dependent calculation of above-threshold ionization. *J. Phys. B*, 29:1667, 1996.

[35] G. Grynberg, A. Aspect, C. Fabre, and C. Cohen-Tannoudji. *Introduction to Quantum Optics: From the Semi-classical Approach to Quantized Light.* Cambridge University Press, 1st edition, 2010.

[36] P. Salieres. Feynman path integral approach for intense laser-atom interaction. *Science*, 292:902, 2001.

[37] J. Mathews and R. L. Walker. *Mathematical Methods of Physics.* W. A. Benjamin, 2nd edition, 1970.

[38] Y. Goldfarb, I. Degani, and D. J. Tannor. Bohmian Mechanics with Complex Action: A New Trajectory-Based Formulation of Quantum Mechanics, 2006.

[39] Y. Goldfarb and D. J. Tannor. Interference in Bohmian mechanics with complex action. *J. Chem. Phys.*, 127:161101, 2007.

[40] Y. Goldfarb, J. Schiff, and D. J. Tannor. Complex trajectory method in time-dependent WKB. *J. Chem. Phys.*, 128:164114, 2008.

[41] J. Schiff, Y. Goldfarb, and D. J. Tannor. Path integral derivations of novel complex trajectory methods. 2008.

[42] B. M. Smirnov and M. I. Chibisov. The Breaking Up of Atomic Particles by an Electric Field and by Electron Collisions. *Sov. Phys. JETP*, 22:585, 1966.

[43] H. R. Reiss. Theoretical Methods in Quantum Optics: S-Matrix and Keldysh Techniques for Strong-Field Processes. *Prog. Quant. Electr.*, 16:1–71, 1992.

[44] P. Eckle et al. Attosecond angular streaking. *Nat. Phys.*, 4:565, 2008.

[45] P. Eckle et al. Attosecond Ionization and Tunneling Delay Time Measurements in Helium. *Science*, 322:1525, 2008.

[46] L. Torlina and O. Smirnova. Time-dependent analytical R-matrix approach for strong field dynamics I: One electron systems. *Phys. Rev. A*, 86:043408, 2012.

[47] L. Torlina, J. Kaushal, and O. Smirnova. Time-resolving electron-core dynamics during strong-field ionisation in circularly polarised fields. *Phys. Rev. A*, 88:053403, 2013.

[48] Z. J. Long and W.-K. Liu. Higher order expansion of Keldysh integral for hydrogen atom and H_2 molecular ion. *J. Mod. Opt.*, 58:1141, 2011.

[49] V. N. Ostrovsky, T. K. Kjeldsen, and L. B. Madsen. Comment on "Generalization of Keldyshs theory". *Phys. Rev. A*, 75:027401, 2007.

[50] S. V. Popruzhenko et al. Strong Field Ionization Rate for Arbitrary Laser Frequencies. *Phys. Rev. Lett.*, 101:193003, 2008.

[51] S. V. Popruzhenko, G. G. Paulus, and D. Bauer. Coulomb-corrected quantum trajectories in strong-field ionization. *Phys. Rev. A*, 77:053409, 2008.

[52] S. V. Popruzhenko and D. Bauer. Strong field approximation for systems with Coulomb interaction. *J. Mod. Opt.*, 55:2573, 2008.

[53] S. V. Popruzhenko et al. Multiphoton ionization of atoms and ions by high-intensity X-ray lasers. *JETP*, 108:947, 2009.

[54] E. Goulielmakis et al. Real-time observation of valence electron motion. *Nature*, 466:700, 2010.

[55] A. N. Pfeiffer et al. Timing the release in sequential double ionization. *Nat. Phys.*, 7:428, 2011.

[56] A. N. Pfeiffer et al. Breakdown of the independent electron approximation in sequential double ionization. *New J. Phys.*, 13:093008, 2011.

[57] A. N. Pfeiffer et al. Attoclock reveals natural coordinates of the laser-induced tunnelling current flow in atoms. *Nat. Phys.*, 8:76, 2012.

[58] D. Kielpinski, R. T. Sang, and I. V. Litvinyuk. Benchmarking strong-field ionization with atomic hydrogen. *J. Phys. B*, 47:204003, 2014.

[59] G. Floquet. Sur les équations différentielles linéaires à coefficients périodiques. *Ann. l'Ecol. Norm. Sup.*, 12:47, 1883.

[60] J. H. Shirley. Solution of the Schrödinger Equation with a Hamiltonian Periodic in Time. *Phys. Rev.*, 138:B979, 1965.

[61] Ya. B. Zel'dovich. The Quasienergy of a Quantum-Mechanical System Subjected to a Periodic Action. *Sov. Phys. JETP*, 24:1006, 1967.

[62] H. Sambe. Steady States and Quasienergies of a Quantum-Mechanical System in an Oscillating Field. *Phys. Rev. A*, 7:2203, 1973.

[63] S.-I Chu and W. P. Rienhardt. Intense Field Multiphoton Ionization via Complex Dressed States: Application to the H Atom. *Phys. Rev. Lett.*, 39:1195, 1977.

[64] S.-I Chu and J. Cooper. Threshold shift and above-threshold multiphoton ionization of atomic hydrogen in intense laser fields. *Phys. Rev. A*, 32:2769, 1985.

[65] S.-I Chu and D. A. Telnov. Beyond the Floquet theorem: generalized Floquet formalisms and quasienergy methods for atomic and molecular multiphoton processes in intense laser fields. *Phys. Rep.*, 390:1, 2004.

[66] N. L. Manakov and A. G. Faĭnshteĭn. Decay of a weakly bound level in a monochromatic field. *Sov. Phys. JETP*, 52:382, 1980.

[67] N. L. Manakov et al. Higher-order perturbation theory effects in the shift and width of atomic levels in an optical field. *Sov. Phys. JETP*, 48:626, 1978.

[68] N. L. Manakov, V. D. Ovisiannikov, and L. P. Rapoport. Atoms in a Laser Field. *Phys. Rep.*, 141:319, 1986.

[69] N. L. Manakov and L. P. Rapoport. Particle with low binding energy in a circularly polarized field. *Sov. Phys. JETP*, 42:430, 1975.

[70] Yu. N. Demkov and V. N. Ostrovsky. *Zero-Range Potentials and Their Applications in Atomic Physics*. Physics of Atoms and Molecules. Springer, 1st edition, 1988.

[71] D. B. Milošević, A. Gazibegović-Busuladžić, and W. Becker. Direct and rescattered electrons in above-threshold detachment from negative ions. *Phys. Rev. A*, 68:050702(R), 2003.

[72] N. L. Manakov and M. V. Frolov. Threshold phenomena in the cross sections for atomic photoprocesses in a strong laser field. *JETP Lett.*, 83:536, 2006.

[73] K. Krajewska, I. I. Fabrikant, and A. F. Starace. Threshold effects in strong-field detachment of H^- and F^-: Plateau enhancements and angular distribution variations. *Phys. Rev. A*, 74:053407, 2006.

[74] M. N. Frolov et al. Description of harmonic generation in terms of the complex quasienergy. II. Application to time-dependent effective range theory. *Phys. Rev. A*, 75:063408, 2007.

[75] N. L. Manakov et al. Threshold phenomena in electron-atom scattering in a laser field. *JETP Lett.*, 87:92, 2008.

[76] M. N. Frolov, N. L. Manakov, and A. F. Starace. Wavelength Scaling of High-Harmonic Yield: Threshold Phenomena and Bound State Symmetry Dependence. *Phys. Rev. Lett.*, 100:173001, 2008.

[77] R. Kopold et al. Channel-closing effects in high-order above-threshold ionization and high-order harmonic generation. *J. Phys. B*, 35:217, 2002.

[78] F. H. M. Faisal. Multiple absorption of laser photons by atoms. *J. Phys. B*, 6:L89, 1973.

[79] H. R. Reiss. Effect of an intense electromagnetic field on a weakly bound system. *Phys. Rev. A*, 22:1786, 1980.

[80] H. R. Reiss. Spectrum of atomic electrons ionised by an intense field. *J. Phys. B*, 20:L79, 1987.

[81] A. Lohr et al. Above-threshold ionization in the tunneling regime. *Phys. Rev. A*, 55:R4003, 1997.

[82] S. V. Popruzhenko. Keldysh theory of strong field ionization: history, applications, difficulties and perspectives. *J. Phys. B*, 47:204001, 2014.

[83] A. I. Nikishov and V. I. Ritus. Ionization of Systems Bound by Short-range Forces by the Field of an Electromagnetic Wave. *Sov. Phys. JETP*, 23:168, 1965.

[84] H. R. Reiss. Relativistic strong-field photoionization. *J. Opt. Soc. Am. B*, 7:574, 1990.

[85] L. A. Lompre et al. Multiphoton Ionization of Rare Gases at Very High Laser Intensity (10^{15} W/cm^2) by a 30-psec Laser Pulse at 1.06 μm. *Phys. Rev. Lett.*, 36:949, 1976.

[86] P. Lambropoulos. Mechanisms for Multiple Ionization of Atoms by Strong Pulsed Lasers. *Phys. Rev. Lett.*, 55:2141, 1985.

[87] M. V. Ammosov, N. B. Delone, and V. P. Krainov. Tunnel ionization of complex atoms and of atomic ions in an alternating electromagnetic field. *Sov. Phys. JETP*, 64:1191, 1986.

[88] F. Yergeau, S. L. Chin, and P. Lavigne. Multiple ionisation of rare-gas atoms by an intense CO_2 laser (10^{14} W/cm^2). *J. Phys. B*, 20:723, 1987.

[89] T. E. Glover et al. Measurement of Velocity Distributions and Recombination Kinetics in Tunnel-Ionized Helium Plasmas. *Phys. Rev. Lett.*, 75:445, 1995.

[90] G. N. Gibson et al. Strong-Field Dissociation and Ionization of H_2^+ Using Ultrashort Laser Pulses. *Phys. Rev. Lett.*, 79:2022, 1997.

[91] J. Muth-Böhm, A. Becker, and F. H. M. Faisal. Suppressed Molecular Ionization for a Class of Diatomics in Intense Femtosecond Laser Fields. *Phys. Rev. Lett.*, 85:2280, 2000.

[92] R. Taïeb, V. Véniard, and A. Maquet. Photoelectron Spectra from Multiple Ionization of Atoms in Ultra-Intense Laser Pulses. *Phys. Rev. Lett.*, 87:053002, 2001.

[93] R. Moshammer et al. Rescattering of Ultralow-Energy Electrons for Single Ionization of Ne in the Tunneling Regime. *Phys. Rev. Lett.*, 91:113002, 2003.

[94] E. Gubbini et al. Core Relaxation in Atomic Ultrastrong Laser Field Ionization. *Phys. Rev. Lett.*, 94:053602, 2005.

[95] R. R. Freeman et al. Above-threshold ionization with subpicosecond laser pulses. *Phys. Rev. Lett.*, 59:1092, 1987.

[96] P. B. Corkum, N. H. Burnett, and F. Brunel. Above-threshold ionization in the long-wavelength limit. *Phys. Rev. Lett.*, 62:1259, 1989.

[97] E. Mével et al. Atoms in strong optical fields: Evolution from multiphoton to tunnel ionization. *Phys. Rev. Lett.*, 70:406, 1992.

[98] G. G. Paulus et al. Above-Threshold Ionization by an Elliptically Polarized Field: Quantum Tunneling Interferences and Classical Dodging. *Phys. Rev. Lett.*, 80:484, 1998.

[99] T. Morishita et al. Accurate Retrieval of Structural Information from Laser-Induced Photoelectron and High-Order Harmonic Spectra by Few-Cycle Laser Pulses. *Phys. Rev. Lett.*, 100:013903, 2008.

[100] M. Okunishi et al. Experimental Retrieval of Target Structure Information from Laser-Induced Rescattered Photoelectron Momentum Distributions. *Phys. Rev. Lett.*, 100:143001, 2008.

[101] M. Busuladžić et al. Angle-Resolved High-Order Above-Threshold Ionization of a Molecule: Sensitive Tool for Molecular Characterization. *Phys. Rev. Lett.*, 100:203003, 2008.

[102] B. Walker et al. Precision Measurement of Strong Field Double Ionization of Helium. *Phys. Rev. Lett.*, 73:1227, 1994.

[103] Th. Weber et al. Correlated electron emission in multiphoton double ionization. *Nature (London)*, 405:658, 2000.

[104] R. Moshammer et al. Momentum Distributions of Ne^{n+} Ions Created by an Intense Ultrashort Laser Pulse. *Phys. Rev. Lett.*, 84:447, 2000.

[105] A. Becker and F. H. M. Faisal. Interpretation of momentum distribution of recoil ions from laser induced nonsequential double ionization. *Phys. Rev. Lett.*, 84:3546, 2000.

[106] R. Kopold et al. Routes to Nonsequential Double Ionization. *Phys. Rev. Lett.*, 85:3781, 2000.

[107] A. S. Alnaser et al. Routes to Control of H_2 Coulomb Explosion in Few-Cycle Laser Pulses. *Phys. Rev. Lett.*, 93:183202, 2004.

[108] P. J. Ho et al. Nonsequential Double Ionization as a Completely Classical Photoelectric Effect. *Phys. Rev. Lett.*, 94:093002, 2005.

[109] P. Koval et al. Nonsequential Double Recombination in Intense Laser Fields. *Phys. Rev. Lett.*, 98:043904, 2007.

[110] S. Gräfe and M. Yu. Ivanov. Effective Fields in Laser-Driven Electron Recollision and Charge Localization. *Phys. Rev. Lett.*, 99:163603, 2007.

[111] A. Rudenko et al. Correlated Two-Electron Momentum Spectra for Strong-Field Nonsequential Double Ionization of He at 800 nm. *Phys. Rev. Lett.*, 99:263003, 2007.

[112] A. McPherson et al. Studies of multiphoton production of vacuum-ultraviolet radiation in the rare gases. *J. Opt. Soc. Am. B*, 4:595, 1987.

[113] M. Ferray et al. Multiple-harmonic conversion of 1064 nm radiation in rare gases. *J. Phys. B*, 21:L31, 1988.

[114] A. L'Huillier, K. J. Schafer, and K. C. Kulander. Higher-order harmonic generation in xenon at 1064 nm: The role of phase matching. *Phys. Rev. Lett.*, 66:2200, 1991.

[115] M. Lewenstein et al. Theory of high-harmonic generation by low-frequency laser fields. *Phys. Rev. A*, 49:2117, 1994.

[116] Ch. Spielmann et al. Generation of Coherent X-rays in the Water Window Using 5-Femtosecond Laser Pulses. *Science*, 278:661, 1997.

[117] Z. Chang et al. Generation of Coherent Soft X Rays at 2.7 nm Using High Harmonics. *Phys. Rev. Lett.*, 79:2967, 1997.

[118] M. Hantschel et al. Attosecond metrology. *Nature*, 414:509, 2001.

[119] M. Drescher et al. Time-resolved atomic inner-shell spectroscopy. *Nature (London)*, 419:803, 2002.

[120] E. A. Gibson et al. Coherent Soft X-ray Generation in the Water Window with Quasi-Phase Matching. *Science*, 302:95, 2003.

[121] E. A. Gibson et al. High-Order Harmonic Generation up to 250 eV from Highly Ionized Argon. *Phys. Rev. Lett.*, 92:033001, 2004.

[122] J. Seres et al. Laser technology: Source of coherent kiloelectronvolt X-rays. *Nature (London)*, 433:596, 2005.

[123] F. Lindner et al. Attosecond Double-Slit Experiment. *Phys. Rev. Lett.*, 95:040401, 2005.

[124] G. L. Yudin, A. D. Bandrauk, and P. B. Corkum. Chirped Attosecond Photoelectron Spectroscopy. *Phys. Rev. Lett.*, 96:063002, 2006.

[125] J. Levesque et al. High Harmonic Generation and the Role of Atomic Orbital Wave Functions. *Phys. Rev. Lett.*, 98:183903, 2007.

[126] M. Spanner and P. Brumer. Probing electron transfer within alkali-metal halides via high-order harmonic generation. *Phys. Rev. A*, 78:033840, 2008.

[127] G. Jordan and A. Scrinzi. Core-polarization effects in molecular high harmonic generation. *New J. Phys.*, 10:025035, 2008.

[128] T. Pfeifer et al. Time-resolved spectroscopy of attosecond quantum dynamics. *Chem. Phys. Lett.*, 463:11, 2008.

[129] Y. Mairesse et al. High Harmonic Spectroscopy of Multichannel Dynamics in Strong-Field Ionization. *Phys. Rev. Lett.*, 104:213601, 2010.

[130] P. B. Corkum. Plasma perspective on strong field multiphoton ionization. *Phys. Rev. Lett.*, 71:1994, 1993.

[131] W. Becker, R. R. Schlicher, and M. O. Scully. Final-state effects in above-threshold ionisation. *J. Phys. B*, 19:L785, 1986.

[132] M. Yu. Kuchiev. Atomic Antenna. *JETP Lett.*, 45:404, 1987.

[133] M. Yu. Kuchiev and V. N. Ostrovsky. Atomic antenna mechanism in HHG and ATI. 2000.

[134] H. B. van Linden van den Heuvell and H. G. Muller. *Multiphoton Processes*. Cambridge University Press, 1988.

[135] T. F. Gallagher. Above-Threshold Ionization in Low-Frequency Limit. *Phys. Rev. Lett.*, 61:2304, 1988.

[136] M. Gavrila. *Atoms in Intense Fields.* Academic, 1992.

[137] J. L. Krause, K. J. Schafer, and K. C. Kulander. High-order harmonic generation from atoms and ions in the high intensity regime. *Phys. Rev. Lett.*, 68:3535, 1992.

[138] K. J. Schafer et al. Above threshold ionization beyond the high harmonic cutoff. *Phys. Rev. Lett.*, 70:1599, 1993.

[139] K. Kondo et al. Wavelength dependence of nonsequential double ionization in He. *Phys. Rev. A*, 48:R2531, 1993.

[140] A. L'Huillier et al. High-order Harmonic-generation cutoff. *Phys. Rev. Lett.*, 48:R3433, 1993.

[141] M. Yu. Ivanov, M. Spanner, and O. Smirnova. Anatomy of strong field ionization. *J. Mod. Opt.*, 52:165, 2005.

[142] I. Barth and O. Smirnova. Nonadiabatic tunneling in circularly polarized laser fields: Physical picture and calculations. *Phys. Rev. A*, 84:063415, 2011.

[143] I. Barth and O. Smirnova. Nonadiabatic tunneling in circularly polarized laser fields. II. Derivation of formulas. *Phys. Rev. A*, 87:013433, 2013.

[144] I. Barth and O. Smirnova. Spin polarized electrons produced by strong field ionisation. *Phys. Rev. A*, 88:013401, 2013.

[145] C. I. Blaga et al. Strong-field photoionizaton revisited. *Nature Phys.*, 5:335, 2009.

[146] T.-M. Yan et al. Low-Energy Structures in Strong Field Ionization Revealed by Quantum Orbits. *Phys. Rev. Lett.*, 105:253002, 2010.

[147] W. Becker and D. B. Milošević. Above-threshold ionization for very low electron energy. *J. Phys. B*, 48:151001, 2015.

[148] L. Torlina et al. Time-dependent analytical R-matrix approach for strong field dynamics II: Many-electron systems. *Phys. Rev. A*, 86:043409, 2012.

[149] K. C. Kulander. Time-dependent theory of multiphoton ionization of xenon. *Phys. Rev. A*, 38:778, 1988.

[150] D. B. Milošević and F. Ehlotzky. X-ray-atom scattering in the presence of a laser field. *Phys. Rev. A*, 58:2319, 1998.

[151] H. G. Muller. An Efficient Propagation Scheme for the Time-Dependent Schrödinger Equation in the Velocity Gauge. *Laser Phys.*, 9:138, 1999.

[152] F. H. M. Faisal. *Theory of Multiphoton Processes.* New York: Plenum, 1987.

[153] L. Dimou and F. H. M. Faisal. New class of resonance in the $e + H^+$ scattering in an excimer laser field. *Phys. Rev. Lett.*, 59:872, 1987.

[154] R. M. Potvliege and R. Shakeshaft. Nonperturbative calculation of partial differential rates for multiphoton ionization of a hydrogen atom in a strong laser field. *Phys. Rev. A*, 38:1098(R), 1988.

[155] R. M. Potvliege and R. Shakeshaft. Multiphoton processes in an intense laser field. II. Partial rates and angular distributions for ionization of atomic hydrogen at 532 nm. *Phys. Rev. A*, 41:1609, 1990.

[156] R. M. Potvliege and R. Shakeshaft. *Adv. At. Mol. Opt. Phys. Suppl.*, 1:373, 1992.

[157] R. M. Potvliege. STRFLO: A program for time-independent calculations of multiphoton processes in one-electron atomic systems I. Quasienergy spectra and angular distributions. *Comp. Phys. Commun.*, 114:42, 1998.

[158] G. S. Voronov and N. B. Delone. Ionization of the xenon atom by the electric field of ruby laser emission. *JETP Lett.*, 1:66, 1965.

[159] G. Petite, P. Agostini, and H. G. Muller. Intensity dependence of non-perturbative above-threshold ionisation spectra: experimental study. *J. Phys. B*, 21:4097, 1988.

[160] S. Augst et al. Tunneling ionization of noble gases in a high-intensity laser field. *Phys. Rev. Lett.*, 63:2212, 1989.

[161] C. Ott et al. Strong-field spectral interferometry using the carrier-envelope phase. *New J. Phys.*, 12:073031, 2013.

[162] G. G. Paulus, W. Nicklich, and H. Walther. Investigation of Above-Threshold Ionization with Femtosecond Pulses: Connection Between Plateau and Angular Distribution of the Photoelectrons. *Europhys. Lett.*, 27:267, 1994.

[163] G. G. Paulus et al. Plateau in above threshold ionization spectra. *Phys. Rev. Lett.*, 72:2851, 1994.

[164] W. Becker, A. Lohr, and M. Kleber. Effects of rescattering on above-threshold ionization. *J. Phys. B*, 27:L325, 1994.

[165] D. B. Milošević and F. Ehlotzky. Influence of screening of the Coulomb potential on the plateau in above-threshold ionization. *Phys. Rev. A*, 57:5002, 1998.

[166] J. B. Watson et al. Nonsequential double ionization of helium. *Phys. Rev. Lett.*, 78:1884, 1997.

[167] M. Lein, E. K. U. Gross, and V. Engel. Intense-field double ionization of helium: identifying the mechanism. *Phys. Rev. Lett.*, 85:4707, 2000.

[168] Th. Weber et al. Recoil-ion momentum distributions for single and double ionization of helium in strong laser fields. *Phys. Rev. Lett.*, 84:443, 2000.

[169] X. Wang and J. H. Eberly. Elliptical trajectories in nonsequential double ionization. *New J. Phys.*, 12:093047, 2010.

[170] A. Fleischer et al. Probing Angular Correlations in Sequential Double Ionization. *Phys. Rev. Lett.*, 107:113003, 2011.

[171] Y. Zhou et al. Classical Simulations Including Electron Correlations for Sequential Double Ionization. *Phys. Rev. Lett.*, 109:053004, 2012.

[172] Y. Zhou et al. Classical description of strong-field double ionization by elliptical laser pulses. *Phys. Rev. A*, 86:043427, 2012.

[173] Y. Zhou, C. Huang, and P. Liu. Revealing the multi-electron effects in sequential double ionization using classical simulations. *Opt. Express*, 20:20201, 2012.

[174] D. A. Papadogiannis et al. Observation of Attosecond Light Localization in Higher Order Harmonic Generation. *Phys. Rev. Lett.*, 83:4289, 1999.

[175] P. M. Paul et al. Observation of a Train of Attosecond Pulses from High Harmonic Generation. *Science*, 292:1689, 2001.

[176] G. G. Paulus et al. Absolute-phase phenomena in photoionization with few-cycle laser pulses. *Nature*, 414:182, 2001.

[177] D. G. Arbo, E. Persson, and J. Burgdörfer. Time Double-Slit Interference in Tunneling Ionization. http://arxiv.org/abs/quant-ph/0605193, 2006.

[178] D. G. Arbo, E. Persson, and J. Burgdörfer. Time double-slit interference in strong-field tunneling ionization. *Phys. Rev. A*, 74:063407, 2007.

[179] A. Baltuška et al. Attosecond control of electronic processes by intense light fields. *Nature*, 421:611, 2003.

[180] M. Meckel et al. Laser-Induced Electron Tunneling and Diffraction. *Science*, 320:1478, 2008.

[181] C. I. Blaga et al. Imaging ultrafast molecular dynamics with laser-induced electron diffraction. *Nature (London)*, 483:194, 2012.

[182] J. Xu et al. Laser-Induced Electron Diffraction for Probing Rare Gas Atoms. *Phys. Rev. Lett.*, 109:233002, 2012.

[183] J. Itatatni et al. Tomographic imaging of molecular orbitals. *Nature (London)*, 432:867, 2004.

[184] M. Lein. Molecular imaging using recolliding electrons. *J. Phys. B*, 40:R135, 2007.

[185] M. Schultze et al. Delay in photoemission. *Science*, 328:1658, 2010.

[186] K. Klunder et al. Probing Single-Photon Ionization on the Attosecond Time Scale. *Phys. Rev. Lett.*, 106:143002, 2011.

[187] H. Akagi et al. Laser Tunnel Ionization from Multiple Orbitals in HCl. *Science*, 325:1364, 2009.

[188] F. H. M. Faisal. Strong-field physics: Ionization surprise. *Nature Phys.*, 5:319, 2009.

[189] W. Quan et al. Classical Aspects in Above-Threshold Ionization with a Midinfrared Strong Laser Field. *Phys. Rev. Lett.*, 103:093001, 2009.

[190] C. Liu and K. Z. Hatsagortsyan. Origin of Unexpected Low Energy Structure in Photoelectron Spectra Induced by Midinfrared Strong Laser Fields. *Phys. Rev. Lett.*, 105:113003, 2010.

[191] D. A. Telnov and S.-I. Chu. Low-energy structure of above-threshold-ionization electron spectra: Role of the Coulomb threshold effect. *Phys. Rev. A*, 83:063406, 2011.

[192] C. Lemell et al. Low-energy peak structure in strong-field ionization by midinfrared laser pulses: Two-dimensional focusing by the atomic potential. *Phys. Rev. A*, 85:011403(R), 2012.

[193] J. Dura et al. Ionization with low-frequency fields in the tunneling regime. *Sci. Rep.*, 3:2675, 2013.

[194] C. Lemell et al. Classical-quantum correspondence in atomic ionization by midinfrared pulses: Multiple peak and interference structures. *Phys. Rev. A*, 87:013421, 2013.

[195] B. Wolter et al. Formation of very-low-energy states crossing the ionization threshold of argon atoms in strong mid-infrared fields. *Phys. Rev. A*, 90:063424, 2014.

[196] M. Uiberacker et al. Attosecond real-time observation of electron tunnelling in atoms. *Nature*, 446:627, 2007.

[197] A. K. Kazansky and N. M. Kabachnik. An attosecond time-resolved study of strong-field atomic photoionization. *J. Phys. B*, 40:F299, 2007.

[198] D. Shafir et al. Resolving the time when an electron exits a tunnelling barrier. *Nature*, 485:343, 2012.

[199] O. Pedatzur et al. Attosecond tunnelling interferometry. *Nat. Phys.*, 11:815, 2015.

[200] R. Reichl, H. Helm, and I. Yu. Kiyan. Photodetachment of H^- in a Strong Infrared Laser Field. *Phys. Rev. Lett.*, 87:243001, 2001.

[201] R. Reichl, H. Helm, and I. Yu. Kiyan. Detailed comparison of theory and experiment of strong-field photodetachment of the negative hydrogen ion. *Phys. Rev. A*, 68:063404, 2003.

[202] B. Bergues, Y. F. Ni, H. Helm, and I. Yu. Kiyan. Experimental Study of Photodetachment in a Strong Laser Field of Circular Polarization. *Phys. Rev. Lett.*, 95:263002, 2005.

[203] A. Gazibegović-Busuladžić, D. B. Milosević, and W. Becker. Gauge dependence of the strong-field approximation: Theory vs. experiment for photodetachment of F^-. *Opt. Comm.*, 275:116, 2007.

[204] M. Bashkansky, P. H. Bucksbaum, and D. W. Schumacher. Asymmetries in Above-Threshold Ionization. *Phys. Rev. Lett.*, 60:2458, 1988.

[205] A. Rudenko, K. Zrost, Th. Ergler, A. B. Voitkiv, N. Najjari, V. L. B. de Jesus, B. Feuerstein, C. D. Schröter, R. Moshammer, and J. Ullrich. Coulomb singularity in the transverse momentum distribution for strong-field ionization. *J. Phys. B*, 38:L191, 2005.

[206] M. Yu. Ivanov, T. Barbec, and N. Burnett. Coulomb corrections and polarization effects in high-intensity high-harmonic emission. *Phys. Rev. A*, 54:742, 1996.

[207] C. Liu and K. Z. Hatsagortsyan. Coulomb focussing at above-threshold ionization in elliptically polarized mid-infrared strong laser fields. http://http://arxiv.org/abs/1109.5645, 2012.

[208] A. Becker and F. H. M. Faisal. Intense-field many-body S-matrix theory. *J. Phys. B*, 38:R1−−R56, 2005.

[209] D. B. Milošević, D. Bauer, and W. Becker. Quantum-orbit theory of high order atomic processes in intense laser fields. *J. Mod. Optics*, 53:125–134, 2006.

[210] P. Salieres, A. L'Huillier, and Ph. Antoine. Study of The Spatial and Temporal Coherence of High-Order Harmonics. *Adv. At. Mol. Opt. Phys.*, 41:83, 1999.

[211] D. B. Milosevic and W. Becker. Role of long quantum orbits in high-order harmonic generation. *Phys. Rev. A*, 66:063417, 2002.

[212] W. Becker, F. Grasbon, and R. Kopold. Above-Threshold Ionization: From Classical Features to Quantum Effects. *Adv. At. Mol. Opt. Phys.*, 48:35, 2002.

[213] D. B. Milosevic and F. Ehlotzky. Scattering and Reaction Processes in Powerful Laser Fields. *Adv. At. Mol. Opt. Phys.*, 49:373, 2003.

[214] D. B. Milošević, G. G. Paulus, and W. Becker. Phase-Dependent Effects of a Few-Cycle Laser Pulse. *Phys. Rev. Lett.*, 89:153001, 2002.

[215] D. B. Milošević, G. G. Paulus, and W. Becker. Above-Threshold Ionization with Few-Cycle Laser Pulses and the Relevance of the Absolute Phase. *Laser Phys.*, 13:948, 2003.

[216] D. B. Milošević, G. G. Paulus, and W. Becker. High-order above-threshold ionization with few-cycle pulse: a meter of the absolute phase. *Opt. Express*, 11:1418, 2003.

[217] D. B. Milošević, G. G. Paulus, and W. Becker. Metering the absolute phase of a few-cycle pulse via its high-order above-threshold ionization spectrum. *Laser Phys. Lett.*, 1:93, 2004.

[218] D. B. Milošević and W. Becker. Attosecond pulse generation by bicircular fields: from pulse trains to a single pulse. *J. Mod. Opt.*, 52:233, 2005.

[219] D. B. Milosevic and A. F. Starace. Static-Electric-Field-Induced, High-Energy Plateau for Scattered X-Ray Photons in Laser-Assisted, X-RayAtom Scattering. *Phys. Rev. Lett.*, 81:5097, 1998.

[220] D. B. Milosevic and A. F. Starace. Phase control of x-ray-atom scattering in the presence of a bichromatic laser field. *J. Phys. B*, 32:1831, 1999.

[221] D. B. Milosevic and A. F. Starace. Intensity dependence of plateau structures in laser-assisted x-rayatom scattering processes. *Phys. Rev. A*, 60:3943, 1999.

[222] D. B. Milosevic and A. F. Starace. Control of High-Harmonic Generation and Laser-Assisted X-ray-Atom Scattering with Static Electric and Magnetic Fields. *Laser Phys.*, 10:278, 2000.

[223] D. B. Milosevic and F. Ehlotzky. Rescattering effects in soft-x-ray generation by laser-assisted electron-ion recombination. *Phys. Rev. A*, 65:042504, 2002.

[224] D. B. Milosevic and F. Ehlotzky. Laser-assisted electron-ion recombination: Emitted photons' spectra and recollision effects. *J. Mod. Opt.*, 50:657, 2003.

[225] N. L. Manakov et al. Plateau effects in the spectra of electrons scattered from atoms in a strong laser field. *JETP Lett.*, 76:258, 2002.

[226] N. L. Manakov et al. Circularly polarized laser field-induced rescattering plateaus in electronatom scattering. *Phys. Lett. A*, 334:197, 2005.

[227] A. Čerkíc and D. B. Milošević. Plateau structures in potential scattering in a strong laser field. *Phys. Rev. A*, 70:053402, 2004.

[228] A. Čerkíc and D. B. Milošević. Potential Scattering in a Bichromatic Laser Field: Plateau Structures. *Laser Phys.*, 15:268, 2005.

[229] D. B. Milošević and W. Becker. Classical cutoffs for laser-induced nonsequential double ionization. *Phys. Rev. A*, 68:065401, 2003.

[230] C. Figueira de Morisson Faria, X. Liu, and W. Becker. Coulomb repulsion and quantum-classical correspondence in laser-induced nonsequential double ionization. *Phys. Rev. A*, 69:021402(R), 2004.

[231] C. Figueira de Morisson Faria, H. Schomerus, and X. Liu. Electron-electron dynamics in laser-induced nonsequential double ionization. *Phys. Rev. A*, 69:043405, 2004.

[232] J. S. Parker. From the UV to the static-field limit: rates and scaling laws of intense-field ionization of helium. *J. Phys. B*, 42:134011, 2009.

[233] J. Caillat et al. Correlated multielectron systems in strong laser fields: A multiconfiguration time-dependent Hartree-Fock approach. *Phys. Rev. A*, 71:012712, 2005.

[234] C. Jhala and M. Lein. Multiconfiguration time-dependent Hartree approach for electron-nuclear correlation in strong laser fields. *Phys. Rev. A*, 81:063421, 2005.

[235] N. Rohringer, A. Gordon, and R. Santra. Configuration-interaction-based time-dependent orbital approach for ab initio treatment of electronic dynamics in a strong optical laser field. *Phys. Rev. A*, 74:043420, 2006.

[236] T. Kato and K. Yamanouchi. Time-dependent multiconfiguration theory for describing molecular dynamics in diatomic-like molecules. *J. Chem. Phys.*, 131:164118, 2009.

[237] S.-K. Son and S.-I Chu. Multielectron effects on the orientation dependence and photoelectron angular distribution of multiphoton ionization of CO_2 in strong laser fields. *Phys. Rev. A*, 80:011403(R), 2009.

[238] M. Spanner and S. Patchkovskii. One-electron ionization of multielectron systems in strong nonresonant laser fields. *Phys. Rev. A*, 80:063411, 2009.

[239] L. Nikolopoulos and K. Taylor. Combined R-matrix eigenstate basis set and finite-difference propagation method for the time-dependent Schrdinger equation: The one-electron case. *Phys. Rev. A*, 78:063420, 2008.

[240] O. Smirnova et al. Strong-field control and spectroscopy of attosecond electron-hole dynamics in molecules. *P. Natl. Acad. Sci. USA*, 106:16556, 2009.

[241] O. Smirnova et al. High harmonic interferometry of multi-electron dynamics in molecules, 2009.

[242] O. Smirnova et al. Attosecond Circular Dichroism Spectroscopy of Polyatomic Molecules. *Phys. Rev. Lett.*, 102:063601, 2009.

[243] M. Abu-samha and L. B. Madsen. Theory of strong-field ionization of aligned CO_2. *Phys. Rev. A*, 80:023401, 2009.

[244] S. Petretti et al. Alignment-Dependent Ionization of N_2, O_2, and CO_2 in Intense Laser Fields. *Phys. Rev. Lett.*, 104:223001, 2010.

[245] Y. Mairesse et al. High Harmonic Spectroscopy of Multichannel Dynamics in Strong-Field Ionization. *Phys. Rev. Lett.*, 104:213601, 2010.

[246] C. D. Lin et al. Strong-field rescattering physics−self-imaging of a molecule by its own electrons. *J. Phys. B*, 43:122001, 2010.

[247] W. Li et al. Visualizing electron rearrangement in space and time during the transition from a molecule to atoms. *P. Natl. Acad. Sci. USA*, 107:20219, 2010.

[248] R. Torres et al. Extension of high harmonic spectroscopy in molecules by a 1300 nm laser field. *Opt. Express*, 18:3174, 2010.

[249] Y. Huismans et al. Time-Resolved Holography with Photoelectrons. *Science*, 331:61, 2011.

[250] X.-B. Bian et al. Subcycle interference dynamics of time-resolved photoelectron holography with midinfrared laser pulses. *Phys. Rev. A*, 84:043420, 2011.

[251] L. Tao and A. Scrinzi. Photo-electron momentum spectra from minimal volumes: the time-dependent surface flux method. *New J. Phys.*, 14:013021, 2012.

[252] A. Scrinzi. *t*-SURFF: fully differential two-electron photo-emission spectra. *New J. Phys.*, 14:085008, 2012.

[253] S. Bauch, L. K. Sørensen, and L. B. Madsen. Time-dependent generalized-active-space configuration-interaction approach to photoionization dynamics of atoms and molecules. *Phys. Rev. A*, 90:062508, 2014.

[254] M. Ruberti, V. Averbukh, and P. Decleva. B-spline algebraic diagrammatic construction: Application to photoionization cross-sections and high-order harmonic generation. *J. Chem. Phys.*, 141:164126, 2014.

[255] E. Assémat, S. Machnes, and D. Tannor. Double ionization of Helium from a phase space perspective. http://arxiv.org/abs/1502.05165, 2015.

[256] H. R. Reiss and V. P. Krainov. Approximation for a Coulomb-Volkov solution in strong fields. *Phys. Rev. A*, 50:R910, 1994.

[257] D. G. Arbo et al. Coulomb-Volkov approximation for near-threshold ionization by short laser pulses. *Phys. Rev. A*, 77:013401, 2008.

[258] S. Basile, F. Trombetta, and G. Ferrante. Twofold Symmetric Angular Distributions in Multiphoton Ionization with Elliptically Polarized Light. *Phys. Rev. Lett.*, 61:2435, 1988.

[259] J. Z. Kamiński, A. Jaroń, and F. Ehlotzky. Coulomb effects in multiphoton above-threshold ionization. *Phys. Rev. A*, 53:1756, 1996.

[260] J. Z. Kamiński and F. Ehlotzky. Effective action approach to high-order harmonic generation. *Phys. Rev. A*, 54:3678, 1996.

[261] D. B. Milošević and F. Ehlotzky. Coulomb and rescattering effects in above-threshold ionization. *Phys. Rev. A*, 58:3124, 1998.

[262] A. Becker et al. Total ionization rates and ion yields of atoms at nonperturbative laser intensities. *Phys. Rev. A*, 64:023408, 2001.

[263] G. L. Yudin, S. Chelkowski, and A. D. Bandrauk. Coulomb continuum effects in molecular interference. *J. Phys. B*, 39:L17, 2006.

[264] G. L. Yudin et al. Attosecond photoelectron interference in the separable CoulombVolkov continuum. *J. Phys. B*, 40:F93, 2007.

[265] O. Smirnova et al. Coulomb–laser coupling in laser-assisted photoionization and molecular tomography. *J. Phys. B*, 40:F197, 2007.

[266] S. V. Popruzhenko et al. Strong Field Ionization Rate for Arbitrary Laser Frequencies. *Phys. Rev. Lett.*, 101:193003, 2008.

[267] O. Smirnova, M. Spanner, and M. Ivanov. Analytical solutions for strong field-driven atomic and molecular one- and two-electron continua and applications to strong-field problems. *Phys. Rev. A*, 77:033407, 2008.

[268] J. Kaushal and O. Smirnova. Nonadiabatic Coulomb effects in strong-field ionisation in circularly polarised laser fields. *Phys. Rev. A*, 88:013421, 2013.

[269] L. Torlina et al. Ab initio verification of the analytical R-matrix theory for strong field ionisation. *J. Phys. B*, 47:204021, 2014.

[270] L. Torlina et al. Interpreting attoclock measurements of tunnelling times. *Nat. Phys.*, 11:503, 2015.

[271] J. Kaushal, F. Morales, and O. Smirnova. Opportunities for detecting ring currents using an attoclock setup. *Phys. Rev. A*, 92:063405, 2015.

[272] N. Rohringer and R. Santra. Multichannel coherence in strong-field ionization. *Phys. Rev. A*, 79:053402, 2009.

[273] I. Barth and O. Smirnova. Hole dynamics and spin currents after ionisation in strong circularly polarised laser fields. *J. Phys. B*, 47:204020, 2014.

[274] J. Kessler. *Polarized Electrons*. Springer Atoms and Plasmas, 1976.

[275] G. N. Watson. *A Treatise on the Theory of Bessel Functions*. Cambridge University Press, 1922.

[276] M. Spanner et al. Reading diffraction images in strong field ionization of diatomic molecules. *J. Phys. B*, 37:L243, 2004.

[277] R. Murray, W. K. Liu, and M. Yu. Ivanov. Partial Fourier-transform approach to tunnel ionization: Atomic systems. *Phys. Rev. A*, 81:023413, 2010.

[278] I. Baz. Lifetime of intermediate states. *Yadern. Fiz.*, 4:252, 1966.

[279] R. Landauer and Th. Martin. Barrier interaction time in tunneling. *Rev. Mod. Phys.*, 66:217, 1994.

[280] E. H. Hauge. Tunneling times: a critical review. *Rev. Mod. Phys.*, 61:917, 1989.

[281] A. M. Steinberg, P. G. Kwiat, and R. Y. Chiao. Measurement of the single-photon tunneling time. *Phys. Rev. Lett.*, 71:708, 1993.

[282] A. L. Cavalieri et al. Attosecond spectroscopy in condensed matter. *Nature (London)*, 449:1029, 2007.

[283] E. P. Wigner. Lower Limit for the Energy Derivative of the Scattering Phase Shift. *Phys. Rev.*, 98:145, 1955.

[284] F. T. Smith. Lifetime Matrix in Collision Theory. *Phys. Rev.*, 118:349, 1960.

[285] M. Ivanov and O. Smirnova. How accurate is the attosecond streak camera? *Phys. Rev. Lett.*, 107:213605, 2011.

[286] J. M. Dahlström, A. L'Huillier, and A. Maquet. Introduction to attosecond delays in photoionisation. *J. Phys. B*, 45:183001, 2012.

[287] R. Pazourek, S. Nagele, and J. Burgdorfer. Time-resolved photoemission on the attosecond scale: opportunities and challenges. *Faraday Discuss.*, 163:353, 2013.

[288] A. Maquet, J. Caillat, and R. Taieb. Attosecond delays in photoionisation: time and quantum mechanics. *J. Phys. B*, 47:204004, 2014.

[289] U. Fano. Spin orientation of photoelectron ejected by circularly polarised light. *Phys. Rev.*, 178:131, 1969.

[290] T. Herath et al. Strong-Field Ionization Rate Depends on the Sign of the Magnetic Quantum Number. *Phys. Rev. Lett.*, 109:043004, 2012.

[291] Z. Walters and O. Smirnova. Attosecond correlation dynamics during electron tunnelling from molecules. *J. Phys. B*, 43:161002, 2010.

[292] C. F. Bunge, J. A. Barrientos, and A. V. Bunge. Roothaan-Hartree-Fock Ground-State Atomic Wave Functions: Slater-Type Orbital Expansions and Expectation Values for $Z = 2 - 54$. *At. Dat. Nucl. Dat. Tab.*, 53:113, 1993.

[293] A. A. Radzig and B. M. Smirnov. *Reference Data on Atoms, Molecules, and Ions*, volume 31 of *Springer Series in Chemical Physics*. Springer, 1985.

[294] G. E. Uhlenbeck and S. Goudsmit. Ersetzung der Hypothese vom unmechanischen Zwang durch eine Forderung bezglich des inneren Verhaltens jedes einzelnen Elektrons. *Naturw.*, 13:953, 1925.

[295] G. E. Uhlenbeck and S. Goudsmit. Spinning Electrons and the Structure of Spectra. *Nature*, 117:264, 1926.

[296] R. T. Cox, C. G. Macilwraith, and B. Kurrelmayer. Apparent Evidence of Polarization in a Beam of β-Rays. *Proc. Nat. Acad. Sci. USA*, 14:544, 1928.

[297] N. F. Mott. The Scattering of Fast Electrons by Atomic Nuclei. *Proc. Roy. Soc. A*, 124:425, 1929.

[298] N. F. Mott. The Polarisation of Electrons by Double Scattering. *Proc. Roy. Soc. A*, 135:429, 1932.

[299] E. Fues and H. Hellmann. *Phys. Z.*, 31:465, 1930.

[300] H. Frauenfelder and A. Rossi. *Meth. Exp. Phys.*, 5, 1963.

[301] P. S. Farago. The Polarization of Electron Beams and the Measurement of the g-Factor Anomaly of Free Electrons. *Adv. Electron. Electron Phys.*, 21:1–66, 1965.

[302] ed by M. Chatwell. *Proc. of the Workshop on Photocathodes for Polarized Sources for the Accelerators*. SLAC, 1993.

[303] J. L. McCarter et al. A low-voltage retarding-field Mott polarimeter for photocathode characterization. http://arxiv.org/abs/1003.5577, 2010.

[304] A. V. Subashiev et al. Spin-Polarized Electrons: Generation and Applications. http://www.slac.stanford.edu/cgi-wrap/getdoc/slac-pub-8035.pdf, 1998.

[305] H. C. Siegmann. Surface and 2D magnetism. *J. Phys. Cond. Matt.*, 4:8395, 1992.

[306] ed A. Boudard and Y. Terrien. *7th International Conference on Polarization Phenomena in Nuclear Physics*. 1990.

[307] B. Kaestner et al. Single-parameter quantized charge pumping in high magnetic fields. *App. Phys. Lett.*, 94:012106, 2009.

[308] V. Galitski and I. B. Spielman. Spinorbit coupling in quantum gases. *Nature*, 494:49, 2013.

[309] P. Lambropoulos. Spin-Orbit Coupling and Photoelectron Polarization in Multiphoton Ionization of Atoms. *Phys. Rev. Lett.*, 30:413, 1973.

[310] P. Lambropoulos. On producing totally polarized electrons through multiphoton ionization. *J. Phys. B*, 7:L33, 1974.

[311] M. R. Teague and P. Lambropoulos. Three-photon ionization with spin-orbit coupling. *J. Phys. B*, 9:1251, 1976.

[312] S. N. Dixit, P. Lambropoulos, and P. Zoller. Spin polarization of electrons in two-photon resonant three-photon ionization. *Phys. Rev. A*, 24:318, 1981.

[313] T. Nakajima and P. Lambropoulos. Electron spin-polarization in single-, two- and three-photon ionization of xenon. *Europhys. Lett.*, 57:25, 2002.

[314] E. Reichert and H. Deichsel. Spinpolarisation durch elektronen-resonanzstreuung an neon. *Phys. Lett. A*, 25:560, 1967.

[315] G. Busch, M. Campagna, and H.-C. Siegmann. Photoemission of Spin-Polarized Electrons from Ferromagnets. *J. Appl. Phys.*, 41:1044, 1970.

[316] H. Boersch, R. Schliepe, and K. E. Schriefl. Polarized electrons by Mott scattering at bulk targets. *Nucl. Phys. A*, 163:625, 1971.

[317] M. Spieweck et al. High-resolution experimental determination of the angular distribution and spin polarization of xenon 7d and 9s photoelectrons and comparison with theoretical results. *Phys. Rev. A*, 58:1589, 1998.

[318] G. G. Paulus et al. Measurement of the phase of few-cycle laser pulses. *J. Mod. Opt.*, 52:221, 2005.

[319] T. Barbec and F. Krausz. Intense few-cycle laser fields: Frontiers of nonlinear optics. *Rev. Mod. Phys.*, 72:545, 2000.

[320] S. T. Cundiff. Phase stabilization of ultrashort optical pulses. *J. Phys. D*, 35:R43, 2002.

[321] H. Niikura, F. Légaré, and R. Hasbani. Sub-laser-cycle electron pulses for probing molecular dynamics. *Nature*, 417:917, 2002.

[322] A. Baltuška et al. Attosecond control of electronic processes by intense light fields. *Nature*, 421:611, 2003.

[323] S. T. Cundiff and J. Ye. Colloquium: Femtosecond optical frequency combs. *Rev. Mod. Phys.*, 75:325, 2003.

[324] G. G. Paulus, F. Lindner, and H. Walther. Measurement of the Phase of Few-Cycle Laser Pulses. *Phys. Rev. Lett.*, 91:253004, 2003.

[325] E. Goulielmakis et al. Direct Measurement of Light Waves. *Science*, 305:1267, 2004.

[326] P. Agostini and L. F. DiMauro. The physics of attosecond light pulses. *Rep. Prog. Phys.*, 67:813, 2004.

[327] M. V. Berry and C. Upstill. IV Catastrophe Optics: Morphologies of Caustics and Their Diffraction Patterns. *Prog. Optics*, 18:257, 1980.